UC Irvine

UC Irvine Electronic Theses and Dissertations

Title
Exploring lipids with nonlinear optical microscopy in multiple biological systems

Permalink
https://escholarship.org/uc/item/2nm4q3vx

Author
Alfonso García, Alba

Publication Date
2016

Copyright Information
This work is made available under the terms of a Creative Commons Attribution License, availalbe at https://creativecommons.org/licenses/by/4.0/

Peer reviewed|Thesis/dissertation

eScholarship.org Powered by the California Digital Library
University of California

UNIVERSITY OF CALIFORNIA,
IRVINE

Exploring lipids with nonlinear optical microscopy in multiple biological systems

DISSERTATION

submitted in partial satisfaction of the requirements
for the degree of

DOCTOR OF PHILOSOPHY

in Biomedical Engineering

by

Alba Alfonso-García

Dissertation Committee:
Professor Enrico Gratton, Chair
Associate Professor Eric O. Potma
Assistant Professor Wendy Liu

2016

Portions of Chapter 5 © 2016 PLOS
Portions of Chapter 6 © 2015 Nature Publishing Group
Portions of Chapter 6 and Chapter 7 © 2016 SPIE
Portions of Chapter 7 © 2014 PLOS
All other materials © 2016 Alba Alfonso-García

TABLE OF CONTENTS

LIST OF FIGURES

LIST OF TABLES

ACKNOWLEDGMENTS

I would like to acknowledge the Balsells-Generalitat de Calatunya Fellowship for their financial support, as well as the National Institutes of Health (NIH) for the grants that have supported my research, including the P41-RR01192 (Laser Microbeam and Medical Program, LAMMP); and the funds from AFOSR (FA9550-10-1- 0538) from the collaboration with Prof. Petra-Wilder Smith.

I acknowledge I have reprint permission from the publishers of my work to incorporate that work in my dissertation. In particular I acknowledge permission from SPIE, PLOS, and the Nature Publishing Group. Individual contributions are pertinently cited.

I'd like to further thank the support, guidance, and encouragement of my advisers Prof. Eric Potma and Prof. Enrico Gratton, and of my committee member Prof. Wendy Liu. I wish to extend my gratitude to all the Potma Lab members. From Jeff and Richa, for welcoming me into the lab and guiding my first research steps, to Alex, for bringing fresh energy and support to my latest projects. I'd like to kindly thank Brian for being always available. I also appreciate the insights brought by the visitng scientstis in the lab during the past 5 years. I also want to express my gratitude to all the members of the Laboratory for Fluorescence Dynamics, with a particular emphasis to Rupsa, reliable collaborator and friend, and Milka, for all her help and teachings on cell culture. Especial thanks also go to the members of the Beckman Laser Insitute, including Prof. Bruce Tromberg, Tatiana, Mihaela, and Jue. Further colleagues I'd like to thank include the members of the Apkarian Lab and the CaSTL center, the Photonics@UCI family, Julia, Laura, Kevin, Aggie, and Tim. I want to acknowledge the BME and Chemistry department staff members as well, always helpful and diligent.

I would like to kindly express my gratitude to all my collaborators from UCI, including the Cinquin Lab; the Liu Lab; the Santos Research Group, especially Kim Gallagher; and from the Gavin Herbert Eye Institute, Prof. James Jester, Prof. Jerry Paugh, and Prof. Cristina Kenney. Also deep gratitude to my collaborators from the Helsinki University, Prof. Elina Ikonen, and Dr. Simon Pfisterer; from the University of Geneva, Prof. Howard Riezman, Dr. Ursula Loizides-Mangold, and Dr. Sophie Clment; and from the University of Colorado, Denver, Dr. Karen Jonscher.

Especial thanks to Bri McWhorter for guiding me to overcome my public speaking fears and to Prof. Roger Rangel for giving me the opportunity to share these experience with the rest of the Balsells fellows, to whom I also want to express my sincere gratitude, and extend it to Pete Balsells for creating these amazing opportunities for young catalan scientists and engineers.

Finally, I want to deeply thank my neighbors and friends for the many great moments, my family for staying close despite being overseas, and Robert, for his unconditional support. A tots, gràcies.

CURRICULUM VITAE

Alba Alfonso-García

EDUCATION

Doctor of Philosophy in Biomedical Engineering **2016**
University of California, Irvine *Irvine, CA, US*

Master of Science in Optics and Photonics **2011**
Karlsruhe Institute of Technology *Karlsruhe, Germany*

Bachelor of Sciences in Physics **2009**
Universitat de Barcelona *Barcelona, Spain*

RESEARCH EXPERIENCE

Graduate Research Assistant **2011–2016**
University of California, Irvine *Irvine, California*

Trainee **August 2011**
EMBL, Cell Biology and Biophysics group *Heidelberg, Germany*

Master Research Assistant **2010–2011**
Heidelberg University *Heidelberg, Germany*

Applications Development Intern **July–Oct 2010**
Leica Microsystems *Mannheim, Germany*

Master Research Assistant **2009–2010**
Karlsruhe Institute of Technology *Karlsruhe, Germany*

Research Intern **Summers 2008 and 2009**
ICFO - The Institute of Photonics Sciences *Castelldefels, Barcelona*

TEACHING EXPERIENCE

Teaching Assistant - Balsells class **2014–2015**
University of California, Irvine *Irvine, CA, US*

PUBLICATIONS

Ultrafast coherent raman scattering at plasmonic nanojunctions. **2016**
The Journal of Physical Chemistry C

Spaceflight activates lipotoxic pathways in mouse liver **2016**
PLoS ONE, 11(4)

Label-free identification of macrophage phenotype by fluorescence lifetime imaging microscopy **2016**
Journal of Biomedical Optics, 21(4)

D38-cholesterol as a Raman active probe for imaging intracellular cholesterol storage **2015**
Journal of Biomedical Optics, 21(6)

Plant growth conditions alter phytolith carbon **2015**
Frontiers in Plant Science, 6

Fluorescence lifetime imaging of endogenous biomarker of oxidative stress **2015**
Scientific Reports, 5

HCV 3a core protein increases lipid droplet cholesteryl ester content via mechanism dependent on sphingolipid biosynthesis **2014**
PLoS ONE, 9(12)

Biological imaging with coherent Raman scattering microscopy: a tutorial **2014**
Journal of Biomedical Optics, 19(7)

ORAL PRESENTATIONS

Visualizing cellular metabolic processes with combined nonlinear optical microscopy **Apr 2016**
Hollywood, FL, US

Targeting lipids with nonlinear microscopy **Oct 2015**
Cal Poly Pomona seminar invited speaker, Pomona, CA, US

Deuterated cholesterol uptake revealed with stimulated Raman microscopy **May 2015**
CLEO, San José, CA, US

Quantification of intracellular lipid droplets in plaque macrophages using coherent Raman scattering microscopy **Sep 2013**
OSA-IONS, Ensenada, Mexico

POSTER PRESENTATIONS

Assessing meibum quality in MGD subjects using stimulated Raman spectroscopy **May 2015**
ARVO annual meeting, Denver, Colorado, US

Characterizing the Nature and Distribution of Phytolith Organic Matter Using Raman Spectroscopy **Dec 2014**
AGU Fall Meeting, San Francisco, CA, US

Visualizing cellular cholesterol uptake with coherent Raman scattering microscopy **Feb; June 2014**
SPIE BiOS, Photonics West 2014, San Francisco, CA, US; EMBO workshop Cellular Imaging of Lipids, Vico Equense, Italy

Characterization of cholesterol crystals and intracellular lipid droplets using coherent Raman microscopy **Jul 2012**
Kern Lipid Conference, Vail, CO, US

Mean effective orientation of the source molecules in second harmonic imaging microscopy of collagen and muscle **Oct; Nov 2008**
LASERLAB Foresight Workshop and Users Meeting Trends of Laser Applications in Biology and Biomedicine, Heraklion, Crete, Greece; The Scientific Meeting of the Network of Excellence Photonics4life, Brussels, Belgium

ABSTRACT OF THE DISSERTATION

Exploring lipids with nonlinear optical microscopy in multiple biological systems

By

Alba Alfonso-García

Doctor of Philosophy in Biomedical Engineering

University of California, Irvine, 2016

Professor Enrico Gratton, Chair

Lipids are crucial biomolecules for the well being of humans. Altered lipid metabolism may give rise to a variety of diseases that affect organs from the cardiovascular to the central nervous system. A deeper understanding of lipid metabolic processes would spur medical research towards developing precise diagnostic tools, treatment methods, and preventive strategies for reducing the impact of lipid diseases. Lipid visualization remains a complex task because of the perturbative effect exerted by traditional biochemical assays and most fluorescence markers. Coherent Raman scattering (CRS) microscopy enables interrogation of biological samples with minimum disturbance, and is particularly well suited for label-free visualization of lipids, providing chemical specificity without compromising on spatial resolution. Hyperspectral imaging yields large datasets that benefit from tailored multivariate analysis. In this thesis, CRS microscopy was combined with Raman spectroscopy and other label-free nonlinear optical techniques to analyze lipid metabolism in multiple biological systems. We used nonlinear Raman techniques to characterize Meibum secretions in the progression of dry eye disease, where the lipid and protein contributions change in ratio and phase segregation. We employed similar tools to examine lipid droplets in mice livers aboard a spaceflight mission, which lose their retinol content contributing to the onset of nonalcoholic fatty-liver disease. We also focused on atherosclerosis, a disease that revolves around lipid-rich plaques in arterial walls. We examined the lipid content of macrophages, whose variable phenotype gives rise to contrasting healing and inflammatory activities. We also proposed new label-free markers, based on lifetime imaging, for macrophage phenotype, and to detect products of lipid oxidation. Cholesterol was also detected in hepatitis C virus infected cells, and in specific strains of age-related macular degeneration diseased cells by spontaneous Raman spectroscopy. We used synthesized highly-deuterated cholesterol to track its compartmentalization in adrenal cells, revealing heterogeneous lipid droplet content. These examples illustrate the potential of label-free nonlinear optical microscopy for unveiling complex physiological processes by direct visualization of lipids. Detailed image analysis and combined microscopy modalities will continue to reveal and quantify fundamental biology that will support the advance of biomedicine.

Chapter 1

Lipids

> "Any of various substances that are soluble in nonpolar organic solvents (as chloroform and ether), that are usually insoluble in water, that with proteins and carbohydrates constitute the principal structural components of living cells, and that include fats, waxes, phosphatides, cerebrosides, and related and derived compounds."[i]

Lipids are key components of the cellular machinery that enables life. Lipids provide structural support and are a source of energy to bring about the innumerable chemical reactions that cells perform untiringly. Phospholipids build the membranes that gives cells their integrity, and keep their organelles organized. Triglycerides are densely packed as energy reservoirs to be burned on demand. Lipids are thus critical for human life. They constitute over 10% of the human body mass (figure 1.1). Lipid related pathologies are on the top of the list of deadliest diseases, and account for billions of dollars in the medical and the pharmaceutical industries.

---

[i] Merriam-Webster's Learner's Dictionary

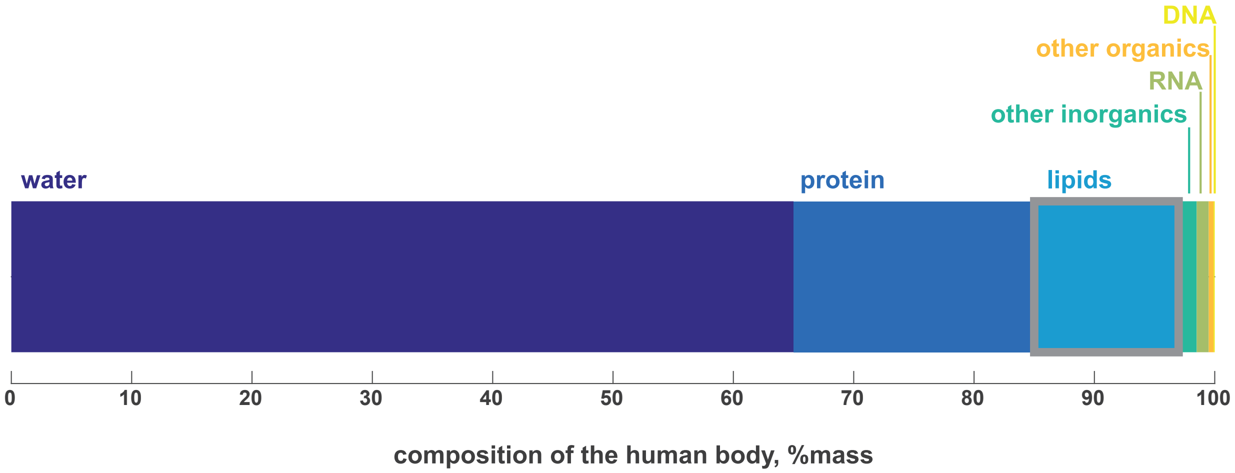

Figure 1.1: Chemical composition of the human body.

1.1 Classification of lipids

The previous broad and loose definition includes over 40,000 lipid structures, identified as of April 2nd 2015, according to the LIPID MAPS database. [ii], the largest public lipid-only database in the world

There are several strategies to classify lipids: according to whether or not they can be broken or hydrolyzed into smaller molecules (simple or complex lipids); according to their water solubility properties (polar, non-polar, or amphiphatic lipids), or in reference to their biosynthetic pathways[1]. The surge in bioinformatics has inspired a comprehensive and systematic classification of lipid structures based on the latter. LIPID MAPS proposes a comprehensive classification mainly based on the hydrophobicity of the chemical constituents of the various lipids. This classification allows for new lipids (natural and synthetic) to be included as they are being discovered (or synthesized). Table 1.1 shows the eight main categories of lipids based on the definition provided by Fahy et al.[2]:

> “Hydrophobic or amphipathic small molecules that may originate entirely

---

[ii] www.lipidmaps.org

Category	**Abbreviation**	**Example**
Fatty acyls	FA	fatty acids
Glycerolipids	GL	triacylglycerols
Glycerophpspholipids	GP	diacylglycerophosphocholines
Sphingolipids	SP	ceramides
Sterol lipids	ST	cholesterol
Prenol lipids	PR	carotenoids
Saccharolipids	SL	acylaminosugars
Polyketides	PK	flavonoids

Table 1.1: Lipid categories, abbreviations and examples. Adapted from[2].

> or in part by carbanion-based condensations of thioesters (fatty acids, polyketides, etc.) and/or by carbocation-based condensations of isoprene units (prenols, sterols, etc.)."

1.2 Cellular lipids

As one of the principal constituents of living cells, lipids are central in human health. Obesity, atherosclerosis, cancer, dementia and other neurodegenerative disorders, or developmental diseases arise from lipid abnormalities. The human body, and the living cell, exhibits a high degree of coordination to keep all the physiological systems working synchronously, that is to keep homeostasis [iii]. This includes the lipid network. Lipid homeostasis falters as a result of lipid excess, deficit, or malfunction of interacting pathways, among other causes, giving rise to the aforementioned diseases. In order to understand the rise of such disorders it is key to know how lipid metabolism [iv] is maintained. For that let us first briefly review the lipid composition, arrangements within the cell, and their transport and distribution around the body.

[iii] Homeostasis: the tendency towards a relatively stable equilibrium between independent elements as maintained by physiological processes.

[iv] Metabolism: the chemical processes that occur within a living organism in order to maintain life.

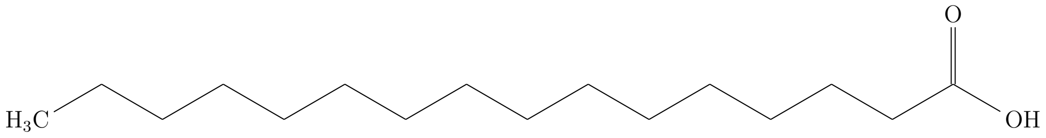

a. palmitic acid

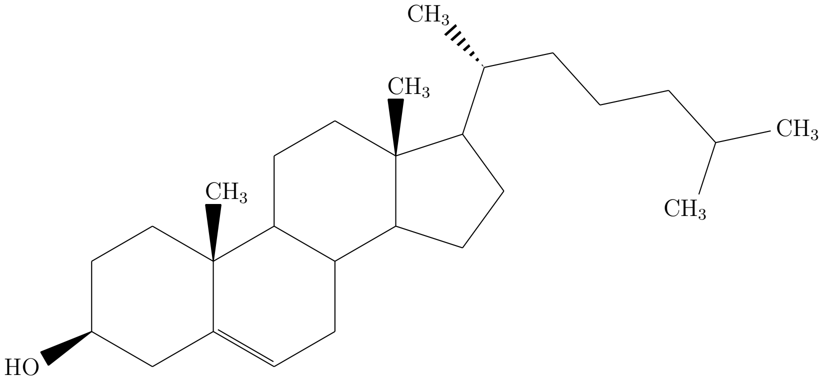

b. cholesterol

Figure 1.2: Example of a) an aliphatic lipid: palmitic acid, and b) a lipid structure with aromatic rings: cholesterol.

1.2.1 Composition and properties of lipids

Fats, oils, waxes, or hormones are some of the organic lipid-base compounds. Lipid structures are composed of sequences of hydrogen and carbon covalent bonds that can be arranged in aliphatic hydrocarbon chains, such as palmitic acid, or in aromatic rings, such as the ones present in the cholesterol molecule (see figure 1.2).

Lipids differ in the number of C-H bonds (the length of the chains or the number of rings), as well as in the additional functional groups that associate with the different subtypes. Fatty acids, for example, terminate with a carboxyl group (COOH), and can be saturated or unsaturated depending on whether they have only single carbon bonds or double carbon bonds, respectively. Waxes, on the other hand, are long chains of hydrocarbons linked through an ester oxygen to a long-chain alcohol. Glycerosphingolipids or sphingolipids are *amphipathic* lipids, they have a polar head with a glycerol and a phosphate group, and hydrophobic hydrocarbon tails. This bipolar character endows them with the ability of

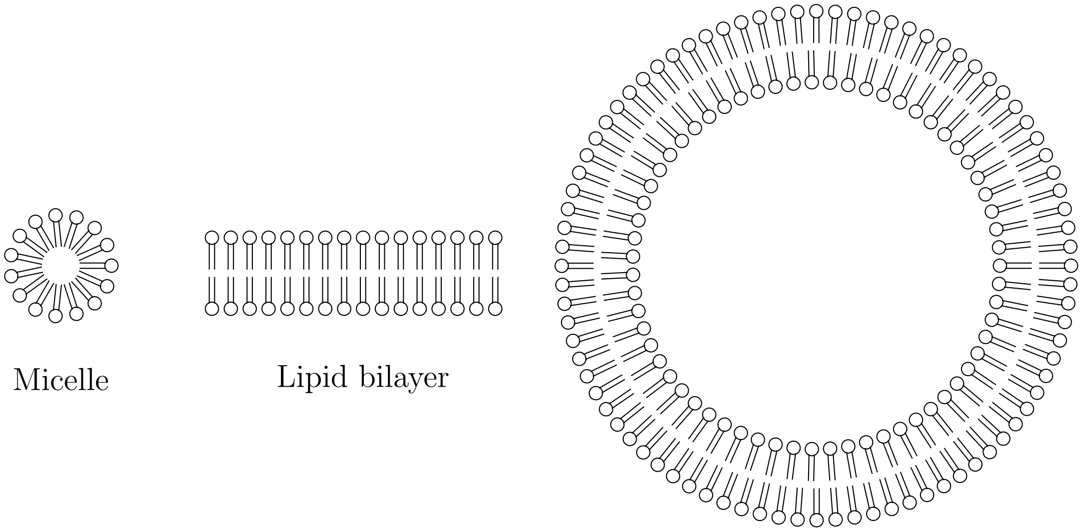

Micelle

Lipid bilayer

Vesicle

Figure 1.3: Phospholipid structures: micelle, lipid bilayer, vesicle.

forming spontaneous ordered molecular aggregates, such as micelles, bilayers, or vesicles (figure 1.3). This has a remarkable impact on life; it is the way membranes are formed and cellular compartmentalization is enabled.

The hydrogen-carbon covalent bonds store large amounts of energy. The average C-H bond energy (standard free energy-change) is 413 kJ/mol. Fatty acids group in threes to a glycerol molecule via an ester linkage to form triacylglycerols, which contain more energy than sugars. These are densely packed into lipid droplets in the cell cytoplasm. Lipid droplets where believed to be inert depots of neutral lipids[3], but the discovery of lipid associated proteins specific to the surface of lipid droplets[4] spurred research that unveiled them as dynamic, functional organelles.

1.2.2 Cellular organization and role of lipids

Lipids serve multiple functions in the living organism. They provide structural support as constituents of the cellular membrane, and the intracellular membranes that compartmentalize the cellular organelles. Glycerophospholipids are the main building blocks of membranes, while sterol lipids, and saccharolipids provide stability and add functionality. The cellular and intracellular membranes separate and compartmentalize biomolecular compounds, a strategy that protects against toxic events.

Lipids are stored in cells as energy reservoirs in the form of acylated amphiphilic alcohols, or neutral lipids (triacylglycerols and steryl esters)[5]. These lipids are insoluble in the cellular cytosol and are not able to integrate efficiently into the membranes, thus they pack into lipid droplets. Ever since 1991, when Constantine Londos' group recognized the existence of the protein perilipin[4], has the scientific community examined with detail the accumulations of lipids inside cells. The importance of this finding lays in the localization of this protein on the surface of such lipid accumulations, which the scientific community has named in a variety of ways: lipid droplets, lipid bodies, adiposomes, etc. In 2006, Martin and Parton made an attempt to unify the nomenclature and suggested the use of lipid droplet to refer to such lipid inclusions in the cytoplasm of cells[6]. Lipid droplets have a central core of neutral lipids, triglycerols and sterol esters in particular, and are lined by a monolayer of phospholipids decorated with free cholesterol and associated proteins, such as the primordial perilipin[5]. These dynamic organelles are involved in multiple physiological processes including lipid, hormone and vitamin synthesis, protein degradation and storage[7], and even virus replication[8,9]. Lipid droplets interact with other intracellular organelles such as the endoplasmic reticulum[10]. Despite all the research being done on this organelle in the last few decades, evidence remains weak and little is understood about their biogenesis, regulatory mechanisms, and interactions with other cellular organelles.

Lipids also serve as hormones. Steroids like cortisol and testosterone, or eicosanoids like arachidonic acid and prostaglandis, are molecules that act as chemical messengers within cells to regulate signal transduction pathways. Estrogen and testosterone are cholesterol derivatives that act as sex hormones for female and male, respectively. Aldosterone regulates blood pressure, and cortisol suppresses the immune system and regulates metabolism. Other hormones, not lipid based such as insulin[11] or leptin[12], also interact and aid in lipid metabolism tasks.

1.2.3 Lipid distribution circuit in the human body

Cholesterol and triglycerides are distributed throughout the body in lipoproteins that circulate in the blood stream (figure1.4). This general transport system delivers dietary lipids and begins in the liver. The system consist of a loop circuit with two branches: the Forward Cholesterol Transport (FCT) and the Reverse Cholesterol Transport (RCT). Ingested cholesterol and triglycerides are first transported from the gut to the liver and further processed to be delivered to the peripheral tissues (FCT). This distribution throughout the body happens through the blood stream. The excess of cholesterol is then returned to the liver, which secretes it into the bile acids and then cholesterol goes to the small intestines to be reabsorbed or excreted from the body (RCT). Neither cholesterol nor triglycerides are water soluble molecules and therefore they are encapsulated in lipoprotein (LP) particles. There are a variety of these LP particles, which can be classified according to their presence in specific parts of the lipid loop circuit. Their lipid and protein content also vary[13]. Briefly, chylomicron particles circulate from the intestine to the liver. Very low density lipoproteins (VLDL) are in charge of transporting cholesterol and triglycerides from the liver. Once VLDL lose their triglyceride content in adipose tissue, where it is stored in gross quantities for posterior energy consumption, cholesterol is still packed in low density lipoprotein (LDL) particles that travel towards the peripheral tissues. In there, LDL containing cholesterol gets internalized by the cells, where it is consumed for membrane construction or as hormone signaling messengers. Finally, the loop is closed by high-density lipoprotein (HDL) particles that bring the excess of cholesterol back to the liver (see figure 1.4)[14].

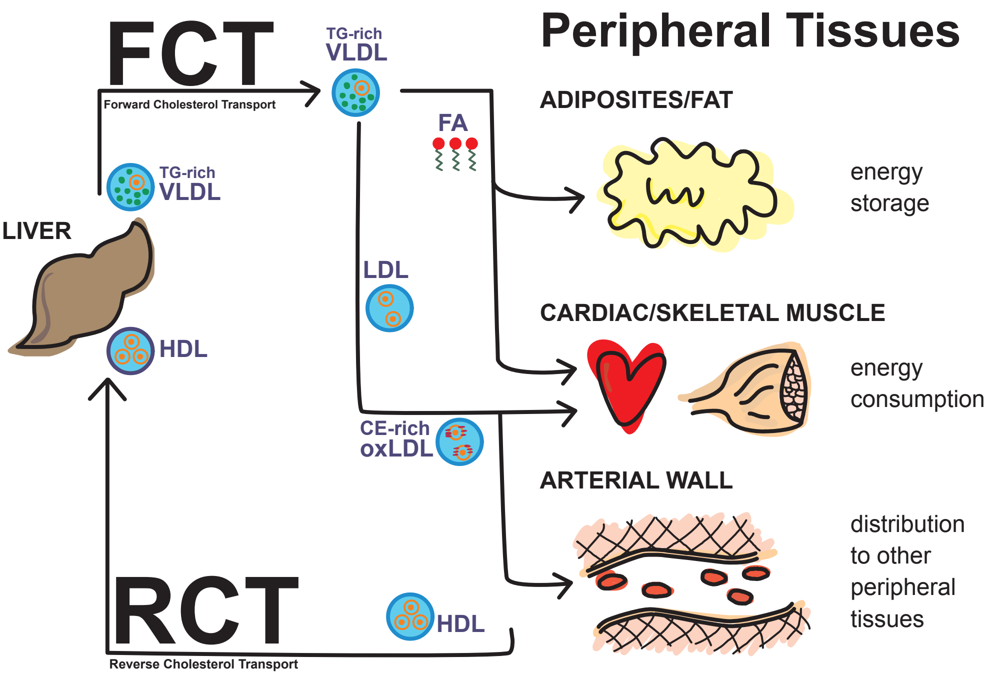

Figure 1.4: Forward and reverse cholesterol transport system. TG rich VLDL: triglycerides rich very low-density lipoprotein; LDL: low-density lipoprotein; CE rich oxLDL: cholesteryl ester rich oxidized LDL; HDL: high-density lipoprotein; FA: fatty acids. Adapted from[14].

1.2.4 Cellular lipid transport and distribution

At the cellular level, cholesterol is synthesized in the endoplasmic reticulum (ER) from acetyl CoA through the mevalonate pathway. Most of this newly formed cholesterol quickly leaves the ER to be distributed into the plasma membrane. Some of it goes through the Golgi first, following the biosynthetic secretory pathway. The cholesterol left in excess in the ER is esterified and stored into the core of cytoplasmic lipid droplets (LD) that protrude from the it (figure 1.5).

Cholesterol is, however, mostly taken up from diet, as are triglycerides. Receptor-mediated endocytosis delivers the dietary lipids packed in low-density lipoproteins (LDL) into the cells. The LDL receptor mechanism begins with clathrin-coated vesicles that take the lipids to sorting endosomes, which separate the particles from the receptor. The receptor protein is recycled back into the membrane, while the LDL particle is transferred into late endosomes to be hydrolyzed. Then, triglycerides, cholesteryl esters, and free cholesterol leave the endosomal system to be distributed into the plasma membrane, the ER, recycling endosomes, or mitochondria. It is still unknown where cholesterol goes first, given the lack of spatio-temporal resolution of traditional assays. Finally, cells eliminate excess cholesterol and triglyceride via exocytosis mechanisms that involve transmembrane proteins, such as the ABC transporter family (figure 1.5)[15,16] .

1.3 Lipid related disorders

Because of the broad impact that lipids have in the human body, alterations in lipid metabolism and transport contribute to many diseases, directly and indirectly. The human body harvests and stores lipids that are further consumed as energy, or membrane and hormone production. Lipid management is tightly regulated to maintain proper body function, otherwise disease may arise from altered lipid homeostasis. Both an excess or a deficit of fat are problematic for human health.

Obesity results from an unbalance between consumed and utilized fats. As a direct consequence, the non-utilized fat accumulates in excess in adipose tissues underneath the skin and around the vital organs, which compromises their function, and leads to serious lipotoxic associated diseases, such as insulin resistance and eventually type-2 diabetes[11]. Excessive triglyceride accumulation in the liver cells (hepatocytes) is the beginning of liver disorders from simple hepatic steatosis (fatty liver disease) to inflammation, fibrosis, and cirrhosis that ultimately leads to liver failure[17].

An excess or a deficit of cholesterol can be highly detrimental during embryogenesis as well as in adult life. A defect in cholesterol biosynthesis has been directly implicated in Smith-Lemli-Opitz syndrome that causes malformation, mental retardation or even death in

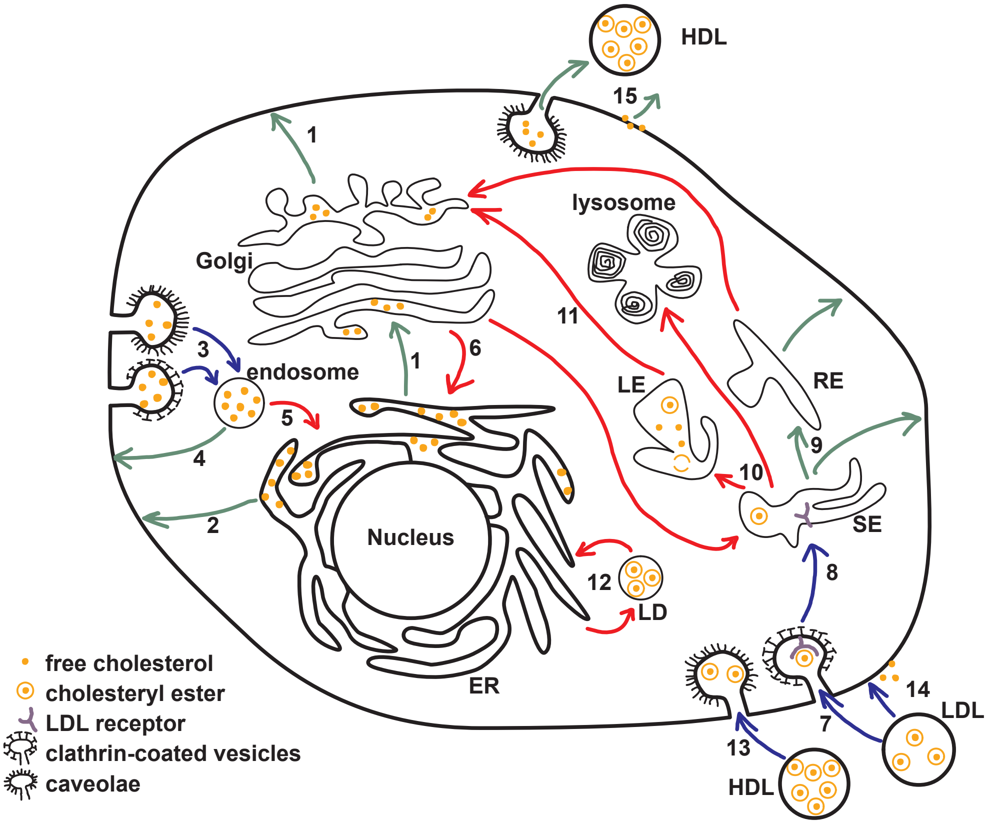

Figure 1.5: Cholesterol is synthesized de novo in the endoplasmatic reticulum (ER) and is transported from it to the Golgi apparatus and further to the plasma membrane (1). Another fraction of the newly formed cholesterol is directly sent into the plasma membrane (2). Cholesterol is also internalized by the plasma membrane via clathrin-coated vesicles and caveolae via endocytosis (3). These cholesterol molecules are transported into endosomes and from there recycled back to the plasma membrane (4) or brought to the ER (5). Pathways going from the Golgi back to the ER have also been described (6). Cholesterol mainly taken up from low-density lipoprotein (LDL) particles via clatherin-coated vesicles (7), which are transported into sorting endosomes (SE) where the LDL receptor is separated from the LDL particles (8). While the LDL receptors and a small fraction of free cholesterol are recycled back to the plasma membrane directly or via the recycling endosomes (RE) (9), the cholesteryl esters in the LDL particles go to late endosomes (LE) and lysosomes where they are hydrolyzed and free cholesterol is released (10). From the endosomes, free cholesterol is transported into the Golgi apparatus(11). Additionally, there is a tracking route from the ER to cytosolic lipid droplets (LD) and vice-versa (12) in which cholesterol is esterified and hydrolyzed. It has been noted that caveolae might be linked to cholesterol uptake from high-density lipoproteins (HDL) (13). In minor quantities, free cholesterol can also move from LDL directly to the plasma membrane (14). In a similar manner, the reverse way is also probable and it may also involve caveolae mediated exocytosis to HDL (15). Adapted from[16].

embryos[18]. Gallstones are composed of cholesterol, among other substances. Interestingly, cholesterol was first discovered in these masses[13]. Neurodegenerative disorders are also related to cholesterol defects. In fact, the brain is the organ with the highest cholesterol levels in the human body. Neurons and glial cells membranes, as well as the myelin sheaths, contain elevated quantities of cholesterol. A miss-regulation of cholesterol levels is implicated in dementia and Alzheimer's disease[19]. Importantly, heavily loaded cholesterol cores are the main feature of atherosclerotic plaques. Cholesterol buildup in the main arteries is the precursor for more serious cardiovascular diseases[20], including cardiac arrest and strokes, and the leading cause of death worldwide[21].

Indirect lipid related disorders include lysosomal storage disorders such as Niemann-Pick type A or B, linked to defects in the breakdown of lipids in late endosomes and lysosomes, which are intracellular trafficking vesicles that permit material transportation and exchange[22].

1.4 Lipid and fluorescence microscopy

The ability of visualizing lipids complements biochemical assays reporting on dynamic and in situ events by which we can learn how lipids behave and interact with other cellular components.

Lipid storage was first visualized with non-fluorescent dyes such as Sudan Black and Oil Red O that targeted the lipid bodies in cells. Sudan Black was first used in bacteria[23] and later applied to visualizing fat storage in c.elegans[24]. Sudan Black staining, however, requires fixation protocols that are not adequate for all kind of applications[25], and it cannot be combined with other labels[26]. Oil Red O (ORO) is also a common stain for lipid droplet imaging. Improved staining protocols even permitted its use in conjunction with other immunolabels. Specific detection methods appeared to circumvent the fact that ORO not only stains lipid droplets but it can also target phospholipids, in which case the emitted color is slightly different[26]. Further improvements set ORO as the gold standard for visualizing lipid droplets, and for identifying foam cells in atherosclerotic environments[27].

As one of the brightest ways to achieve chemical selectivity in cellular biology, fluorescence microscopy offers some lipid labels and analogues useful to track various types of lipid in living cells and organisms. Among them Nile Red and BODIPY-conjugated fatty acids stand out. Nile Red staining of intracellular lipid droplets in mammalian cells marked the point of adoption of this labeling technique[28], but this staining method is not specific enough; it labels not only neutral lipids in lipid droplets but also phospholipids, cholesterol, cholesteryl esters, and even free albumin.[29,30] BODIPY-conjugated fatty acids are used to monitor fatty acid uptake in mammalian cells[31], and BODIPY-cholesterol is used to detect the traffic of small cholesterol molecules[32,33], and to study lipid pathways in cells[34], and in larger organisms such as zebrafish[35] and c.elegans[36]. A compilation of lipid bodies staining protocols with fluorescent probes was provided by Melo et al.[3]

Imaging cholesterol was not possible in living cells due to a lack of suitable fluorescent probes that mimic cholesterol's biophysical and biological properties for a long time.[37] In the mid 1990's dehydroergosterol (DHE), a natural occurring fluorescent analog of cholesterol, was discovered[38]. Unfortunately, its requirements for far and near ultraviolet excitation light are inconvenient for extended biological applications. Also, its transport pathways differ from those of endogenous cholesterol, and its fluorescence properties highly depend on the local micro-environment[39]. Photobleaching occurs rapidly for DHE, which concentrates its applications in fluorescence recovery after photobleaching (FRAP) experiments[40]. Another widely used fluorescent label for cholesterol is filipin. Filipin is a naturally fluorescent compound that binds to cholesterol but not to cholesteyl esters, hence it allows for cholesterol detection in cellular membranes[41]. However it only permits qualitative analysis since its fluorescence is not proportional to the cholesterol content[39], and it doesn't allow live cell imaging because it perturbs the bilayer structure[41]. Laurdan is yet another fluorescent probe to study membrane lipids. As an environmentally sensitive probe it informs about the phase subdomains of membranes as they transform from gel to fluid[42]. Laurdan has extensively been used to analyze cholesterol content in the plasma membrane[43]. Other methods to image phospholipids include fluorescce from nitrobenzoxadiazole (NBD)-conjugates derivatives[44,45].

These fluorescent tags allow to visualize subtle changes of fat levels, but uptake and transport properties of these dyes, as well as their physical properties, determine the success of the visualization. Some studies have brought into question the reliability of these stains, as in multiple occasions they indicate trends contrary to those observed by biochemcial assays. Lipophilic dyes present several inconsistencies, and fixation artifacts. And incorporation of hydrophobic dyes can cause phase separation or induce lipid-raft formation that perturb cellular signaling[46–48].

In addition to the probes' reliability, fluorescent labeling of lipids have four main shortcomings[49]:

- Completeness and uniformity. Fluorescent agents such as Nile Red and Oil Red O distribute unevenly and sometimes can color non-lipid structures[30,50].
- Invasiveness. Some fluorescent agents interfere with cellular function.
- Photobleaching. All fluorophores photobleach over time, which limits the observation time window.
- Specificity. Contrary to proteins, lipids can not be transgenically labeled with fluorescent dyes, labeling needs to come from external agents, but not all lipids can actually be associated with one.

The ideal case scenario is to observe a system with minimal perturbation. For that, label-free methods are of interest. Autofluorescence form endogenous cellular compounds provide a means for examining metabolic processes as we will see in chapter 6. Coherent Raman scattering microscopy offers chemical sensitivity by exploiting intrinsic properties of the molecules to generate contrast, and it is at the center of the work presented in this thesis.

1.5 Lipid vibrations

Another way to differentiate lipids is to make use of their vibrational properties. Raman spectroscopy probes the vibrations of the chemical bonds in molecules. Every molecule has a set of vibrational resonances that constitute its molecular fingerprint or signature. In spite of such signatures, Raman spectra of molecules with similar motifs are fairly comparable, and difficult to differentiate. Proteins, for example, perform an extremely diverse set of functions, but exhibit only a limited set of chemical groups, resulting in negligible or extraordinarily subtle differences in their Raman spectra[49]. Lipids, on the other hand, are better suited to be discriminated based on their Raman spectra. The high concentration of lipids in biological samples (lipid droplets) makes lipids a good target for vibrational imaging. Lipids' Raman spectra stand out from that of other biomolecules because of their characteristic chemical structure, formed by carbon-hydrogen bonds arranged in chains or rings. These arrangements of carbon and hydrogen come in different flavors, each vibrating at a slightly different frequency. Methyl ($-CH_3$), methylene ($=CH_2$), and methine ($=CH-$) stretching modes define the CH-stretching range of the Raman spectrum (2800 to 3050 cm^{-1}) and are the source of strong Raman resonances, commonly used in vibrational imaging. The fingerprint region of the spectrum ($\sim$800 to 1800 cm^{-1}) is also populated with a diverse set of molecular vibrations that enables a deeper chemical analysis, as it contains resonances other than CH-stretching modes: bending or scissoring modes, and vibrations from bonds between other chemical groups that contain oxygen, nitrogen or phosphorus. A relation of the most common vibration modes used for the study of lipid structures is detailed in table

2.4.

Raman spectra of lipids can therefore be discriminated from other compounds in the biological samples, which enables chemical specificity. It is more challenging however, to discriminate between different lipid types, specially if they co-exist in the same focal volume. It is for that reason that Raman sensitive alternative markers have been developed. These include deuterium and alkyne labels. Replacing hydrogen by deuterium shifts the vibrational frequencies to a silent region of the Raman spectrum, devoid of endogenous resonances, enhancing the specificity of the probe. This approach has been used to visualize intracellular hydrodynamics in single living cells[51], to observe phospholipids as they undergo phase segregation in lipid bilayers[52,53], to distinguish among individual neutral lipids[54] or drug components[55]. More recently, de novo protein synthesis has been studied by incorporating metabolic deuterated amino acids in cells[56]. An alternative label to deuterium are alkyne-tags, that also vibrate within the silent portion of the Raman spectra (∼2000-2300 cm^{-1})[57–60].

Isotope labels are efficient Raman labels[61] as they

1. are very small - virtually the same size as the target molecule,
2. have a minimal chemical impact,
3. have a minimal disruption to the regular cell function, and
4. do not photobleach and persist during long timescale imaging.

For the above reasons, CRS microscopy is the chosen tool for biological imaging in this work. Lipids have strong vibrational signatures that permit rapid CRS imaging, facilitating studies that examine large tissue areas or large number of cells, as well as dynamic event or live samples. CRS microscopy enables chemical quantification of biological phenomena without compromising spatial resolution.

Chapter 2

Experimental techniques

Nonlinear optical (NLO) microscopy is gaining popularity as a standard technique for imaging biological samples in research laboratories around the world (see figure 2.1). It provides a minimally invasive method to visualize biological samples in a state close to their natural environment. The main characteristic of NLO microscopy is the nonlinear dependence of the signal with the incident light intensity, endowing this technique with very special qualities. For a nonlinear interaction of photons to occur, high photon densities are necessary, as well as temporal and spatial coherence. The nonlinear effect occurs only at the focal volume, where the probability that multiple photons are absorbed simultaneously by the sample is the highest. As a result, NLO microscopy techniques are capable of providing depth sectioning, and out-of-focus photodamage is practically nonexistent. In addition, longer wavelengths (near-infrared) can be used to achieve these nonlinear processes. Longer optical wavelengths are also beneficial for imaging biological samples, as they scatter less and thus penetrate deeper, which allows for imaging thick tissues. Moreover, water absorption can be neglected for near-IR light, this is important due to the large portion of water present in biological samples (figure 1.1). Finally, light emitted from nonlinear interactions is easy to discriminate from the excitation light, as they are spectrally apart. To achieve the high photon densities,

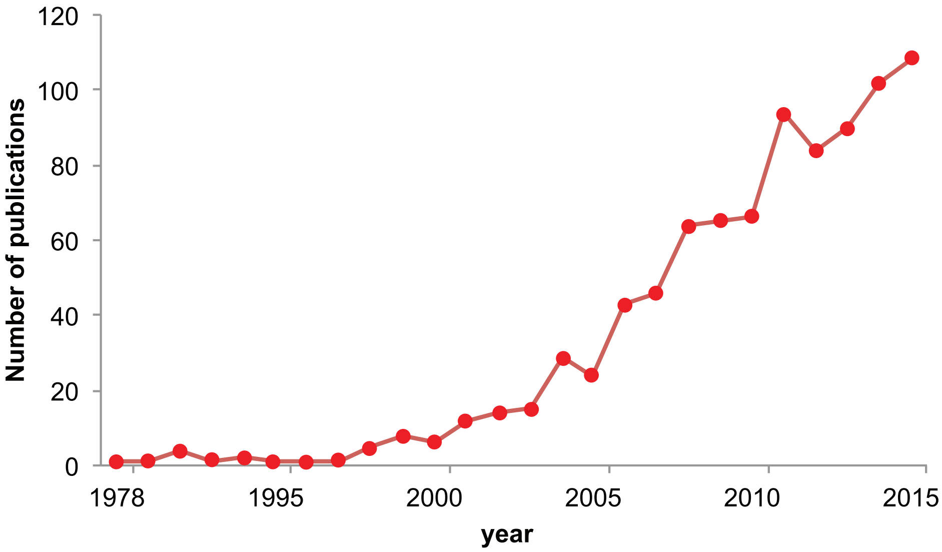

Figure 2.1: Number of publications on nonlinear optical microscopy, according to PubMed.

Technique	Avreb.	contrast mechanism
Two-photon excited fluorescence	TPEF	electronic motions
Coherent Raman scattering	CRS	vibrational modes
Second harmonic generation	SHG	non-centrosymmetric molecules
Third harmonics generation	THG	third-order susceptibility variations
Sum frequency generation	SFG	IR and Raman modes

Table 2.1: Listing of nonlinear optical microscopy techniques, their common abbreviations, and their contrast mechanism.

as well as the spatial and temporal coherence, high intensity light sources, such as pulsed laser light, are required[62]. Table 2.1 lists the most common nonlinear optical microscopy techniques and the contrast mechanism they rely on.

Coherent Raman scattering (CRS) microscopy is the principal focus of this thesis. Sporadically, and when the project so requires, second harmonic generation (SHG) and two-photon excited fluorescence (TPEF) were also used. In particular, TPEF was employed to study the lifetime of endogenous co-enzymes in live cells in a label-free approach to discriminate between cellular phenotypes (chapter 6).

The following sections describe the basics of CRS, starting with the spontaneous Raman scattering phenomenon. Coherent Raman scattering techniques are discussed next, followed by an introduction to fluorescence lifetime imaging microscopy (FLIM).

2.1 Raman microscpectroscopy

2.1.1 The Raman effect

Light scattering phenomena are routinely used to study light-matter interactions. The most basic scattering phenomena is known as Rayleight scattering. A photon with a given energy undergoes an elastic interaction with the material, and the emitted photon conserves this given energy. Rayleight scattering (figure 2.2 A) is relevant for interactions with heterogeneous media or particles much smaller than the wavelength of the incident photon. The scattered intensity is proportional to ν_o^4 or $1/\lambda_o^4$, where ν_o and λ_o are the frequency and the wavelength of the incident photon.

When the interaction results in an emitted photon with different energy than the incident, the process is inelastic. Raman scattering is an example of inelastic scattering. Given an incident photon of energy $h\nu_1$, there is a Stokes Raman scattering event when the emerging photon is of lower energy, or frequency $h\nu_S = h\nu_1 - h\nu_V$, producing a red-shift of the radiated light (figure 2.2 B). There is an anti-Stokes Raman scattering event when the radiated photon is of higher energy or frequency $h\nu_A = h\nu_1 + h\nu_V$, and there is a blue-shift of the radiated light (figure 2.2 C). The difference in energy of the incident and the emitted photons is due to the interaction with the vibrational states (of frequency ν_V) of the molecules on the sample. The spectrum of light scattered by each material will be different and representative of the molecules that in contains. It will always contain a portion of Rayleigh scattering at the incident wavelength as well, and it will have red- and blue-shifted sidebands, corresponding to the Stokes and anti-Stokes resonances, illustrated in figure 2.2 E.

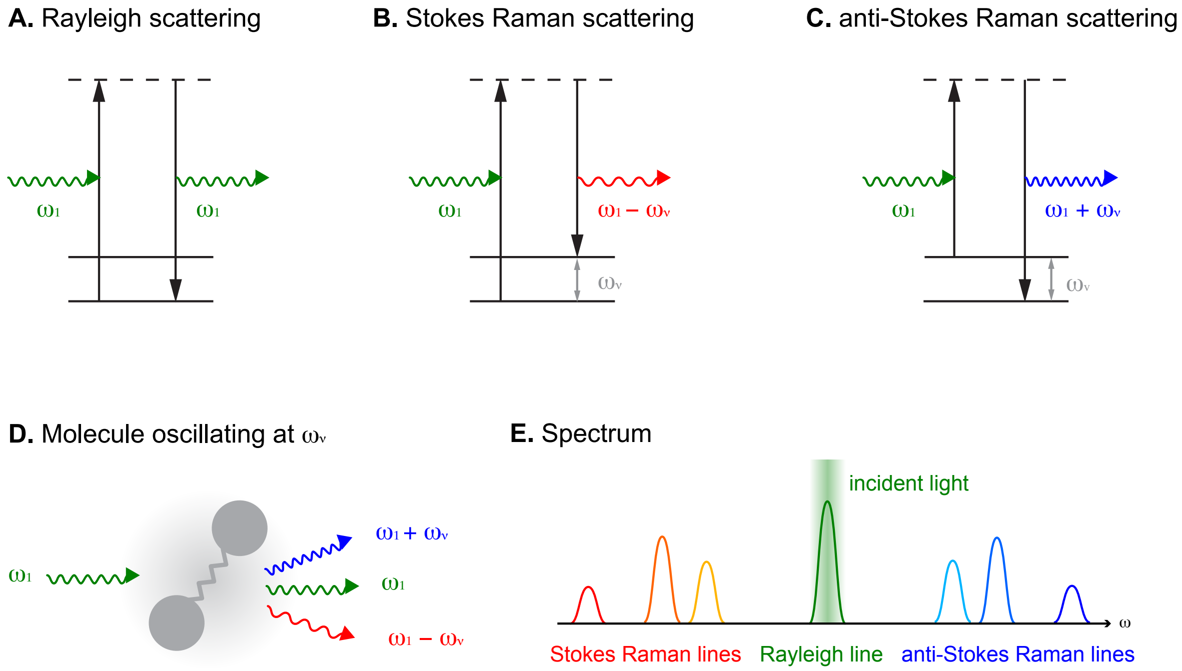

Figure 2.2: A) Rayleight scattering, B) Stokes Raman scattering, and C) anti-Stokes Raman scattering processes. D) Schematic of a vibrating molecule and all the scattered light. E) Schematic spectrum with the incident light, and the corresponding scattering lines.

Because of its inherent nature this type of scattering process is known as spontaneous Raman scattering and, although earlier predicted, it was first observed by C. V. Raman and K. S. Krishnan in 1928. In a short note to Nature[63], they described it as "a new type of secondary radiation" in the following situation:

> "...in every case in which light is scattered by the molecules in dust-free liquids or gases, the diffuse radiation of the ordinary kind, having the same wave-length as the incident beam, is accompanied by a modified scattered radiation of degraded frequency."

2.1.2 Properties of the Raman signal

As Raman and Krishnan pointed out, the so-called Raman scattering is very weak. They used a focused beam of sunlight as a "very powerful illumination" source to observe a *feeble* scattered light[63]. The intensity of the Raman signal ($I(\omega_S)$) is proportional to the cross section ($\sigma(\omega_S)$) of the sample molecules, which denotes the Raman scattering efficiency of these molecules,

$$I(\omega_S) = Nz\sigma(\omega_S)I_o \tag{2.1}$$

where N is the molecular number density, z is the length of the sample, and I_o is the intensity of the incident light. Note that typical cross sections of organic liquids are on the order of 10^{-29}cm^2, which corresponds approximately to 1 in 10 million photons that undergo Raman scattering if the incident light travels through 1 cm of liquid[64]. This analogy taken to the microscopic world of biology is translated into $\sim 10^5$ photons scattered per second when 10 mW of laser light passes through 1 μm^3 of organic liquid. Considering that the Raman signal is isotropic and we only detect in one direction, only a fraction of these photons will be eventually collected to acquire information, a fraction below 100 photons per millisecond.

Spontaneous Raman signal is linearly proportional to the incident power, and proportional to the number of oscillators in the sample, which makes it a quantitative technique. Spontaneous Raman is also an incoherent signal, because all the oscillators in the material vibrate independently with different phases, rendering the radiated waves uncorrelated with one another.

With spontaneous Raman scattering we can interrogate a sample at specific locations to learn about its chemical composition. It is even possible to raster scan the laser beam (or the sample) to create chemical maps, where each pixel contains not one intensity value, but an entire Raman spectrum. However, the properties of spontaneous Raman scattering complicate its use for biomedical studies, specially if imaging microscopy at rapid rates are relevant for the study. Coherent Raman scattering techniques, which are nonlinear and coherent, overcome some of the previous limitations, in particular, they are capable of fast imaging.

2.2 Coherent Raman scattering microscopy

2.2.1 CRS, a nonlinear optical process

Coherent Raman scattering (CRS) microscopy is based on the Raman effect, hence relies on vibrational contrast to generate chemical maps. Contrary to spontaneous Raman, CRS exhibits a nonlinear dependence on the incoming fields and produces coherent radiation. CRS microscopy takes full advantage of the coherent radiation that provides strong Raman signals and enables fast image acquisition. This last property is key for most biological imaging applications, and in particular for high throughput analysis and dynamic studies.

CRS signals find their origin in the dipole moment (μ) induced by the driving fields, which describes the motion of the electron displacement ($r(t)$) from the equilibrium position as:

$$\mu(t) = -e \cdot r(t) \tag{2.2}$$

where e is the charge of the electron. The addition of the dipole moments from the several molecules in the sample defines the macroscopic polarization as:

$$P(t) = N\mu(t) \tag{2.3}$$

where N is the number of electric dipoles per unit volume. The polarization can be written as a function of the driving electric field, which can be expanded as a power series because the relation between polarization and electric field also has nonlinear components:

$$P(t) = \epsilon_o \chi E(t) = \epsilon_o[\chi^{(1)}E(t) + \chi^{(2)}E^2(t) + \chi^{(3)}E^3(t) + ...] \tag{2.4}$$

where ϵ_o is the electric permittivity in vacuum, and $\chi^{(n)}$ the nth order of the material susceptibility.

Coherent Raman effects are $\chi^{(3)}$ processes, governed by the third order contribution of the polarization response of the material, that can be expressed in terms of the incoming fields as:

$$P_l^{(3)}(t) = \sum_{ijk} \chi_{ijkl}^{(3)} E_i E_j E_k \tag{2.5}$$

2.2.2 CRS signals

CRS probes Raman active vibrations. All the modes that are available with spontaneous Raman also exhibit CRS contrast. In this case, we drive the Raman vibrations by simulating the sample with two incident fields: the pump (E_p), and the Stokes (E_S), with frequencies ω_p and ω_S, respectively. When the difference frequency of these fields ($\Omega = \omega_p - \omega_S$) matches a resonance of the sample, namely a vibrational mode (ω_ν), four new frequency components are generated:

1. $\omega_S - \Omega$: coherent Stokes Raman scattering (CSRS).
2. $\omega_p - \Omega = \omega_S$: stimulated Raman gain (SRG).
3. $\omega_s + \Omega = \omega_p$: stimulated Raman loss (SRL).
4. $\omega_p + \Omega$: coherent anti-Stokes Raman scattering (CARS).

While the spontaneous Raman signal (figure 2.3 A) is linearly dependent on the intensity of the incoming field, CRS signals are nonlinearly dependent. The advantages of NLO microscopy apply to CRS. It is capable of depth sectioning, permits a deeper penetration depth, and has diminished photodamage compared to linear microscopy. The absence of photobleaching is also a competitive advantage with respect to fluorescence microscopy.

Spontaneous Raman is incoherent, each molecule has an electron cloud that oscillates independently and radiates at a different phase than the neighboring molecule. Conversely, CRS is a coherent technique. The phase of the electronic oscillations is driven by the incoming fields, thus all the molecules in the sample move in synchrony, with a well defined phase. This property has important consequences. First, the signal yield is greater than in a spontaneous Raman scattering process. Second, the signal is no longer isotropic, but it propagates in a well-defined direction, making it easier and more efficient to detected. These properties favor fast biological imaging.

2.2.3 CARS and SRS

We further concentrate on two out of the four frequency components generated in a CRS interaction, CARS and SRL.

Coherent anti-Stokes Raman Scattering (CARS; figure 2.3 B) signals scale with the intensities of three fields and exhibit a square modulus dependence on the material's nonlinear susceptibility (χ_{NL}). It also has a quadratic dependence on the number density, as a consequence of the coherent summation of the individual fields, making it much stronger than spontaneous Raman. Importantly, the CARS interactions generate at a brand new frequency (i.e. color): $\omega_p+\Omega$. This frequency can be detected with a photodetector provided the correct spectral bandpass filter precedes it.

The SRL signal, on the other hand, is emitted at the same frequency as one of the incoming fields, ω_p. The detection of SRL is based on the phase relation between this signal and the incident field. High-frequency modulation techniques allow to detect the imaginary part of the nonlinear susceptibility, assigning a linear dependence on χ_{NL} to SRL and making it dependent on the product of two intensities, rather than three, like it is for CARS. In this case, SRL signal is linearly dependent on the molecular number density. From now on we will refer to SRL as simply SRS (stimulated Raman scattering, figure 2.3 C).

Other relevant differences between CARS and SRS are summarized in table 2.2. Of particular interest is the nonresonant background contribution to the CARS signal, which is absent in SRS. This is to be considered when choosing between CARS or SRS for a particular application. In cases where the signal of interest is weak, SRS might provide a better

A. Spontaneous Raman scattering

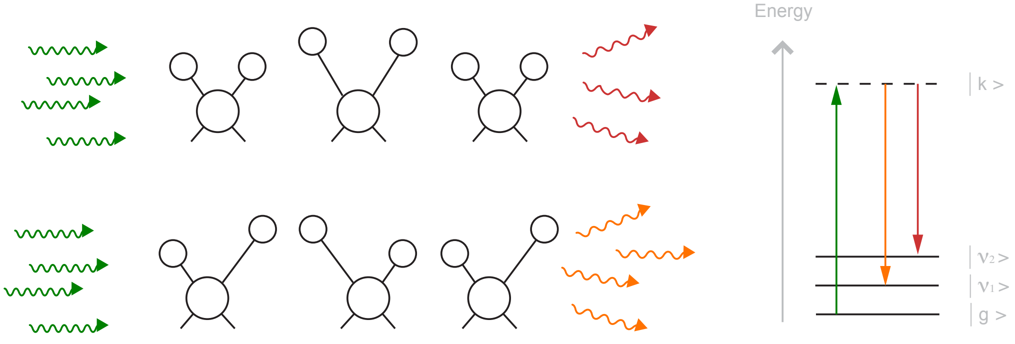

B. Coherent anti-Stokes Raman scattering (CARS)

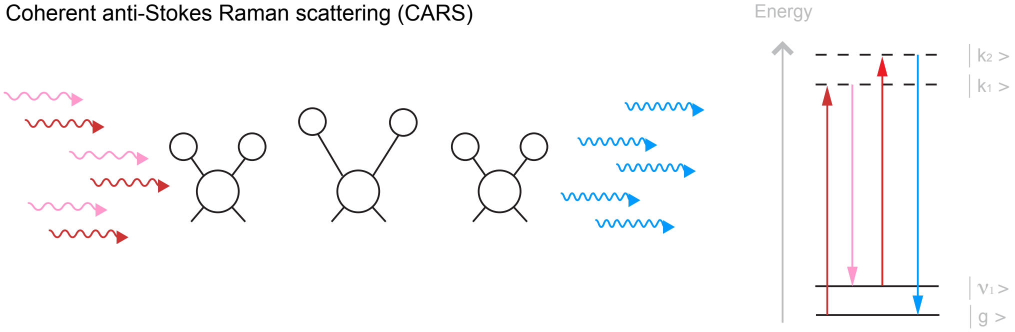

C. Stimulated Raman scattering (SRS)

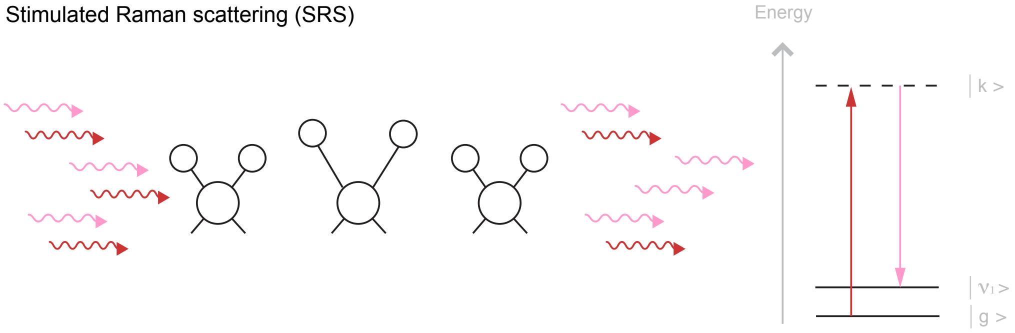

Figure 2.3: Schemcatic scattering representations and Jablonski energy diagrams for A) spontaneous Raman scattering, B) coherent anti-Stokes Raman scattering (CARS), and C) stimulated Raman scattering (SRS).

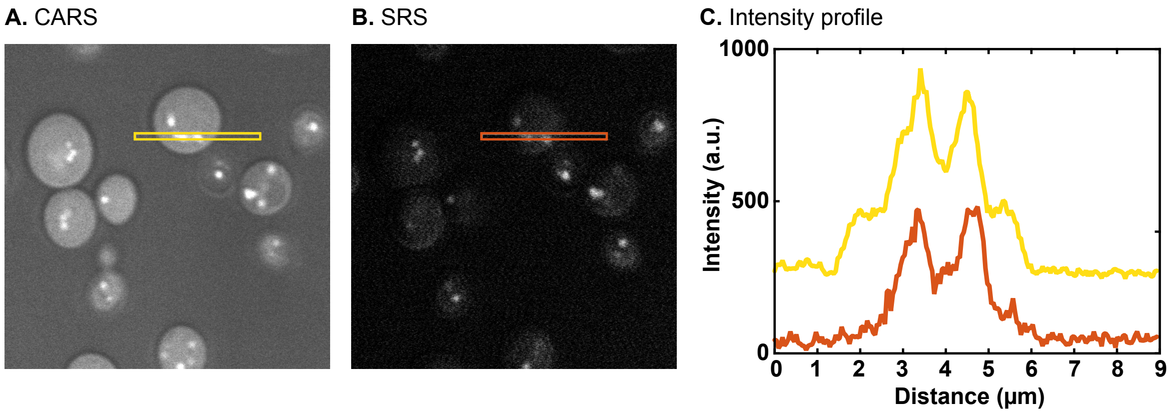

Figure 2.4: Nonresonant background in CARS and SRS. A) CARS and B) SRS images of yeast cells. C) Intensity profile of selected region of interest in each image.

	CARS	SRS
Type of process	parametric	energy transfer
Nonresonant background	Exist	Absent
Raman Spectrum	Distorted	Exact
concentration dependence	linear to quadratic	linear
Point spread function	Nonexistent	Existent
Fluorescence background	Contamination by two-photon	Not susceptible to

Table 2.2: Comparison of CARS signal and SRS signal, adapted from[66].

outcome due to its higher signal-to-background ratio. The nonresonant background in CARS, however, might be useful in some applications where a context image is useful, for example to delineate yeast cells outline (figure 2.4), or to identify macrophages or cells in liver tissue in order to count their lipid droplet content, as we will discuss in chapter 5. The capability to reconstruct the Raman spectrum also differs. SRS offers a straightforward method, whereas CARS spectra need to be fitted and further processed to resemble the Raman signatures[65]. For this reason we have chosen to use SRS microscopy to biochemically characterize the samples.

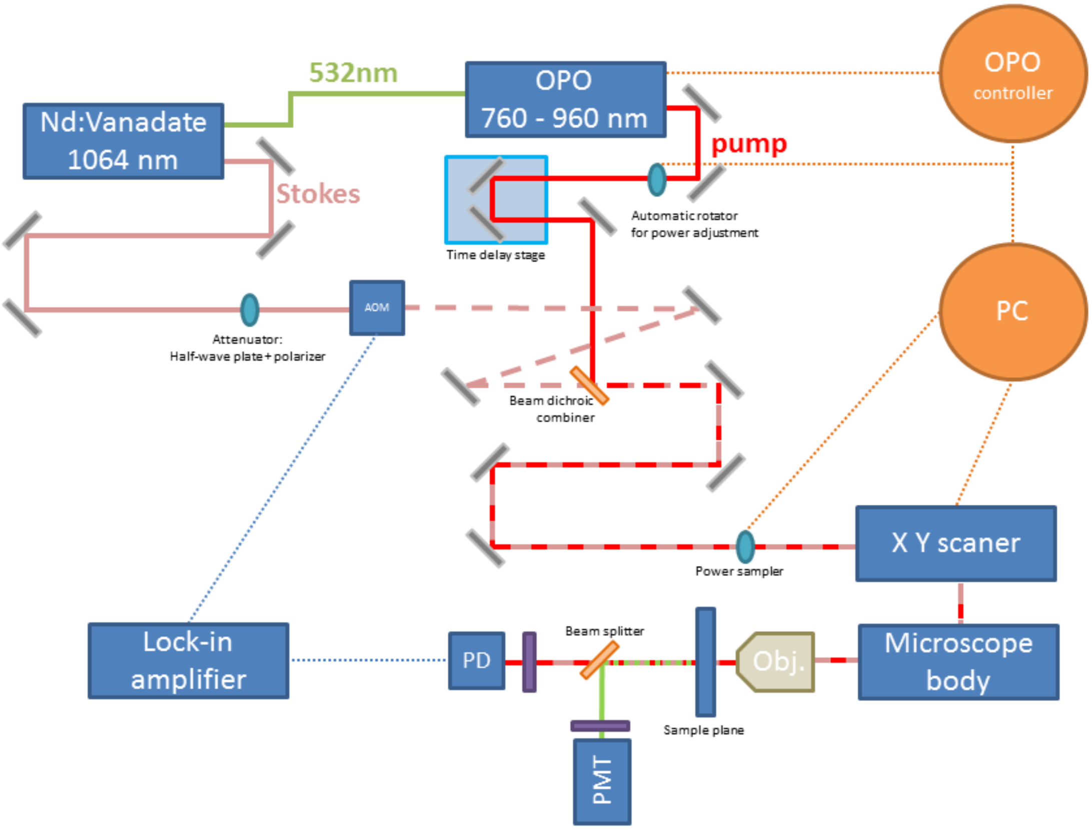

Figure 2.5: Coherent Raman Scattering microscope scheme. OPO: optical parametric oscillator; AOM: acousto-optic modulator; PD: photodiode; PMT: photomultiplier tube; Obj.: objective; PC: personal computer.

2.2.4 The CRS microscope

The CRS imaging system that we use for the applications in this thesis consists on 4 main modules: light source, optical path, scanner and microscope, and detection apparatus (see figure 2.5).

1. **Light source**

   A Mode-locked Nd:Vanadate laser (Picotrain; High-Q, Hohenems, Austria) with two outputs, one at 1064nm, the so-called Stokes beam, and another one at the second harmonic of the first one, 532nm, that is used to pump an optical parametrical oscillator

(OPO; Levante Emerald, Berlin, Germany). The output signal of the OPO is tunable from 700 to 980nm. The coarse tuning depends on the temperature of the OPO crystal and the fine tuning comes from the angle adjustment of a Lyot filter. At each OPO crystal temperature, a certain λ range, spanning from 6nm up to 10nm, is accessible by tuning the angle of the Lyot filter. Both lasers emit picosecond pulse trains at 76MHz repetition rate. Each pulse is 7ps at full width half maximum (FHWM).

2. **Optical path**

   The Stokes beam passes through an acoustic-optic modulator (AOM; Crystal Technology, Palo Alto, CA) that modulates the signal at 10 MHz, necessary to detect the stimulated Raman loss signal. The AOM is placed at the focal point of a telescope that expands the beam. Then, the Stokes beam passes through an iris diaphragm that blocks the zeroth order diffracted beam. We use the first order diffraction from the AOM because the zeroth order cannot be modulated to 100%. The Stokes beam is finally directed towards a dichroic beam combiner, where it is overlapped to the pump beam. The pump beam is provided by the OPO and is directed to a time-delay stage, used to temporally overlap the two beams. It is then steered to the dichroic beam combiner. The collinearly overlapped beams are sent to the microscope scanner with a set of mirrors.

3. **Scanner and microscope**

   The collinearly overlapped pump and Stokes beams pass through a laser scanner unit equipped with a set of galvanometer mirrors that scan the beam both in X and Y dimensions. The beam then enters the inverted microscope FluoView 300 IX71 (Olympus, Center Valley, PA) to finally pass though an objective and reach the sample at the sample plane.

4. **Detection**

   This system allows for 3 simultaneously imaged channels as previously mentioned.

> In the forward direction there is a photo-multiplier tube (PMT R3896; Hamamatsu, Hamamatsu City, Japan) used to detect CARS or SHG signal, depending on the filter placed in front of it. For detecting CARS we will use a 625nm filter with a 95nm bandwidth and for the SHG signal a 400nm filter with 40nm of bandwidth (Thorlabs, Newton, NJ). To detect the modulated pump intensity there is a photodiode (PD, FDS1010; Thorlabs) connected to a home-built lock-in amplifier that demodulates the signal. There is a short wave pass 945nm filter (Semrock, Rochester, NY) in front of the PD to block the 1064nm Stokes beam. In the backwards direction there is another PMT that can be used to detect E-CARS or additional TPEF.

Other setup configurations for CARS and SRS spectral imaging are based on spectral multiplexing and temporal focusing approaches. Multiplexing CARS or SRS require a femtosecond broadband source that provides the spectral bandwidth and a picosecond narrowband that determines the spectral resolution[67]. The SRS configuration required additional lock-in amplifier technology that complicates the instrumental setup significantly[68,69].Spectral focusing imaging is achieved by broadband laser sources and the time delay between the two lasers is scanned to obtain spectral resolution[70–73].

2.2.5 Hyperspectral SRS imaging

Hyperspectral SRS refers to the Raman spectrum reconstruction process carried out by SRS imaging. To achieve it in our setup, the pump frequency (ω_p) is swept across the desired portion of the spectrum that wants to be reconstructed. The tuning of the pump beam is possible by adjusting the crystal temperature, the lyot filter, and the cavity length of the OPO. Every time ω_p is tuned to a new position, the total laser power that goes into the sample is re-adjusted to be kept constant throughout the entire experiment. It is a straightforward procedure: set a pump frequency, adjust the power, take an image, change

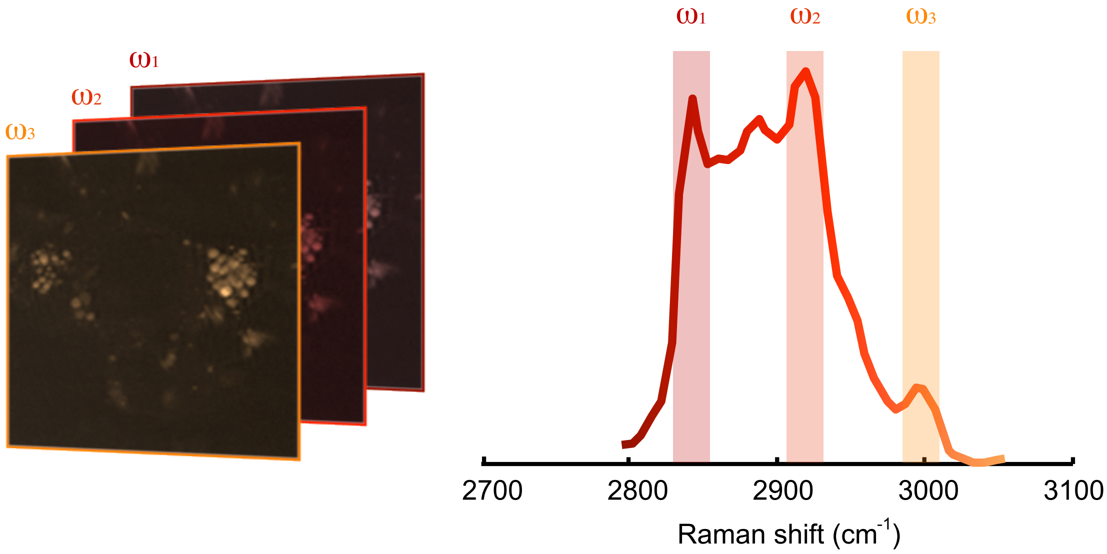

Figure 2.6: Schematic representation of hyperspectral SRS: images are collected at consecutive wavenumbers to reconstruct portions of the Raman spectrum. Depicted here the CH stretching band of a lipid droplet in Y1 adrenal cells and corresponding images acquired at three different colors ω_1, ω_2, ω_3, as examples.

	λ_p (nm)	Raman shift (cm^{-1})
CH band	820 to 803	2796.6 to 3054.8
CD band	880 to 855	1965.1 to 2297.4
Fingerprint	$\sim$ 900	$\sim$ 1600

Table 2.3: Pump wavelengths corresponding to the Raman shifts of interest for hyperspectral SRS interrogation at the CH, CH and fingerprint bands.

the pump frequency by a desired increment and repeat. By the end, a three-dimensional cube of images is generated, with spatial information on the x, and y axis; and chemical information on the z axis (figure 2.6).

Our setup is optimized for the CH stretching band, using wavelengths from 803 to 820 nm, but it is also capable to image in other useful windows of the Raman spectra, such as the CD band or the fingerprint (see table2.3).

Chapter 3 explores some methodologies to analyze these hyperspectral SRS data cubes.

Mode	Description	Raman shift range (cm^{-1})
CH def.	Methane deformation	~ 1440
C=C	conjugated carbon-carbon double bond stretch	~ 1590
C=C	carbon-carbon double bond stretch	~ 1660
C=O	ester bond stretch	~ 1730
CH_2-ss	Methylene symmetric stretch	2845 - 2850
CH_3-ss	Methyl symmetric stretch	2865 - 2875
CH_2-as	Methylene asymmetric stretch	2880 - 2910
CH-ss	Methane symmetric stretch	2900 - 2915
CH_3-as	Methyl asymmetric stretch	2960 - 2970
(C=)CH	Methane stretch	~ 3015

Table 2.4: Characteriztic vibrational bands of lipids.[74,75]

2.3 Raman contrast of lipids

Lipids have very specific Raman signatures due to their high concentration of CH bonds that vibrate at slightly different frequencies depending on the lipid specific structure. Chemical specificity is achieved by exploring the differences in the Raman spectra.

Due to their nature based on C-H bond interactions, lipids vibrate at well established frequency bands, namely the CH stretching band (from 2800 to 3100 cm^{-1}), and the fingerprint region (from 800 to 1800 cm^{-1}). These bands are charactersitic of different vibrational modes of the CH bonds or the CC bonds, compiled in table 2.4.

Quantitative information about the lipid composition of biological samples can be obtained form the analysis of the Raman spectra. The degree of saturation is measured by the relative intensity ratio between the double bond stretches and the methane deformations (I_{1660}/I_{1440}) in the fingerprint[76,77], or examining the peak at ~ 3015 in the CH stretching band[78]. The packing order of the lipid chains is estimated by the ratio between the symmetric CH stretching mode intensities (I_{2885}/I_{2850})[79]. The particular lipid class (sterol vs aliphatic) can also be inferred from the Raman spectra[80].

Figure 2.7 shows the Raman spectra from a variety cholesteryl esters, cholesterol, retinol,

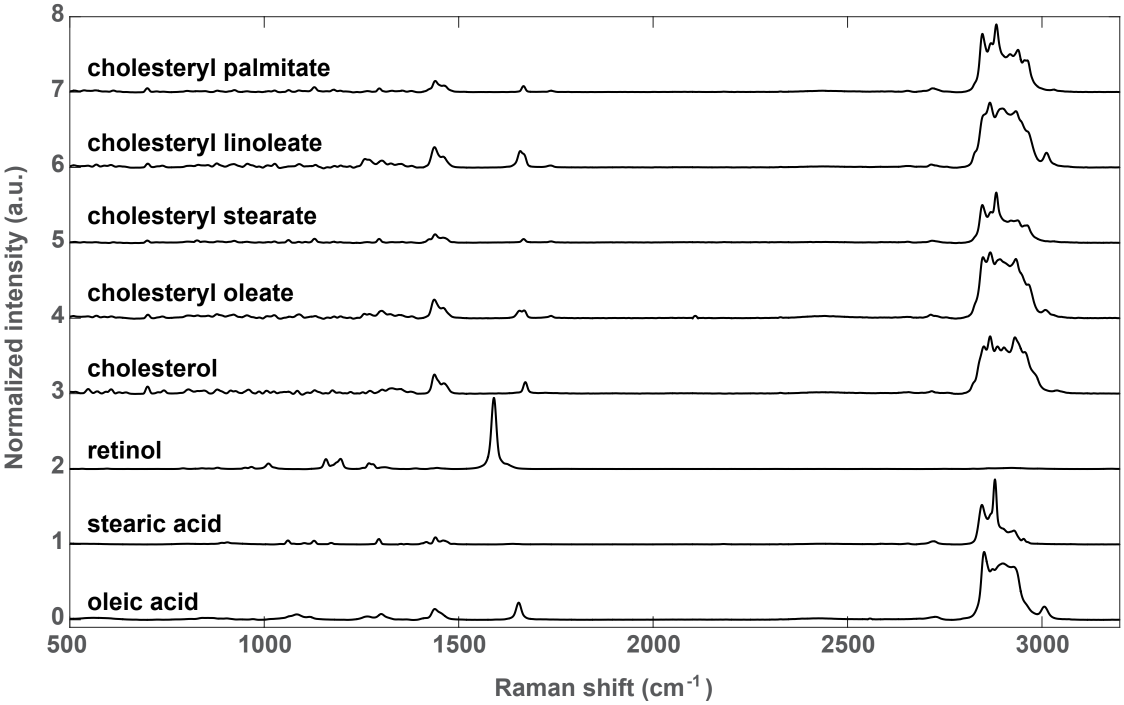

Figure 2.7: Raman spectra of cholesteryl esters, free cholesterol, retinol, stearic acid, and oleic acid.

and the fatty acids, stearic acid and oleic acids. Notice the prominent CH stretching band in all of them, except for retinol, whose conjugated double bond system has a Raman band at $\sim 1600\ cm^{-1}$ that overwhelms every other contribution. The ripples on the CH band are characteristic of every lipid, as is the relative intensities of the peaks in the upper fingerprint region (1200 - 1800 cm^{-1}).

2.4 Fluorescence Lifetime Imaging Microscopy

Fluorescence lifetime imaging microscopy contrast comes from the spatial variations of fluorescence lifetime within the imaged specimen. An excited molecule resides in the excited state for a few nanoseconds before relaxing back to the ground state. The relaxation process can be radiative, and thus emit a photon, or non-radiative. The molecular lifetime is defined by the average time the molecule spends in the exited state before returning to the ground state, by any pathway.

$$\tau = \frac{1}{\Gamma + k_{nr}} \tag{2.6}$$

where Γ is the rate of the emissive decay pathways and k_{nr} the rate of the non-radiative decays[81].

Lifetime measurements are advantageous over steady-state fluorescence intensities for multiple reasons. First, steady-state measurements are limited by spatial variations in the path length, light scattering effects, and available number of fluorophores. Second, the lifetime of a fluorophore is independent of its concentration. Third, the local microenvironment (pH changes, ion activity, energy transfer) affects the fluorophore lifetime, converting it into a sensor of the environment.

Time-resolved fluorescence measurements were pioneered by Sacchi's[82] and Fernandez's[83] groups in the late 1970's and 80's, but their lifetime measurements were performed in small regions of the samples. With instrumentation development lead by Alsins[84], Minami[85] and Kusurni[86] in the late 1980's, which improved instrumentation sensitivity, lifetime imaging microscopy became a reality. Oida et al. provided in 1993 the first description of a FLIM microscopy that acquired images based on time-resolved fluorescence measurements, which they called "flimscopy"[87]. In parallel, Gratton[88], Gadella[89], and Lakowicz[90] groups developed frequency domain FLIM approaches.

Fluorescence lifetime imaging microscopy (FLIM) measures the lifetime of fluorophores, independently of their intensity and concentration. Fluorescence lifetimes are typically on the order of nanoseconds, and depend on the structure of the fluorophore as well as their microenvironment (temperature, polarity, pH, etc.)[91].

The temporal evolution of the emitted fluorescence intensity can by described by a single exponential decay as:

$$I(t) = I_o e^{-\,t/\tau} \tag{2.7}$$

where I_o is the intensity at time $t = 0$, t is the time after the absorption, and τ is the fluorescence lifetime (equation 2.6).

Time-domain FLIM uses pulsed illumination to excite the molecules and trigger the exponential intensity decay, which is measured either by time-correlated single photon counting (TCSPC) or by gating strategies. The first option consist on recording the time in which individual photons are collected, and fitting a histogram of the individual events to an exponential decay function. The second option relies on detecting collections of different time windows of the decaying fluorescence intensity. Both techniques in the time-domain require to fit the data to exponential decays in order to obtain the lifetimes, a task that is tedious and often times challenging, specially for multi-exponential decays.

Frequency-domain FLIM employs high-frequency intensity modulated light sources and detection schemes for fast lifetime imaging acquisitions. In this case, the emitted fluorescence will follow the modulation patter of the excitation light with a phase shift (ϕ_ω) and an amplitude modulation (m_ω) that directly depends on the molecular lifetime (τ) and the modulation frequency of the light source (ω). See figure 2.8 for a schematic representation.

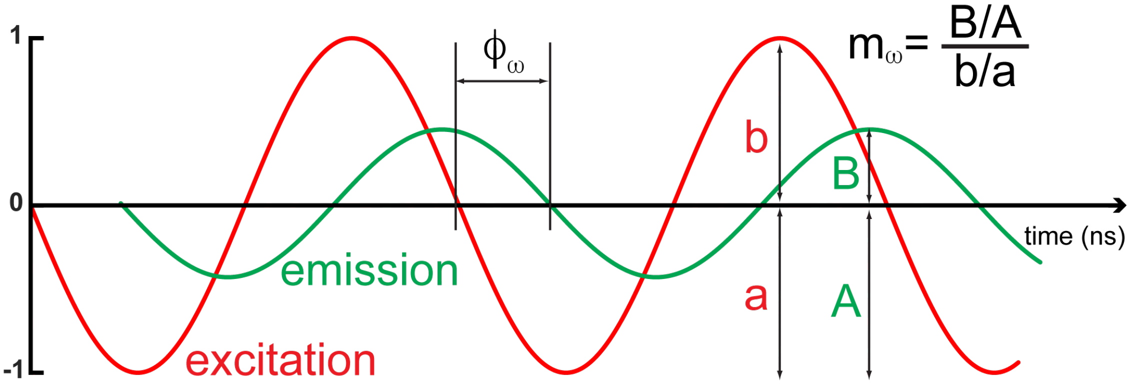

Figure 2.8: Frequency-domain FLIM. Sinusoidal excitation signal modulated at frequency ω, and emission signal with phase shift ϕ_ω and a modulation intensity m_ω.

$$tan(\phi_\omega) = \omega\tau \tag{2.8a}$$

$$m_\omega = \frac{1}{\sqrt{1+(\omega\tau)^2}} \tag{2.8b}$$

where $\omega = 2\pi f$, and f is the laser repetition rate[81].

A common method to visualize frequency-domain FLIM data is known as the phasor approach, in which the modulation and phase are represented in a polar plot where g is the horizontal axis, and s the vertical axis, such that

$$g(\omega) = m_\omega \cdot cos(\phi_\omega) \tag{2.9a}$$

$$s(\omega) = m_\omega \cdot sin(\phi_\omega) \tag{2.9b}$$

The coordinates $g(\omega)$ and $s(\omega)$ can also be represented as the components of the Fourier

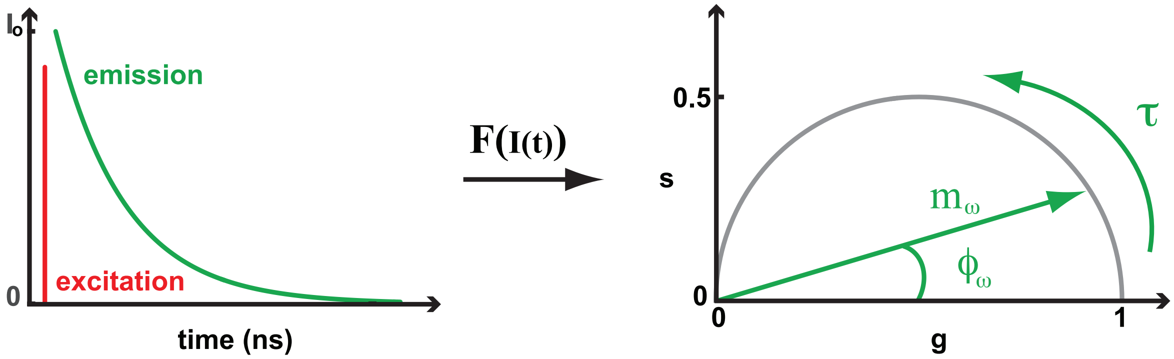

Figure 2.9: Fluorescence emission temporal evolution and the phasor approach given by the Frourier transform on the intensity decay. τ: lifetime, ϕ_ω: emission phase shift, m_ω: emission modulation intensity.

transformation of the fluorescence intensity variation with time (figure 2.9),

$$\int_0^\infty I(t)\mathrm{e}^{j\omega t}\,\mathrm{d}t = \int_0^\infty I(t)(cos(\omega t) - jsin(\omega t))\,\mathrm{d}t \tag{2.10}$$

normalizing by the total intensity:

$$g(\omega) = \frac{\int_0^\infty I(t)cos(\omega t)\,\mathrm{d}t}{\int_0^\infty I(t)\,\mathrm{d}t} \tag{2.11a}$$

$$s(\omega) = \frac{\int_0^\infty I(t)sin(\omega t)\,\mathrm{d}t}{\int_0^\infty I(t)\,\mathrm{d}t} \tag{2.11b}$$

In case the decay is characterized by a single exponential decay (as in equation 2.7)

$$g(\omega) = \frac{1}{1+(\omega\tau)^2} \tag{2.12a}$$

$$s(\omega) = \frac{\omega\tau}{1+(\omega\tau)^2} \tag{2.12b}$$

In case of multiple exponential decays contributing to the lifetime of a pixel,

$$g(\omega) = \sum_k \frac{f_k}{1 + (\omega\tau_k)^2} \tag{2.13a}$$

$$s(\omega) = \sum_k \frac{f_k \omega\tau_k}{1 + (\omega\tau_k)^2} \tag{2.13b}$$

where f_k is the intensity weighted fractional contribution of the component with lifetime τ_k[92].

This can be graphically represented in the complex plain, where single exponential decays are represented by phasors along a semicircle of lifetime 0 in ($g = 1$, $s = 0$), and infinite lifetimes in ($g = 0$, $s = 0$), the origin of coordinates (see figure 2.9). In this representation, samples with a lifetime defined by a multi-exponential decay will appear as phasors inside the semicircle. By the law of phasor addition, a bi-exponential decay will have a phasor along the line that joins the two single exponential decay components, that sit in the semicircle. For an element described by three exponential decays, the individual decays will form a triangle, and the resulting phasor will be within the triangle.[92,93] This representation can be mapped back to the image, where areas of similar composition will have neighboring phasors in the plot that can be grouped together and identified back in the image. This property simplifies the analysis and provides a fitting-free approach for identifying the areas of the image with similar and different lifetimes.

FLIM data can be acquired with two photon microscopy, which allows to probe endogenous fluorophores such as tryptophan or NAD(P)H. The lifetime of these fluorophores ranges from 0.1 ns to 7 ns, see table 2.5 for a detailed list.

The fluorescence lifetime images presented in this thesis were acquired with a Zeiss LSM

fluorophore	excitation (nm)	emission (nm)	lifetime (ns)
tryptophan	280 (mac) 250-310	350 (max)	3.03
NAD(P)H free	300-380	450-500	0.3
NAD(P)H protein bound	300-380	450-500	2.0-2.3
FDA	420-500	520-570	2.91
FDA protein bound	420-500	520-570	<0.01
lipofuscin	340-395	540, 430-460	1.34

Table 2.5: Endogenous fluorophore excitation, emission, and lifetimes values. Adapted from[91].

710 microscope (Carl Zeiss, Jena, Germany). A Titanium:Sapphire MaiTai laser (Spectra-Physics, Mountain View, CA) with 100 fs pulses and 80 MHz repetition rate was used as a two-photon excitation source at 740 nm. The laser light was focused through a 40x, 1.2 N.A., water immersion objective (Carl Zeiss, Oberkochen, Germany). The autofluorescence was detected with a photomultiplier tube (PMT; H7422P-40, Hamamatsu, Japan) after passing through a bandpass 460/80 nm filter. A dichroic filter at 690 nm served to separate the excitation from the emission signals. Fluorescence lifetime data were acquired using an A320 FastFLIM FLIMbox (ISS, Champaign, IL). The lifetimes of at least 100 photos per pixel were analyzed from 60 frames acquired per image at 3 mW of power in the sample plane. The scan speed was set at 25.21 $\mu s/pixel$, and the image size at 256 by 256 pixels, which span across 154 μm. The lifetime of rhodamine 110 was measured to calibrate the FLIM system, as it is established at 4 ns.

The SimFCS software, developed at the Laboratory of Fluorescence Dynamics (LFD, UC Irvine), was used to collect and process these FLIM data. As previously described, the fluorescence intensity decay associated to each pixel of the FLIM image is mapped into the two coordinates (g,s) system, the so-called phasor plot[92,93].

Chapter 3

Methodology

3.1 Big Data in microscopy

Big Data is nowadays a hot topic in many fields. With the Internet up and running for a couple of decades, the boom of social media platforms, and personalized mobile applications that curate incalculable amounts of personal data, new techniques to manage these datasets are blossoming. In biomedical applications Big Data is a concept that applies not only to the personal medical records and vital constants that now we can easily monitor with our smart-phones, watches (Apple watch[i], Samsung gear [ii]), or bracelets (Fitbit [iii]), but also to cell sequencing, such as genomics, with the gene sequencing becoming more affordable and mainstream[iv]. A study done in 2015 compared four Big Data domains, namely Twitter, YouTube, astronomy and genomics[94]. This study discussed the challenges that genomics will face in the near future in terms of data acquisition, storage, distribution, and analysis.

Microscopy was, in principle, not recognized as a Big Data generator, but this paradigm is

---

[i] http://www.apple.com/watch/health/

[ii] http://www.samsung.com/us/support/get-started/gear-s2/s-health/

[iii] https://www.fitbit.com/

[iv] https://cloud.google.com/genomics/

changing. With better computers and microscopes, traditional approaches fall short to handle the amount of data that scientists eagerly generate. Light-sheet microscopy, for example, is able to follow embryogenesis, and create *digital embryos* in which the nuclei position can be tracked during more than 24 hours, one minute at a time[95,96]. Superresolution microscopy also requires the acquisition of large amounts of data to resolve biological structures beyond the diffraction limit[97–99]. This opens the door to exploring a myriad physiological processes with very high spatio-temporal resolution. It is imperative that we set an infrastructure that is not only capable to acquire large amounts of information, but also manages it wisely and efficiently to obtain analytic results of out it, or else these data become futile.

As image processing tools thrive in other fields, and become faster and available, the microscopy community borrows and implements them with great success. A group at UCLA has recently created an integrated platform capable of imaging single cells and classify them without labels making use of deep learning analysis[100]. This method, that boosts performance compared to traditional flow cytometers (100.000 cells/s vs 2.000 cell/s classified, respectively), could be used in caner diagnostics, drug development studies, or to investigate biofuel production, to name a few.

We implement multivariate analysis and machine learning algorithms for chemical identification and segmentation of lipid features in large datasets of coherent Raman scattering images.

3.2 CRS image processing

A typical optical microscopy image is an array of intensities in the xy spatial plane. Often, a third dimension is added to explore the depth of the sample and to generate volumes. In vivo applications of optical microscopy in dermatology relay on the capacity to look deep below the skin surface[101]. For cell biology studies traditionally carried on the flat petri dish, this three-dimensional image modality is becoming popular. It allows to image the cells in an environment that better mimics their natural milieu. For example, tumors are three-dimensional masses whit specific properties to this geometry, which are not available when studying cancer cells in the two-dimensional plane[102,103]. In addition to spatial depth, biological dynamics are also of interest. Time series analysis become relevant to follow drug effects[55], or wound healing[104]. This makes the data package four-dimensional[105]. On top of it, chemical imaging techniques, like coherent Raman scattering microscopy, adds an extra layer of complexity, perhaps even in form of a fifth dimension, if all other dimensions are also explored. Brain tumors were detected with SRS microscopy in vivo inside the brain by rapid, label-free detection of endogenous markers imaged at different frequencies[106]. Combining nonlinear optical microscopy techniques provides multimodal information on biological samples, but also increases data analysis complexity[107]. It is an exiting time to develop image processing strategies capable of handling with detail all the multimodal and multidimensional images obtained with NLO microscopy.

Our typical multidimensional data space is composed by the spatial x and y coordinates, and the wavelength information along the third dimension. The main challenges we face in this work are: 1) the identification of lipid reservoirs, and 2) the (bio)chemical characterization of the samples. For its chemical selectivity and sensitivity, CRS is chosen to image lipids, with lipid droplets at the center of interest relevant to many lipid-related physiological process.

To address the first challenge, the CRS microscope was tuned at a specific frequency, usually the symmetric stretching vibration mode of the CH_2 bonds (2845 cm^{-1}). As a result, we obtain chemical images, where only these bonds densely packed into lipid droplets appear as bright objects. CARS is preferred in situations where we can benefit from the additional nonresonant background, for example, to add context to those lipid droplets and be able to identify the cell's nuclei and plasma membrane (see figure 2.4). SRS is preferred when the substance of interest is present at low concentrations, in which case the detected signals are so weak that a high signal-to-background ratio is imperative.

To tackle the second challenge the CRS microscope was used in the SRS mode. Hyperspectral SRS stacks directly reconstruct portions of the Raman spectrum. In this case, each image in the stack is taken at a different color (matched vibrational frequency), and the intensity plotted along the third-dimension of the data cube provides a direct representation of the Raman spectrum of the sample. CARS is also capable of reconstructing the Raman spectrum, but additional post-processing is required[65].

Both challenges, quantifying the lipid droplet properties in a biological system and analyzing the chemical composition of a sample, require the acquisition of hundreds, if not thousands, of images per project. These images contain themselves hundreds of features that can be used to describe the samples: morphological cues, localization parameters, chemical characterization, element interactions, etc. These are too many images and features to be processed one by one manually. Automated tools capable of handling big datasets such as machine learning techniques, commonly applied for image processing and speech recognition, become useful to our field.

Image segmentation methods are commonly applied for lipid droplet quantification. In section 3.3, we discuss an automated machine learning based scheme to detect intracellular lipid droplets and extract quantitative information. We used this method to examine the lipid metabolism of macrophages, cells of the immune system crucial in the progression of atherosclerotic plaques (chapter 5).

Adding the chemical characterization to the samples require a third dimension added to the spatial dataset: color. The generated spectral data can be examined in multiple ways depending on the prior knowledge of the sample and the ultimate goal of the analysis. We implement multivariate analysis, such as vertex component analysis (VCA), as a robust method to analyze spectral data. We combined VCA with other clustering algorithms and machine learning classification for deeper inspection of Meibum secretions (chapter 4). Deuterated cholesterol was specifically located within cells by means of VCA analysis (chapter 7).

3.3 Lipid droplet segmentation

High throughput studies are used to elucidate general trends on biological responses to specific behaviors, treatments, disease, etc., by means of statistical analysis. For that, hundreds or thousands of cells (in culture or as part of tissues) need to be imaged and analyzed in realistic time-frames. A star application for CRS in that realm is the analysis of lipid droplets. The objective is to monitor the changes in intracellular lipid deposits as a result of treatment.

At first, this seems an easy task. Lipid droplets are generally spherical organelles, that appear as very bright circles in the two-dimensional CRS image. A simple intensity threshold segmentation is, in first approximation, enough to acquire number and size of each lipid droplet. Automating the process to screen hundreds of images poses a question: do all the images respond well to the same intensity threshold? If the images were taken with the exact same imaging parameters maybe yes, but even in that case, slight laser power fluctuations, non-homogeneous sample illumination, and inherent sample inhomogeneities rule a more realistic no. Also, lipid droplets might not be well isolated and surrounded by a dark cellular background, but rather clustered on top of each other. Lipid droplets tend to have heterogeneous sizes when lipid metabolism is altered, they can be as small as < 1 μm or as large as 10 μm diameter bodies, or can even present themselves as puddles of lipid irregularly shaped. These inhomogeneities call for more sophisticated approaches.

In 2008, Hagmar et al. compared four theoretical models for lipid droplet segmentation of CARS images[108]. They conclude that a simple global thresholding approach is insufficient for CARS images, as it underestimates the droplet size or misjudges the weaker entities. Their analysis shows that watershed and level set segmentations work alright for well-defined objects, but that the best approach for complex biological samples is local thresholding. The same group applied this approach to analyze the lipid droplets in yeast cells a year later[109]. A different approach was taken by Vogler et al. to segment CARS images[110]. They perform an exhaustive analysis of the intensity histograms of the images to differentiate between the different contrast mechanisms that contribute to the CARS image, namely interference effects, nonresonant background, and the vibrationally resonant signal. All these methods are still not automated. Medyukhina et al. set the basis for an automated segmentation of CARS images in their 2012 work, in which they make use of gray-scale and intensity gradient information to segment cells and nuclei in nonlinear microscopy images[111]. In 2013, Chen et al. presented a fully automated image analysis method based on maximum entropy thresholding (MET) to quantify intracellular lipid droplets[112]. These are only a handful of examples that illustrate the evolution of the task: from simple global thresholding tests in an image per image basis, to more sophisticated automated approaches.

Indeed, thresholding-based segmentation methods are well suited for processing lipid droplet images, where droplets appear as bright objects on a dark background[109,112,113]. For CARS images, where lipid droplets display a wide range of pixel intensities compared to the background, it is difficult to select one unique threshold that separates foreground pixels from background pixels[108]. To this end, we have developed a novel image segmentation algorithm to process CARS images of lipid droplets that relies on machine learning based classification.

The algorithm that we use first assumes that all lipid droplets have one unique local maximum. Watershed transformation is then applied to separate the image into distinct regions of interest that have either one or zero lipid droplets. The intensity threshold to delineate each lipid droplet differs in each region of interest and is computed by optimizing the difference of local foreground to background intensities. This generates candidate segmentations for

Image Specific	Lipid droplet specific	
	Shape-based features	Intensity-based features
percentile	area, convex area	Statistics on the intensity of pixels inside the segmentation
skewness	eccentricity, axis lengths	Statistics on the intensity of pixels outside the segmentation
kurtosis	solidity, curvyness	Comparison of the previous

Table 3.1: Lipid droplet segmentation features for the machine learning algorithm used in chapter5 to count lipid droplets in macrophages.

Image #	True Positives	False Positives	False Negatives	Recall	Precision
32	79	18	20	0.798	0.8144
218	8	3	3	0.727	0.727
376	217	12	20	0.916	0.948
564	374	47	34	0.917	0.888
1679	111	45	21	0.841	0.712
3136	487	2	91	0.843	0.996
TOTAL	**1276**	**127**	**189**	**0.871**	**0.9095**

Table 3.2: Validation parameters from the lipid droplet segmentation algorithm. Total data set = 3833 images. Precision = 90.95%, recall = 87.10%.

every region of interest, regardless of whether the region contains zero or one lipid droplet. To identify the candidate segmentations that truly contain a lipid droplet we train a classifier (the list of features is given in table 3.1).

With the classifier output and additional cell segmentation we obtain the number of lipid droplets in every single cell we imaged (see Figure 5.4), and their physical properties such as size and intensity. A validation analysis concluded this method has a precision of 90.95% and a recall of 87.10% (figure 3.1 and table 3.2.).

This algorithm was implemented to analyze the lipid droplet content of individual macrophages with distinct phenotypes in chapter 5.

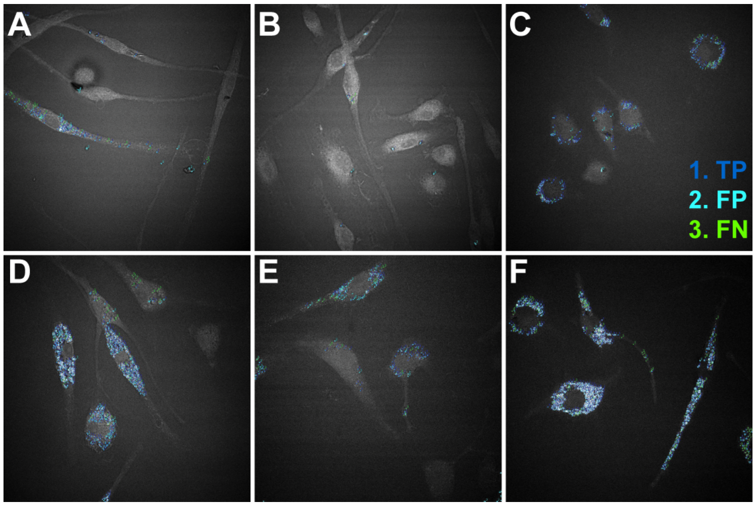

Figure 3.1: Subset of images used for validating the lipid droplet segmentation machine learning algorithm.

3.4 Spectral analysis

Hyperspectral SRS images are typically three-dimensional data cubes. In our case, the first two dimensions belong to the traditional x and y spatial coordinates of an image, while the third dimension is reserved for the spectral features (color λ or frequency ω). The data cubes are intensity arrays, where each plane reconstructs an image with a single type of molecular vibrations - characterized by a color, and the depth collects information from the different colors, or molecular vibrations in the samples. These datasets are on the order of millions of data points. In our case, with a typical image size of 512 by 512 pixels, and about 40 points per spectra, we surpass the 10M data points for a single hyperspectral SRS (hsSRS) image. This number rapidly increases with the progression of an experiment. It can be even larger, if a third spatial dimension is of interest (four-dimensional data sets) or even if time series analysis is required (i.e. dynamic studies; up to five-dimensional data sets). It is imperative to find global solutions to manage and treat all the data in a systematic and reliable way.

Chemical maps result from linear analysis when the system composition and spectral calibration of the individual chemical species are available. The lack of such information makes multivariate analysis the preferred choice. The downside is that given no ground truth it is difficult to asses the accuracy of the interpretations. Multivariate analysis (MVA) include data reduction algorithms such as principal component analysis (PCA), or spectral unmixing methods such as vertex component analysis (VCA). MVA methods have previously been used in confocal and coherent Raman studies. For example, VCA was applied to confocal Raman microscopy images to track the distribution of polyemers in plant cells[114]. PCA was applied on hyperspectral CARS to identify cholesterol crystals in atherosclerotic plaque[115]. A less common approach was taken by Fu and Xie when they borrowed for CRS data the phasor approach more commonly applied in FLIM and FRET microscopy[116]. They presented a cell segmentation approached based on spectral phasor analysis of the hyperspectral SRS scans. Shortly, the spectral data can be Fourier transformed into a polar plot representation in which each point represents a full spectrum at a particular pixel. Clusters of phasors can be mapped back to the image to identify areas of closely resembling Raman spectra, providing a chemical segmentation of the image. Machine learning algorithms have also been applied to Raman[117] and to CARS[118] microscopic images to identify subcellular compartments using florescence images for training purposes.

Every project has different needs, so the metrics we are ultimately interested in differ, and most importantly, so does the nature of the samples. In spite of that, there are specific commonalities that can be exploited to generate standard ways to retrieve data from hsSRS images. All the analysis that follows has been implemented in Matlab and is tailored to the images acquired by our CRS setup.

3.4.1 Data preparation

We collect SRS images either manually or with the the lab-built *specscan.py* python code that automates the process. As a result N images in *.tif* format and a *.txt* file are generated.

For convenience, the code *LoadSRSStack.m* was developed to load datasets with as many hsSRS stacks as desired. This function groups the data into a single matrix, where each rows corresponds to each pixel on the entire dataset, and each columns to a spectral feature (wavelength/Raman shift) of the dataset. This function also retrieves the pump wavelength of each data point from the *.txt* file generated by the python code *specscan.py*, at the end of each hsSRS stack, and uses the *wavenumberCONV.m* function to convert it from $\lambda(nm)$ to $\omega(cm^{-1})$. The output data can be analyzed together as a whole, for example in batch-level multivariate analysis (see below), or as individual images.

Despite SRS is essentially free from nonresonant background, it is not free from all sorts of noise. Often, the signals we are interested in are so small that an increased gain of the detector is required, which contributes into increased background noise. In other occasions, we are interested in isolating specific parts of the sample, i.e. lipid droplets in cells or tissues, and thus the rest of the tissue or cell cytoplasm becomes the background. The function *SRSbkgcorrect.m* allows the user to select a portion of the image that corresponds to background, and the average spectra of the selected area is subtracted to the entire image. This corrects for background contributions and it also takes care of additional baselines. Even thought *specscan.py* corrects the power every time the imaging wavelength is changed, to keep power constant throughout a hsSRS stack, we often encounter and an overall baseline added to the final spectra that is common to all the pixels in the image. Subtracting the spectrum of a background area in the image usually solvents this inconvenience.

3.4.2 Data clustering and classification

Raman spectra are reconstructed by plotting the intensity versus the pump wavelength ($\lambda(nm)$), or the Raman shift frequency ($\omega(cm^{-1})$), for each pixel in the image. That provides information on the chemical characteristics on each area in the imaged sample. Visualizing this chemical information is of interest for rapid inspection and careful interpretation of the samples.

Displaying the image at one particular color indicates the presence of a particular bond, and perhaps component, in the sample, but ensemble analysis to visualize the overall composition of the samples is preferred. Multivariate analysis (MVA) is a popular strategy that provides a statistical approach to analyzing data composed by more than one variable. In our case, it provides a visualization method for hyperspectral images, by assigning the same color to pixels with the same spectral features, or pertaining to the same chemical component. Multivariate analysis are essentially unsupervised algorithms that group observations into multiple categories based on inherent similarities or distances without previous knowledge on the available groups. Principal component analysis (PCA) is a multivariate analysis approach that performs data reduction by regrouping the observations such that the variance of the data is best explained. By taking only those principal components that explain the most variance, the amount of data is reduced without a significant loss of information. Vertex component analysis (VCA) is another MVA method that provides an intuitive way to unmix spectral data. Both PCA and VCA represent the data in a space where it might be easier to find groups or data clusters. To find those clusters we can apply machine learning and statistical approaches. K-means clustering analysis (KMCA) is another unsupervised method that identifies spectra of similar features and groups them together. Machine learning classifiers, on the other hand, are supervised algorithms that assign the observations to a category on the bases of pre-established connections within a training dataset of known classification. We discuss some of these approached below.

The results of any of these MVA, clustering, or classification analysis benefit from having a well-conditioned input dataset. Z-score normalization (equation 3.1), for example, prevents the result of the processing to be affected from intensity variation effects, and reduces the noise contribution into the analysis.

Z-score normalization:

$$\overline{S_p} = 0 \tag{3.1a}$$

$$\sigma_{S_p} = 1 \tag{3.1b}$$

Figure 3.2 exemplifies the effect of a z-scored dataset. Figure 3.2 A illustrates a K-means cluster analysis done with raw data and it returns four groups that differentiate on the pixel intensity variations, rather than in spectral features, as does the analysis in figure3.2 B, where the data has been previously corrected to have mean 0 and std 1 (z-score). The analysis performed in each case yields very different results as quantified by the number of pixels classified into each group (insert histograms in figure 3.2) and visualized in the images below the spectra.

Principal Component analysis

Principal component analysis (PCA) is a MVA method based on orthogonal transformations and projections of the data, from possibly correlated variables, to convert it into a set of independent variables, called principal components. The principal components (PCs) are statistically found in order of decreasing variance. The first principal component accounts for the largest variability of the dataset, the second one is orthogonal to the first and explains the second largest variance of the dataset, and so on. PCA provides a data reduction step without loss of information, as the number of principal components is smaller than the number of observations, but yet most of the variance of the system is explained by the firsts PCs. PCA has been previously used for hsSRS and hsCARS before[115].

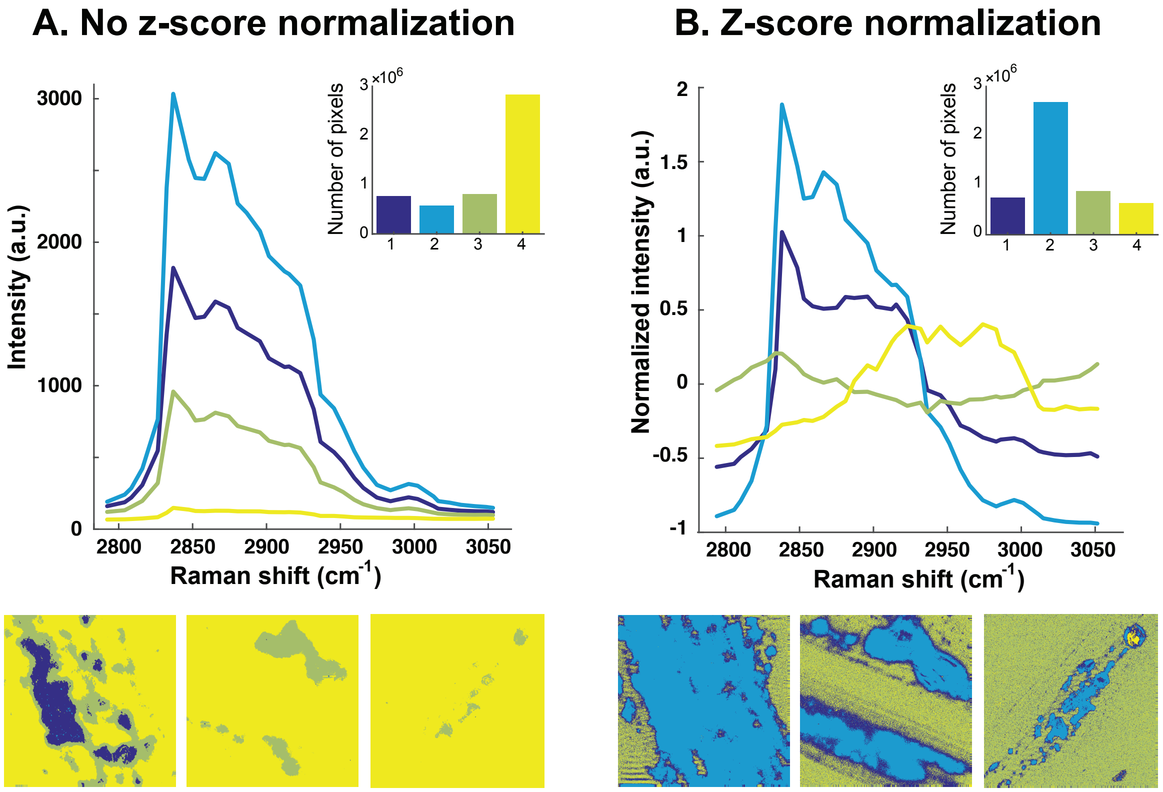
A. No z-score normalization

B. Z-score normalization

Figure 3.2: K-means cluster analysis A) without, and with B) previous z-score normalization of the input data. Image size ∼ 82 μm.

Vertex Component Analysis

Vertex component analysis (VCA) is a more intuitive approach to analyze mixed spectral vectors, such as the ones in hyperspectral SRS. VCA is an unsupervised algorithm that projects the data into a simplex geometry by means of singular value decomposition (SVD). It assumes the different components of the sample are linearly mixed together. A detailed derivation can be found in Nascimento et al. article[119]. The vertices of the defined simplex are occupied by the extremes of the projection, so-called *end-members.* VCA assumes there is at least one spectrum in the data set for each pure components of the mixture. The algorithm first projects the data iteratively onto perpendicular directions of the subspace defined by the end-members already determined, one after the other, until all the end-members are visited and the mixer matrix M is created (equation 3.2).

The model defines each spectrum (S; size p x q, p spectra of q spectral points) as a linear combination of the pure spectra, or end-members (M; size l x q, l end-member spectra of q spectral points), weighted by the abundance matrix (A; size p x l), which is determined in a second step by multiplying the mixer matrix (M) pseudoinverse with the original spectral data (S). It also assumes there is a noise level associated to the measures (N; size p x q) (see equation3.2b).

Initial spectral data:

$$S_{ij} = [I_{ij}^{\lambda_1}, I_{ij}^{\lambda_2}, ..., I_{ij}^{\lambda_q}] \tag{3.2a}$$

Vertex Component Analysis:

$$S = AM + N \tag{3.2b}$$

$$M = [m_1, m_2, ...m_l] \tag{3.2c}$$

$$A = [\alpha_1, \alpha_2, ...\alpha_l]^T \tag{3.2d}$$

VCA reduces the dimension of the spectral space from q to l, with $q >> l$, providing an easier problem to handle.

In regard to the biological projects presented in this thesis, VCA becomes the preferred strategy to explore the data and learn about the chemical composition of the different samples.

Typical hsSRS stacks in the CH region of the Raman spectra contain 37 to 40 data points (oversampling/undersampling justification). Taking the upper limit, a single hsSRS stack is composed of 512x512x40=10.485.760 data points, arranged as 40 images of 512x512 pixels, or 262.144 spectra of 40 points. VCA reduces the dimension of the dataset to as little as 3 images of 512x512 pixles, and provides a comprehensive visualization output.

The number of end-members is an input to the algorithm. An empirical approach can be taken in which we manually explore the result of various choices of end-member numbers. This is actually recommended when little is known about the nature of the samples. Because VCA is an unsupervised method, every run might deliver a slightly or dramatically different output. An analysis of this differences results very informative. If a more systematical approach is desired, or in combination of the empirical method, the number of principal components that explain the most variance (running the hsSRS through PCA) gives an indication on how many end-members best describe the dataset. Prior knowledge of the data also helps. In most of our cases we are interested in obtaining a map of the overall

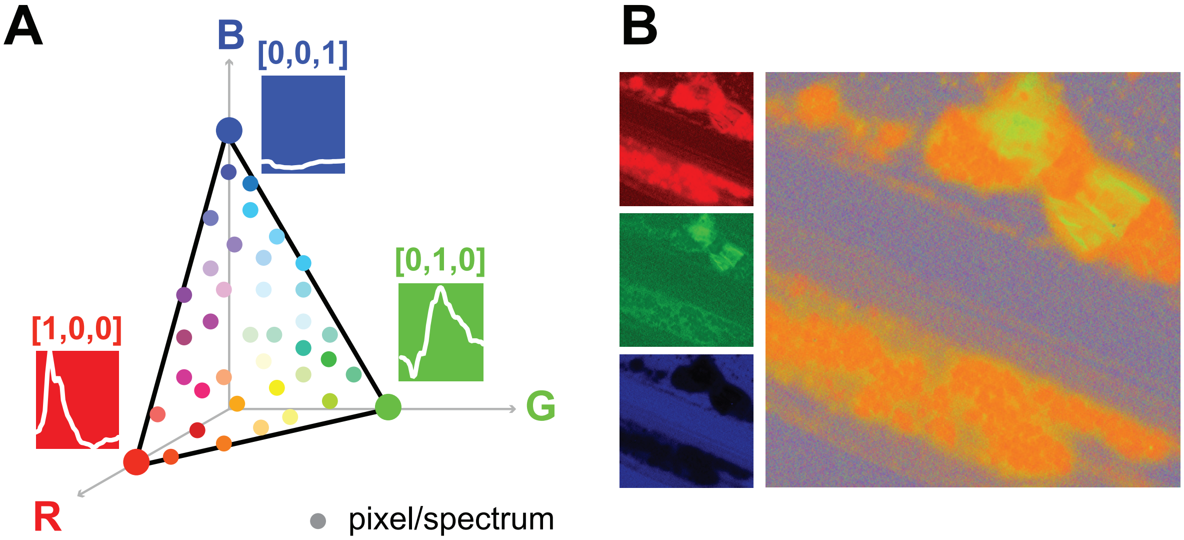

Figure 3.3: VCA scheme for 3 end-members. A) End-member spectrum-color assignation in the RGB color space. B) RGB basis-images recovered from the VCA analysis and final reconstruction as a chemical map.

protein and lipid in the samples. In that case, three end-members is a good starting point, provided there is always some background. If different types of lipids are present in the sample, more end-members could yield to the desired solution.

Let us keep the example of three end-members. In that case the simplex that VCA will use is a triangle. First, it will find the purest spectra on the image, provided there is at least one pixel with unmixed, pure, spectrum of the components of interest. Then, it will describe all other spectra in the hsSRS stack as linear combination of the three end-members spectra. For visualization purposes, each end-members is assigned a color in of the three-dimensional RGB space (figure 3.3 A). Any other color space is just as valid and this strategy can be adapted to as many end-members one defines, though if it is more than 4 visualization becomes challenging. Now, every pixels is color-coded and similar colors imply similar spectral characteristics. The image can be easily reconstructed to a chemical map (see figure 3.3 B).

The Matlab function *VCAonSRSimage.m* is designed to analyze hsSRS stacks. It requires a folder with the *.tif* stacks of interest and the corresponding *.txt* files, and the number of end-members desired. This function uses the aforementioned *LoadSRSstack.m* to load the data and generate the features matrix, and the Matlab build-in VCA function to perform the analysis. It returns the basis-spectra and corresponding coefficients for each pixel, as well as the input data rearranged in convenient matrices for further analysis. A quick inspection of the returned basis-spectra is usually done before assigning specific colors to the specific end-members, and the images are reconstructed using the output of the function.

K-means clustering analysis

K-means clustering analysis (KMCA) is another unsupervised algorithm that groups data into a predefined number of clusters k. For spectral data, the algorithm groups spectra with similar features together, by assigning each spectrum to the group that minimizes the sum of distances between original spectra (S_p^J) and the mean spectrum of the assigned cluster (m_k), so-called centroids:

$$min(\sum(S_p^J - m_k)) \tag{3.3a}$$

$$m_k = \frac{1}{J}\sum_{i=1}^{J} S_p^i \tag{3.3b}$$

At first, J spectra are randomly assigned to each cluster k, and the mean of each cluster (m_k) is computed. The K-means algorithm examines the distance between each spectrum and the computed cluster centroids, and if the spectrum of interest is not assigned to the group with the closest mean, it is re-assigned to the one that minimizes such distance. As an iterative process, this step is repeated until all spectra are located in the cluster with the nearest centroid, or until the overall sum is minimized[120].

To select the number of clusters in the K-means algorithm, as well as the number of end-members in the VCA algorithm, it is useful to examine the data with principal component analysis (PCA) first. PCA results are less intuitive when applied to (Raman) spectral information, particularly of a reduced portion of the Raman spectra; there are not that many data points in each spectrum for a meaningful data reduction step. However, the number of principal components that explain the most variance can be used as a starting point to decide the number of clusters and end-members of the previous algorithms.

Classifiers

Machine learning classifiers attempt to identify the category to which a new observation belongs to, taking as reference a training set with observations of known category. In the most strict sense, classifiers are supervised learning algorithms. Clustering approaches, such as K-means clustering analysis, are unsupervised learning algorithms.

Some common classifiers include logistic regression or naive Bayes classifiers, which are both linear classifiers, support vector machines, k-nearest neighbor, decision trees-based random forests, or neuronal networks.

A random forests (RF) algorithm is an ensemble learning method that classifies new data according to pre-established relations with a training dataset. It is an ensemble of decision trees each of which issues a vote, the mots popular class is elected winner and determined to be the class of the particular data point under scrutiny[121]. This is a supervised algorithm; once the algorithm is trained against a specific classification, it can identify the same classes in new data sets, considerably speeding the process up.

3.4.3 Batch-level multivariate analysis

The previous data analysis methods can be applied at single hsSRS images for individual analysis, or to an ensemble of measurement. When the ground truth is missing, unsupervised methods provide a description of the chemical composition of the sample that can be used for quantification, but these methods might yield a slightly different result every time they are implemented. Comparing results across images is delicate due to the lack of commonality. In such cases running the analysis once for the entire dataset warranties an unbiased comparison.

Running the analysis on the entire dataset might be however computationally costly. Combining different approaches becomes a good strategy. We have develop a batch-level multivariate analysis that combines VCA, KMCA, and RF classification to analyze big datasets on a study that aims to characterize the lipid-rich secretions of Meibomian glands (chapter 4). The overall methodology is described next.

A random subset of hyperspectral SRS images was selected as training set. VCA with three end-members was applied to unmix the spectral information. This step re-distributes the data into a new RBG color space. Every spectrum of the training dataset is represented by a color defined as the linear combination of the three end-members and weighted with VCA output coefficients, enabling the reconstruction of chemical maps that describe each sample. However quantification remains challenging. Similar colors now mean similar spectral features but without clear thresholds among classes. Thus K-means clustering analysis is applied to group similar spectral classes into six groups that quantify biochemical distribution of the samples. Finding out the number of clusters highly depends on the nature of the sample. In our case, where we wanted to discriminate between lipids and proteins as we will explain in chapter 4, stating with three groups seemed appropriate. The three groups belong to lipid, protein, and background. An inspection to the spectra classified into each group revealed a large variability in the lipid group. More clusters were intended but the

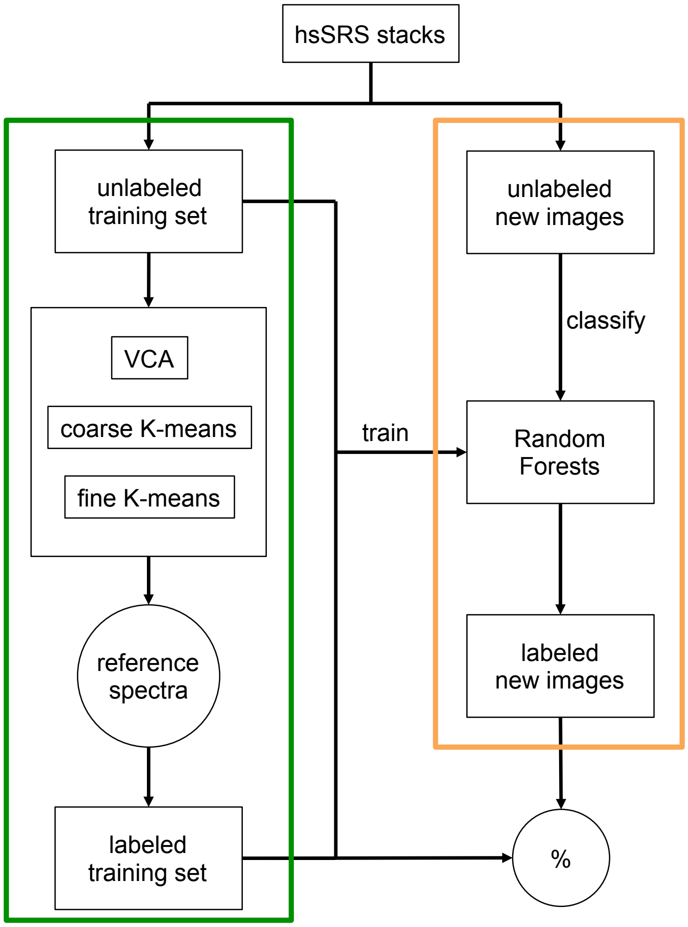

Figure 3.4: Methodology diagram. Green box: unsupervised identification of the chemical composition. Orange box: supervised learning and classification of the new samples. hsSRS: hyperspectral stimulated Raman scattering, VCA: vertex component analysis.

result was not robust, showing different groups at each implementation and often doubling the categories. A nested KMCA targeting only the initial lipid cluster was applied. We found four extra sub-clusters that revealed meaningful information form the dataset, obtaining a total of six reference spectra that best describe the training set. To analyze the rest of hsSRS scans we train a RF classifier with the training set images and the retrieved spectral clusters. After calibrating the RF, we run the remaining images through it and obtain their direct classification. This speeds up the process and permits an unbiased comparison of the different images to proceed with further biomedical analysis.

Chapter 4

Meibum: case study

Dry eye disease affects a considerable portion of the elderly population, but its diagnostic is inefficient, and its cause remains elusive. A complete biochemical characterization of the tear film lipid layer, the main component in jeopardy in dry eye disease, is nonexistent and difficult to attain. With the aim of defining a reference on its composition we characterize the biochemical composition Meibomian gland secretions, the main contributor to the tear film lipid layer. Coherent Raman scattering hyperspectral imaging in the CH spectral band is coupled to multivariate analysis to generate chemical maps of the meibum secretions that indicate variations on the protein and lipid contributions as the disease progresses.

4.1 Introduction

Dry eye disease causes irritation in the eye and blurred vision, as a consequence of eye dryness. This increasingly prevalent condition of the tear film poses a significant burden on the patient's daily life. Current diagnostic methods and classification of various stages of dry eye disease rely and the good judgment of clinicians. Even thought there are some standardized guidelines on how to identify and classify a dry eye patient, a lack of quantitative methods based on the biochemistry of the process prevent an objective diagnostic. Usually the properties of the tear film are examined to obtain a degree of disease, not even professionals agree on.

Dry eye is defined as a tear film instability. The tear film is an aqueous layer on top of the cornea that contains a lipid-rich layer in the posterior-most part, which protects the eye surface. The main source of lipids on tear film lipid layer are the Meibomian glands, located in the upper and lower eyelids. These glands secrete lipid that redistributes on the tear film with every blink. The specific role of meibum secretion in the progression of dry eye disease remains unclear, but it is to expect that the composition of meibum affects the composition of the tear film lipid layer, and it is hypothesized that it may play an important role in tear film related disorders, such as dry eye.

To establish a quantitative correlation between the quality of the meibum and the degree of dry eye severity, we revisit the lipid composition of meibum in healthy subjects and patients with different severity of dry eye disease. A study with human subjects has been designed (UCI IRB HS# 2014-1510 *Correlates of Meibomian Gland Dysfunction and Dry Eye Severity*) by our collaborators at the Gavin Herbert Eye Institute of UC Irvine. Our contribution to the study consists on examining the biochemical composition of meibum secretions extracted from a variety of patients with Raman microscpectroscopy, with the ultimate goal of establishing correlations between the meibum composition and the clinical parameters used currently to diagnose dry eye disease.

4.1.1 The tear film and the meibomian glands

The tear film makes the posterior-most part of the eye covering the top of the cornea. In the 1950s a three layer model was proposed to describe the composition of the tear film[122]. The current model is based on those three layers, but it features undefined boundaries between them (see figure 4.1), as the tear film is rather a dynamic entity with complex chemical composition. The three main layers are:

1. Glycocalyx layer: A hydrophilic mucin-enriched layer, of high viscosity, due to the high abundance of membrane-bound proteins and mucins.
2. Aqueous layer: A hydrophilic aqueous layer, with water soluble proteins, mucins, and salts.
3. Tear film lipid layer: A lipid layer with a higher hydrophobic character that contains both lipids and proteins. More recent models subdivide this layer into 2 additional sub-layers, nonpolar lipids on the outermost part and polar lipids in the inner part, with the hydrophilic heads in contact with the aqueous layer and their hydrophobic tails staked in the nonpolar lipid sublayer.

The function of the lipid tear film is to slow down the evaporation of the aqueous part of the tear film, to preserve a clear optical surface and to form a protective barrier against microbes and organic matter, such as dust and pollen[122,123]. Its complex composition includes several kinds of lipids, a plethora of proteins, and also inorganic salts.

The principal source of lipids in the tear film lipid layer is the Meibomian gland system[122,124]. Meibomian glands, or *glandulae tarsales*, are sebaceous glands located at the margins of the upper and lower eyelids of humans and mammals. They are named after Heinrich Meibom, a german physician and anatomist, who provided the first acuarate description of these holocrine glands in 1666[1]. The sebum secretion produced by these glands was termed *meibum* in 1981 by Nicolaides et al.[125]. These secretions contain a complex mixture of lipids including cholesteryl esters, triacylglycerols, phospholipids, wax esters, free cholesterol, and fatty acids. Cholesteryl and wax esters are the most prominent components as they account for $\sim 60\%$ of the meibum lipids[122] (see table 4.1, adapted from[126]).

Lipid class	% of total meibum lipid (w/w)	Reference
Wax esters	41 ± 8	[127]
Cholesteryl ester	~ 30	[128,129]
cholesterol	<2	

Table 4.1: Main lipids in human meibum.

4.1.2 Dry eye disease

In 2007 the International Dry Eye Workshop established a new definition for dry eye[130]:

> "Dry eye is a multifactorial disease of the tears and ocular surface that results in symptoms of discomfort, visual disturbance, and tear film instability with potential damage to ocular surface. It is accompanied by increased osmolarity of the tear film and inflammation of the ocular surface."

This definition replaced the one established in 1995 by the National Eye Institute and the Industry of Dry Eye Workshop, which referred mainly to the abnormal evaporation of the tear film and didn't specify the effect of dry eye on visual function.

The prevalence of dry eye disease depends highly on the age group, and ranges from 5% to over 30%, being more prevalent in elderly citizens. About twice as much women than men of age 50 or older suffer from it. Older people and women are thus the most affected demographics[131].

The most common symptoms of dry eye disease include tearing, irritation, itching, blurred vision, and increased blinking frequency. These symptoms cause pain and decreased visual performance, degrading the patients' quality of life and affecting their daily routines[131].

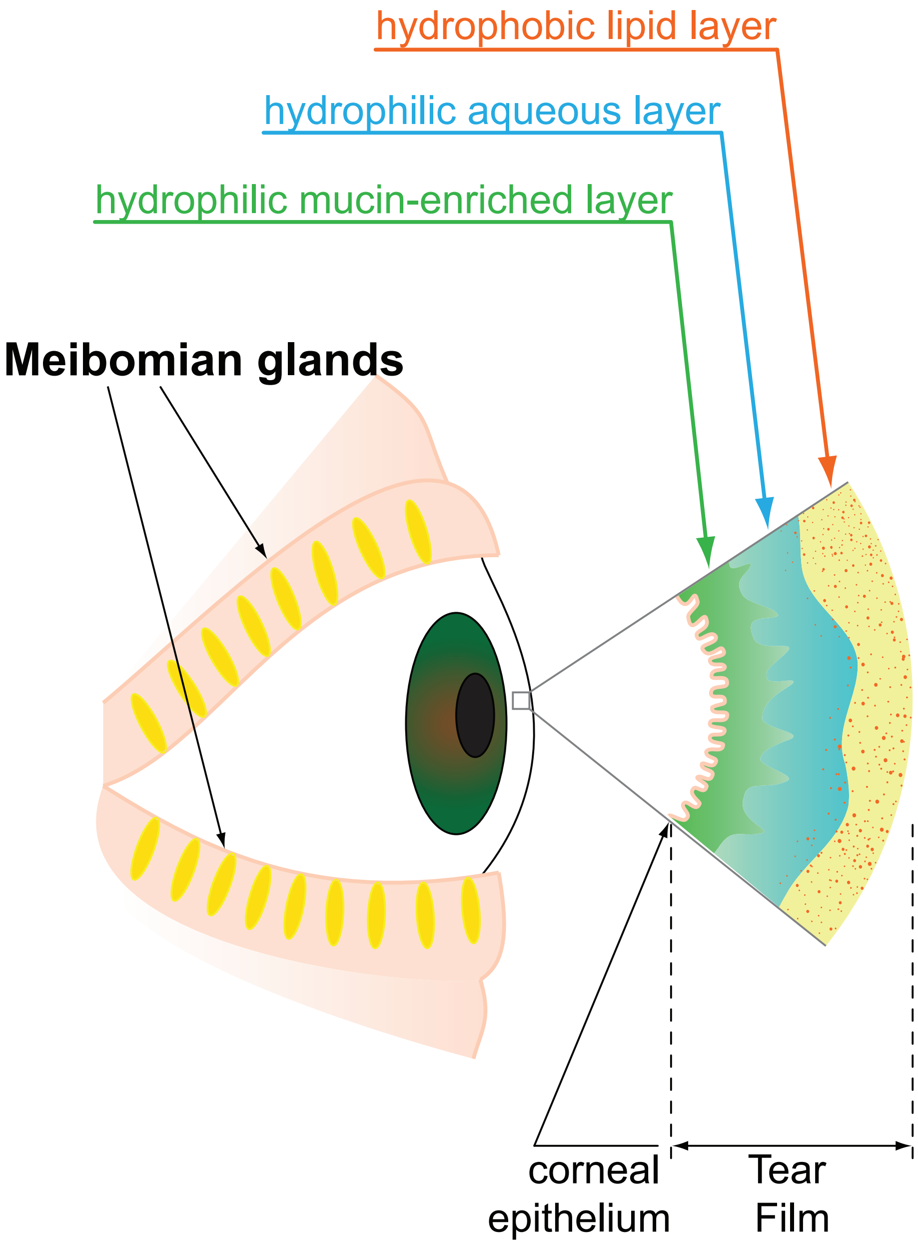

Figure 4.1: Meibomian glands in the upper and lower eyelids, and tear film detail with the three layers that follow the corneal epithelium, from anterior to posterior part: hydrophilic mucin-enriched layer, aqueous layer, and hydrophobic lipid layer.

There are two types of dry eye: aqueous tear-deficient dry eye (ADDE) and evaporative dry eye (EDE). The former entails a failure of the lacrimal secretory function, and the latter implies an excessive water loss from the ocular surface, with a normal lacrimal secretory function[130]. The causes for EDE can be intrinsic, extrinsic, or a combination of both. Intrinsic causes include meibomian gland dysfunction (MGD) or disorders of the lids and low blink rates. Extrinsic causes account for vitamin A deficiency, contact lens wear, or allergic conjunctivitis, among others.

As the most important source of lipids to the tear film lipid layer, dysfunctional meibomian glands is one of the most common causes of EDE[124]. We focus here on evaporative dry eye disease and its connection with meibum secretions.

There is no gold standard diagnostic method for dry eye disease. Clinitians combine a large variety of test to obtain a final diagnostic. These include ocular surface staining, tear film stability tests, reflex tear flow, and tear osmolarity tests. Meibomian gland expression is a parameter of high relevance, however, it is defined in a very loose way based on the appearance of the secretion (from clear oily-looking in healthy patients to opaque tooth paste-like in the most sever cases).

4.1.3 Raman measures on Meibum

Chromatographic (thin layer chromatography (TLC), gas chromatography (GC), or liquid chromatography (LC)) and spectroscopic (UV/VIS, fluorescence, infrared (IR), mass spectroscopy (MS)) studies point out the different composition of meibum in health and dry eye patients, but do not provide strongly conclusive results[1]. Raman spectroscopy has also been applied to the eye in numerous occasions, and it was used to characterize the human meibum lipid in 2009[132], but had a limited success in differentiating meibum from healthy and diseased patients. More recently, coherent Raman scattering microscopy has been used to examine the Meibomian glands of mice[133,134]. These studies show a purification of the lipid fraction as meibum matures from the acinus of the Meibominal glands, to the central duct, to the output orifice, where it is finally released (by a blink)[134]. This purification consist on clearing out the protein fraction of the meibocytes (cells that produce the lipid content on the Mebomian glands). The latter study also points towards an increased contribution of protein in mice meibum secretions when these are under desiccating stress, mimicking dry eye conditions. That paves the road to hypothesize normal meibum might have less protein contribution released to the tear film lipid layer than altered meibum.

Hyperspectral SRS in the CH stretching window of the Raman spectra (2800 - 3100 cm^{-1}) is informative of the lipid, and the overall protein content of the sample. A variety of lipid profiles can be identified if the samples has regions with pure components. When there is a mixture of lipids, the disentanglement becomes challenging. However, lipids can be told apart from protein based on their different vibration modes that arise from being CH_2 and CH_3 rich, respectively. These two modes are representative of the biomolecular class and suffice to be resolved with hsSRS in the CH region.

4.2 Experimental details

4.2.1 Clinical data collection and evaluation

Meibum secretions are collected from the central portion of the lower eyelid, unless otherwise noted. For collection, the lower eyelid is everted and the margin is wiped gently using a sterile Q-tip. The Meibomian gland expressor (also known as Korb device in honor of its inventor, Dr. Donald Korb, figure 4.2 A) is applied to the cleaned portion of the lower eyelid for 10-15 seconds (figure 4.2 B and C), and the expressed meibum is collected using an ophthalmic spatula (18-380 Miltex Ellis Foreign Body Spud; Steele Supply Company, St.

Figure 4.2: A) Korb device. B) Clinical use of the Korb device for collection of meibum samples. C) Detail of the previous. Courtesy of Dr. J. Paugh.

Joseph, Michigan, USA). The meibum sample is then smeared onto a clean microscope slide for micro-spectroscopy processing, which is further sandwiched with a thin coverslip hold with double side sticky-tape, and kept at room temperature until SRS imaging.

During the visit to the clinic for sample collection, additional standard dry eye tests are also performed.

- **Meibomian gland expression (MGE)** is graded on a clinical scale based on the secretion appearance. 0 = normal(clear and oily), 1 = cloudy, 2 = cloudy with particles, 3 = inspissated or toothpaste looking. MGE correlates with the cloudiness, color, and viscosity of the meibum secretion.
- **Tear breakup time (TBUT)** measures the time it takes for the tear film to breakup after a blink, in seconds. The measurement is done by staining the eye with sodium fluorescein. This quantity is believed to be directly related to the quality of lipid portion of the tear film, short breakup times correlate with poor tear lipid quality or quantity.
- **Corneal staining** is assessed by the NEI scale and the Oxford scheme and is used to inspect the quality of the corneal surface. Damage in the corneal surface epithelium

leads to the sensation of pain.

- **Tear osmolarity** is also measured. It is negatively correlated to TBUT, as short breakup times also imply increased water evaporation leading to increased tear film osmolarity.
- Questionnaires to asses the **symptoms and the pain level** are also filled in by the patient. Examples of these questionnaires are the OSDI (Ocular Surface Disease Index), the Shein questionnaire or the MDG questionnaire.

4.2.2 Sample imaging and data collection

Two types of images were acquired. First, single color image tiles at 2850 cm^{-1} were taken to reconstruct the entire meibum secretion as a mosaic. These imaging was done with a 20x objective with no extra magnification (pixel size of 1.38 μm). ImageJ was used to reconstruct the mosaics.

Second, hyperspectral SRS (hsSRS) stacks of 37 colors were acquired from one to three zoomed-in areas of the sample. The 20x objective with a 3x magnification factor was employed (pixel size of 0.46 μm). HsSRS stacks of meibum in the CH stretching region were composed of 37 images of 512 by 512 pixels, accounting for a total of 262,144 spectra of 37 data points per image. This clinical study aimed to examine at least 100 patients, with at least two samples per patient (one from each eye) we obtained over 200 samples. An average of two hsSRS stacks per sample were collected to account for intrasample variations. That yielded $>$ 400 hsSRS stacks to analyze, or a total of 104,857,600 spectra to examine and compare, with at least 3.88x10^9 data points. An efficient method to extract information out of these data is imperative. The hyperspectral SRS stacks were processed with customized Matlab code based on the clustering and classification methodology defined in chapter 3, and detailed in the next section.

4.2.3 Hyperspectral data analysis

The aim for the hyperspectral SRS data analysis is two-folded:

1. Characterize the chemical classes that best define the meibum secretions.
2. Classify new images into predefined chemical classes in a fast and reliable way.

We have limited prior knowledge on the patients' meibum secretions. We know they contain lipids, and potentially protein. But we don't have details on the specific composition and location of these biomolecules within the sample for each patient. Hence, an unsupervised approach, with no assumptions, is required to find the sample composition. Because the data set is composed of multiple observables, namely 37 spectral features, we chose multivariate analysis (MVA) for the task.

MVA on each individual sample becomes unpractical if the results are to be compared across samples. Because of the unsupervised nature of the MVA, the result for each individual image (or hsSRS stack) strongly depends on the input data. Despite the similarities in composition among samples, the algorithms focus on different attributes for each image, which result in slightly different spectral signatures retrieved as the composition descriptors, complicating the comparison and the interpretation of the results. To amend that risk, we perform batch-level MVA; all the hsSRS stacks are re-organized as a single dataset to which the multivariate analysis is applied.

The associated computational costs to batch-level MVA analysis are high. In addition, if new samples want to be added to the study at later times, the analysis would need to be repeated from scratch. The process is time consuming and inefficient. To circumvent this inconvenience we fragment the dataset into two groups: a training set and a new images set.

The training set consists of a subset of data with 19 hsSRS stacks from 17 different pa-

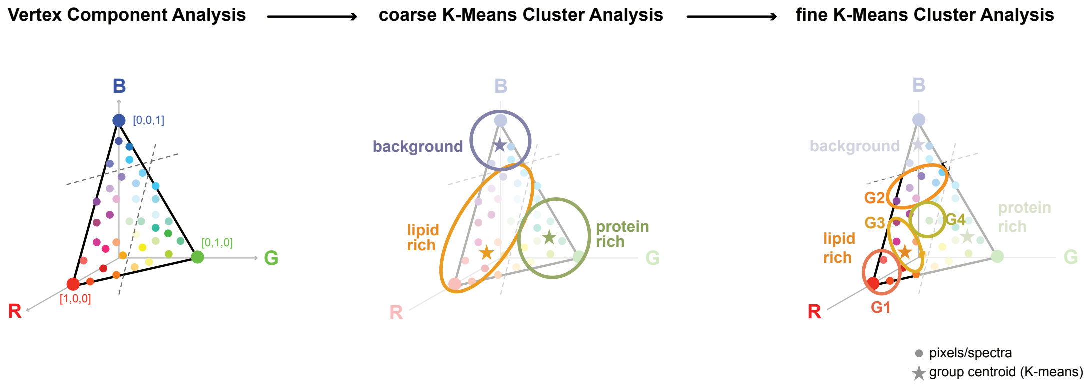

Figure 4.3: Multivariate analysis sequence applied to the training set to obtain the reference spectra. First, the data are processed by vertex component analysis (VCA). Second, k-means cluster analysis (KMCA) with k = 3 is applied to the VCA output to generate three groups with the main components of the sample: background, lipid-rich group, and protein-rich group. Third, a second KMCA with k = 4 provides additional segmentation of the lipid-rich group.

tients. These samples were chosen to have a broad representation of all kind of spectral and morphological features found in the dataset, when this was 43 patients long.

The result of the MVA on the training set yielded six spectral classes that define the meibum samples, including background from the microscope slide. The spectral classes were obtained after a sequence of multivariate analysis schematized in figure 4.3.

Once the reference spectra are established we trained a random forest classifier to accomplish the second task: classify the new images dataset. The diagram in figure 3.4 shows the overall methodology.

We next detail each step of the methodology applied to the meibum secretion samples.

VCA analysis of the training set

Vertex component analysis (VCA) is applied to the 19 hsSRS stacks of the training set. First, the data was standardized by a z-score normalization to avoid intensity variation effects.

Because the samples are mainly composed of lipids, proteins, and the slide background, three end-members suffice to describe the gross-composition of the the meibum secretions. Each end-member is the spectrum of a single pixel in the entire training set, and is assigned to a vertex of a simplex (a triangle in this case), as we saw in chapter 3, figure 3.3. Colors were then assigned to this triad of spectra. We used the RGB color space, and we assign blue to background, red to lipid (or the basis spectrum with a prominent 2845 cm^{-1} peak), and green to protein (basis spectrum with a predominant contribution from the peak at 2930 cm^{-1}). Each other spectrum in the training set was then defined as a linear combination of the three end-members:

$$S^i = c_r^i \cdot m_r + c_g^i \cdot m_g + c_b^i \cdot m_b \tag{4.1}$$

where $[c_r, c_g, c_b]$ are the color coefficients of each pixel i as determined by the VCA output, and by extension of each spectrum. Consider red = [1, 0, 0], green = [0, 1, 0], and blue = [0, 0, 1]. As a result, the 37-dimensional hsSRS stacks in the training set can now be represented as a single false-colored image, or chemical map. Figure 4.4 A shows the three basis spectra resulting from VCA and three reconstructed images.

The result of the VCA not only provides a first segmentation of the data, but also an important data reduction step. The dimension of the spectral space is reduced from 37 to 3. From 184,287,232 data points (19 images of 512x512 pixels with 37 spectral points per pixel) to 14,942,208 data points (19 images of 512x512 pixels with only 3 features per pixel), which is an 8% of the initial data set. This reduction also diminishes the impact of the noise that contribute to the images. Meibum chemical maps were reconstructed by overlaying the resulting three RGB components. Areas of similar color have similar spectral features, thus similar composition.

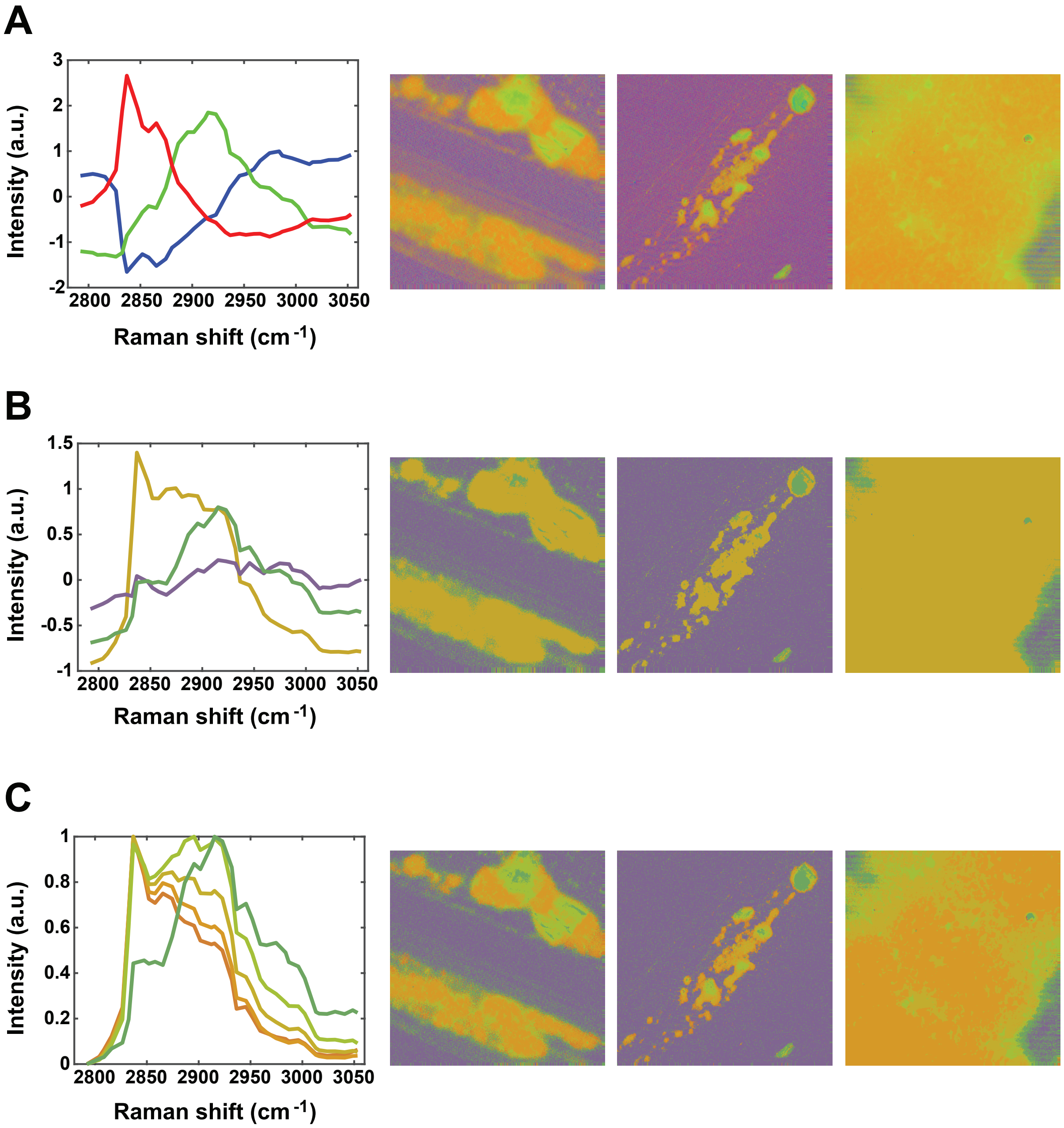

Figure 4.4: Multivariate analysis output. Spectra and image reconstruction examples from A) VCA analysis on the training set, B) coarse KMCA with k = 3 on the VCA output color space, and C) final result after the fine KMCA with k = 4 on the lipid-rich group from the first KMCA, plus the protein group (normalized intensities). Image size ∼ 82 μm.

The basis spectra are however extreme indicators with unclear association with a biochemcial component. Also, the images feature a continuum of colors challenging to classify for further quantification. In order to gain biochemical character for the basis spectra and to facilitate quantification we implement a K-means clustering analysis (KMCA) on the color space defined by the VCA output, which is less noisy and more intuitive than the initial space, as now every point is a complete spectrum.

Note, that principal component analysis (PCA) provides an indication of the number of end-members or clustering groups that are more significant for the dataset. We found that the first two principal components (PC1 and PC2) represent the lipid and protein content of the secretions (figure 4.5). But they do not account for most of the variance of the training set (figure 4.5 insert). Additional principal components (i.e. PC3) have significant contributions but correspond to noisy spectra. This is indicative of the high degree of variability of the samples, especially due to some impurities that are found across the dataset, such as makeup contamination. The images in the right panel of figure 4.5 show the intensity maps for the first three principal components (PC1, PC2, PC3) of three hsSRS stacks in the training dataset. Nonetheless, the PCA analysis indicated a minimum of 3 components to describe the sample, namely lipid, protein, and background contributions, as we intuitively chose for the VCA analysis.

K-means cluster analysis of the training set

A three-group K-means clustering algorithm (KMCA) on the VCA color output identified the main biochemical components of the meibum samples (protein- and lipid-rich areas, and background). The retrieved groups have a centroid (average) spectrum that is familiar to the Raman-versed reader (figure 4.4 B). The output clusters are populated with J spectra,

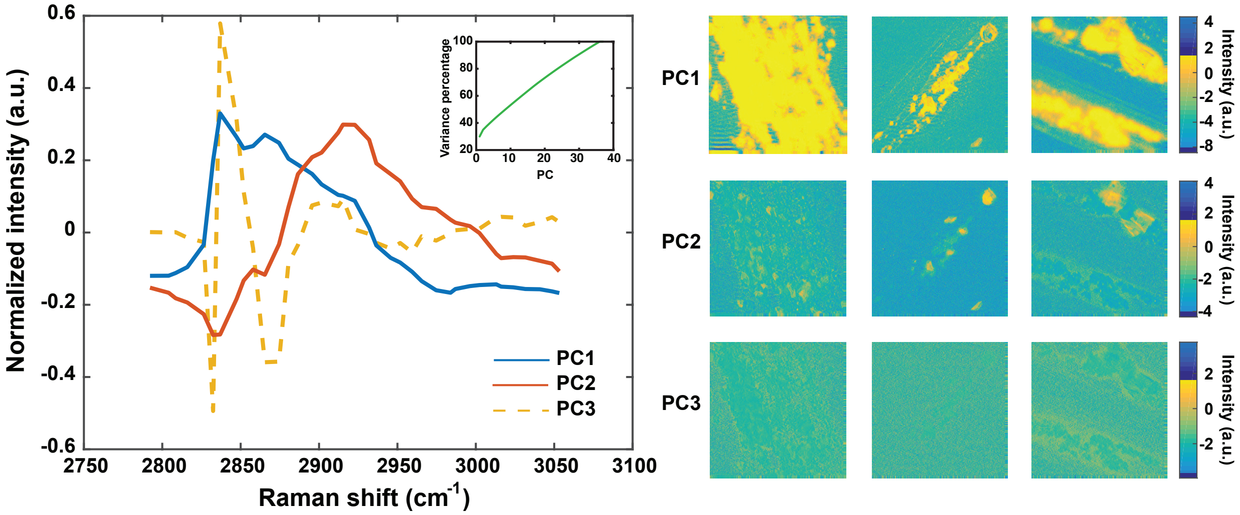

Figure 4.5: Principal component analysis (PCA) applied to meibum secretions. Left panel: Spectra of the first three principal components (PCs). Insert: variance percentage explained by the PCs. Right panel: Image representation examples of the first three PCs. Image size $\sim 82\ \mu m$.

which distance to the centroid of the group (n_k) is minimized:

$$min(\sum(S_J^i - n_k)) \tag{4.2a}$$

$$n_k = \frac{1}{J}\sum_{i=1}^{J} S^i = \frac{1}{J}\sum_{i=1}^{J}(c_r^i \cdot m_r + c_g^i \cdot m_g + c_b^i \cdot m_b) \tag{4.2b}$$

Applying a KMCA to the raw data right away provided disappointing results. First the difference in spectral intensities prevailed over differences in spectral features (see figure 3.2 A). Second, even with a z-score normalization the results do not offer the same dynamic range as the VCA output (figure3.2 B), because KMCA performs averages of the spectral groups, losing detailed information of the sample. A sequential implementation of VCA followed by KMCA resulted more effective. VCA identified the extreme contributions of the dataset that define the three major spectral classes, and it assigned maximum intensity to these three end-members, significantly reducing the contribution of noise from potential contamination.

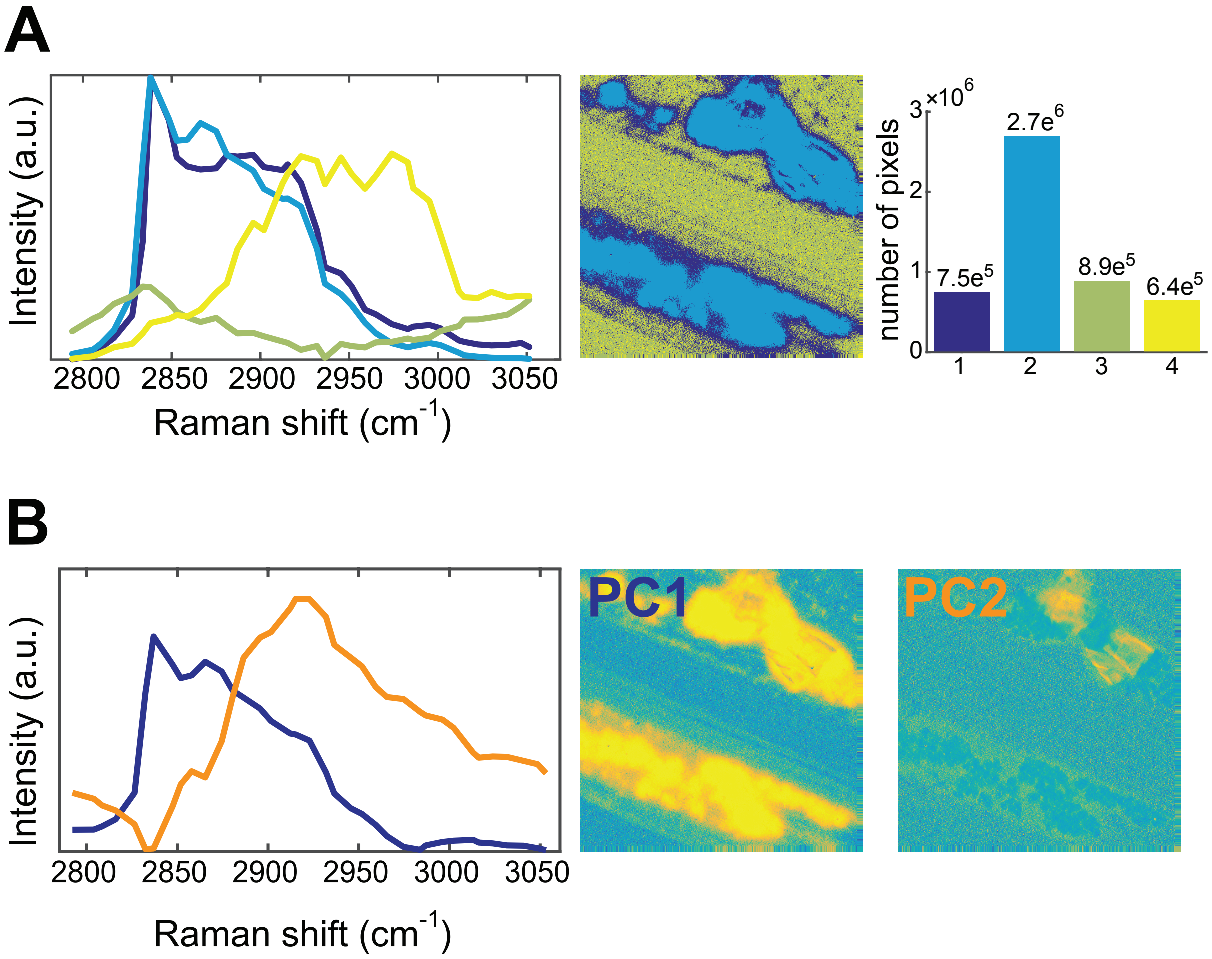

Figure 4.6: A) K-means cluster analysis with k=4 output centroids (average spectra of the four groups) and reconstructed image. B) Principals components PC1 and PC2 spectra and corresponding images. Image size $\sim 82\ \mu m$.

In the reduced three-dimensional space, with biochemical relevant coordinates, KMCA is not only more computationally efficient, but also has a guide to statistically identify the groups and variations within the sample with greater detail than in the original 37-dimensional space.

An initial KMCA with k = 3identified the three biochemical relevant clusters and provided average chemical maps. The analysis of the spectral variation within each cluster unveiled a big spectral divergence on the lipid-rich group. Interestingly, the spectral variation was relevant to the case study, as the working hypothesis is based on a variation in the protein fraction of the samples linked to the progression of the disease. A second KMCA implementation only on the lipid-rich cluster of the first KMCA yielded average spectra that exhibited such a variation in the vicinity of the CH_3 stretching resonance. We chose four groups (k = 4) that partition the lipid-rich regions into sub-groups with increasing levels of protein content (approximately 33%, 50%, 75%, and 100%). A bigger k oversampled the data, and fewer groups (smaller k) were not representative enough of this specific dataset. The result of the second K-means provided a graded variation of the contribution of methyl group in the samples, indicative of protein. Although we shall not forget that these spectra might be indicative of other lipid species that are also find in meibum in smaller concentrations.

Together with the protein spectra from the first KMCA (100% protein peak with no methylene contribution), the 5 spectra define a scaled lipid-to-protein ratio. Figure 4.4 C shows the 5 reference spectra and three reconstructed images, which also include the background pixels identified in the first KMCA. Note the similarity with the direct VCA output (figure 4.4 A). Now, we have a quantifiable segmentation of the images, as the groups are clearly defined by a single index, without compromising on spectral variety.

Overall, this nested clustering approach defined a set of reference spectra that simplify the description of the samples: from the first (coarse) KMCA the background and the protein spectra, and form the second (fine) KMCA the lipid-protein scale. Translated to the images, we can quantify the fraction of pixels, or area, that belongs to each group.

4.2.4 Classification

In the previous step, we retrieved six spectral classes that characterize the chemical composition of the meibum secretions, fulfilling the first goal of this data analysis. With these reference spectra tackled the second goal by training a classifier capable of quantifying the new images of the dataset.

nTrees	InBagFraction	MinLeafSize	oobError	Sensitivity	Specificity
20	0.5	1	0.15	0.939	0.949
20	0.5	3	0.15	0.937	0.951
20	0.5	10	0.14	0.940	0.951
20	0.5	100	0.15	0.936	0.939
20	0.7	3	0.15	0.937	0.951
60	0.7	3	0.125	0.949	0.955
100	0.5	100	0.15	0.944	0.939

Table 4.2: Settings of the RF calibration: nTrees: number of trees in the forest; InBagFraction: fraction of input data to sample, out of the randomly selected 85% of the total training set; MinLeafSize: minimum number of observations per tree leaf. Performance of the RF classifier: oobError: minimum of the out-of-bag error estimates of the forest.

Before classifying the new hsSRS stacks that are not part of the training set, the classifier was calibrated. We chose a Random Forests classifier for the task, as it is intuitive, fast, and robust. More details are described in chapter 3.

For this case study we use the dataset defined by the previous 19 images to train the classifier. We get the z-scored spectra from 85% of this dataset to be the training set, and the reference spectral classes obtained with the previous clustering steps, which are considered to be the true class category of each spectrum. Remember that we do not have an absolute ground truth in this experiment. To calibrate the classifier we tune three particular properties: the number of trees in the forest (nTrees), the fraction of input data to sample (InBagFraction) out of the randomly selected 85% of the total training set, and the minimum number of observations per tree leaf (MinLeafSize). As output, or classifier performance metric, we have the out-of-bag (oob) error, and the sensitivity and specificity. Table 4.2 shows a relation of the input settings and the output observations that help determine the calibration of the classifier. Note that many more combinations and other parameters can be altered which might yield a better result.

The oobError refers to the minimum of the out-of-bag error estimates of the forest (each tree has an out-of-bag error estimate). This is computed using the sample points not chosen

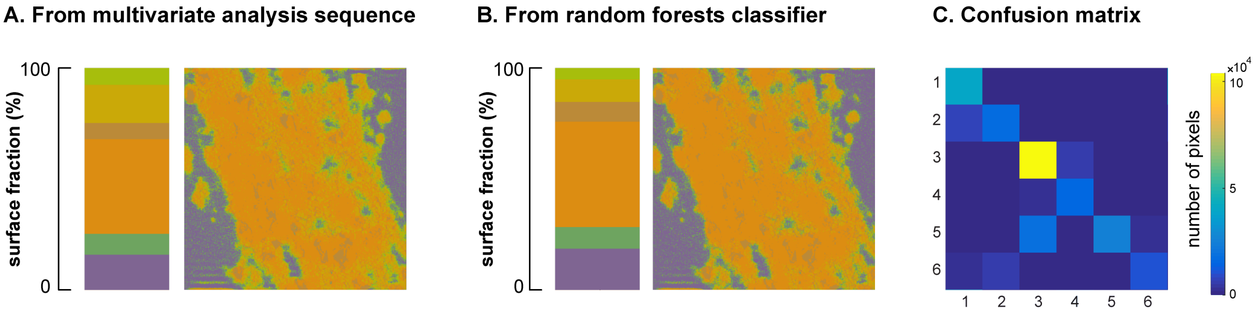
A. From multivariate analysis sequence

B. From random forests classifier

C. Confusion matrix

Figure 4.7: Random Forest (RF) classifier performance. An image from the training set was left out of the calibration set and used to validate the performance of the RF classifier. A) Result out of the training set multivariate analysis. B) Result out of the random forests classifier. C) Comparison in a confusion matrix that shows the number of pixels that belong to group x and are classified into group y, with x,y = [1 2 3 4 5 6]. Image size $\sim$ 82 μm.

by each specific tree (the fraction of input data not to sample, or out-of-bag), which is an inherent property of the classifier itself. There is room for improvement on that end. In addition to it, we have set aside a 15% of the input data not to be considered in the classifier training tasks, and use it as test dataset. Knowing the true class for these points, and running it though the trained classifier, also gives an estimate on how well this performs. From this analysis we extract the sensitivity and the specificity of the classifier, which turn out to be remarkably good.

For the present analysis we chose the following calibration parameters: nTrees = 20, InBagFraction = 0.5, MinLeafSize = 10. However, analysis with other settings (i.e. nTrees = 60, InBagFraction = 0.7, MinLeafSize = 3) will be done in the near future. With the classifier calibrated, we interpreted the rest of meibum secretion samples, without the need of MVA pre-clustering.

An image from the training dataset was left out of the calibration dataset and used for posterior validation of the classifier performance. Figure 4.7 compares the groups obtained straight form the MVA clustering sequence (A) with the classification output without previous MVA processing (B). At first glance the images are almost identical. The histogram of the surface fraction for each group reveals slight differences that are further quantified in the confusion matrix (C). The confusion matrix shows the number of pixels that belong to group y (vertical axis) according for the results obtained in figure 4.7 A, and classified in group x (horizontal axis) according for the results obtained in figure 4.7 B. Notice how a small fraction of pixels/spectra that belong to group $y = 5$ are missclassified into group $x = 3$. More subtle differences include pixels classified into group $x = 2$, which belong to group $y = 6$, these two groups are the protein-rich groups.

4.2.5 Correlation with the clinical data

Once the methodology is established, we can obtain the percentage of area sample in each biochemical class for each hsSRS stack. This metric may be used to compare the fraction of lipid and protein across meibum secretions of different patients.

Next steps include the investigation of correlations between the biochemical composition from the multivariate analysis and the clinical parameters evaluated at the time of the sample collection.

4.3 Results and discussion

The CH-stretching band of the Raman spectra of biological samples is indicative of its lipid composition and overall protein content. However, it is challenging if not impossible to single out a specific components, as they are usually mixed together within the same focal volume. Nonetheless, the window is packed with information that can be carefully extracted and used to explain the general biochemical properties of lipid-rich samples, such as meibum secretions.

Raman spectroscopy in the fingerprint region was used to examine Meibomian glands and meibum secretions, because this window is rich of chemical information. However, most studies were done in cuvette measurements of bulk meibum in which a point sample was representative of the whole. Similar approaches with other spectroscopic techniques provided high degree of composition information but lacked spatial resolution. Raman imaging were the entire spectrum is obtained for each pixel of the sample is possible, but it is extremely slow. To speed up the process coherent Raman scattering was used, compromising on spectral resolution. CRS imaging on mice meibomian glands informed about the composition and spatial distribution of the glands. CRS imaging on the fingerprint region is also possible, but the signals at low Raman shifts are weak and have no easy interpretation, as they may be originated from a handful of chemical bonds, not exclusive to a single biochemical component.

We applied CRS in form of hyperspectral SRS (hsSRS) to examine the meibum secretions in the CH stretching window of the Raman spectrum, where the signal is strong and meaningful. This allowed us to reconstruct chemical maps of the meibum secretions and learn about the composition and conformation changes as a function of dry eye disease severity.

4.3.1 Training set processing

The result of processing the training set through the MVA is depicted in figure 4.8. Images reconstructed by VCA have a rich dynamic range of colors that identify substructures within the meibum secretions with great detail (figure 4.8 A). To be able to quantify what part of the area belongs to protein- or lipid-rich groups we proceeded a KMCA implementation, from which we extracted six reference spectra (figure 4.8 B). The fraction of pixels in each spectral group, for each image, is presented in figure 4.8 C, and the final reconstructed images with the six spectral classes - each represented by a different color - are shown in figure 4.8 D.

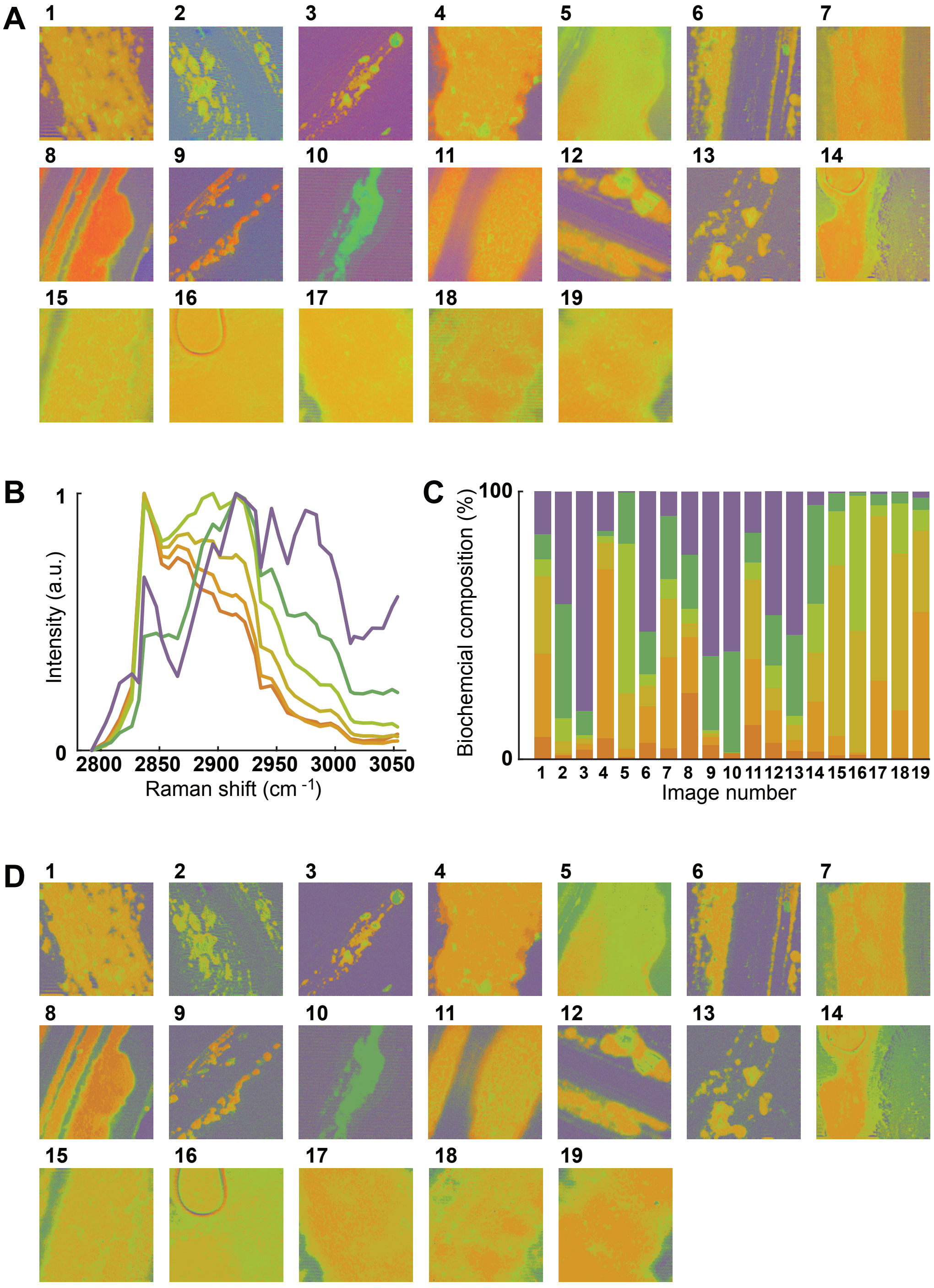

Figure 4.8: Multivariate analysis sequence applied on the training set. A) VCA output images. B) Refenrece spectra. C) Composition fraction into each group. D) Reconstructed images after the overall KMCA on the VCA output. Image size $\sim 82\ \mu m$.

Note the variation of lipid classes across the images, which is quantified in the composition fraction histogram. This subset of data illustrates the variation of structures and composition across meibum secretions from different patients. Relevant substructures include solid protein blocks depicted in darker green, wax ester-rich lipid globules in darker orange, or large areas of lipid-protein mixtures in lime green.

4.3.2 Bulk analysis of the classified images

Once the training set was characterized, and the Random Forests classifier was calibrated, obtaining new analysis from new hsSRS images was fast and easy. The only pre-processing required from new hsSRS was z-score normalization, in order to directly compare the results with the reference spectra. Figure 4.9 shows a batch of images classified with the calibrated RF and the corresponding histogram with the protein and lipid fractions. Note that the histograms were normalized to only account for meibum secretion, no background was included. The composition fraction of each sample may be used as a metric for further classification and correlation with the clinical data.

4.3.3 Large sample, small sampling

Meibum secretions can be as long as $> 1\ cm$ of continuous material, or as small as some specks distributed on the slide. Despite CRS microscopy allows rapid inspection of large areas, rather than single point measurement, the achieved field of view is small compared to the large meibum secretions. To obtain an accurate representation of the secretion, accounting for intrasample variability or homogeneity, at least two subsections were sampled. In order to detect the morphological details of the samples, hyperspectral imaging was done in zoomed-in areas that further limit the field of view to $\sim 82\ \mu m$.

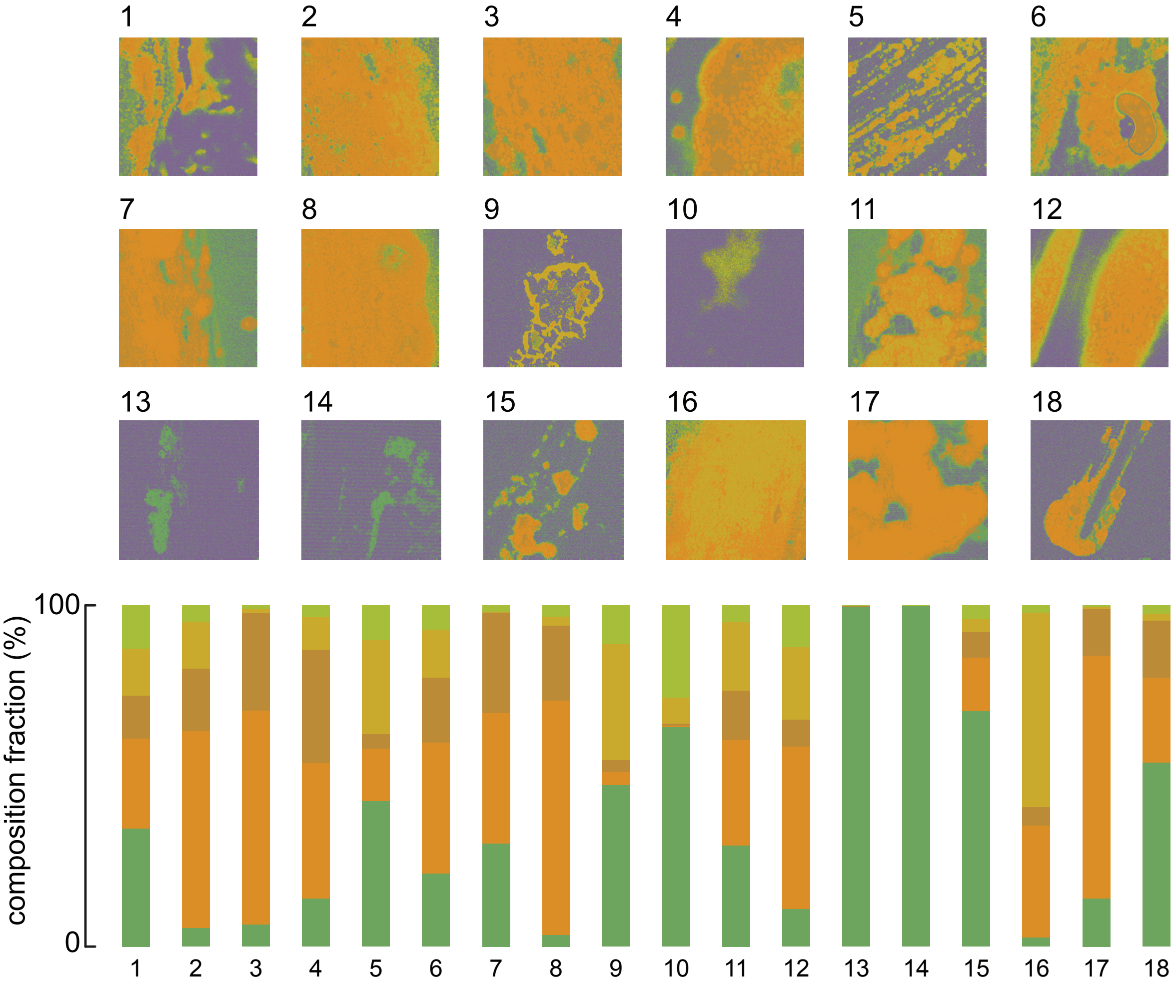

Figure 4.9: Classification results of a new subset of hsSRS images through the RF classifier. Images and corresponding composition fractions are shown. Image size ~ 82 μm.

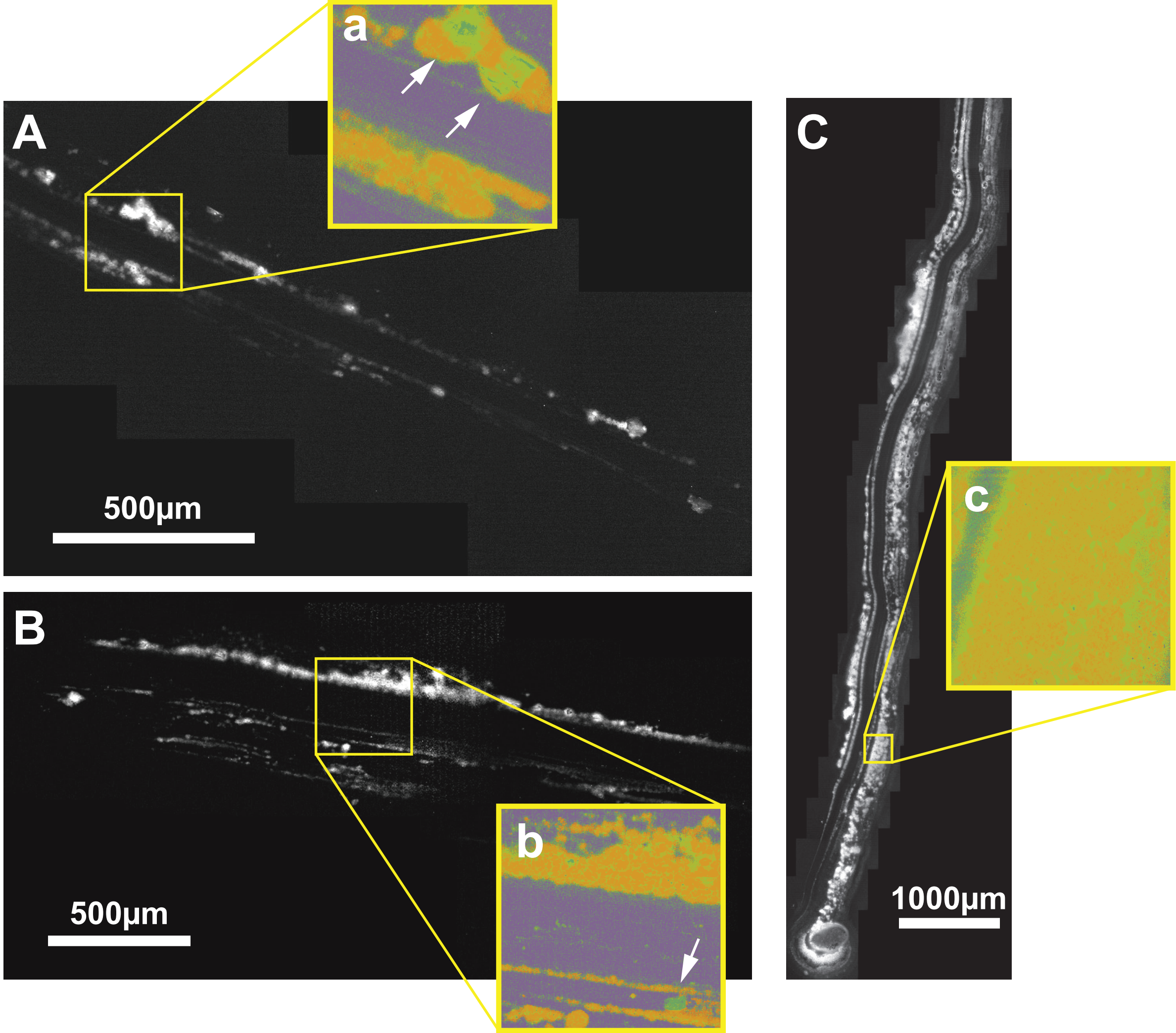

Figure 4.10: A-C) Mosaics of three meibum secretion at 2850 cm^{-1}, with a-c) detail chemical map acquired after MVA, image size $\sim 82\ \mu m$. White arrows point to protein-rich structures.

The areas selected for imaging include structures representative of the particular secretion. Figures 4.10 A-C show three reconstructed mosaics (gray scale images) taken at 2850 cm^{-1}. Each one includes a detail section analyzed through the MVA sequence to obtain the corresponding chemical map (figure 4.10 a-c, color images).

Different structures were identified in the single color image which show different biochemical composition in the chemical maps. A common structure features lipid-rich globules surrounded by protein-rich areas. Angular, crystal-looking blocks are present with variable frequency along some meibum secretions. These blocks are mainly composed of protein (green angular structures, figure 4.10 a and b, white arrows). Lipid puddles as big as > 100 μm in diameter were also found in some secretions (see top part of image 16 in figure 4.8 A and D, or right side of image 6 in figure 4.9 for a small puddle). It might be worth analyzing the frequency and the size of the protein blocks and the lipid puddles in each secretion, as they might be correlated with the severity of the dry eye case.

Other particular structures found in these samples were small, bright dots, with no spectral features. It is my hypothesis that these dots correspond to makeup contamination, among other reasons, because only samples from female donors contain them. These bright sports would hinder the spectral analysis if only VCA or KMCA was applied independently. The MVA sequence analysis overlooks them, considering their signal as noise. Training set samples 2 and 5 contain these makeup traces (see figure 4.8 A and D).

4.3.4 Lipid and protein segregation

We identified an apparent segregation of protein and lipid within the meibum samples. Lipids were arranged as orange blobs (up to ~ 10 μm in size) embedded within a green protein-rich matrix. Figure 4.11 shows three representative examples of this organization captured by KMCA (A). Each of the images belongs to a different patient and has different predominant contribution form the lipid fraction. Secretion number 1 contains the largest contribution of wax esters-rich areas in a continuous mass that is decorated with protein-rich sections. The edges of the secretion concentrate the purest wax ester contributions. Samples number 2 shows very clear segregation between the lipid and the protein phases and features fragmented lipid globules of various lipid classes (dark orange blobs versus ocher blobs). Secretion number 3 shows the higher degree of lipid-protein mixture of the three. The most abundant lipid class in this sample has a high contribution of the methyl stretches. The

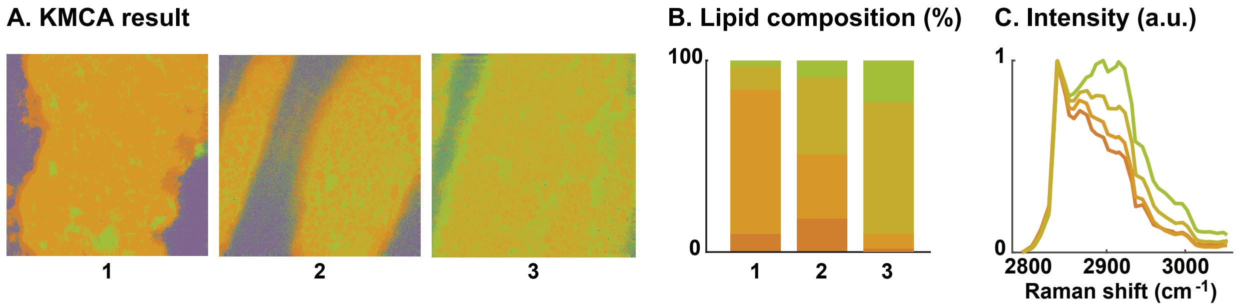

Figure 4.11: Lipid fraction varies across samples of different patients. A) KMCA images from three different patients. Image size ∼ 82 μm. B) Corresponding lipid composition according to the spectral groups depicted in C) normalized reference spectra.

overall color is less red, and its lipid globular structure is less defined than in the previous sample. Both samples 2 and 3 suggest that the lipid fraction (oranges) is embedded in a protein-rich matrix (greens).

4.3.5 Eyelid location analysis

In order to address whether the composition of meibum secretions from meibomian glands situated in different parts of the eyelid is comparable or not, multiple secretions were extracted from a subset of patients. Figure 4.12 shows the lipid and protein composition and the corresponding images from two sets of samples collected from two different subjects. Despite only a limited portion of the secretion samples was measured, the data provide an indicative measure of the overall sample composition. In this case, sample 46 contains more overall protein than sample 45. The location of the Meibomian gland the secretion is extracted from does not affect the result dramatically, as there is, from this set of data, as much variability within the same secretion as there is between neighboring secretions. Further analysis with additional patients would elucidate clearer trends.

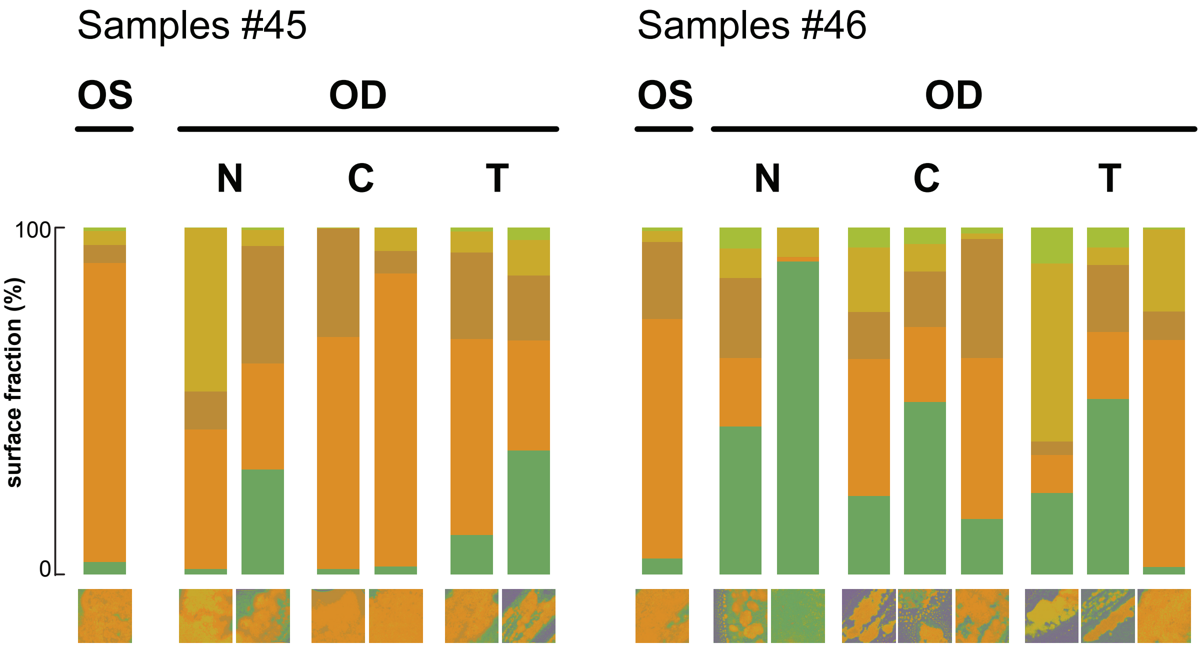

Figure 4.12: Meibum composition analysis of secretions from the left eye (OS), and the nasal (N), central (C), and temporal (T) parts of the right eye (OD), for two different subjects (number 45 and number 46). Image size $\sim 82\ \mu m$.

4.4 Concluding remarks

Given all the acquired data and a robust image processing stream, further analysis will unveil trends that might (or might not) be correlated to the severity of dry eye disease. Parameters to consider in the analysis include:

1. Lipid and protein fraction contribution to each individual stack.
2. Morphological parameters of the sample (number of angular protein blocks, size of lipid globules, etc.)
3. Composition variability within secretions.
4. Composition variability across secretions from different Meibomian glands of the same patient.

Once the morphological and compositional properties of the meibum secretions are specified, we suggest to explore correlations with the clinical data by means of linear regression or more sophisticated statistical techniques.

We have build a solid data analysis infrastructure capable of systematic quantification of meibum secretions, based on coherent Raman scattering imaging of the CH stretching moieties of the samples and batch-level multivariate analysis coupled to machine learning classification. Further analysis of the acquired data together with the clinical evaluations performed by the doctors could provide valuable information on the understanding of dry eye disease progression. A basic understanding of the biochemical changes occurring during the development of dry eye disease may stimulate new diagnostic protocols and strategies for potential alleviation methods of this irritating eye disease.

Chapter 5

Lipid accumulation as a hallmark for disease

Disruption of lipid homeostasis may result in excessive intracellular lipid accumulation. Cells control excessive lipid content by packing lipids it into dedicated droplets that initially protects against cytotoxicity. However, over-accumulation has negative consequences to human health. Spaceflight-induced alterations affects numerous organ systems in the body, including the lipid liver metabolism, which remains unexplored. Raman microspectroscopy combined with metabolomics and transcriptomics analysis were used to investigate altered hepatic lipid metabolism on mice that reside aboard a space shuttle. Early signs of liver injury were found in the form of increased lipid droplet accumulation and retinol loss in the spaceflight mice, which raise concern that long-duration spacial travels may increase the risk for nonalcoholic fatty liver disease. Atherosclerosis is also characterized by lipid accumulation. Macrophages, scavenger cells in atherosclerotic lesions, exhibit a variety of polarization states that influence their ability to handle lipid. Macrophage's lipid accumulation was quantified by coherent Raman scattering microscopy combined with machine learning segmentation algorithms. We found that pro-inflammatory macrophages have a tendency to become foam cells upon stimulation with excess lipid, while pro-healing macrophages tend to remain lean, despite not being fully resistant to become lipid-laden cells.

5.1 Spaceflight activates lipotoxic pathways in the liver

This work has been published in the following paper:

Jonscher, K. R., Alfonso Garcia, A., Suhalim, J. L., Orlicky, D. J., Potma, E. O., Ferguson, V. L., et al. (2016). Spaceflight Activates Lipotoxic Pathways in Mouse Liver. PLoS ONE, 11(4), e0152877.

5.1.1 Introduction

Nonalcoholic fatty liver disease (NAFLD) is characterized by the over-accumulation of lipids in form of lipid droplets in the liver cells. On Earth, although still unclear, some of the possible causes of NAFLD include obesity and diabetes[17]. NAFLD however, could also be a systemic effect of microgravity and other spaceflight environment factors such as radiation and oxidative stress[135,136].

Spaceflight conditions alter regular body activity as we know it. In times when space journeys are longer (NASA's one-year mission [i]), projected to go further (journeys to Mars [ii]), and not only limited to professional astronauts (Virgin Galactic [iii], and Space Adventures [iv]), knowledge of body reactions to the space environment gains particular importance. Scientists are studying the effects of microgravity on bone and muscle, as well as in the brain and on cardiovascular function[137–139]. Of particular interest to us are the effects of microgravity on

---

[i] https://www.nasa.gov/content/one-year-crew

[ii] http://www.mars-one.com/, http://mars.nasa.gov/programmissions/science/goal4/

[iii] http://www.virgingalactic.com/

[iv] http://www.spaceadventures.com/

hepatic energy and lipid metabolism. The importance of finding how hepatic function is altered as a result of spaceflights lies in the relevant role of the liver in orchestrating gross-metabolism. It has been shown that NAFLD increases the risk for further pathologies such as cardiovascular problems, type-2 diabetes, and hepatocellular cancer[140].

In collaboration with Dr. Karen Jonscher from the University of Colorado School of Medicine and her colleagues, we participated in a novel systems biology approach to address functional liver changes in mice aboard the space transportation system STS-135 during 13 days, on the last US space shuttle mission, launched on July 8, 2011. The full study comprises data from a variety of techniques, featuring transcriptomics, metabolomics, liquid chromatography/mass spectroscopy, gas chromatography/mass spectroscopy, pathway analysis, microscopy (CARS, SRS, SHG, TPEF, immunohistochemistry), and Raman spectroscopy.

5.1.2 Experimental details

Two groups of 15 nine-week old weight-matched female C57BL/6J mice were considered for the experiment. Both groups of mice were placed in animal enclosure modules (AEM). One group, referred to as FLT, was then brought to the Space Shuttle Atlantis (STS-135) for 13.5 days, while the other, referred to as AEM, was kept at the Space Life Sciences Laboratory (SLSL) at the Kennedy Space Center. Both groups were given the same diet, based on NASA NuRFB foodbars[141]. Ground control (AEM) mice were kept under environmental conditions that mimic those of the flight group as much as possible (temperature, humidity, light:dark cycle, food and water intake).

Mice of both groups were weighted before and after the journey, and euthanized after the return of the flight group. Mice tissues were then distributed between different research groups. We received half livers from 6 mice in each group that had been dissected, flash frozen in liquid nitrogen, and fixed. For the microscopy studies, liver cryosections of ~ 12

	AEM	**FLT**	**FLT/AEM**	**p-value**
Food intake (g)	4.08±0.10	4.09±0.18	1.00	0.865
Δ Body Mass (g)	-1.18±0.24	-2.28±0.57	1.93	0.036 (*)
Δ % Fat	4.12±0.77	5.05±1.84	1.22	0.022 (*)

Table 5.1: Food intake and body composition measurements for AEM controls and FLT mice. Values presented are mean ± SEM. p-values obtained with a two-tailed Student's t-test, * for $p<0.05$. Data from n=6 mice per group.

μm thickness were placed on microscope slides, rinsed with cold phosphate-buffered saline (PBS) to remove Optimal Cutting Temperature (OCT) solution [v] (used to prepare the samples) and sandwiched with a thin coverslip.

5.1.3 Results and discussion

Both mice groups lost weight over the course of thirteen days, but the flight (FLT) group lost double the amount of weight than the ground controls (AEM). A larger weight loss in the flight group was expected as astronauts also lose body weight on their trips due to muscle atrophy[137]. Interestingly, the fat mass of both groups was not significantly different. Instead, the lean body mass was accounted for the weight difference between the two groups. Overall, this makes the flight group of mice have a significantly larger percentage of body fat. Table 5.1 summarizes the weights of food intake, body mass increment, and percentage fat increment for each mice group during the length of the experiment.

Because liver is an important player for metabolic processing of excess lipid, our task was to study its appearance in CARS microscopy. FLT mice livers had more lipid droplets (LDs) than ground controls, as illustrated in figure 5.1. The overall CARS signal intensity from FLT mice livers was about 3.5 higher than that of the AEM control group. Accordingly, spaceflight mice showed increased levels of triglycerides, as measured by colorimetric assays,

---

[v] OCT contains polyvinyl alcohol (PVA), which has a strong Raman mode at $\sim 2912\ cm^{-1}$ that interferes with the CH stretching signal from the samples.

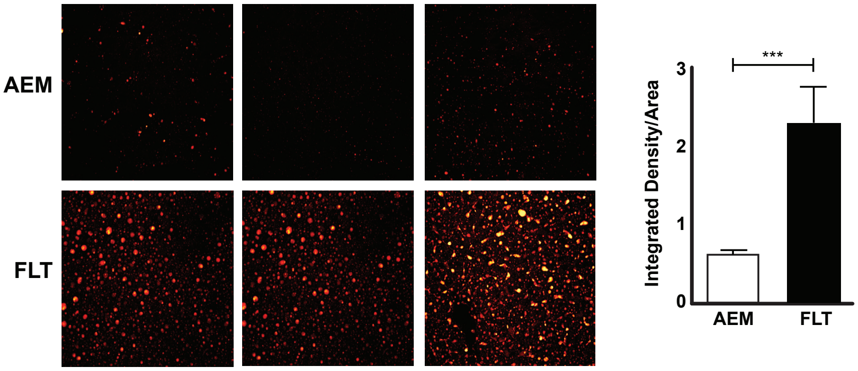

Figure 5.1: Spaceflight mice have increased accumulation of hepatic lipid droplets. Frozen liver cryosections were imaged by CARS at 60x magnification. Representative images are shown from 3 different animals in each group. Images form the AEM ground control group are in the top panel, and from FLT mice in the bottom panel. Multiple regions were images from 2 cryosections taken at different tissue depth per animal. Images were processed using ImageJ and integrated pixel intensity measured for each unit area. A Mann-Whitney test was used to compare integrated intensity values between groups. *** $p < 0.001$.

and indicated by triglyceride biosyntheic pathways up-regulation. These test indicate a shift in the balance between lipid synthesis and oxidation. Increased lipid storage is likely to protect against the excess lipid.

In addition to the increased abundance of lipid droplets in the flight mice, we studied whether the composition of the droplets would also differ between the two groups. We used spontaneous Raman spectroscopy to probe individual lipid droplets first, and hyperspectral SRS to investigate larger areas of the liver containing multiple lipid droplets. We did not observe significant differences in the smaller LDs, but we did find a significant variation in a fraction of the largest LDs. While the typical lipid indicators remained unchanged in both groups, a peak at 1593 cm^{-1} was not present in all LDs of the flight cohort. Figure 5.2, panel A, shows an SRS image at $\sim 1593 cm^{-1}$ of a ground mice (AEM) liver section with bright lipid droplets. In contrast, the spaceflight mice (FLT) image (figure 5.2 panel C), excited at the same frequency, exhibits lipid droplets with lower intensity, almost near the background intensity level. When imaged at $2845 cm^{-1}$, liver sections of both ground and spaceflight groups display intense and well defined lipid droplets, figure 5.2 panels B and D, respectively. The reconstructed Raman spectra, from the hsSRS images (Figure 5.2 E - red curves) confirm this discrepancy in the vicinity of the 1593 cm^{-1} peak. The C=C stretching mode at 1660 cm^{-1}, characteristic of unsaturated lipids, as well as the C-H stretching band (2800-3050 cm^{-1}) appear almost identical for both groups. Table 5.2 shows the relevant vibrational modes and their molecular assignments. Additional spontaneous confocal Raman spectra (Figure 5.2 E - black curves) confirms the similarities throughout the entire spectral span examined (from 1400 to 3100 cm^{-1}). The notable difference between the Raman spectra of both groups is the lack of the 1593 cm^{-1} peak in the spaceflight mice, which closely matches the spectral differences seen in the hsSRS images.

The only noticeable difference in composition of mice exposed to microgravity was in the 1593 cm^{-1} peak, which was assigned to retinoids (figure 5.3). Retinol is a dietary fatty acid with conjugated C=C double bonds, present in the mice diet (NuRFB foodbars). The strong resonance of retinol's conjugated double bond system overwhelms other Raman contributions. Thus retinol has a negligible effect on the CH bands, not affecting the 3010 cm^{-1} peak (=C-H), and hence the saturation ratio (I_{3010}/I_{2845}), which doesn't change from one group to the other.

The liver is the largest storage of retinol in the body. Specifically, 80% of the total retinoids in the whole body, which comprises vitamin A and its metabolites, are stored in lipid droplets in hepatic stellate cells (HSC), in form of retinyl esters[142]. We observe a loss of retinoids in the spaceflight mice livers, which might be a sign of HSC activation, perhaps initiated by the exposure to the stress associated to the space environment. Metabolomics and transcriptomic studies made on these same samples showed changes in the FLT livers that suggest the activation of lipid metabolism pathways such as the PPAR-α pathway. Retinoids released from activated HSC trigger transcriptional programs mediated by nuclear receptors that are relevant to these lipid metabolic pathways[142].

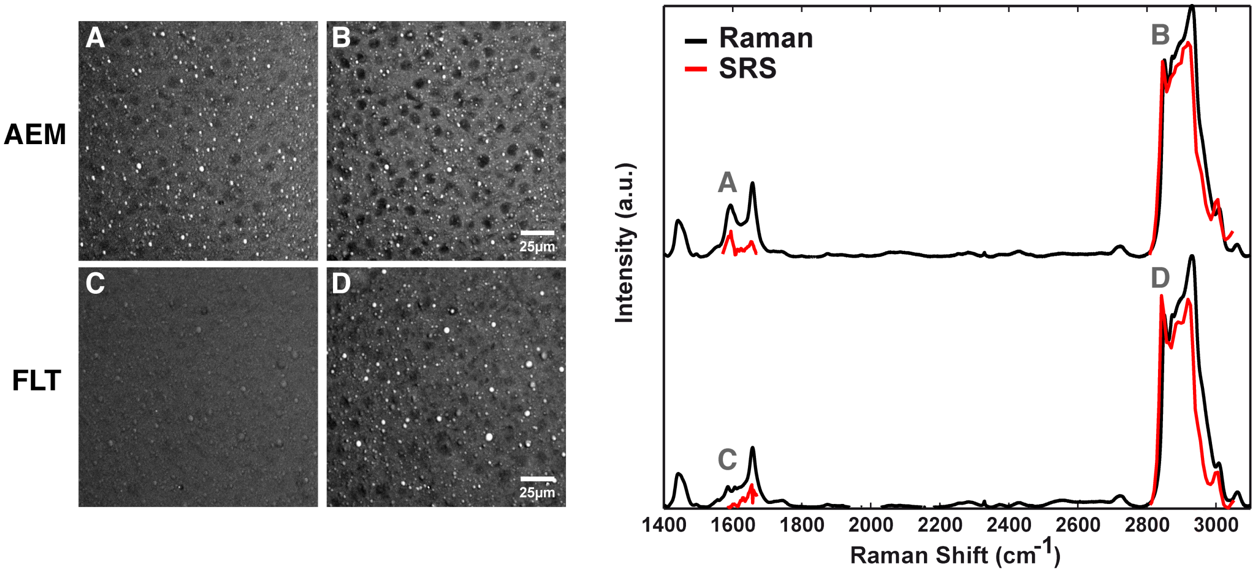

Figure 5.2: Lipid droplets in spaceflight mouse liver have reduced retinol content. Space flight mice may lack retinol. Stimulated Raman scattering (SRS) images of liver sections revealed a decreased intensity of the embedded lipid droplets at $\sim 1593\text{cm}^{-1}$ for spaceflight mice (FLT, image c) with respect to ground mice (AEM, image a), and show no difference at 2845cm^{-1} (images b and d), the CH_2 symmetric stretching band characteristic of lipids. Hyperspectral SRS imaging around the two frequencies of interest unveil a quasi-identical spectra of the lipid droplets of the two mouse groups, except for the peak at $\sim 1593\text{cm}^{-1}$ (red curves). Spontaneous Raman spectra (black curves) agree with the SRS results.

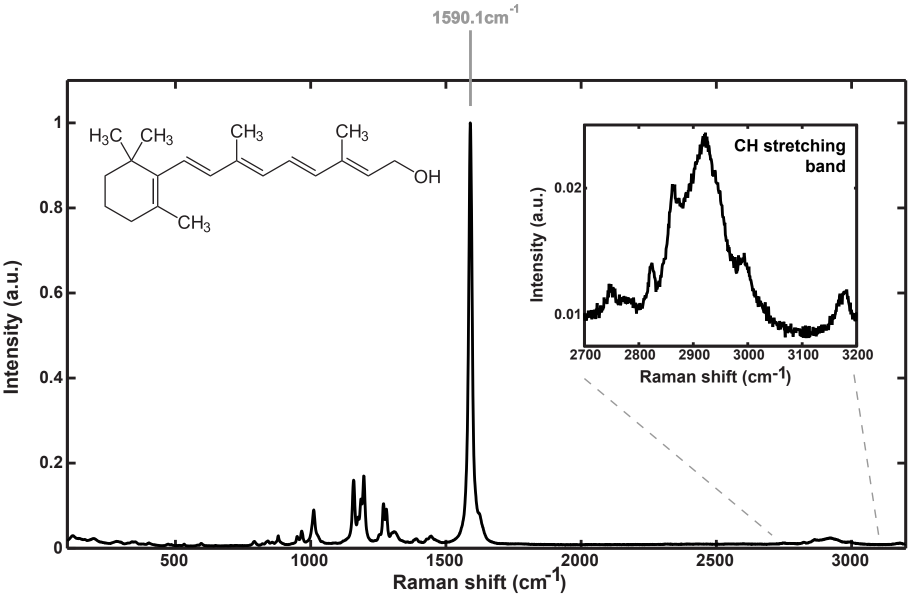

Figure 5.3: Raman spectrum and molecular structure of retinol.

Raman shift (cm^{-1})	**Molecular vibration**
1440	Lipid/protein, CH deformation
1593	Retinol, conjugated C=C stretch
1660	Lipids, C=C stretching band
2845	Lipids, CH_2 symmetric stretch
2885	Lipids, CH_2 asymmetric stretch
2950	Lipid/protein, CH_3 stretch
3010	Lipid, =CH stretched

Table 5.2: Raman shifts and associated molecular vibrations[143–145].

5.1.4 Concluding remarks

Spaceflight mice lost a significant amount of lean body mass, compared to the ground controls, which is consistent with human studies on spaceflight journeys or bed rest[137]. As a consequence, the total percentage of fat in the mice body increased, and so did the total amount of hepatic triglycerides. Indeed, more lipid droplets were found in the spaceflight livers by CARS imaging, which was in agreement with the upregulation of genes involved in triglyceride biosynthesis. The Raman analysis of lipid droplet composition points towards potential initiation of hepatic stellate cell (HSC) activation induced by spaceflight factors. Spontaneous confocal Raman of individual lipid droplets, and hyperspectral SRS imaging of larger areas, showed a notable difference between spaceflight and ground control livers at the band assigned to the vibration of conjugated C=C double bonds ($\sim 1953\ cm^{-1}$), a Raman mode indicative of retinol esters, which are densely packed into lipid droplets of the HSC in the liver under regular physiological conditions. HSC release retinoids upon activation that affect other metabolic pathways, which were also found to be altered in the spaceflight mice, such as a high upregulation of the PPAR-α pathway that plays an important role in lipid metabolism as it is involved in fatty acid uptake, mitochondrial β-oxidation, triglyceride turnover, and bile synthesis/secretion, among others. All these symptoms may ultimately lead to NAFLD[146,147].

This study exemplifies the potential of CRS imaging as a visualization partner to *omic* studies, including genomics, proteomics, and metabolomics. The consequences of certain gene activation or metabolic pathways, up- or downregulated, have visible effects that can be monitored by CRS microspectroscopy. In particular, CRS microscopy has the ability of interrogating large areas at rapid rates, useful not only for morphological inspection, but also for fast chemical imaging of multiple structures simultaneously. In this case, information from multiple lipid droplets was acquired in a single SRS hyperstack image, compared to multiple single measurements taken on individual lipid droplets by confocal Raman spectroscopy. Confocal Raman is particularly useful as a first inspection tool to identify possible markers of interest. Once these have been identified, CRS microspectroscopy offers a high-throughput analysis tool with spatio-chemical resolution.

5.2 Lipid accumulation patterns in polarized macrophages

5.2.1 Introduction

Macrophages, atherosclerosis scavengers

Atherosclerosis is a chronic inflammatory disease that also revolves around abnormal accumulation of fat. It is characterized by the interaction of lipoproteins, the immune system, and the arterial wall. As a result, lipid-rich plaques grow into the arterial lumen. These plaques often remain stable, but some may eventually rupture and form thrombosis, leading to myocardial infarction or stroke[148].

Plaque starts forming when low-density lipoproteins (LDL), circulating within the blood stream, traverse the vessel wall in susceptible regions of the endothelium. Once in the sub-endothelial space, LDL particles are retained and modified into oxidized LDL (oxLDL) particles[149,150]. The presence of the modified lipoproteins triggers an inflammatory reaction, to which the immune system responds by recruiting monocytes at the lesion site. The recruited monocytes adhere to the endothelium and also migrate through it, into the vessel intima, where they differentiate into macrophages that uptake the modified lipoproteins, and eventually become foam cells[151,152]. Depending upon the biological mediators present within the plaques milieu, different macrophage phenotypes arise, generating a heterogeneous macrophage population. At one end of this spectrum, in the first line of defense, macrophages exposed to inflammatory signals polarize towards a classically activated, inflammatory phenotype (M1) and secrete proinflammatory cytokines and reactive species. At the opposite end of the spectrum, macrophages present within a wound healing environment polarize towards an alternatively activated, prohealing phenotype (M2) and facilitate processes involved in tissue repair[153–155]. Even though being a simplified approach, the classification of macrophages as either M1 or M2 is used as a paradigm to study their role in the pathogenesis of atherosclerosis[148,151,156]. It is believed that proinflammatory cells uptake massive amounts of oxLDL, and rapidly become foam cells promoting inflammation, while prohealing macrophages play an atheroprotective role[149,150,157].

The cytokines macrophages are in contact with in the plaque microenvironment determine the cells' polarization state. Currently, it is widely accepted that T-helper 1 (Th1) cytokines, such as interferon-γ (IFN-γ) and interleukin-1β (IL-1β) promote differentiation of monocytes into proinflammatory M1 macrophages, whereas Th2 cytokines, such as interleukin-4 (IL-4) and IL-13, polarize monocytes into prohealing M2 macrophages[156]. Additionally, within the plaque environment there are other inflammatory mediators, like the bacterial endotoxin lipopolysaccharide (LPS), which has also been linked to a macrophage proinflammatory response[151,152,158].

Lipid accumulation patterns in polarized macrophages

Studies examining how the polarization state of macrophages influence their ability to handle lipids within plaques or in vitro yielded varied results. It is conventional wisdom that proinflammatory macrophages accumulate more lipid droplets and more readily transform into foam cells compared to prohealing macrophages[159]. Recently, however, this picture has been contested by several studies that have shown that pro-healing macrophages have a higher propensity to become lipid-laden cells[160–162]. Moreover, foam cells within atherosclerotic plaques have been shown to exhibit a mixture of surface markers of both phenotypes[163,164]. These conflicting observations have prevented a cohesive understanding of the correlation between macrophage polarization and intracellular lipid content. To address this question, a more thorough and systematic investigation of how different polarization conditions influence lipid uptake is necessary.

Standard methods to evaluate lipid accumulation in cells include biochemical assays and imaging techniques. Biochemical assays work well for quantification of intracellular lipid content[165–167], but lack the spatial resolution needed to identify cell-to-cell variation. Conversely, imaging stains such as Oil Red O provide spatial resolution[26], but lack chemical selectivity and may produce labeling artifacts, which prove problematic when quantitative accuracy is desired[30,50,168].

Nonlinear vibrational microscopy, on the other hand, is a label-free method that generates chemical contrast[74]. Nonlinear Raman microscopy, including coherent anti-Stokes Raman scattering (CARS), is particularly useful for quantitative lipid analysis because of its fast imaging capability[64], important when collecting statistically meaningful data from a large number of cells. CARS microscopy has been used successfully in quantitative analysis of lipids in cells[169], atherosclerotic plaques[115,170], and even entire organisms[76].

Using label-free CARS microscopy and machine learning-based lipid analysis, we establish a relation between macrophage polarization and lipid accumulation. The automated tools enable the imaging and lipid analysis of more than 4000 cells, providing statistically meaningful relations between macrophage phenotype and intracellular lipid content. We find that macrophages stimulated with interferon-γ (IFN-γ) and lipopolysaccharide (LPS), which induce a pro-inflammatory phenotype, accumulate more lipid droplets and more readily become foam cells when compared to macrophages treated with interleukin-4 (IL-4) and interleukin-13 (IL-13), which induce a pro-healing phenotype. Furthermore, pro-inflammatory macrophages accumulate more lipid droplets the longer they are in contact with a lipid-rich medium. However, we also find that pro-healing macrophages are not fully resistant to becoming foam cells, as a considerable fraction of cells treated with pro-healing polarizing cytokines also accumulate significant amount of lipid droplets. Additionally, we determine that LPS is a key factor in lipid accumulation, and pre-treatment with LPS induces an increase in lipid droplets in all macrophage subtypes.

5.2.2 Experimental details

Cell culture

Mouse bone marrow-derived macrophages (BMDM) were isolated from femurs of female, 6-12 week old C57BL/6J mice and cultured as described[171], in medium containing 10% fetal bovine serum, 100 U/ml penicillin, 100 $\mu g/ml$ streptomycin, and 10% media conditioned by Ltk-cells expressing recombinant MCSF ectopically. On day 7, 3x10^5 BMDMs were seeded on glass coverslips. The following day, cells were transferred to similar media containing either lipoprotein-depleted bovine serum (LPDS; Alfa Aesar) or normal fetal bovine serum (FBS) and then stimulated with cytokines. Lipopolysaccharides (LPS; Sigma) and interferon-γ (IFN-γ; R&D) were used at 10 ng/ml, and IL-4 and IL-13 (Biolegend) were used at 20 ng/ml. After 24 hours of cytokine stimulation, media was replaced (with lipoprotein-depleted

Phenotype (cytokines)	Diets	Time Points
M0 (none)	FBS (+ control)	0 hours
M1 (IFN-γ + LPS)	LPDS (- control)	24 hours
M2 (IL-4 + IL-13)	oxLDL (at 20, 40, 100 μg/mL)	48 hours

Table 5.3: Combinations of these macrophges' polarization, diet, and culture time make the groups considered for this experiment.

serum (LPDS) or normal media, per the experimental condition, Table 5.3) and cells were exposed to 0, 20, or 40 $\mu g/ml$ oxidized human low-density lipoprotein (oxLDL; Alfa Aesar) for the remaining duration of the experiment. Cells were fixed at each time point of the lipid accumulation experiments in 10% neutral buffered formalin for 15 minutes and kept in PBS at 4°C until CARS imaging.

CARS imaging

The CARS microscope was set to excite the CH_2 symmetric stretching mode (at 2845 cm^{-1}), abundant in lipid molecules. Images were taken with a 60x 1.2NA water immersion objective lens (UPlanSApo, Olympus), which allowed for a crisp visualization of the small lipid droplets that macrophages might accumulate in their cytoplasm upon treatment. The pixel size was set to 0.15 μm. Ten to twelve images were taken for every group (see table 5.3). Macrophages from at least three mice per group were independently imaged.

Image processing

Identifying correlations between macrophage phenotype and lipid accumulation requires imaging and analyzing a large number of cells. High throughput imaging benefits from automated analysis that reduces imaging processing time, and human errors. In order to analyze the lipid handling behavior of the different macrophages subsets, we counted the number of lipid droplets that macrophages accumulate over the course of hours immerse in

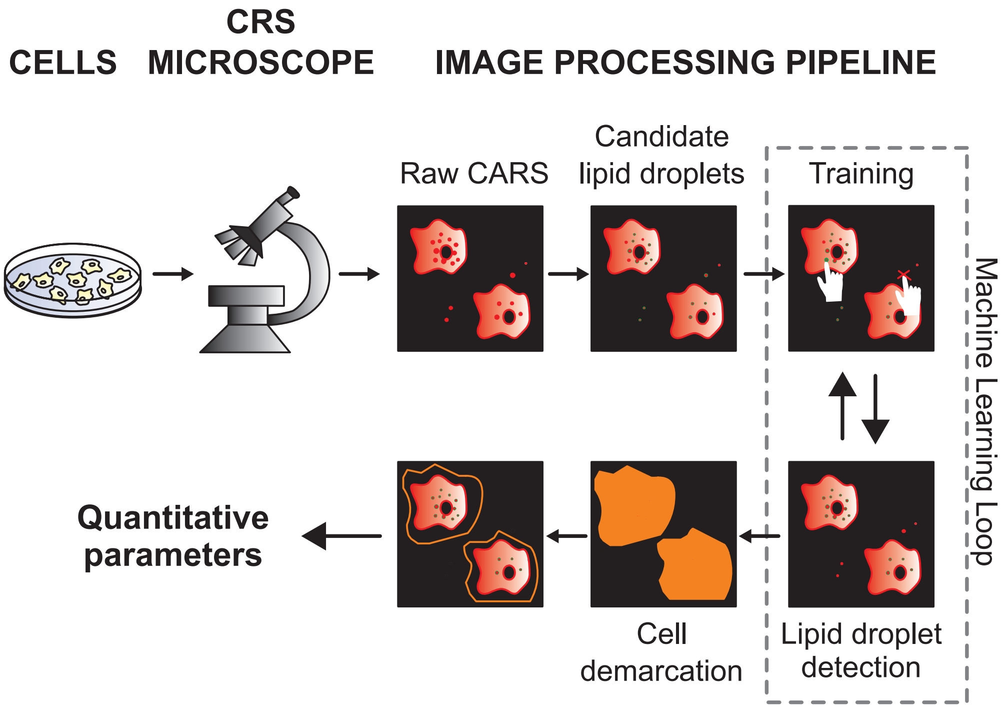

Figure 5.4: Experiment pipeline. Culture the cells, image them under the CRS microscope and process the raw CARS images with the machine learning based algorithm that identifies and segments the lipid droplets in each individual cell.

lipid-rich media. Thresholding-based segmentation algorithms are appropriate to quantify lipid droplets, identified as bright blobs on a dark background. Because global thresholding algorithms perform poorly with CARS images[108], and watershed segmentation[113] delivers an inaccurate output if used alone, local thresholding methods are preferred[108,109]. Other segmentation techniques include maximum entropy thresholding, which provide successful automatic segmentation[112]. Here we use an alternative approach based on machine learning classification to identify lipid droplets. We combine watershed segmentation with local thresholding to identify lipid droplet candidates. We then train a classifier based on a series of lipid droplet features (see table 3.1) and finally, with additional cell segmentation, we obtain the number of lipid droplets in each cell. Over 4000 cells were imaged and analyzed in total. Additional details on the machine-learning segmentation of lipid droplets can be found in chapter 3 and it is summarized in figure 5.4.

Statistical analysis

All the experiments were independently performed with cells derived from three different mice in each experimental condition. The average number of lipid droplets for every macrophage phenotype studied was computed for each mouse. Here we present the average over three mice ± standard error of the mean (SEM)., and the probability density distribution of the number of lipid droplets over the entire population of cells imaged. Statistical differences between two groups was computed by the Student's t-test, and between multiple groups using analysis of variance (ANOVA). Differences were considered significant when $p < 0.05$.

5.2.3 Results

Macrophage polarization influences the accumulation of lipid droplets

We examined lipid accumulation using CARS imaging of macrophages induced towards a pro-inflammatory (M1) or pro-healing (M2) phenotype by cytokine stimulation, and found that macrophages of different phenotypes accumulate significantly different amounts of lipid. Cells were stimulated with cytokines to induce polarization, cultured within a lipoprotein deficient serum (LPDS), and then treated with oxidized low-density lipoprotein (oxLDL) for 24 hours. We found that cells polarized with LPS and IFN-γ, which induce a proinflammatory phenotype, accumulated significantly more lipid when compared to cells polarized with IL-4 and IL-13, prohealing phenotype, and to those left unpolarized. Images of macrophages containing lipid droplets were quantified using the machine learning-based segmentation algorithm, previously described (see figure 5.4). Figures 5.5 A-C show a representative example of a CARS image for each macrophage polarization culture. Note how the signal from the lipid droplets in pro-inflammatory cells (panel A) overwhelms the cytoplasm background.

The brightness and contrast of panels B and C was altered to make the cytoplasm visible, given the lack of lipid droplet signal in pro-healing and unpolarized macrophages. Figure 5.5 D shows the average number of lipid droplets in each culture of macrophages treated with oxLDL for 24 hours.

Indeed, proinflammatory macrophages significantly store more lipid droplets (54.1±6.3) than prohealing (12.0±0.3) and unpolarized (7.0±1.9) macrophages. The probability density distribution of the number of lipid droplets accumulated by each group is depicted in figure 5.5 F. This further shows how unpolarized macrophages (n = 187) rarely contain lipid droplets, as the probability to find zero droplets in them is the highest and rapidly decays, nearing zero for over 20 lipid droplets. For prohealing macrophages (n = 155), the probability of zero droplets is also dominant, but it is less intense. The probability to find over 20 lipid droplets in a cell is also very low, but it sustains at similar values until over 120 lipid droplets. Finally, proinflammatory macrophages (n = 99) have a wide distribution of probabilities that ranges form zero to over 200 lipid droplets detected in individual cells.

Similar trends were observed when cells were treated with FBS-containing culture medium, or lipoprotein deficient serum only (figure 5.6). In the FBS cultures, proinflammatory macrophages (with a total of 191 individual cells binned across 3 different mice) accumulate an average of 47.9±12.1 LDs over 24 hours culture, and 43.2±4.1 LDs over 48 hours. Prohealing macrophages (a total of 208 from 4 different mice) have a significantly lower accumulation rate, 7.7±5.6 LDs over a 24 hour period, and 1.4±1.0 LDs after 48 hours. The accumulation by unpolarized cells (337 cells from 4 different mice) is insignificant, it amounts to 0.14±0.06 LDs after 24 hours and 0.30±0.12 LDs after 48 hours. Again, macrophages in LDPS cultures exhibit the same overall behavior. Pro-inflammatory macrophages (363 cells in 5 different mice) accumulate on average 37.1±9.4 LDs in 24 hours LPDS culture, and 43.0±8.3 LDs in 48 hours LPDS cultures. Prohealing macrophages (225 cells from 5 mice) reported a minimal accumulation of 0.9±0.2 LDs after 24 hours and 1.5±0.9 LDs after

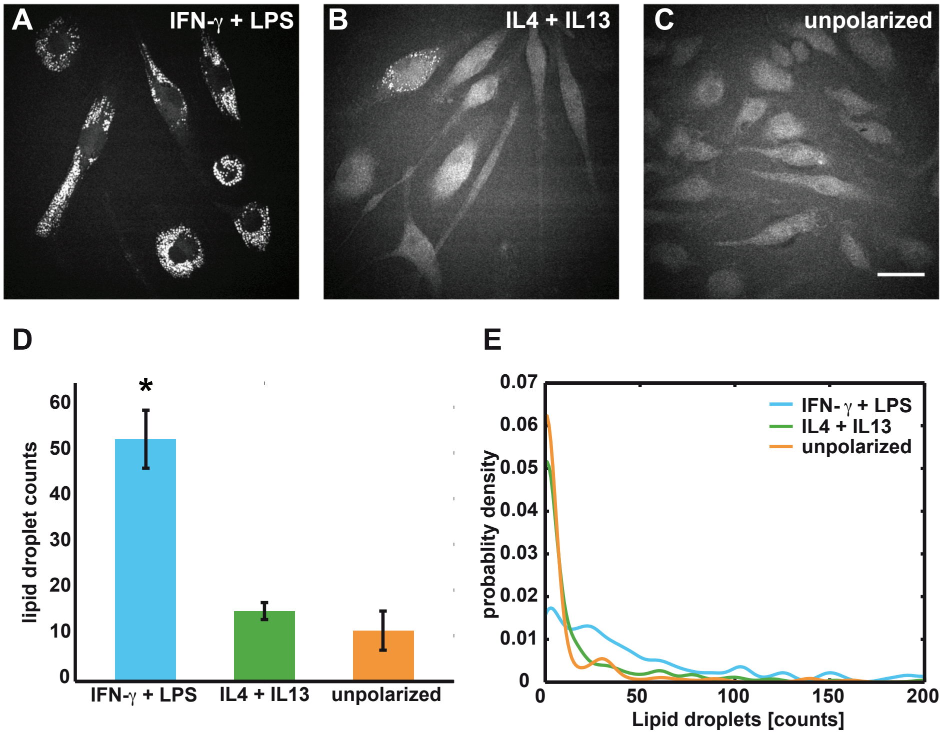

Figure 5.5: Accumulation of LDs by polarized macrophages in oxLDL. A) Coherent anti-Stokes Raman scattering (CARS) image of proinflammatory macrophages treated with INF-γ and LPS. B) CARS image of pro-healing macrophages treated with IL-4 and IL-13. C) CARS image of unpolarized macrophages. Scale bar = 25 μm. D) Average number of lipid droplets per cell for each macrophage group when cultured with oxLDL during 24 hours. *$p<0.05$. E) Probability density estimate of the number of lipid droplets for every macrophage phenotype.

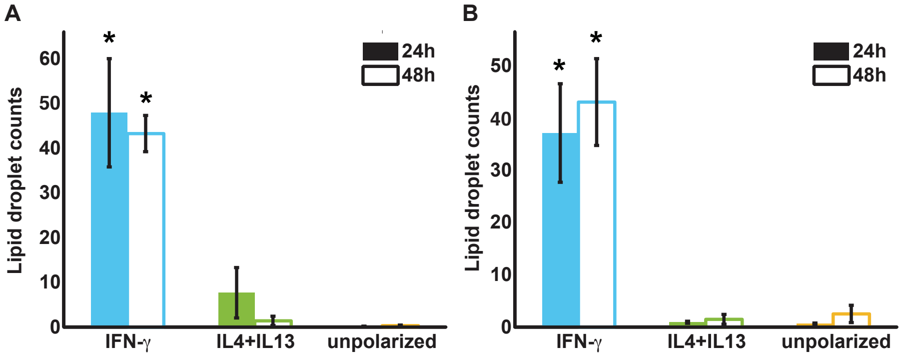

Figure 5.6: Average number of lipid droplets per cell for each macrophage group when cultured in A) FBS and B) LPDS, during 24 hours (filled bard) and 48 hours (stripe bars). $^*p<0.05$.

48 hours. Similarly, unpolarized macrophages accumulate 0.6±0.1 LDs after 24 hours and 2.5±1.7 LDs after 48 hours.

The average lipid droplet size was $\sim 1.5\ \mu m$ and it was found to remain invariable among the different groups.

Culture independent lipid accumulation and foam cell transformation

In response to a lipid-rich environment, macrophages are capable of transforming into foam cells, a key development in atheroprogression[172]. Despite their general resistance to lipid accumulation, a fraction of pro-healing macrophages accumulate significantly more lipid droplets than the majority of the population (Figure 5.7A and B), when additionally treated with oxidized oxLDL. Due to a lack of a quantitative definition for foam cells, we define a foam cell rate (FCR) as:

$$FCR = \frac{\text{number of cells above } TH}{\text{total number of cells}} \cdot 100 \tag{5.1}$$

where TH is the threshold number of intracellular lipid droplets within the cell. This aims to quantify the amount of cells that appear as foamy in a given population.

Figure 5.7 shows CARS images of foam cells in a proinflammatory culture (panel A), and a pro-healing culture (panel B, arrow). The FCR for cells treated with M1-inducing cytokines is consistently higher at all threshold values when compared to the FCR for cells treated with cytokines that induce M2-macrophages, which in turn had a higher FCR than unpolarized cells (Figure 5.7 panel C). Interestingly, we also observed differences in the FCR over time. The foam cell rate of cells treated with M1 cytokines increased between 24-48 hours after the addition of lipids, whereas for cells treated with M2 cytokines FRC did not change, and for unpolarized cells it was reduced during this period of time.

The duration of the oxLDL exposure influences lipid droplet accumulation

We next examined the changes in lipid droplet accumulation over a longer duration of oxLDL exposure. With increasing time of exposure to oxLDL from 0 to 48 hours, the extent of lipid droplet accumulation in macrophages treated with IFN-γ and LPS concomitantly increased (see figure 5.8A-C, and the widening blue curve in D). In contrast, the amount of lipid droplets in macrophages treated with IL-4 and IL-13 remained constant from 24 to 48 hours after treatment, but it was larger than at time zero (figure figure 5.8 D, green curve). Finally, the number of lipid droplets in unpolarized macrophages is reduced with incubation time (figure 5.8 D orange curve). Before being fed oxLDL, macrophages treated with IL-4/IL-13 or untreated macrophages were likely to have 0 to 20 lipid droplets; however when treated with additional oxLDL, macrophages treated with IL-4/IL13 develop more lipid droplets, with a significant portion of cells exhibiting 50 to 100 lipid droplets. On the other hand, pro-inflammatory macrophages may contain up to 100 lipid droplets prior to the addition of oxLDL. Over time this distribution widens, showing that these cells store more lipid droplets the longer they are exposed to an oxLDL-enriched medium.

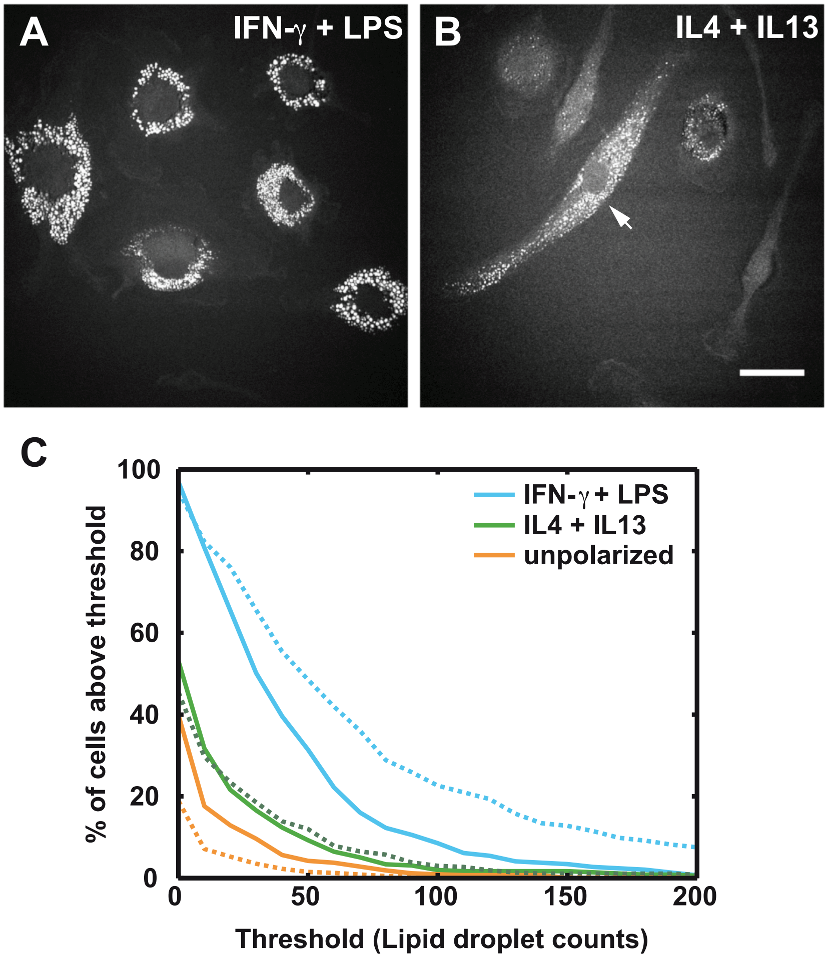

Figure 5.7: Foam cell form upon oxLDL stimulation regardless of polarization state. A) CARS image of foam cells in macrophages stimulated with IFN-γ and LPS. B) CARS image of a foam cell in macrophages stimulated with IL-4 and IL-13 (arrowhead). Scale bar = 25 μm. C) Foam cell rate, or percentage of cells above threshold, found in IFN-γ/LPS, IL-4/IL-13, and untreated macrophages cultured with oxLDL after 24 hours (solid lines) and 48 hours (dashed lines).

Lipopolysaccharide is a major factor that determines lipid droplet accumulation

Lipopolysaccharide (LPS), an endotoxin found in gram-negative bacteria, is known to have potent inflammatory effects[158]. In order to test the impact of LPS on intracellular lipid accumulation, we treated the cells with different combinations of cytokines, with and without LPS. We found that macrophages treated only with IFN-γ, which independently leads to a pro-inflammatory phenotype, accumulate less lipid droplets than those additionally cultured with LPS (figure 5.9). Macrophages treated with IL-4/IL-13, also showed an increase in the number of their intracellular lipid droplets when additionally stimulated with LPS. Macrophages solely treated with LPS develop significantly more lipid droplets than those treated with no polarization factors at all, suggesting that LPS may have a dominant effect on how cells handle lipids.

Furthermore, increasing the concentration of IFN-γ led to a correlated increase in the number of lipid droplets accumulated by the macrophages (figure 5.10). Together, these observations suggest that the specific diet and amount of cytokine stimulation play important roles in regulating the amount of lipid accumulation in macrophages, and that indeed the plaque's micro-environment ultimately dictates the evolution of macrophage phenotype.

5.2.4 Discussion

CARS combined with machine learning asses lipid accumulation patterns

Macrophages conduct critical functions in the progression of atherosclerosis[151]. It remains controversial, however, how macrophage subtypes respond to the lipid-rich matrix of the developing plaque. A common trait of plaques is the abundance of foam cells: macrophages with a high content of lipids, in the form of cytosolic lipid droplets. The ability of each macrophage subtype to accumulate lipid may constitute a differentiating parameter between phenotypes. In this study, we used vibrational microscopy together with machine learning-based segmentation to detect and quantify lipid droplets in prohealing and proinflammatory macrophages subtypes. CARS offers an imaging method that is label-free, chemically selective and fast enough to screen thousands of cells in a realistic amount of time. Machine learning-based segmentation automates the recognition of such lipid droplets and speeds up the analysis process significantly.

We examined cytosolic lipid droplet accumulation in macrophages under a set of culture conditions that aim to simplify the environment these cells encounter in atheroma. We focused on the differentiation factors and biological mediators (e.g. oxLDL, cytokines, endotoxins), leaving aside interactions with other cell types (e.g. endothelial cells and smooth muscle cells), and extra cellular matrix elements. We found that although proinflammatory cells accumulate more lipid droplets than prohealing cells, the latter are also capable of becoming foam cells.

Proinflammatory macrophages accumulate more lipid than prohealing macrophages

Macrophages stimulated with proinflammatory mediators interferon-γ (IFN-γ) and lipopolysaccharides (LPS), the so-called proinflammatory macrophages, accumulate more lipid droplets than any other tested macrophage subtype. We found that proinflammatory cells accumulate significant amounts of lipid droplets when grown in regular medium based on fetal bovine serum (FBS; figure 5.6 A), when exposed to high lipid levels (media containing oxidized low-density lipoproteins (oxLDL); figure 5.5), and even when starved in lipoprotein-deficient serum (LPDS; figure 5.6 B). These diets are posterior to the differentiation period, in which the cells are cultured with FBS containing media. Note that standard FBS medium contains appreciable quantities of lipids. On the other hand, unpolarized and prohealing macrophages, those stimulated with interleukin 4 (IL4) and interleukin 13 (IL13), show only a slight increase in lipid droplet accumulation when grown in a oxLDL-rich medium compared to basal medium. The latter subtypes seem to exhaust previously accumulated lipid pools when starved in a lipid-poor medium. These results are in agreement with the observation of Chinetti-Gbaguidi et al. and support the traditional belief that proinflammatory macrophages accumulate more lipid droplets than prohealing macrophages[159].

Foam cell formation in pro-healing macrophages

Given the lack of a quantitative definition for foam cell, we adopt a quote by Libby et al., who state that foam cell is a term that reflects the microscopic appearance of these lipid-laden macrophages[172], and extrapolate Schaffners approach, who distinguish them as large, round, markedly vacuolated cells[173], to any kind of shape and heavily vacuolated macrophages. A subset of the prohealing macrophage population shows an accentuated increase in lipid droplets that may qualify them as foam cells (figure 5.7). It is unknown whether these cells keep their prohealing phenotype and what triggers the mechanisms to store higher amounts of lipids. Macrophages are extremely plastic and can switch phenotype, making it possible for prohealing macrophages to transform into proinflammatory cells[174,175], which then become foam cells. This event may have a low probability and thus happen only rarely, affecting only a sub-section of the population of prohealing cells. We suggest performing an experiment with fluorescent markers for inflammatory cues and simultaneously imaging with CARS and TPEF to identify the phenotype of foam cells encountered in prohealing cultures.

Proinflammatory and prohealing macrophages have different lipid accumulation rates

Proinflammatory and prohealing macrophages also differ in their ability to accumulate lipid over time. While proinflammatory macrophages show an increased reservoir of lipid droplets the longer they are exposed to oxLDL-enriched media, there is no such evidence for prohealing macrophages (figure 5.8). Additionally, proinflammatory macrophages fed simply with FBS or with LPDS do not show a significant difference on lipid droplet accumulation over the studied period of time. This fact may indicate that proinflammatory macrophages exacerbate their proinflammatory behavior in the presence of oxLDL. Collecting more and more lipid droplets over time may increase their probability of becoming foam cells. In these terms, proinflammatory macrophages seem to be a major force in arresting lesion progression. However, how this exactly translates to atheroprogression remains to be investigated.

Lipopolysaccharides have a synergetic effect on the accumulation of lipid droplets

Lipopolysaccharides (LPS) have been reported as proinflammatory mediators of atherosclerosis[158]. We altered the LPS content on the differentiation factors with the aim of identifying whether LPS has any impact on the number of accumulated lipid droplets in each macrophage subtype. By removing LPS from the proinflammatory mediators, and adding it to the prohealing mediators and the unpolarized subset of macrophages, we found that LPS has indeed an inflammatory effect (figure 5.9). The trend points to larger accumulation of lipid droplets when LPS is present in the differentiation factors used to obtain any of the macrophage phenotypes. Interestingly, macrophages stimulated only with IFN-γ or only with LPS accumulate less lipid droplets than when these two mediators are combined. Similarly, when LPS is combined with IL4 and IL13, the cells also show an enhanced capability of gathering cytosolic lipid droplets. Summarizing, a differentiation strategy based on LPS combined with either group of cytokines produces macrophages more apt to accumulate lipids. This might indicate a synergetic effect between the cytokines and the endotoxin.

5.2.5 Concluding remarks

We have seen a different behavior from different macrophage phenotypes, but we also observe, quite systematically, that a subpopulation of the prohealing cohort have similar lipid accumulation outcomes to proinflammatory cells when stimulated with oxLDL. There is much controversy in the literature as to how these different macrophage phenotypes react to lipid excess. This response is important for understanding the progression of atherosclerosis, and other diseases, and to be able to combat them efficiently.

The plaque micro-environment contains a cocktail of cytokines and messenger mediators that will determine the fate of the recruited monocytes. But this is not a static environment, the concentration of proinflammatory and prohealing cues changes constantly. In addition, what we call proinflmmatory macrophages and prohealing macrophages are only the extremes of a continuum of macrophage subtypes with slightly different functions and properties. Moreover, these macrophages exhibit high degrees of plasticity[156], a single cell can switch from one state to another given the adequate conditions.

As early as 1999, proinflammatory macrophages (M1) were detected in human plaque[176]. By 2007, prohealing macrophages (M2) were also part of the plaque landscape[177], but they were identified to occupy a different area within plaque than the foamy M1 cells. Between 2011 and 2012, several contradicting reports discussed the role and characteristics of M1 and M2 within plaque. To name a few, Chinetti-Gbaguidi et al. found that M1 cells stored more and larger lipid droplets, while M2 cells had defective cholesterol efflux, but an increased content of cholesterol esters, and that these were less likely to become foam cells[159]. Van Tits et al. in 2011, on the other hand, brought evidence that M2 macrophages were more susceptible to foam cell formation than M1, showing that oxLDL render M2 cells proinflammtory[162]. In 2012, Finn et al. claimed that M2 macrophages uptake oxLDL but fail to produce cholesteryl esters, have an increased cholesterol efflux, and thus do not become foam cells[178]. Another example is the Oh et al. study, which argues in favor of the increased capability of M2 macrophages to become foam cells, compared to M1 macrophages. They found higher levels of cholesterol and cholestryl esters in M2 cells, compared to M1[160]. In 2013, Rousselle et al, claimed again that M2 cells are more susceptible to foam cell formation[161].

All these studies, however, define M1 and M2 macrophages in slightly different ways, and use different sets and combinations of cytokines to polarize these cells. Also, some of the studies are done in human plaques and others in mice models. Interestingly, Stöger et al., in 2012, found markers of both M1 and M2 macrophages in ruptured plaques, and claimed that foam cells ambiguously express M1 and M2 surface markers[163]. In 2013, Leitinger et al. stated that foam cells have no distinct M1 or M2 phenotype, and that both M1 and M2 are foam cells precursors[164].

In essence, macrophage role and evolution in atherosclerosis is a complex process. The balance between inflammatory and anti-inflammatory cues present in the plaque site controls the progression of the disease[152]. Our in vitro study with bone derived mice macrophages, agrees with the classical notion that M1 cells (proinflammatory macrophages) are more predisposed to become foam cells than M2 or prohealing macrophages. But judging from the number of lipid droplets accumulated in macrophages, quantified by machine learning segmentation of CARS images, we also find that M2 cells are not fully resistant to become foamy. There is some underlying mechanism that turns on the lipid accumulation activity in a subset of the prohealing cultures when further stimulated with oxLDL. What happens to these cells is unclear. It could be that they lost the prohealing phenotype and switch in favor of a proinflammatory behavior. It could be that they remain with a prohealing phenotype according to some markers, but activate alternative lipid metabolism pathways. It is also possible that they become yet a third type of macrophage with a completely different phenotype.

In conclusion, identifying what macrophages subtypes contribute to the foam cell population in atherosclerotic plaques is of interest to assess the sate of the lesion, maybe even predict its evolution, to be able to apply efficient treatment. Currently, we lack the necessary information to assess the macrophages' phenotype after the diet experiment, thus it is challenging to make statements about the state of the investigated macrophages. Immunofluorescence labeling with surface or cytoplasmic markers, or label-free fluorescence lifetime imaging microscopy might be useful techniques to address these questions and will be explored in chapter 6.

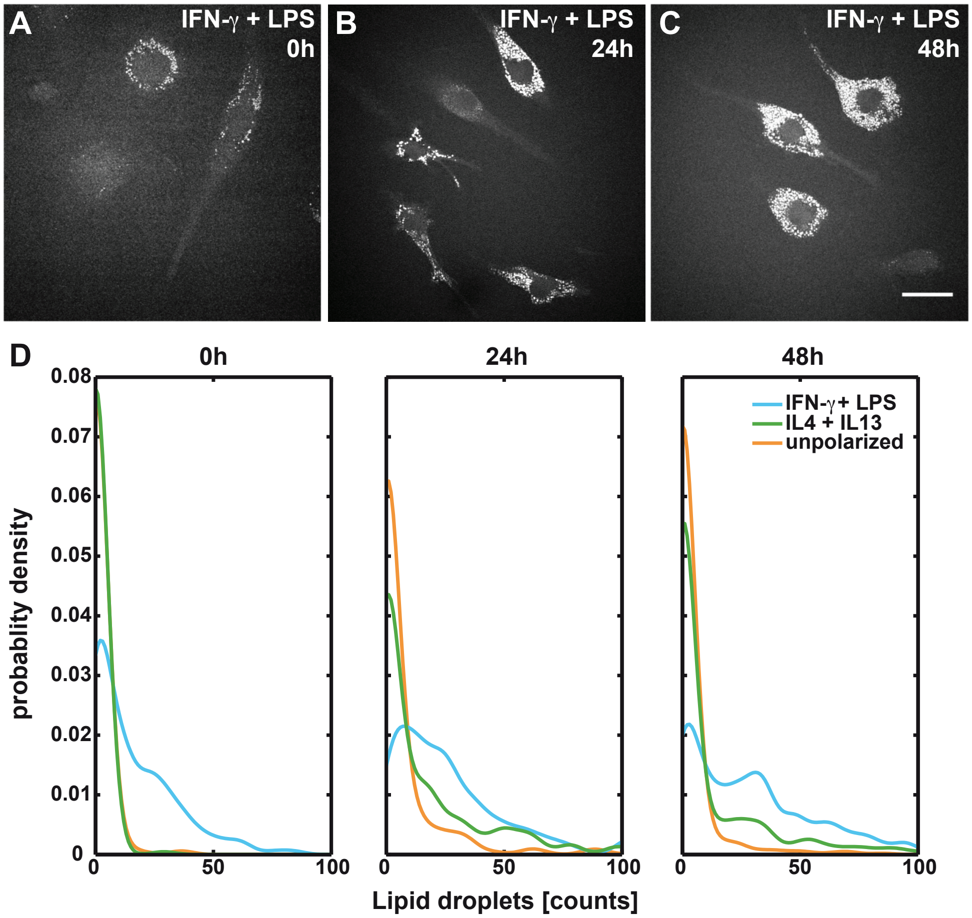

Figure 5.8: Lipid droplet accumulation increases with oxLDL exposure time only in pro-inflammatory macrophages. CARS images of pro-inflammatory macrophages A) before starting the oxLDL diet, B) after 24 hours in culture with oxLDL, and C) after 48 hours with oxLDL. Scale bar = $25\mu m$. D) Probability density estimate of the number of lipid droplets for macrophage treated with IFN-γ/LPS, IL4/IL13, or left unpolarized at 0, 24, and 48 hours after exposure to oxLDL.

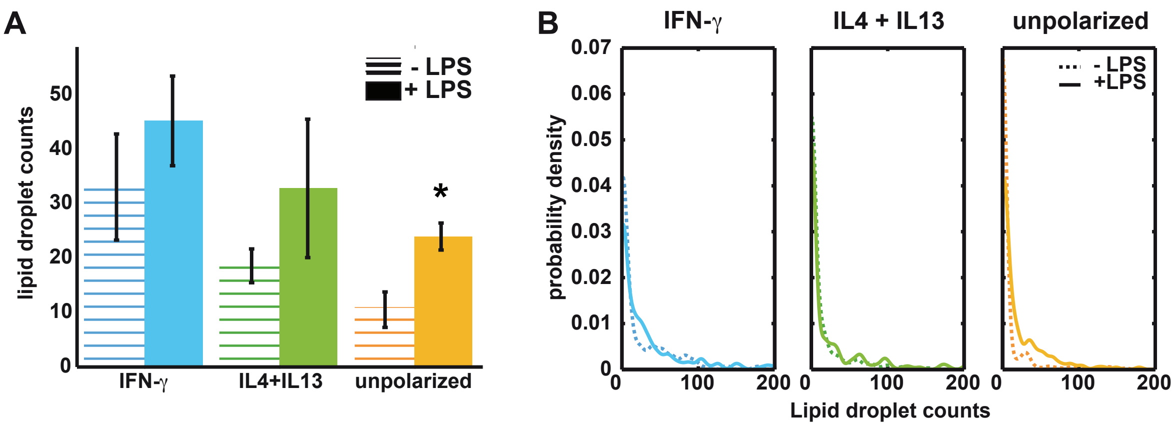

Figure 5.9: Culture with LPS increases the number of lipid droplets in macrophages. A) Quantification of the average number of lipid droplets per cell for each macrophage group induced without and with LSP. *P<0.05. B) Probability density estimate of the number of lipid droplets accumulated by each macrophage phenotype stimulated with (solid lines), and without (dashed lines) lipopolysaccharide.

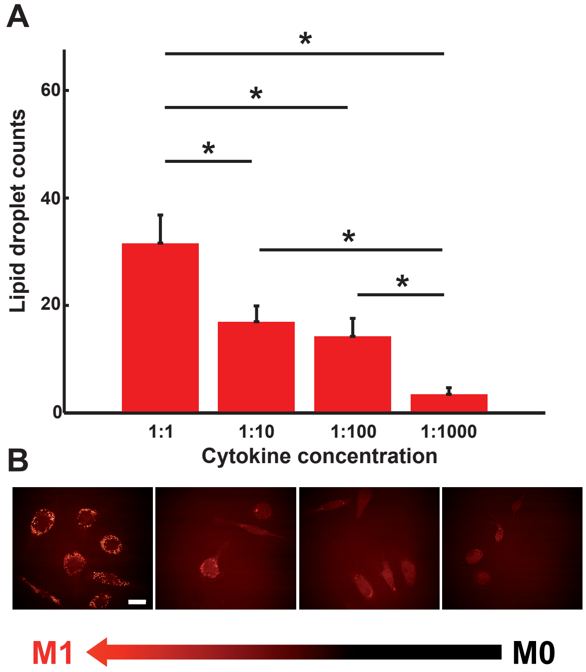

Figure 5.10: Culture with increased concentrations of interferon-γ (IFN-γ) increases the number of lipid droplets in macrophages. A) Quantification of the average number of lipid droplets per cell for each macrophage group polarized with increasing concentrations of IFN-γ. *p<0.05. B) Representative CARS images for each group featuring increased concentration of IFN-γ from unpolarized (M0) macrophages to proinflammatory (M1) phenotype. Scale bar = 20 μm.

Chapter 6

FLIM: a label-free tool for probing metabolism

Metabolism is a highly complex infrastructure of chemical reactions that constitute living organisms. Among techniques that enable interrogation of biological samples with minimum disturbance, two-photon fluorescence lifetime imaging microscopy (FLIM) permits monitoring of endogenous markers indicative of metabolic states in living cells and tissues. FLIM complements and adds a visual level to traditional biochemical assays that are rather destructive. Here we discuss the use of FLIM to distinguish between macrophages' phenotypes based on their metabolic state. Proinflammatory macrophages present a glycolitic phenotype while prohealing macrophages rely on oxidative phosphorylation to produce energy. This trait reflects the overall NADH binding state in the cells, yielding distinct autofluorescence lifetimes that can be used as a label-free marker. Other autofluorescence signals with distinct lifetimes arise from subcellular structures that colocalize with lipid-rich areas. Foam cells exhibit a longer fluorescence lifetime from regions rich in lipid droplets, as verified with additional CARS imaging. Even longer lifetimes were detected from pools of lipids, which may arise from products of oxidation.

6.1 Label-free identification of macrophage phenotype by fluorescence lifetime imaging microscopy

This work has been published in the following paper:

Alfonso Garcia, A., Smith, T. D., Datta, R., Luu, T. U., Gratton, E., Potma, E. O., and Liu, W. F. (2016). Label-free identification of macrophage phenotype by fluorescence lifetime imaging microscopy. Journal of Biomedical Optics, 21(4), 046005.

6.1.1 Introduction

Methods to distinguish different macrophage phenotypes are important for basic biological studies, and may also be beneficial for diagnosis of diseases in which macrophages are involved, atherosclerosis for instance. Traditionally, the identification of macrophage subpopulations has relied heavily on quantifying the expression of proinflammatory and prohealing markers through immunolabelling or analysis of gene expression. Common markers include inducible nitric oxide synthase (iNOS) and arginase-1 (Arg1)[163,179] or surface markers such as CD86[163,180–182], and CD206[159,177], which report on the proinflammatory and the prohealing state of the cell, respectively. Antibody- or nucleic acid-mediated interrogation of the cells state are widespread techniques, but typically require elaborate biochemical protocols that contain many steps[181,183–186]. These techniques are generally not capable of assessing live cells in their native environments, since cells are detached from the surface, lysed, and/or fixed. In order to assess the dynamics of phenotypic changes of cells during the course of complex cellular studies and treatments it would be desirable to employ a method that is based on endogenous markers and therefore compatible with live cell and tissue imaging. Given the role of macrophages in the pathogenesis of many diseases, methods to image their phenotype within live animals will also be beneficial.

As a reflection of their distinct functions, classically and alternatively activated macrophages have been shown to differ in their metabolic state as well as in their capacity to store lipid droplets. While classically activated macrophages produce energy via aerobic glycolysis, alternatively activated macrophages obtain energy from fatty acid oxidation and undergo oxidative phosphorylation[155,187]. These pathways produce reduced nicotinamide adenine dinucleotides (NADH) with different binding properties: freely diffusing NADH is a product of glycolysis[188], whereas NADH binds to mitochondrial shuttles (i.e. malate-aspartate) to undergo oxidation[189]. The binding state of NADH in the cells translates into different fluorescence lifetimes of this autofluorescent co-enzyme (free ($\sim$0.4ns) or bound (2-4ns)), principally due to the quenching state of adenine[90]. Therefore, fluorescence lifetime analysis can gauge the metabolic state of the cell, and may be used to assess macrophage phenotype in live cells and in a label-free manner.

Here we present a label-free method capable of recognizing macrophage subpopulations of living cells. This method may be used in conjunction with a recently reported label-free technique that distinguishes inflammatory and healing macrophages based on their differences in angular light scattering[190]. Our method is based on 2-photon fluorescence lifetime microscopy (FLIM) of NADH, and can readily be extended to in vivo studies, which is not feasible for light scattering measurements. In addition, the phasor approach to FLIM simplifies the data analysis process to the visual inspection of clusters, especially if measured lifetimes arise from complex multi-exponential decays[92]. In such cases, the commonly used direct fitting approach may prove challenging. However, in the phasor plot representation, the lifetimes emerge as clustered distributions that can be assigned directly to different macrophage phenotypes, a technique previously reported for the metabolic state of germ cells[191] or neural stem cells[192]. NADH quantification through the redox ratio has also been employed to determine stem cell differentiation[193]. In the cell cytoplasm a combination of freely diffusing and bound NADH is found. When excited at the correct wavelength, and in the absence of other exogenous or exotic fluorescent components, NADH is the main autofluorescent species that contributes to the optical emission, yielding a linear combination of the single exponential decays of free and bound NADH in the phasor plot[90,194]. We demonstrate that this approach allows the identification of macrophage phenotype in cell populations and that this method retains its robustness and ease of use under a variety of conditions.

6.1.2 Experimental details

Cell culture

As for the lipid droplet counting experiment, mouse bone marrow-derived macrophages (BMDM) were isolated from femurs of female, 6- to 12-week-old C57BL/6J mice and cultured as described[171] in medium containing 10% fetal bovine serum (FBS), 100 Uml penicillin, 100 *μgml* streptomycin, and 10% media conditioned by Ltk-cells expressing recombinant MCSF ectopically. On day 7, $3\ \ 10^5$ BMDMs were seeded on glass coverslips. The following day, cells were transferred to similar media containing either lipoprotein-depleted bovine serum (LPDS; Alfa Aesar) or normal FBS and then stimulated with cytokines. Lipopolysaccharides (LPS; Sigma) and interferon-γ (IFN-γ; R&D) were used at 10 *ngml*, and IL-4 and IL-13 (Biolegend) were used at 20 *ngml*. After 24 h of cytokine stimulation, media was replaced (with lipoprotein-depleted or normal media, per the experimental condition) and cells were exposed to 0 or 40 *μgml* oxidized human low-density lipoprotein (oxLDL; Alfa Aesar) for the remaining duration of the experiment.

Immunolabeling

After the live cell FLIM experiments, cells were fixed for further immunolabeling in 100% methanol and washed with 1% bovine serum albumin (BSA; MP Biomedical) in PBS. Cells were blocked with 5% normal donkey serum and stained for arginase-1 with a goat polyclonal primary antibody (1:50; Santa Cruz) and Alexa 594-conjugated donkey anti-goat IgG (1:500; Jackson ImmunoResearch). After washing in 1% BSA, cells were blocked a second time with 5% normal goat serum and stained for iNOS with a rabbit polyclonal primary antibody (1:50; Santa Cruz) and Alexa 488-conjugated goat anti-rabbit IgG (1:200; Jackson ImmunoResearch). Nuclei were visualized with Hoechst 33342.

FLIM, data acquisition and processing

Fluorescence lifetime imaging microscopy (FLIM) was employed in the two-photon configuration described in chapter 2. To examine the lifetime of the different macrophages subpopulaitons, the phasor approach was used for the analysis.

Statistical analysis

Statistical significance between the phasors of the examined macrophage groups was determined by the Students t-test, and considered positive for $p < 0.05$. The analysis was performed on 3 to 7 images per each group as indicated in each experiment. Cells from at least two separate mice were obtained, and a total of 12 to 32 cells were analyzed for each condition.

6.1.3 Results and discussion

Fluorescence lifetime imaging microscopy of free and bound NADH in unpolarized macrophages

As already mentioned, it is well established that macrophages stimulated with interferon-γ (IFN-γ) and lipopolysaccharides (LPS) or with interleukins 4 and 13 (IL-4 and IL-13) render

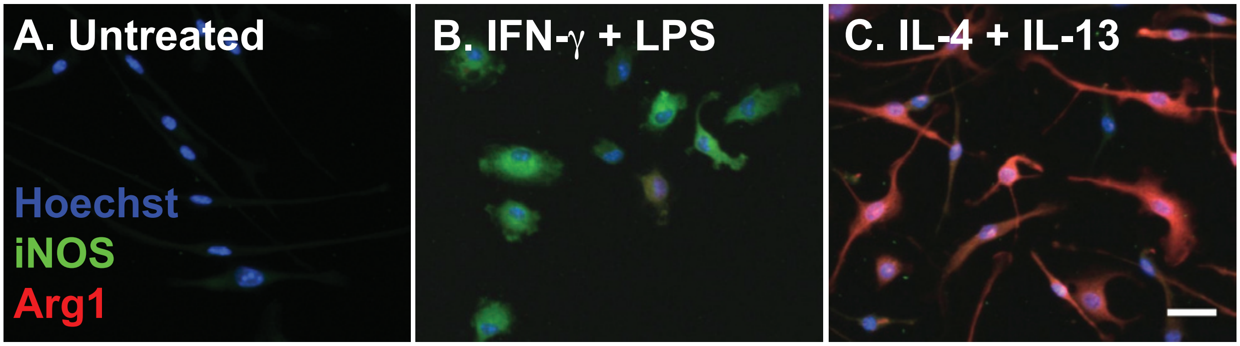

Figure 6.1: Representative immunofluorescence images of macrophages polarized with IFN-γ and LPS or IL-4 and IL-13, or untreated, and stained for the pro-inflammatory marker inducible nitric oxide synthase (iNOS, in green), the pro-healing marker arginase-1 (Arg1, in red), and the cell nuclei (Hoechst 33342, in blue). Macrophages polarized with IFN-γ and LPS express higher levels of iNOS, while macrophages polarized with IL-4 and IL-13 express predominantly Arg1. Scale bar = 25 μm.

proinflammatory or prohealing polarization states, respectively[158,181,195]. We confirm this by immunofluorescence staining for the proinflammatory marker inducible nitric oxide synthase (iNOS; in green) and the prohealing marker arginase-1 (Arg1, in red) (Figure 6.1). IFN-γ/LPS polarized macrophages express higher levels of iNOS, while IL-4/IL-13 stimulated macrophages express predominantly Arg1, as expected. Nuclei were counterstained with Hoechst 33342, indicated in blue.

Before interrogating the polarized macrophages with FLIM, we first study NADH lifetime maps of unpolarized macrophages that we will use as reference. Figure 6.2 A shows an autofluorescence image of untreated macrophages, and figure 6.2 B shows a map based on lifetime contrast. The color coding is derived from the phasor plot in figure 6.2 C. In this plot, the lifetime distributions of pure free NADH and NADH bound to lactate dehydrogenase (LDH) are indicated. The two distributions are found at opposite sides of the unit semicircle, also known as the universal circle[92], which starts at point (1,0) for zero lifetime species, and continues on to point (0,0) for infinite lifetime species. Freely diffusing NADH has a lifetime of ~ 0.4 ns and NADH bound to LDH has a longer lifetime of ~ 3.4 ns, the latter varies slightly with binding protein. Both lifetimes are characterized by a single exponential decay

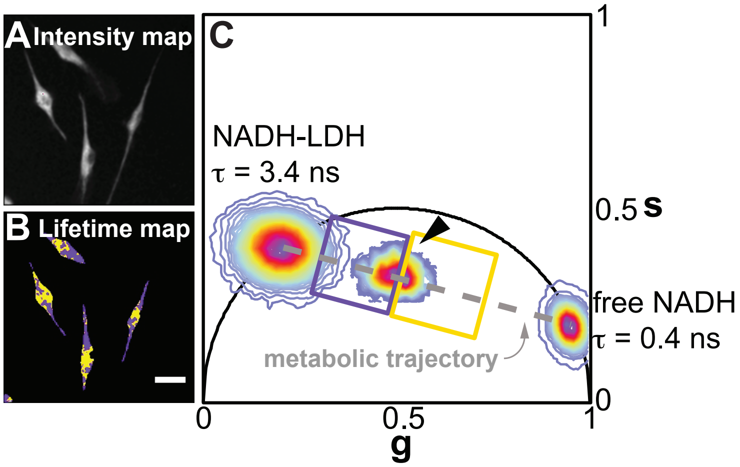

Figure 6.2: A) Autofluorescence intensity images of untreated macrophages. B) Corresponding lifetime image with color code according to squares selected in C: purple areas have a more bound NADH character, while yellow areas a more free NADH character (scale bar = 25 μm). C) Phasor plots of NADH bound to lactate dehydrogenase (LDH), free NADH, and the cells in image A/B (arrowhead). The line that joins the free with the bound NADH phasors, centered at 0.4 ns and 3.4 ns lifetimes, respectively, defines the metabolic trajectory. The cells phasor lies along this line, as a linear combination of the two lifetimes.

and therefore lie on the semicircle[196].

The two NADH states define the extremes of the so-called metabolic trajectory in the phasor plot[196,197]. In the cellular cytoplasm we find both species at different ratios, which yield a lifetime distribution that falls along the metabolic trajectory (figure 6.2 C, arrowhead). This lifetime distribution (or phasor) can be characterized as the linear combination of the free NADH and bound NADH phasors. The phasor approach to FLIM permits a rapid identification of changes in the lifetime distributions[92]. The metabolic state of the cell can be determined by the position of the phasor along the metabolic trajectory. We divide the lifetime distribution of untreated macrophages through the center of mass in two parts along the metabolic trajectory, so that the fraction of pixels in each section is 0.5 ± 10%. The left part contains the pixels that are closer to the bound NADH extreme of the metabolic trajectory (purple square), while the right part has those closer to the free NADH end (yellow square). In this two-color representation, each pixel in the lifetime image in figure

6.2 B is presented as either purple or yellow. The color coding can be interpreted as a relative measure of bound versus free NADH: purple represents more bound character, a lower free to bound NADH ratio, and yellow represents less bound character, a higher free to bound NADH ratio. Using these analysis regions as a reference, we can examine how the phasors of the polarized macrophages move along the metabolic trajectory, and thus quantify the changes in the ratio of free to bound NADH for each group.

FLIM identifies different lifetime distributions in polarized macrophages

Using this approach, we next examine NADH lifetime distributions of polarized macrophages. Figure 6.3 A shows an image with lifetime contrast obtained from unpolarized cells, and the accompanying color scheme is defined in the phasor plot of figure 6.3 B. As before, the cells display different color regions, corresponding to relative changes in the fluorescence lifetime, although the shape of the overall lifetime distribution may vary slightly from analysis of different cell populations. Using the same definition of the lifetime contributions as in figure 6.3 B, figure 6.3 C shows a lifetime image of cells treated with IFN-γ and LPS, corresponding to proinflammatory macrophages. Compared to untreated cells, the IFN-γ/LPS cells have a phasor slightly shifted towards the free NADH end of the trajectory (figure 6.3 D), which translates into larger yellow areas in the cells (figure 6.3 C). This is expected, as IFN-γ/LPS macrophages turn on glycolytic pathways for energy generation[198]. In contrast, cells treated with IL-4 and IL-13, have a higher contribution from bound NADH, as indicated in purple, as shown in figure 6.3 E. The phasor plot in figure 6.3 F is now shifted towards the direction of pure bound NADH, with effectively longer lifetimes. This observation is consistent with the notion that alternatively activated macrophages favor oxidative phosphorylation[199], which requires protein-bound NADH[188]. IL-4/IL-13 treated macrophages show a markedly elongated profile compared to IFN-γ/LPS and unpolarized macrophages, this is expected as macrophage elongation has been previously related to an

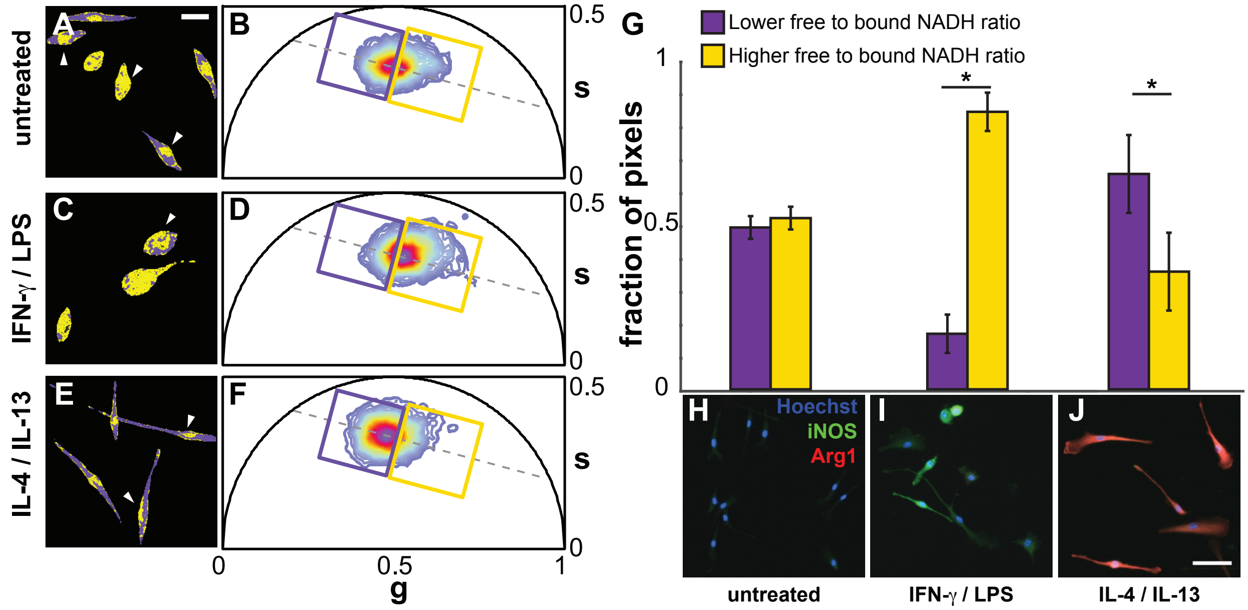

Figure 6.3: A) Untreated macrophages lifetime map (scale bar = 25 μm), and B) corresponding phasor plot. The purple and yellow squares select the areas in the cells with more bound NADH character, and more free NADH character, respectively, and are kept constant throughout the entire analysis. C) Inflammatory macrophages, polarized with IFN-γ and LPS, and D) corresponding phasor plot, shifted towards a markedly free NADH character. E) Healing macrophages, polarized with IL-4 and IL-13, and F) corresponding phasor plot, shifted towards the bound NADH side of the plot. G) Average fraction of pixels in each square, normalized to the total number of pixels in both squares, for the three macrophage cultures, the error bars correspond to the standard deviation. * $p < 0.05$, Student t-test. H) Immunofluorescence images of the untreated macrophage culture, I) the IFN-γ and LPS polarized culture, and J) the IL-4 and IL-13 polarized culture stained for iNOS (green), Arg1 (red), and nuclei using Hoechst 33342 (blue). Scale bar = 50 μm.

alternatively activated phenotype[184].

In an effort to quantify the metabolic state of the cells we compute the fraction of pixels in each image that fall into the predefined lifetime categories (indicated here by the purple and yellow squares in the phasor plot). Figure 6.3 G shows the results of averaging the fraction of pixels (fop) over 3 images for the unpolarized cells, with a total of 14 cells from two different mice, and over 7 images for the polarized groups, that contained a total of 21 and 32 cells for each inflammatory and healing macrophages, respectively, obtained from three separate animals. Untreated macrophages show roughly equal amounts of short and longer lifetimes, as defined by the chosen purple ($\text{fop}_{\text{lower free to bound NADH ratio}} = 0.49 \pm 0.03$) and yellow ($\text{fop}_{\text{higher free to bound NADH ratio}} = 0.51 \pm 0.03$) subgroups (figures 6.3 A and B). However, macrophages polarized with IFN-γ and LPS have a significant increase in the fraction of yellow pixels ($\text{fop}_{\text{higher free to bound NADH ratio}} = 0.83 \pm 0.06$ versus $\text{fop}_{\text{lower free to bound NADH ratio}} = 0.17 \pm 0.06$), those that report an increase in glycolytic metabolism. These cells are depicted mainly as yellow in figure 6.3 C. Macrophages treated with IL-4 and IL-13 have the opposite behavior, the fraction of pixels within the purple square ($\text{fop}_{\text{lower free to bound NADH ratio}} = 0.65 \pm 0.12$) is significantly larger than those in the yellow square ($\text{fop}_{\text{higher free to bound NADH ratio}} = 0.35 \pm 0.12$). As a result, the cells are colored predominantly in purple in figure 6.3 E. After FLIM imaging the cells were fixed and stained to examine their expression levels of proinflammatory and prohealing markers (figure 6.3 H-J). The stained cells confirm the correlation between NADH metabolism and macrophage phenotype, as IFN-γ and LPS treated cells have higher expression of iNOS (figure 6.3 I) and Arg1 expression predominates in IL-4 and IL-13 treated cells (figure 6.3 J).

In addition to evaluating the aggregate response of a population of cells with the overall lifetime distribution, the phasor approach to FLIM also permits the visualization of intracellular features with different lifetime properties. More specifically, the nuclear regions in the cells tend to have a higher free NADH concentration (as shown in yellow) in the lifetime images (white arrowheads in figures 6.3 A, 6.3 C, 6.3 E), whereas the cellular cytoplasm displays a higher concentration of bound NADH (as shown in purple). A shift towards free NADH in the nuclei has been previously reported using this same method to identify early stages of cellular differentiation[200].

Besides a rapid visualization method, the phasor approach can be used to classify the cells according to their average individual phasor value. In that regard, figure 6.4 depicts the aggregate phasor distribution of untreated and polarized macrophages, and locates the position of single cells analyzed within the distribution. The purple and yellow squares are

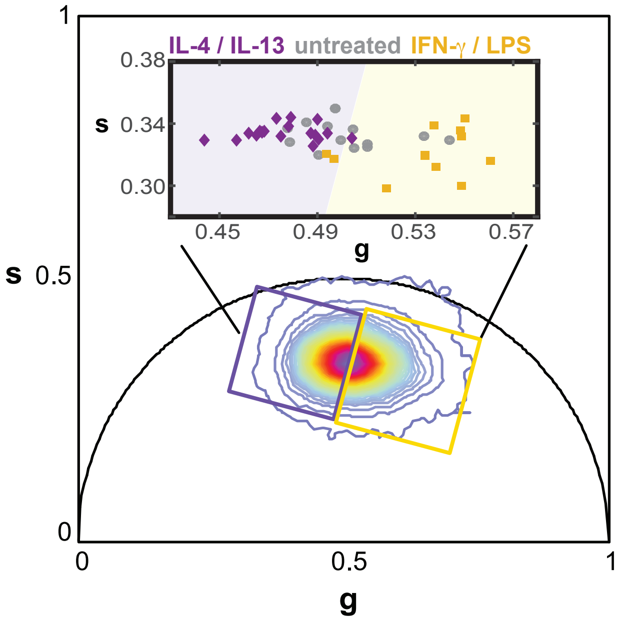

Figure 6.4: The phasor plot agglutinates the lifetime distributions of the cells in the untreated and the polarized macrophages. The purple and yellow squares are located in the same position for the entire analysis. The insert zooms into the core of the phasor to show the average phasor point of each cell analyzed across separate macrophage cultures. The shaded areas align with the squares position.

kept constant, and divide the zoomed in area in shaded purple and yellow regions for reference. We find two clear groups, the IL-4/IL-13 polarized macrophages (purple diamonds) fall within the purple square, with higher contribution of protein-bound NADH, and the IFN-γ/LPS polarized macrophages (yellow squares) fall into the yellow area with lower lifetimes, assigned to higher contribution of free NADH. Unpolarized macrophages stretch across the areas, with a skewed preference towards the left side of the plot, indicative of an oxidative metabolism basal state[186,198].

NADH lifetime detected by FLIM is a robust indicator of macrophage glycolytic state

Given that macrophages are involved in the progression of cardiovascular disease, a condition in which the cellular microenvironment contains significantly more lipid, we were interested to know whether or not the presence of lipid influenced the polarization of macrophages as determined by FLIM. We interrogated polarized macrophages with low (lipoprotein deficient serum, LPDS, based medium) or excess (oxidized low-density lipoprotein, oxLDL, containing medium) lipid. Notably, none of the cells in these conditions appeared to accumulate significant amounts of lipid droplets. We find the same results: inflammatory macrophages (cells polarized with IFN-γ and LPS) have a significantly larger fraction of glycolytic pixels in both cases; whereas healing macrophages (cells polarized with IL-4 and IL-13) significantly bind more NADH to protein to undergo oxidative phosphorylation than inflammatory cells do (figure 6.5 I), independent of the lipid environment. The fraction of pixels quantified in figure 6.5 I are the average 5 to 7 images that contained a total of 12 to 23 macrophages from two separate mice. IFN-γ/LPS-stimulated macrophages treated with LPDS (N = 6 images, 12 cells) have in average a $\text{fop}_{\text{lower free to bound NADH ratio}} = 0.27 \pm 0.14$ and $\text{fop}_{\text{higher free to bound NADH ratio}} = 0.73 \pm 0.14$, while IL-4/IL13-stimulated macrophages treated with LPDS (N = 5 images, 23 cells) have in average a $\text{fop}_{\text{lower free to bound NADH ratio}} = 0.57 \pm 0.05$ and $\text{fop}_{\text{higher free to bound NADH ratio}} = 0.43 \pm 0.05$. Macrophages stimulated with oxLDL followed the same trend, provided the cells are not foamy, the average fraction of pixels and standard deviation for IFN-γ/LPS-stimulated macrophages (N = 7 images, 15 cells) are $\text{fop}_{\text{lower free to bound NADH ratio}} = 0.24 \pm 0.10$ and $\text{fop}_{\text{higher free to bound NADH ratio}} = 0.76 \pm 0.10$, and for IL-4/IL13-stimulated macrophages (N = 5 images, 18 cells) are $\text{fop}_{\text{lower free to bound NADH ratio}} = 0.61 \pm 0.09$ and $\text{fop}_{\text{higher free to bound NADH ratio}} = 0.39 \pm 0.09$. Once again this is visually translated at the cellular level by yellow in the IFNγ/LPS cases (figures 6.5 A and C), and purple in the IL-4/IL-13 cases (figures 6.5 B and D). We further confirmed by immunofluorescence staining that cells in these conditions maintained their phenotypic markers, as shown in figures 6.5 E-H. Thus, this method appears robust to alterations in the presence of different lipid microenvironments.

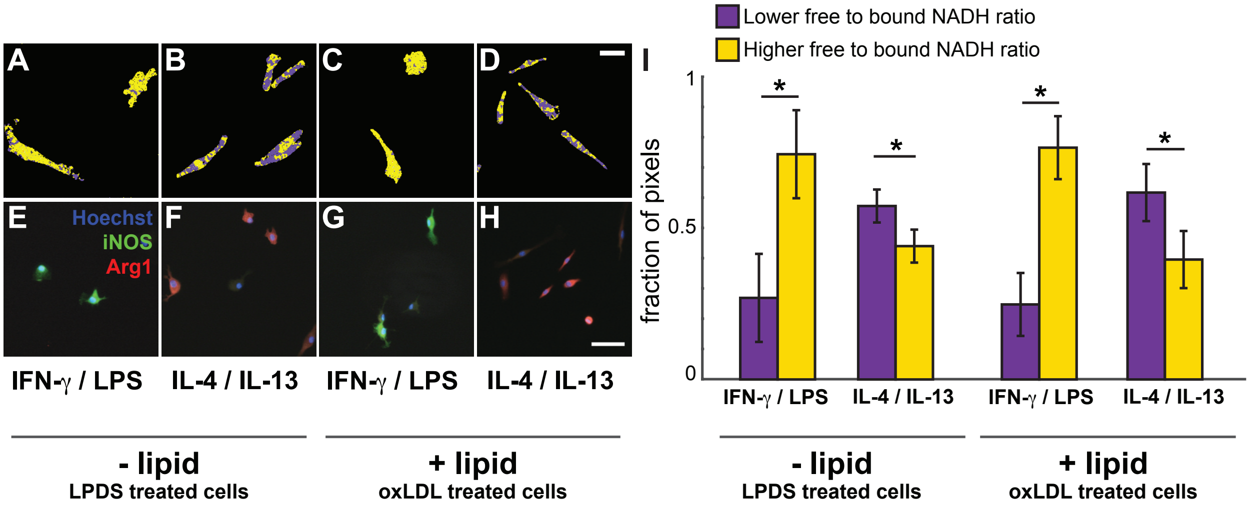

Figure 6.5: Macrophages polarized with IFN-γ and LPS and macrophages polarized with IL-4 and IL-13 treated with lipoprotein deficient serum (LPDS) and with oxidized low-density lipoproteins (oxLDL) maintain their glycolytic phenotype. A-D) Lifetime maps (scale bar $= 25\mu m$), and E-H) immunofluorescence images of the corresponding macrophage groups stained for iNOS (green), Arg1 (red), and nuclei with Hoechst 33342 (blue). Scale bar $= 50$ μm. I) Average fraction of pixels in the yellow and purple squares, normalized to the total fraction of pixels, for each group of macrophage culture, the error bars correspond to the standard deviation. * $p < 0.05$, Student t-test.

6.1.4 Concluding remarks

NADH fluorescence lifetime imaging microscopy provides a label-free, non-destructive means to identify the phenotype of live macrophages. FLIM indicates the metabolic state of polarized macrophages; whether the cells shift to a glycolytic state or rather switch to an oxidative metabolism, corresponding to a classically activated versus an alternatively activated phenotype, respectively.

Immunoassays or genetic-based assays to detect phenotypic markers are the standard techniques used to identify macrophage polarization states, but typically require cells to be fixed or lysed and to undergo an elaborate staining protocol. The FLIM phasor approach presented here allows characterization based on endogenous labels, which requires no sample preparation, and, most importantly, permits imaging of live cells directly in tissues. While this is not definitive to pinpoint the exact phenotype of a particular macrophage, as inflammatory and healing are extreme states, and to completely identify the exact phenotype of macrophages (especially in situ) multiple tests are recommended[186], FLIM and the phasor approach provide an effective threshold to differentiate between glycolytic and oxidative metabolisms. In addition, this method provides the ability to examine the metabolic state of the cells in real-time, allowing for a fast identification of macrophage state. This is particularly advantageous in dynamic studies that require controlled tracking of the phenotype as a given treatment evolves. Furthermore, since macrophages play a critical role in many diseases including cancer and cardiovascular disease[201,202], non-invasive imaging tools to evaluate macrophage behavior during the progression of disease may provide critical insight towards understanding their role in pathogenesis.

6.2 Label free identification of foam cells by fluorescence lifetime imaging microscopy

6.2.1 Introduction

Macrophages in atherosclerotic lesions uptake the lipid accumulated at the plaque site, and often become foam cells. As pointed out earlier in chapter 5, it has been conventional belief that the proinflammatory macrophages (M1) are more prone to foam cell formation, despite some studies that concluded that prohealing macrophages (M2) predominantly turn foamy. Posterior studies find that both M1 and M2 are foam cell precursors, and that in fact, foam cells ambiguously express M1 or M2 surface markers[163,164]. Foam cells may have a phenotype completely different from that of M1 or M2 macrophages.

Using the FLIM approach described in section 6.1, we analyze the fluorescence lifetime of foam cells arising from both M1 and M2 macrophage cultures treated with oxidized low-density lipoprotein (oxLDL), with the aim to address the metabolic traits of lipid-laden macrophages.

6.2.2 Experimental details

We polarized macropahges with Th1 and Th2 cytokines as described in chapter 5, followed by a 24 hour oxLDL treatment after a 24 hour intermission in which the cells were cultured in LPDS. This is a relevant step for stimulating foam cell formation, as pre-culture in LPDS stimulates lipid uptake when available[203]. In fact, we found that skipping this step diminishes the lipid droplet formation ability of the cells significantly, as the cells cultured with oxLDL in the previous section, in which no LPDS pre-culture was effectuated, displayed negligible levels of lipids droplets.

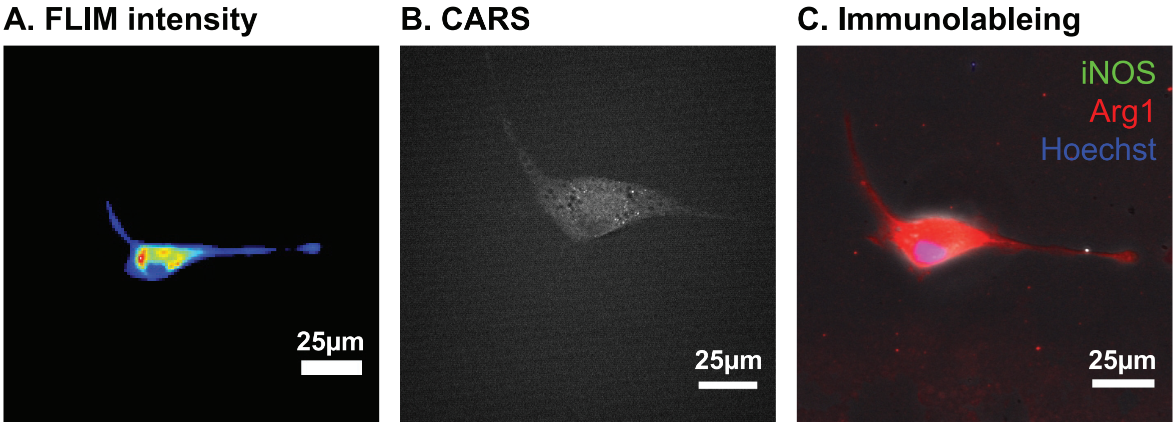

Figure 6.6: Pro-healing macrophage (M2) imaged with A) FLIM, B) CARS, and C) immunofluorescence, with iNOS in the green channel, Arg1 in the red channel, and Hoechst in the blue.

Most M1 macrophages transformed into foam cells upon oxLDL treatment, while only a portion of the M2 population did, in agreement with our measurements in chapter 5. We then imaged live cells with two-photon FLIM, with the same settings employed in section 6.1, followed by CARS imaging, with the cells still alive, to image their lipid content. The same cells were then fixed with methanol for posterior immunolabeling staining. Unfortunately, only the M2 well survived the fixation step. Figure 6.6 shows the same M2 macrophage imaged with FLIM and CARS, and the corresponding immunolabeling stained image, illustrating the potential of this approach to perform cell level analysis.

Note that the localization of the same macrophages with the three different microscopes was facilitated by the use of glass bottom dishes with integrated grids. μ-Dish 35 mm, high Glass Bottom Grid-50 and 500 dishes (ibidi USA, Madison, WI) were used for this particular experiment.

6.2.3 Results and discussion

The phasor analysis of the macrophages treated with oxLDL can be divided in two groups, as shown in figure 6.7. The cells from the M1 and M2 groups that did not turn into foam cells compose the first group, whereas the cells from either subtypes that become foamy compose the second group. The center of mass of the average phasor from non foam M1 cells (3 images and 4 cells) is closer to the free NADH end of the metabolic trajectory than the center of mass of the average phasor from non foam M2 cells (9 images and 14 cells), which has a slight shift towards the bound NADH side of the metabolic trajectory, according to previous experiments (section 6.1). Interestingly, the average phasors of foam cells, both found in M1 (8 images and 14 cells) and M2 (6 images and 9 cells) cultures, are even more shifted towards the bound NADH end of the metabolic trajectory. This is due to an additional contribution to the overall lifetime (red square in figure 6.7) that maps back to lipid-rich areas in the cells, as shown by the CARS images of the same cells.

The results of FLIM and CARS microscopy can be overlapped for a cell by cell case, allowing deeper analysis on the origin of the autofluorescent signals. Figure 6.8 A-C displays an example of overlap between the images acquired with the FLIM and CARS of a proinflammatory (M1) macrophage. The cytoplasm is colored blue in the FLIM map, while the nucleus appears green, and colocalizes with the darker area in the center of the cell in the CARS image. The red areas in the FLIM image colocalize with bright areas in the CARS image, which correspond to lipid droplets. This is a consistent trend in all foam cells analyzed, independently of their M1/M2 origin. Figures 6.8 D and E show individual phasors for each proinflammatory (M1) and prohealing (M2) macrophage imaged (both foam and non foam cells). The phasor contribution of each cell is divided into three sub-phasors derived form the different sub-cellular structures previously identified (i.e. cytoplasm in blue, nucleus in green, and lipid-rich areas in red). Note that the nuclear contribution has the higher free NADH ratio, the lipid-rich areas have a longer lifetime, with phasors featuring a

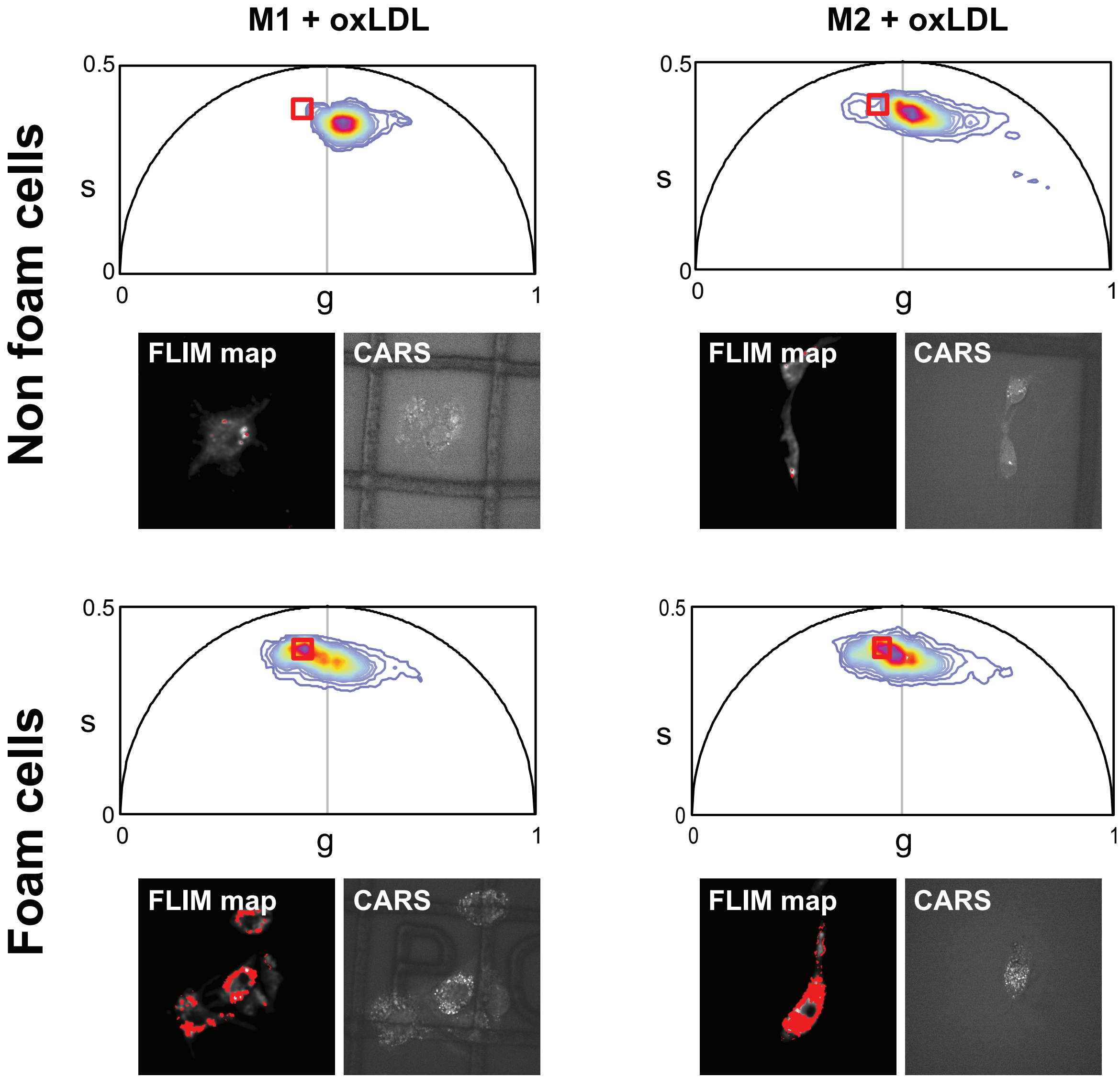

Figure 6.7: Phasor plots and exemplar FLIM/CARS images for M1 and M2 macrophages treated with oxLDL. The top row contains cells that did not turn foamy, the bottom row contains data from foam cells.

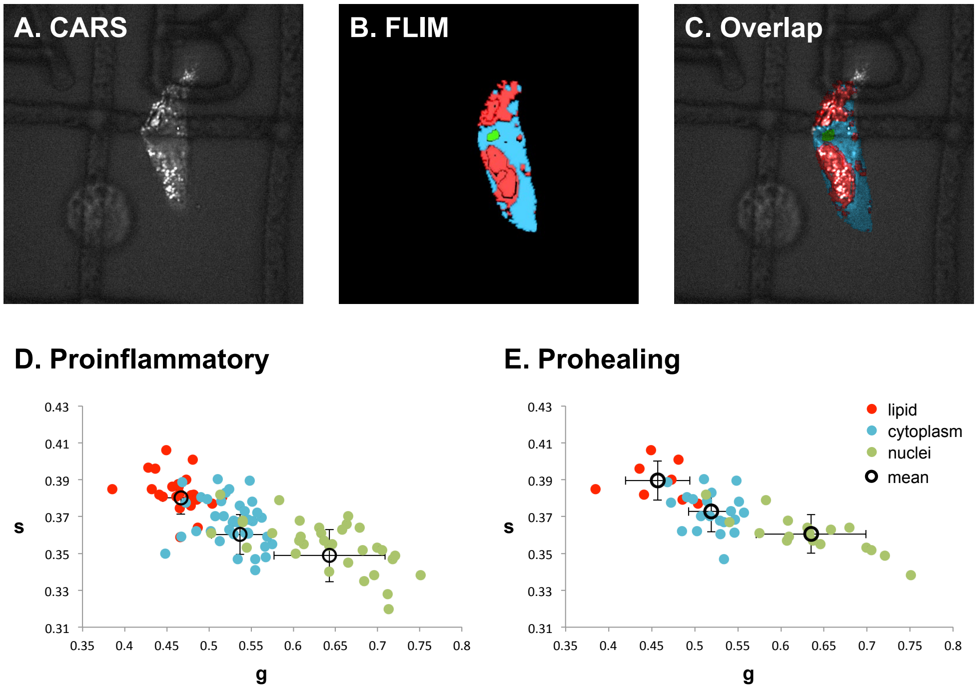

Figure 6.8: Sub-cellular structures have different lifetimes that appear as different contributions in the phasor plot. A-C) CARS, FLIM map, and overlap of the former two images of a pro-inflammatory macrophage. D-E) Phasor plot of individual cells contribution from each sub-cellular structure (red: lipid, blue: cytoplasm, green: nucleus) and the average and standard deviation for proinflammatory and prohealing macrophages, respectively.

larger contribution from bound-NADH, and the cytoplasm phasors bridge the gap between the previous two cellular structures.

6.2.4 Concluding remarks

The longer lifetime contribution is of unknown origin. It appears to colocalize with lipid droplets, or lipid-rich areas, however aliphatic lipids are generally non-fluorescent. Additional experiments should be carried out in order to address the nature of this signal. High-resolution FLIM imaging, with a larger magnification factor for instance, would reveal greater detail about the spatial origin of the different lifetimes. The degree to which the longer lifetime correlates with the position of lipid droplets could aid the interpretation of its origin.

Any attempt to assign an origin to this longer lifetime autofluorescnce is, at this point, mere speculation. The higher resolution FLIM images coupled with magnified CARS images could aid in locating the signal to the periphery or the interior of the lipid droplets. In this case, the hypothesis could point towards increased NADH binding to some lipid droplet specific enzyme with high affinity, therefore shifting the balance towards higher contributions of bound NADH along the metabolic trajectory. If the signal is located within the lipid droplet, it may be attributed to lipophilic structures, for example carotenoids, which have the ability to autofluoresce due to their highly conjugated double bond system. Carotenoids exhibit a broad absorption spectrum in the UV range ($\sim$350-500 nm)[204,205]. We used a two-photon 740 nm excitation source, which could potentially excite some carotenoids. Fluorescence spectral analysis of the absorption and emission properties of the samples would be informative. Other highly conjugated lipophilic structures could also be considered as candidates, as well as changes in the local micro-environment, such as the pH of the cell or the viscosity of the local medium, which can affect the fluorescence lifetime.

Further investigations may include mass-spectroscopic and Raman spectroscopic analysis of the cells, with particular emphasis on the lipid droplet portion, in the look out for highly conjugated lipid structures, or lipid-droplet specific enzymes with high affinity for NADH.

Interestingly, autofluorescence has already been proposed as a contrast mechanism to differentiate between different atherosclerotic plaques compounds, including collagen, elastin, and even cholesterol[206,207]. It was claimed that lipids, including free cholesterol, exhibit fluorescence under intense UV laser excitation, but the exact origin of such fluorescence has not been elucidated. It has been shown that carotenoids accumulate in atherosclerotic plaque[208], making these isoprenoids possible candidates for the origin of these long lifetime signals.

The distinct lifetime associated with the foam cells could be used as a label-free biomarker that complements the M1/M2 lifetime differentiation characterized in section 6.1, when cells are not foamy. Together, these label-free approaches could provide rapid in vivo visualization of different macrophages subpopulations in plaques, and could eventually be extended to the analysis of other inflammatory processes where macrophages are essential.

6.3 Fluorescence lifetime imaging of endogenous biomarkers of oxidative stress

This work has been published in the following paper:

Datta, R., Alfonso-Garcia, A., Cinco, R., and Gratton, E. (2015). Fluorescence lifetime imaging of endogenous biomarker of oxidative stress. Scientific Reports, 5, 9848.

6.3.1 Introduction

Reactive oxygen species (ROS) are chemically reactive molecules that contain oxygen, involved in cellular metabolism and homeostatis. When present at moderate, physiological concentrations, ROS act as signaling messengers to regulate the cell's state. However, increased concentrations of ROS cause oxidative stress that can lead to protein and DNA damage and/or lipid peroxidation, which in turn affects the normal functioning of the cell[209–211]. Due to their implication in numerous diseases, including atherosclerosis, cancer, and neurodegenerative disorders[212–217], detection of ROS can be used to follow progression and treatment. Fluorescent markers specific to ROS molecules are available, but once again they involve the addition of exogenous materials. Additionally, the task of labeling and/or detecting ROS is not simple, because these are highly unstable molecules. The products of ROS are more stable and are used as an indirect measure of ROS themselves. These techniques try to identify the damage ROS has caused or quantify the levels of antioxidats and redox molecules.

The present study shows the correlation of a distinct autofluorescence long lifetime signal with lipid-rich areas, and suggests a label-free approach to ROS detection. We hypothesize that the detected long lifetime species (LLS) is a product of lipid oxidation by ROS. In order to guide the firsts steps towards the source identification of the LLS signal, we perform CARS, third harmonic generation (THG), and confocal Raman on lipid-rich samples. We found that the LLS signals come from areas that co-localize well with lipid areas in: 1) freshly excised white adipose tissue, and 2) cells in culture with extra oleic acid in the media. Here we characterize a non-invasive, label-free method to identify a biomarker of oxidative stress.

6.3.2 Experimental details

Sample preparation

HeLa cells were grown in Dulbecco's Modified Eagle Medium (DMEM), supplemented with 10% fetal bovine serum, and 1% penicillin streptomycin (100 U/ml) at 37°C in a 5% CO incubator. For oleic acid (OA, Sigma-Aldrich, St. Louis, Missouri) treatment, the cells were cultured in 5% lipoprotein deficient serum (LPDS; Intracel, Frederick, Maryland) and 95% DMEM for 24 hours. Fatty acid free bovine serum albumin was prepared by dissolving bovine serum albumin (BSA powder; Sigma-Aldrich) in 5% LPDS media. 400 mM oleic acid was prepared as a complex with BSA (OA/BSA) at molar ratio of 2:1. Cells were treated with OA/BSA complex overnight. For controls, three different dishes of HeLa cells were cultured in normal media and 5% LPDS media. For imaging, the cells were plated in glass bottom dishes (Matek Corporation, Ashland, Massachusetts). Prior to FLIM imaging, the oleic acid fed cells were washed with 1X Dulbeccos Phosphate Buffered Saline, DPBS (Sigma-Aldrich). For CARS imaging, media was replaced with DPBS. 4% Paraformaldehyde (Sigma- Aldrich) solution was prepared to fix the cells for Raman spectroscopy measurements.

White adipose tissue was obtained from 5 month old adult female mice. Approximately 3 *mm* diameter portions of fat from perigonadal and flank white adipose tissue depots were freshly excised from the mice and subsequently embedded in 1% low melt agarose in HBSS heated to 37°C between coverslips separated by 0.2 *mm* spacers. All imaging were strictly performed within 1 hour of tissue extraction. All animal procedures were performed with strict adherence to NIH OLAW and institutional IACUC guidelines.

Imaging instrumentation

Fluorescence lifetime imaging measurements of HeLa cells were performed on the Zeiss LSM 710 microscope described in chapter 2. FLIM data was acquired using A320 FastFLIM FLIMbox (ISS, Champaign, IL).

FLIM and third harmonic generation (THG) imaging of tissue sample were acquired using a custom-built upright deep tissue imaging microscope. The operation principle has been discussed previously[218]. For FLIM measurements, tissue sample was excited at 740 *nm* and the emission filter employed was a bandpass 405 - 590 *nm*. For THG, excitation at 1038 *nm* was used and signal was collected with a bandpass filter 320 - 390 *nm*. Both FLIM and THG signals were collected in transmission geometry on the same sample. For FLIM and THG data acquisition and processing, the SimFCS software developed at the Laboratory of Fluorescence Dynamics (LFD, UC Irvine) was used.

Coherent anti-Stokes Raman scattering (CARS) images were obtained with the microscope described in chapter 2. Spontaneous Raman spectra from the lipid droplets present in the cells were acquired with a commercial Raman microscope (InVia Confocal; Renisahw, Wotton- under-Edge, Gloucestershire, UK). The excitation wavelength at 523 *nm* was focused into the sample with a 50x objective, and the scattered light was sent into the spectrometer that contained a 2400 *l*/*mm* grating. The autofluorescent lipid droplets were identified based on morphology. The Raman spectrum was then taken with 10 *s* integration time, and the baseline was estimated by minimizing a non-quadratic cost function.

6.3.3 Results and discussion

FLIM phasor signature of a long lifetime species

We detect a strong and unique long lifetime species (LLS) in freshly excised white adipose tissue (figure 6.9) on the order of 7.89 ns. This contribution is found on the universal circle of the phasor plot, suggesting it is the result of a single exponential decay, which indicates the existence of a pure chemical species within the lipid droplets of the adipocytes, different from the autofluorescent NADH, which has a shorter lifetime in cells (1-2 ns). The NADH and LLS contributions from the adipose tissue marked in the phasor plot (figure fig:LLS1 C) with a red and a blue circle, respectively, are mapped back onto the fluorescence intensity image of the adipose tissue (figure fig:LLS1 A) to generate a binary FLIM map (figure fig:LLS1 B). The LLS areas fall exclusively within the big lipid droplets of the adipocytes (in red) and the areas surrounding the droplets are depicted in blue, indicating the presence of NADH.

This LLS signal was not found in brown adipose tissue. White adipose tissue has been linked to high levels of oxidative stress implicated in obesity and type 2 diabetes, and fluorescent lipid peroxidation products have been identified in these adipocytes with big lipid droplets[219]. The emitted fluorescence spans a wide range from 430 to 490 nm[220], in which we detect the LLS signals.

Therefore, we suggest that this strong signal from the LLS define an oxidative stress axis on the phasor plot that branches off of the metabolic trajectory, defined by free and bound NADH lifetimes (figure 6.10). Together with the phasor distribution of free NADH (0.4 ns) and NADH bound to lactate dehydrogenase (LDH; $\sim$ 3.4 ns), we can define a triangle in the phasor plot that contains any mixture of the three components as a linear combination

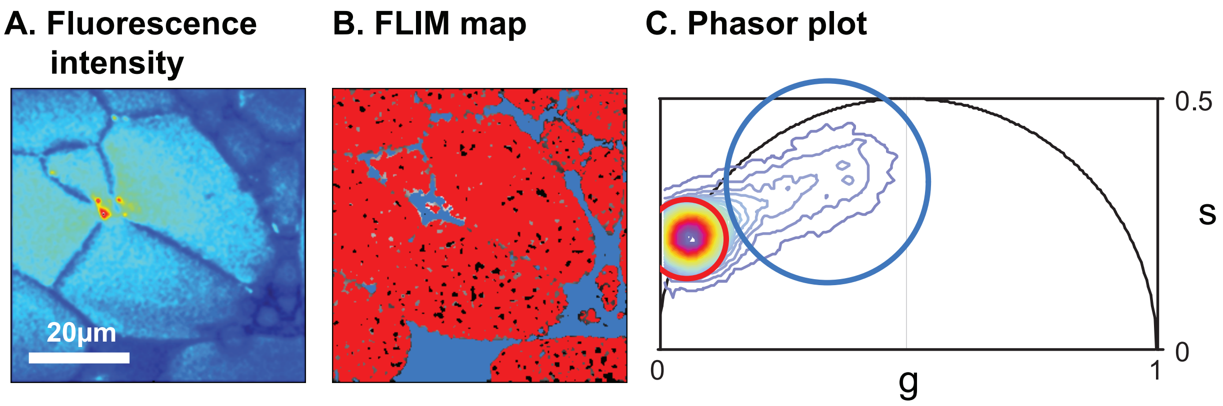

Figure 6.9: Unique fluorescence long lifetime signature (LLS) in white adipose tissue. A) Average fluorescence intensity image of white adipose tissue excited at 740 nm. Scale bar = 20 μm. B) FLIM pseudo-colored map with red and blue corresponding to the phasor contribution form the LLS and NADH, respectively, as selected in the phasor plot. C) Corresponding phasor distribution. The red circular cursor selects the long lifetime distribution while the blue circular cursor highlights the NADH phasor contributions.

of the lifetimes from the separate species, as dictated by the law of phasor addition[92].

Long lifetime species in HeLa cells treated with oleic acid

In order to further characterize the origin of the LLS associated with lipid, we treated HeLa cells with oleic acid to stimulate the formation of lipid-rich areas, or lipid droplets. Oleic acid has been linked to increased generation of ROS and oxidative stress[221,222]. As control, we also cultured HeLa cells in regular media and lipoprotein deprived serum (LPDS), which are not expected to generate elevated numbers of lipid droplets, nor cause additional stress. Figure 6.11 shows two HeLa cells, one treated with oleic acid (OA) and another one in regular culture media. Figure 6.11 A shows the brightfiled transmission images, figure 6.11 B the autofluorescence intensity, and figures 6.11 C and D highlight the areas that have a lifetime rich in LLS component (in red) and rich in NADH (in blue), respectively. Note that the red areas are confined in very specific regions, which the transmission image suggest might be lipid droplets. The cell treated with oleic acid shows a larger red area than the one in regular medium, and the phasor distribution highlighted by the red cursor is more prominent

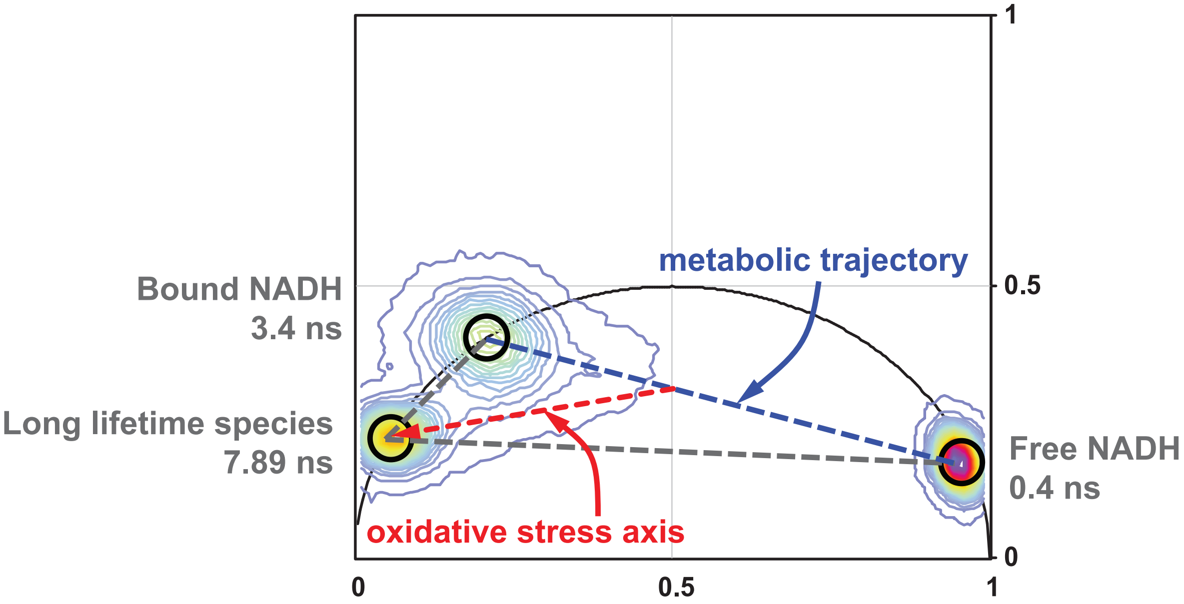

Figure 6.10: LLS FLIM signature defines a new oxidative stress axis on the phasor plot. The phasor plot features a triangle formed by the FLIM fingerprints of free 2.5 mM NADH in solution, NADH bound to 0.75 U/ml lactate dehydrogenase (LDH) enzyme, and the unique LLS FLIM signature from lipid droplets in perigonadal white adipose tissue of female mouse. From the law of phasor addition, a system containing mixtures of these three species will fall within the triangle joining the three phasors. In addition to the metabolic trajectory defined by the NADH axis, a new oxidative stress axis is defined, which branches off of the metabolic trajectory and points towards the LLS phasor.

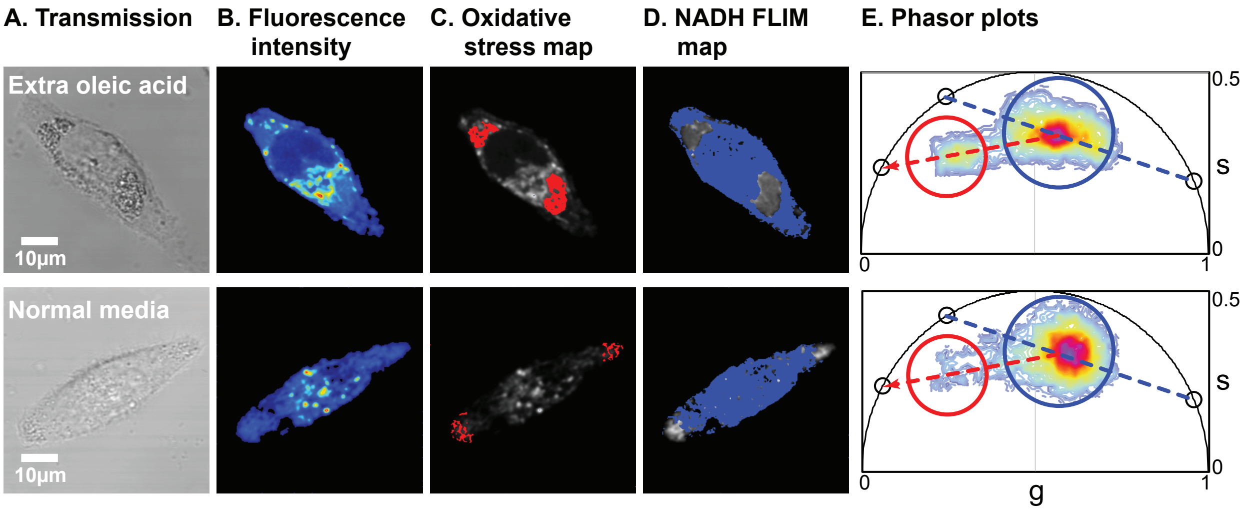

Figure 6.11: FLIM phasor of an oleic acid fed HeLa cell (top row), and a regular medium fed HeLa cell (bottom row). A) Transmission image, B) fluorescence intensity image, C) oxidative stress FLIM map, D) NADH FLIM map, and E) corresponding phasors for two HeLa cells. Scale bar = 10 μm

than the corresponding regular medium. Over all, the cells treated with oleic acid exhibit more areas with the long lifetime species contribution, but the control HeLa cells cultured in normal media also displayed the LLS phasor distribution in few occasions, usually in areas with lipid droplets near the cellular membrane.

Figure 6.12 A shows the average phasor distribution from a population of 55 HeLa cells in OA (distributed in 12 images), which exhibit a tail that follows the oxidative stress axis, depicted in a red doted line. The average phasor of cells in regular medium (58 cells from 12 images; figure 6.12 B), or in LPDS (54 cells form 12 images; figure 6.12 C) do not have that extra component pointing towards the LLS species, or it is negligible. The total average phasor plot of all the cells is included in figure 6.12 D. The LLS rich area is selected with a red window, and the number of pixels per each cell treatment that fall within the selected lifetime is quantified. OA treated cells have over a 6-fold increase in the percentage of pixels with this long lifetime (figure 6.12 E).

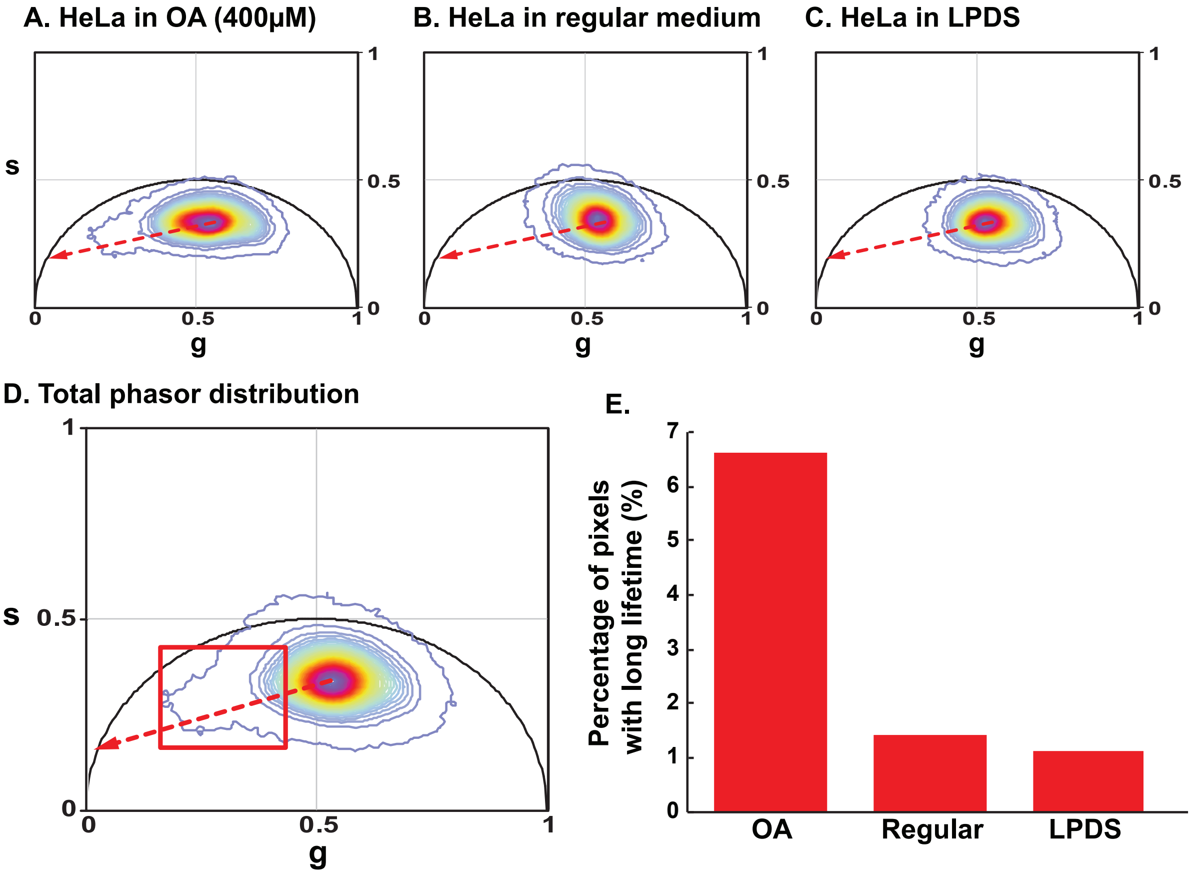

Figure 6.12: LLS contribution increases in oleic acid treated HeLa cells. Phasor distribution of HeLa cells A) treated with 400 *mM* oleic acid (OA) for 24 hours, B) in regular media, and C) in lipoprotein deficient serum (LPDS). The red dotted line shows the oxidative stress axis. D) Joint phasor plot of the above culture conditions with LLS window (red square) selecting pixels with longer lifetime. E) Percentage of pixels within lifetime in the LLS red window in the three groups.

Use of nonlinear label-free microscopy techniques to determine the origin of the autofluorescence signal

In order to further characterize the source of the long lifetime signal we combined FLIM imaging with CARS on the same cells. The CARS images verify the presence of lipid droplets in the areas that exhibit this long lifetime (Figure 6.13), especially in the OA treated group. Interestingly though, the LLS signature does not emerge from all the lipid droplet areas in the cells equally, but rather from a subpopulation of them. What makes these lipid droplets subpopulation different remains to be investigated.

Additional test that prove the correlation of the LLS signal with lipid droplets were done in this study by means of third harmonic generation (THG) microscopy. THG is sensitive to the interfaces between media with different optical properties such as the third order nonlinear susceptibility, refractive index, and dispersion. In particular, it has been shown that the interface between lipid droplets and the cellular surroundings produces strong THG contrast[223].

Chemical analysis by Raman spectroscopy

For chemical characterization of the lipid associated species with the long lifetime autofluorescent signal we obtained Raman spectra from regions in oleic acid treated cells that displayed the LLS FLIM signature. An example is shown in figure 6.14, where two HeLa cells loaded with oleic acid are features. Figure 6.14 A shows the autofluorescence intensity image, figure 6.14 B shows the FLIM map highlighting in red the presence of the long lifetime species, and figure 6.14 C shows the corresponding phasor plot with the LLS phasor distribution selected with a red circle. The top Raman spectrum in figure 6.14 D corresponds to the big lipid droplet indicated by the red arrow in figure 6.14 B. For reference, the Raman spectrum of pure oleic acid has been included in the bottom of figure 6.14 D. The only clear

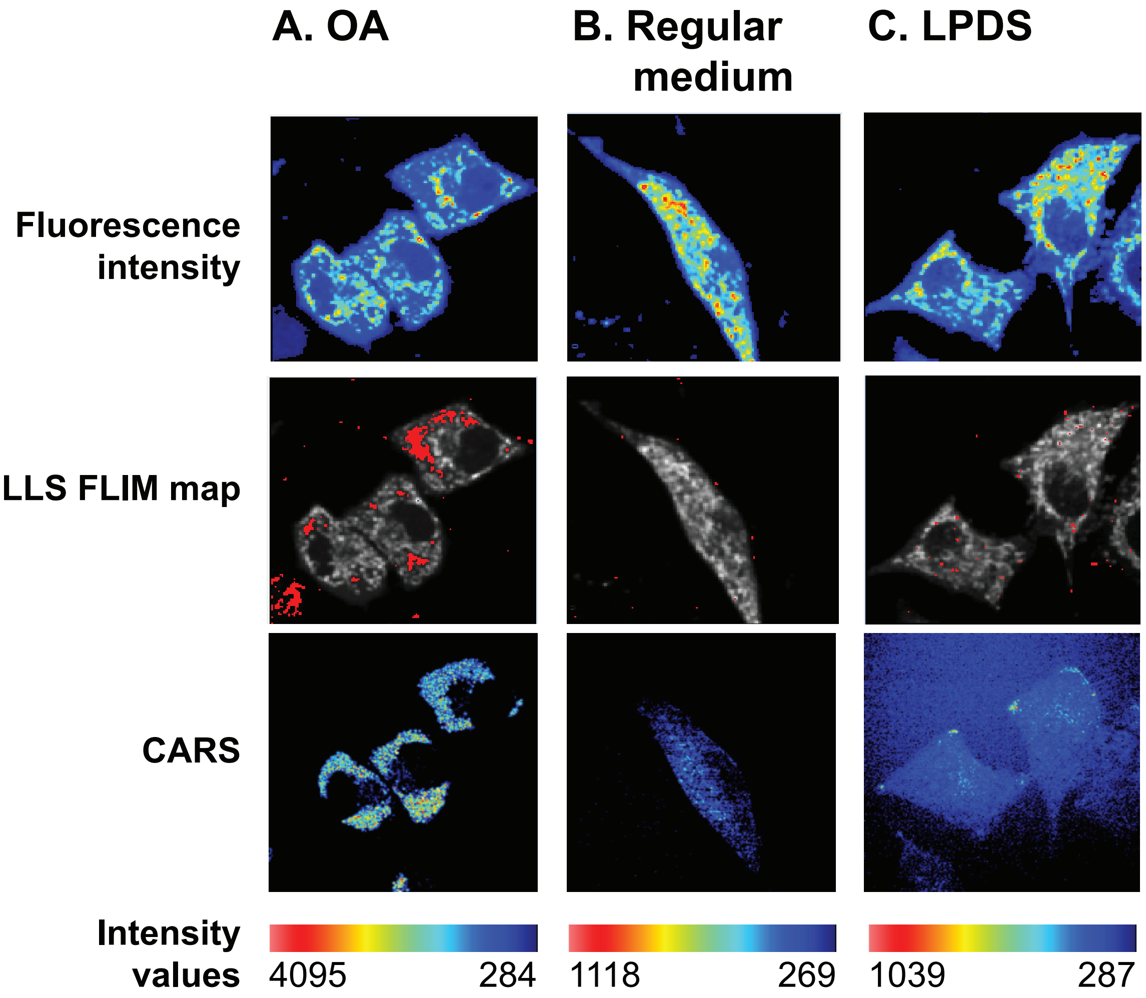

Figure 6.13: Images of HeLa cells in A) oleic acid-rich medium (OA), B) regular medium, and C) lipoprotein deprived serum (LPDS). Top panels show fluorescence intensity images, middle panels LLS FLIM maps in red, overlapped to the fluorescence intensity images in gray-scale, and bottom panels belong to corresponding CARS images.

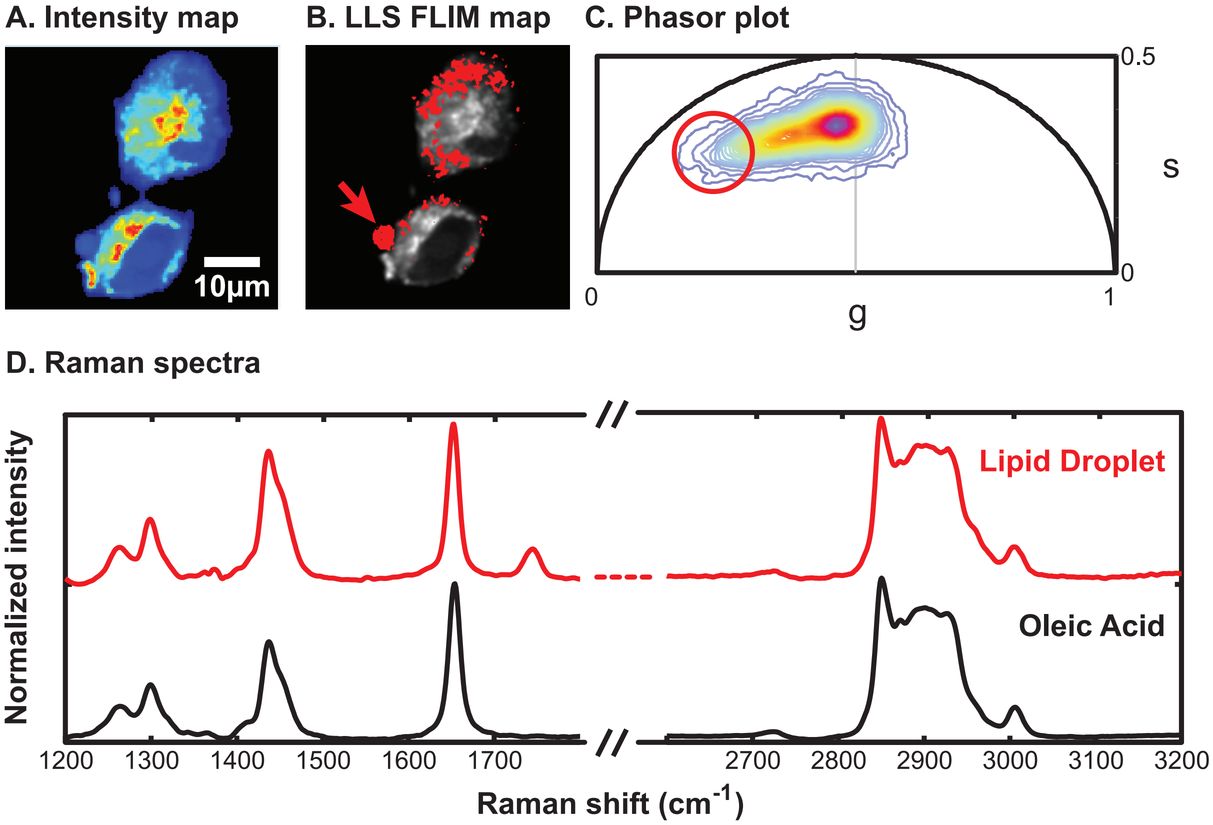

Figure 6.14: Chemical characterization of LLS by Raman spectroscopy. A) Fluorescence intensity image of fixed oleic acid fed HeLa cells. Scale bar = 10 μm B) LLS FLIM map in red. Red arrow points to the big lipid droplet with LLS signal from where the Raman spectrum was acquired. C) Phasor plot of the corresponding cells, with the LLS distribution selected in a red circle. D) The red curve is the Raman spectrum from the lipid droplet of interest (marked by a red arrow in B), the black curve is the Raman spectra from 90% pure oleic acid.

difference between the two spectra is the additional peak at 1746 cm^{-1} that is assigned to C=O stretching mode of the ester bonds present in the lipid droplet spectrum, signal of esterified fatty acids, as it is expected within lipid droplets. The spectra shown in figure 6.14 D have been independently normalized by sections. The fingerprint region was normalized to the 1646 cm^{-1} Raman band, whereas the CH stretching region was normalized to the 2845 cm^{-1} Raman band.

6.3.4 Concluding remarks

This work identifies an autofluorescent species with a unique long lifetime around 7.8 ns, which is distinct form the common NADH lifetime found in most cells (1-2 ns). We encounter that most of the long lifetime fluorescence emerges from lipid-rich areas with granular structures, which CARS and THG identified as lipid droplets.

The lifetime was quantified from a pure chemical contribution found in adipocyte lipid droplets from freshly excised mice white adipose tissue. FLIM phasor analysis of these samples revealed a prominent contribution off from the common NADH cellular signal placed along the metabolic trajectory. This new phasor was situated on the long lifetime side on top of the universal circle, which implies this chemical species' fluorescent temporal evolution is characterized by a single exponential decay.

As previously mentioned in the last section, aliphatic lipids are not fluorescent. However, lipid droplet associated autofluorescence has been identified in the past, including lipofuscin granules and retinosomes. Lipofuscin granules are found in human retinal pigment epithelial cells, fibroblasts among other cell types, and have been suggested as an indicator of oxidative stress[224,225]. Stringari et al reported existence of long lifetime species ($\sim$ 8 ns) in human embryonic stem cells and co-localized these lipid granules with 4,4-difluoro- 1,3,5,7,8-pentamethyl-4-bora-3a,4a-diaza-s-indacene (BODIPY493/ 503), which is a stain for neutral lipids[226]. They established that the autofluorescent species with long lifetime were not associated to lipofuscin, which has a much shorter lifetime ($\sim$ 385 ps[227]). It is thus unlikely that the LLS reported in this study is related to lipofuscin. Retinosomes are lipid droplets containing retinol or any of its derivatives (retinoic acid, retinyl esters, etc.), which also autofluoresce[166,228]. The lifetime fingerprint of pure retinol and retinoic acid is shorter than the LLS lifetime, which makes them poor candidates for the LLS species. Furthermore, retinol and retinoic acid have a very prominent Raman band in the 1590 - 1600 cm^{-1} range that was not observed in our Raman spectra[144]. Other isoprenoids, such as carotenoids, would also exhibit this intense Raman band associated to the conjugated double bond system.

We hypothesize that the detected long lifetime signature originates from products of lipid peroxidation[220], thus providing an indirect measure of oxidative stress. Due to the omnipresence of ROS in pathological conditions, a biomarker for oxidative stress could be used to elucidate pathways of disease development. Autofluorescence of oxidized lipid has the potential to be such a biomarker and in this work we show a unique detection approach by employing two-photon FLIM imaging. Even though multiphoton microscopy still has limited application in clinical settings, it improves penetration for deep tissue imaging and in vivo animal models. Moreover, this method can be applied to imaging live cells and freshly excised tissue, as we have demonstrated.

The long lifetime species FLIM signature of oxidized lipids detected using the phasor approach is a promising, non-invasive tool to detect oxidative stress in biological systems. As far as we know, this is the first time a label-free fluorescent technique has been proposed for this purpose. As shown in this work, phasor analysis of FLIM allows an efficient way to uniquely identify intrinsic, autofluorescent marker of oxidative stress in cell cultures as well as tissue samples.

Chapter 7

Cholesterol, an elusive player

Cholesterol is a ubiquitous molecule involved in multiple physiological pathways. Altered cholesterol metabolism has a major impact that manifests in a wide range of disease form cardiovascular to neurological disorders[229,230]. Free cholesterol is found in the plasma membrane and other intracellular membranes and is believed to regulate the fluidity of the membrane. Larger concentrations of cholesterol are stored in form of cholestryl esters in lipid droplets. These deposits are the primary focus of investigation in this section, we present two approaches to detect cholesterol in intracellular lipid droplets.

First, a purely spectroscopic approach reveals a cholesterol marker in form of a subtle shoulder at about 1670 cm^{-1}. This contribution is detected in lipid droplets from a specific hepatitis C virus infected group of cells, which is linked to fatty liver disease. The cholesterol shoulder marker also appears in a different system, namely human retinal pigment epithelial cells from patients with dry age-related macular degeneration disease. The second approach consists on the characterization of a more robust cholesterol marker. The shoulder at 1670 cm^{-1} is systematically detected in confocal Raman spectroscopy, but it is too weak and close to the 1655 cm^{-1} prominent peak to be used for imaging with CRS microscopy.

Thus, the use of isotope labels that strongly vibrate in a clear region of the Raman spectrum is considered. In the last section we analyze the performance of highly deuterated cholesterol, and use it to study cholesterol intracellular distribution.

7.1 A label-free cholesteryl ester marker

7.1.1 HCV 3a core protein increases lipid droplet cholesteryl ester content

This work has been published in the following paper:
Loizides-Mangold, U., Clment, S., Alfonso Garcia, A., Branche, E., Conzelmann, S., Parisot, C., et al. (2014). HCV 3a Core Protein Increases Lipid Droplet Cholesteryl Ester Content via a Mechanism Dependent on Sphingolipid Biosynthesis. PLoS ONE, 9(12), e115309.

Introduction

Hepatitis C virus (HCV) infections alter the lipid metabolism of the host. As a result, some HCV patients develop steatosis, also known as fatty liver disease. That accumulation of fat in the liver can result in liver failure. The mechanisms by which HCV promotes hepatic steatosis are still unclear and is the focus of a big field of research. It is not the aim of our contribution to this project to elucidate the mechanisms by which HCV is link to fatty liver, but to provide tools that might aid in that task. This project was done in collaboration with a group of researchers of the University of Geneva School of Medicine, in Geneva, Switzerland.

HCV is a blood-borne virus that is mainly transmitted via intravenous injection (of drugs), or blood transfusions/haemodialysis. About 2.8% of the global population is estimated to be infected with HCV[231], and 80% of these patients develop fatty liver (or steatosis)[232,233].

There are 7 types of hepatitis C viruses, also known as genotypes. That means that there are 7 families of HCV sharing common genetic information. The genetic information of each family determines how the virus performs, and thus how it responds to treatment, for example. It has been shown that all genotypes interfere with lipid metabolism, but the family with higher prevalence of developing hepatic steatosis is genotype 3a[234]. There is something in those genes that makes this particular genotype special to alter how the liver processes fat. In particular, HCV 3a genotype is related to hepatic cells (hepatocytes) with very large lipid droplets, and with increased levels of a specific set of lipids, namely cholesteryl esters[235].

Experimental details

Our collaborators at the University of Geneva performed lipidomic profiling of HCV core protein expressing-Huh-7 cells and examined the lipid content of purified lipid droplets isolated from HCV 3a core expressing cells. They found increased levels of cholesteryl esters and ceramides, but not of triglycerides and free cholesterol, in cells expressing the steatogenic HCV 3a core protein. They saw a reduction of the cholesteryl ester levels in 3a transduced Huh-7 cells upon treatment with statins, such as lovastatin, pravastatin or fluvastatin. These treatments also reduced the average lipid droplet size. These measurements were done by staining the cells with Oil Red O, which we know might result in artifacts, including the labeling of non lipid structures or the fusion of lipid droplets.

Our particular task was to corroborate the presence of large lipid droplets in the cells transfected with HCV-3a, and analyze possible lipid content variations among the lipid droplets of cells infected with different HCV genotypic families. We used label-free coherent Raman scattering microscopy to visualize the lipid droplets, and confocal Raman spectroscopy to examine the lipid composition of individual lipid droplets in each group of transfected cells.

Results and discussion

Figure 7.1 A shows the average Raman spectra of lipid droplets found in Huh-7 cells that were either oleic acid-loaded, untransduced, transduced with GFP, HCV 3a, or 2a core. CARS images of Huh-7 cells showed that oleic acid-loaded cells exhibited the highest number of intracellular lipid drolets, whereas HCV 3a-transduced cells contained mostly large size lipid droplets (figure 7.1 C). The Raman spectra of lipid droplets found in cells transduced with HCV 3a core mimicked that of oleic acid-loaded cells with the exception of a small, but identifiable shoulder at 1670 cm^{-1} (second curve in figure 7.1 A), situated besides the more prominent peak at 1655 cm^{-1}. The 1670 cm^{-1} band is evident in the oleic acid/ HCV 3a difference spectrum (green dotted line). This contribution is less prominent or nonexistent in the other groups. The 1670 cm^{-1} band, which is prominently present in the Raman spectrum of pure cholesterol (7.1 B), can be attributed to the C=C stretching vibration in the 6-membered cycloalkane ring of the steroid. Pure oleic acid has a strong contribution at 1655 cm^{-1}, corresponding to the C=C stretching vibration in the unsaturated lipid chain in triglycerides (7.1 B). This peak is seen in all the groups, indicating that triglycerides are the major component of lipid droplets in each of the groups. The Raman spectrum of cholesteryl esters, such as cholesteryl oleate exhibits a combination of the 1655 cm^{-1} and 1670 cm^{-1} bands, producing a double-peak band structure (7.1 B). Thus, the presence of the 1670 cm^{-1} shoulder is an indication of the presence of cholesteryl ester, which appears more prominent in HCV 3a core lipid droplets.

Concluding remarks

In conclusion, it was determined that cells infected with the steatogenic HCV 3a core protein accumulate more choleteryl esters, but not triglycerides, in large lipid droplets. They also found increased levels of ceramides, which do not accumulate in lipid droplets, but promote

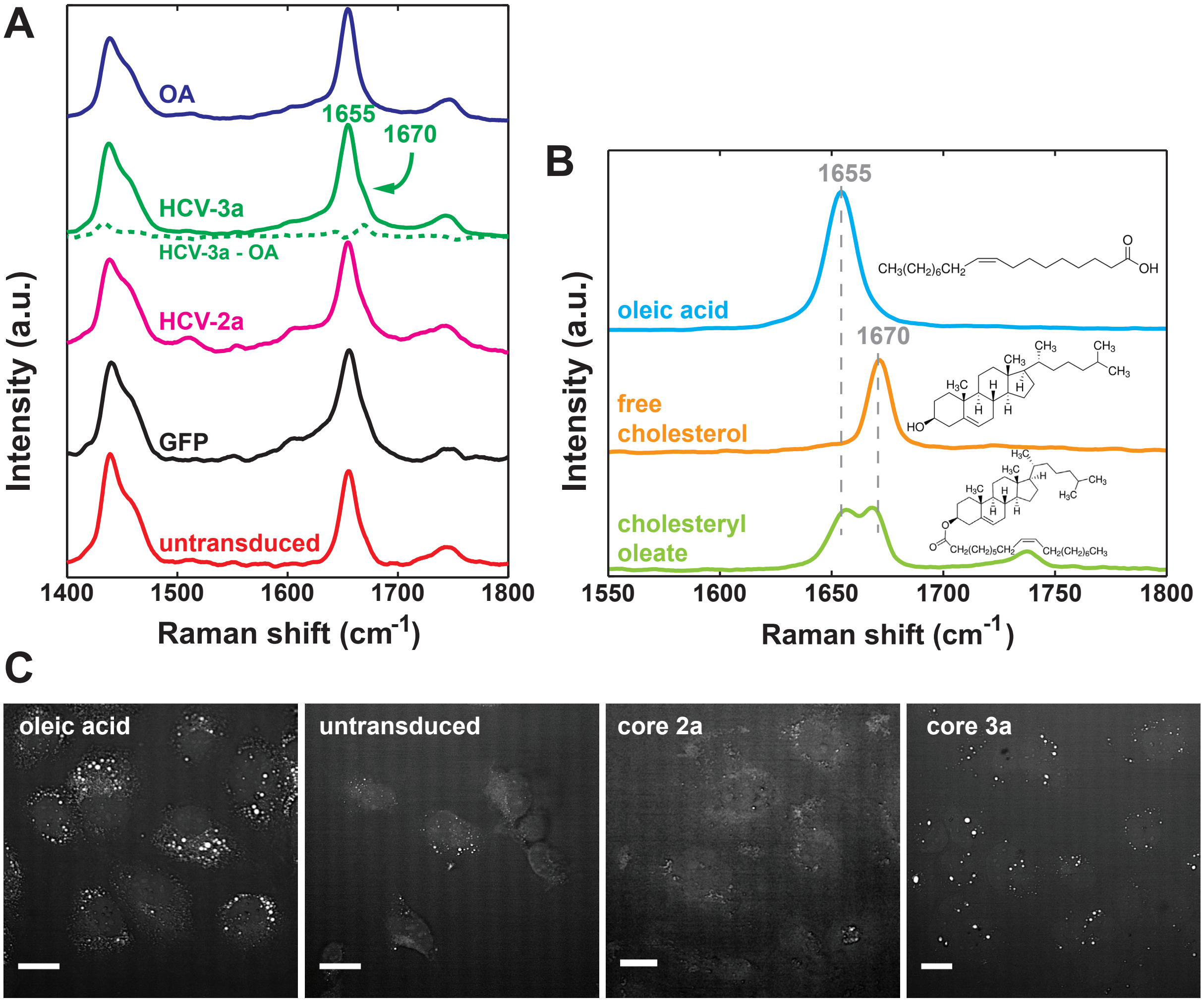

Figure 7.1: A) Average Raman spectra of the lipid droplets found in oleic acid loaded (OA), transduced with HCV core 3a-lentivector (HCV-3a), transduced HCV core 2a-lentivector (HCV-2a), transduced with GFP and untransduced hepatoma Huh-7 cells in the fingerprint band. Notice the region of interest from $1600cm^{-1}$ to $1800cm^{-1}$ where the HCV-3a shows an extra shoulder at $1670cm^{-1}$, besides the oleic acid peak at $1655cm^{-1}$. This contribution is made more evident when the oleic acid contribution is subtracted from the HCV-3a spectrum, a little peak appears at $1670cm^{-1}$ as the difference between the two spectra. B) Raman spectra and molecular structure of oleic acid, free cholesterol and cholesteryl oleate. C) Coherent anti-Stokes Raman scattering (CARS) images of the hempatoma Huh-7 cells trated with 200μM oleic acid, untransduced, and transduced with the HCV core 2a- and 3a-lentivectors, respectively. Scale bars = 25μm

the increase in cholestryl esters possibly serving as signaling messengers. These findings provide new mechanistic insights into HCV-induced statosis.

Our contribution is in accordance with the lipidomic studies performed by our collaborators, and serves yet as another example as how label-free microscopy techniques, such as Raman spectroscopy and coherent Raman scattering microscopy, provide biological insight that complements traditional biochemical assays in biomedical studies.

7.1.2 Age-related macular degeneration linked to cholesterol pathways

Introduction

Age-related macular degeneration (AMD) causes loss of vision. Macular degeneration can be either dry, when the center of the retina degrades, or wet, when blood vessels grow abnormally under the retina[236]. Humans from specific population origins have been found to have increased risk or particular protection against AMD. These populations differ in their mitochondrial haplogroups, which are different patterns of mitochondrial DNA (mtDNA) single nucleotide polymorphisms. It has been suggested that mtDNA may act as modifiers of the effects that nuclear genes and environmental factors cause related to AMD. To isolate the effects of different mtDNA haplogroups, our collaborators at the Gavin Herbert Eye Institute, at the University of California Irvine, lead by Dr. Cristina Kenney, have developed a model of human cytoplasmic hybrids, or cybrids, with identical nuclei but different mitochondrial DNA. They are examining the cholesterol biosynthesis and transport pathways in these cybrids coming from different haplogroups, in particular the K and the H haplogroups. Multiple studies suggest that the K haplogroup mtDNA may create a unique micro-environment that contributes to disease susceptibility[237–244].

Experimental details

Raman spectra from intracellular lipid droplets present in each cybrid group were acquired with a commercial Raman microscope (InVia Confocal; Renisahw, Wotton-under-Edge, Gloucestershire, UK). Spectra were taken with a 532 *nm* excitation laser beam focused to the sample by a 100x 1.3NA oil immersion objective. For each group, seven to ten lipid droplets were investigated in the fingerprint region (1200 - 1800 cm^{-1}) and the CH stretching region (2700 - 3100 cm^{-1}). Each spectrum had the fluorescence baseline manually subtracted, and was subsequently smoothed with a Savitzky-Golay filter implemented in Matlab. Finally, the Raman spectra were averaged together within each group, and normalized to the peak of maximum intensity (fingerprint: 1657 cm^{-1}, CH: 2851 cm^{-1}) for each region independently.

Results and discussion

Again in this case we provide additional information to the biochemical assays by means of label-free microspectroscopy. We used Raman spectroscopy to reveal the chemical composition of the intracellular lipids droplets in retinal pigment epithelial (RPE) cells from different cybrid groups. The H cybrids and the K cybrids examined in this section show analogous lipid signatures (figure 7.2). The most prominent bands in the fingerprint region (1200 - 1800 cm^{-1}) are located at 1265 cm^{-1} (C=C stretching), 1300 cm^{-1} (CH_2 deformations), 1657 cm^{-1} (C=C stretching), and 1439 cm^{-1} (CH_2 deformations) and indicate the presence of both saturated and unsaturated lipids (see table 7.1). There is an additional band at 1744 cm^{-1} from the esterified lipids. In the higher wavenumber range, we find the CH stretching band with a dominant peak at 2851 cm^{-1} (CH_2 symmetric stretches of lipids) and a contribution from the =CH vibrations at 3011 cm^{-1}, again sign of unsaturated lipids.

We found no difference between the lipid content of intracellular lipid droplets in cybrids created from the first three different patients we examined. However, the investigation of a

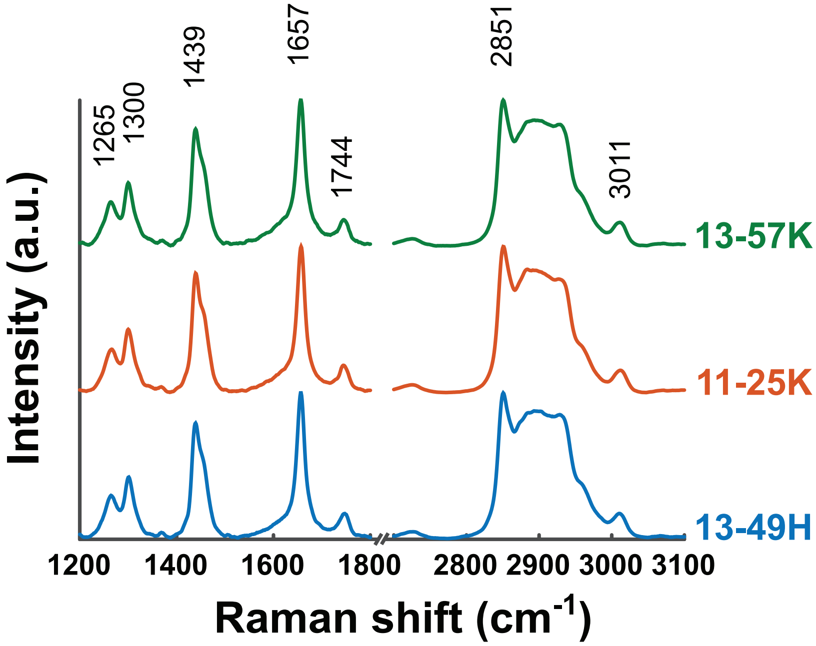

Figure 7.2: Average Raman spectra of lipid droplets in CYB#13-49H, CYB#11-25K and CYB#13-57K in the fingerprint (1200 - 1800 cm^{-1}) and the CH stretching (2700 - 3100 cm^{-1}) regions. Prominent lipid bands are marked.

Raman shift (cm^{-1})	Bond assignation	molecular assignment
1300	$\delta(CH_2)$	
1439	$\delta(CH_2)$	saturated lipids
2851	$\nu_s(CH_2)$	
1265	$\delta(=CH)$	
1657	$\nu(C=C)$	unsaturated lipids
3011	$\nu_{ss}(=CH)$	
1744	$\nu(C=O)$	esterl carbonyl

Table 7.1: Raman bands present in the lipid droplets spectra and their bond and molecular assignments[245]

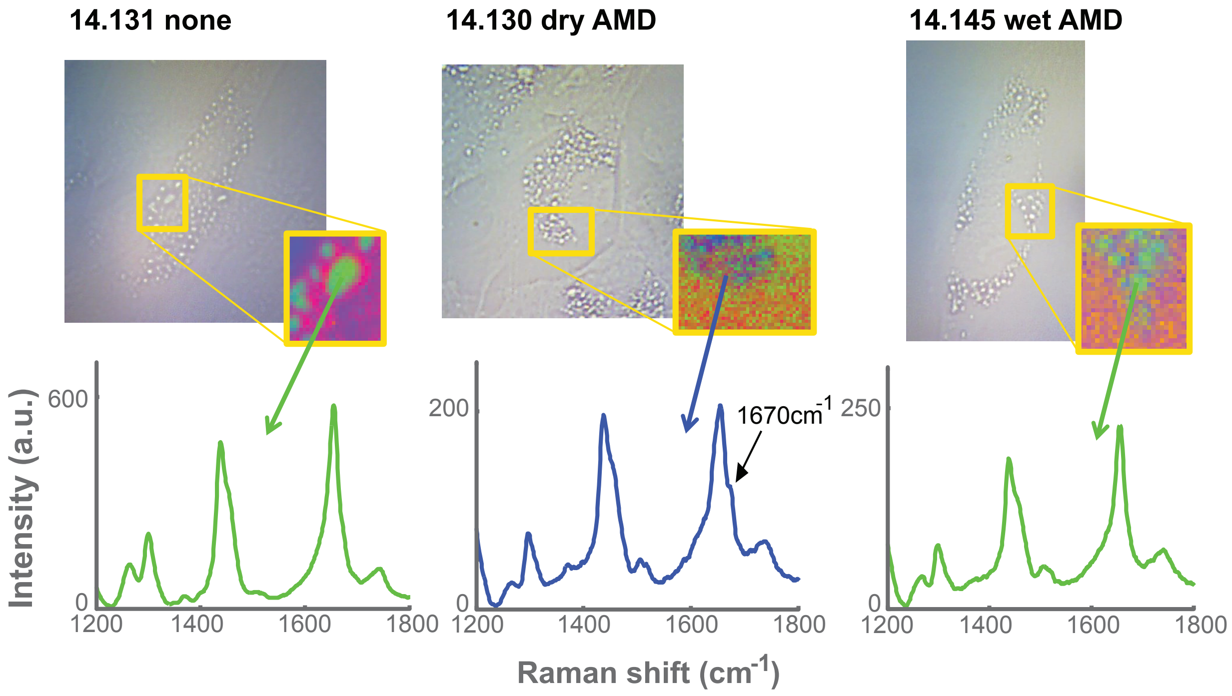

Figure 7.3: Retinal pigment epithelial cells with no associated disease (14.131 none), with dry AMD (14.130 dry AMD), and with wet AMD (14.145 wet AMD) were analyzed with confocal Raman spectroscopy. Brightfield transmission images of the cells are shown for each group, with a small area highlighted in which confocal Raman imaging was performed. The colors in the small area are the result of the vertex component analysis of the spectral information of the region. The lipid droplet content has the end-member spectra depicted in the plots beneath the images.

set of patients with and without AMD yielded a new set of RPE cybrid cells with interesting differences in their cholesterol content.

Raman maps of small areas of the RPE cells with intracellular lipid droplets identify typical lipid profiles within the droplets (figure 7.3). We examined samples coming from healthy patients (labeled none), and from patients with dry and wet AMD. While the three groups look remarkably similar, the dry AMD cell showed an extra shoulder at 1670 cm^{-1}, due to C=C vibrations of an aromatic structure, that we identified as a possible cholesterol marker in the HCV study[246]. The shoulder is located besides the 1650 cm^{-1} peak, assigned to C=C vibrations of aliphatic substances.

The Raman maps were analyzed with vertex component analysis to extract the main chemical components of the imaged samples. A prominent contribution was extracted from the lipid droplet areas which matched the individual Raman measurements taken on the same cells, see figure 7.4, which shows a collection of Raman spectra from 9-10 individual lipid droplets in each group. Note that all the spectra collected from lipid droplets in the dry AMD group exhibit the shoulder mode at 1670 cm^{-1}.

Concluding remarks

The cybrids examined in this study derive from a limited number of patients. It would be premature to conclude that dry AMD has clear consequences on cholesterol pathways based on the one patient examined, as cybrids created from other dry AMD patients may not have the same cholesterol contribution. If the same trend cannot be reproduced, this cholesterol marker could be linked to other attributes of the particular patients that display it. Contrarily, if the cholesterol assigned shoulder appears consistently in this variation of AMD diseased cells, or it appears for a specific subset of patients sharing the same haplogroups, cholesterol pathway alterations could be drawn, together with the biochemical assays performed on the same samples.

At this point more data needs to be acquired and thoroughly inspected to establish correlations with the haplogroup origin of each patient, in order to draw conclusions. But once again, this preliminary results illustrate the potential for a consistent cholesterol ester marker that appears clearly in Raman spectra of lipid droplets, without the need of additional exogenous labels.

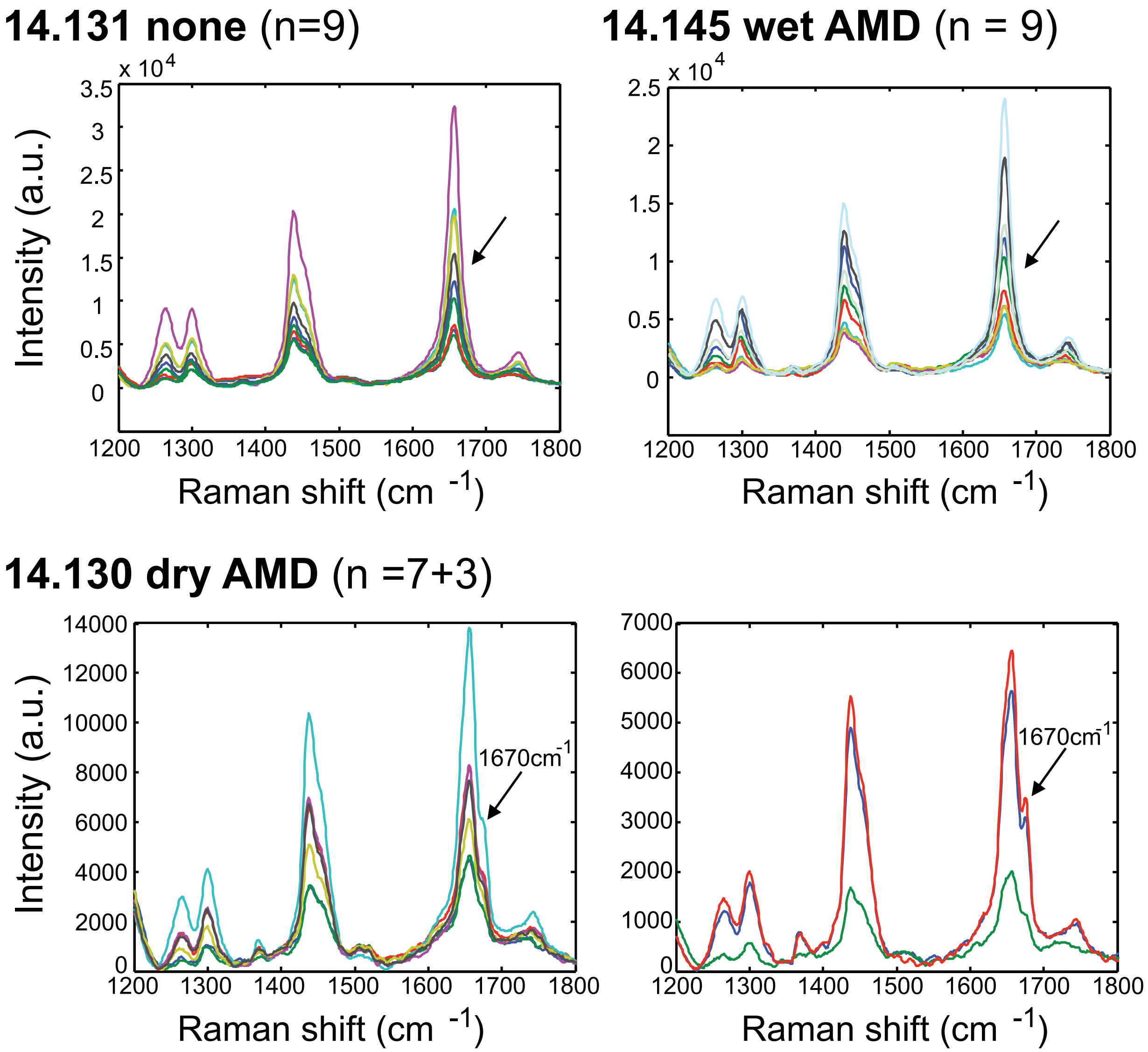
14.131 none (n=9)

14.145 wet AMD (n = 9)

14.130 dry AMD (n =7+3)

Figure 7.4: Raman spectra of individual lipid droplets (LDs) in retinal pigment epithelial cells from a healthy patient (14.131 none, 9 LDs examined), a patient with wet AMD (14.145 wet AMD, 9 LDs examined), and a patient with dry AMD (14.130 dry AMD, 10 LDs examined in two different sessions). Arrows point to the 1670 cm^{-1} shoulder contribution, that is only present in the dry AMD patient.

7.2 D38-cholesterol as a Raman active probe for imaging intracellular cholesterol storage

This work has been published in the following paper:

Alfonso Garcia, A., Pfisterer, S. G., Riezman, H., Ikonen, E., and Potma, E. O. (2016). D38-cholesterol as a Raman active probe for imaging intracellular cholesterol storage. Journal of Biomedical Optics, 21(6), 061003.

7.2.1 Introduction

Cellular cholesterol storage and transport has been visualized mostly using fluorescence techniques. Measurements based on dehydroergosterol, a fluorescent cholesterol analog, have been helpful in elucidating cholesterol trafficking mechanisms[247]. Other fluorescent labels including filipin[248], which associates with cholesterol in membranes, and fluorescently tagged cholesterols, such as BODIPY-cholesterol[33], have unveiled information on recruitment of cholesterol to membranes[41]. Nonetheless, the use of fluorescent lipids can produce unwanted artifacts[50,168,249], including altered lipid metabolism and detachment of the fluorescent label from the sterol.

Raman active labels offer an alternative to fluorescent probes. Unlike fluorescent labels, Raman markers are unaffected by photobleaching effects, enabling sustained imaging of cells. More importantly, the spatial extent of Raman active modes is limited to a single or a few chemical bonds, which is much smaller than the chemical structure of fluorescent moieties. Raman labels can be chosen from spectral signatures of the endogenous compound or from chemically modified probes that enhance the Raman response and selectivity. The Raman spectrum of endogenous cholesterol exhibits several spectral features that can be utilized as marker bands. This notion has been used to selectively visualize cholesterol crystals in tissues using nonlinear Raman imaging techniques, such as coherent anti-Stokes Raman scattering (CARS)[115,250,251] and stimulated Raman scattering (SRS)[252,253] microscopy.

However, non-crystalline pools of cholesterol in cells are often complex mixtures of lipophilic constituents, rendering the intrinsic spectral signatures of the compound insufficient for uniquely identifying cholesterol in intracellular environments. To improve selectivity, chemical analogues of cholesterol may be used, selected for their unique Raman response[61]. Several Raman labels with large Raman cross sections and signatures in quiet spectral regions, such as alkyne tags[57,58], have been shown to be tolerated by live cells, enabling the rapid visualization of selected metabolites, nucleotides and protein residues in cells with SRS imaging[59,60]. Recently, this principle has been extended to imaging cholesterol by substituting part of the molecules aliphatic tail with a phenyl capped diyne moiety[254]. The phenyl-diyne cholesterol exhibits a very high Raman cross-section and, relative to a terminal alkyne group, phenyl-capping gives rise to reduced cytotoxicity.

Nonetheless, although alkyne moieties are structurally small, they represent a chemical group that is foreign to the intracellular environment. While a Raman probe like phenyl-diyne cholesterol may display limited cytotoxicity, it is unknown how the foreign chemical structure may affect various downstream processes relevant in cholesterol homeostasis. In order to minimize artifacts beyond cytotoxicity, Raman probes that display minimal chemical dissimilarities with natural cholesterol are of interest. In this regard, probes based on the substitution of hydrogen by deuterium are particularly attractive, as the chemical properties of deuterated isotopologues closely resemble those of their endogenous counterparts. Deuterium-based Raman labels have been successfully used in nonlinear optical imaging applications to help increase specificity to water dynamics[51], selected phospholipids[52,53], neutral lipids[69,80,255], and protein metabolism[56,256].

Labels based on stable isotopes, including deuterium, have found widespread use in clinical applications. Because the level of toxicity of pharmacological substances and their deuterated analogues is typically identical, deuterated substances are widely used in clinical studies aimed at studying metabolism and movement of drugs in humans[257]. Similarly, deuterated cholesterol has been clinically administered to humans without harmful side effects, underlining the biocompatibility and usefulness of deuterated cholesterol probes.

In this work, we explore the utility of deuterated cholesterol as a Raman probe. Despite the fact that deuterated cholesterol is commercially available, only a maximum of seven hydrogen atoms are replaced by deuterium (D7-cholesterol). Hence, the retrieved Raman response in the spectral range characteristic of the C-D stretching mode is found to be relatively weak, reducing the effectiveness of the probe. To boost the sensitivity, we have optimized a procedure for producing D38-cholesterol, a probe that features an average of 38 C-D bonds and an improved Raman cross section in the 2100 cm^1 spectral range. With this increase in the degree of deuteration, we show that D38-cholesterol can be detected at physiologically meaningful levels in cells using rapid SRS imaging. Using hyperspectral SRS and multivariate analysis, we demonstrate that D38-cholesterol is readily internalized by cells and is naturally esterified and stored in lipid droplets. In addition, we use D38-cholesterol to study heterogeneity in cholesterol storage in steroidogenic cells.

7.2.2 Experimental details

D38-Cholesterol

Deuterated cholesterol was produced by a yeast strain (RH6829) engineered to produce cholesterol instead of ergosterol[258]. An overview of the cholesterol biosynthetic pathway and principles of biosynthetic isotopic labeling has been published[259].Yeast growth media for isotopic labeling was 0.7% yeast nitrogen base (US Biological), 0.5% yeast extract (BD), 1.25% glucose, 30 mg/l uracil and leucine in deuterium oxide (99.8%, ARMAR, Switzerland). Precultures (1 ml) in this medium were used to inoculate 2 liters of media, which were grown

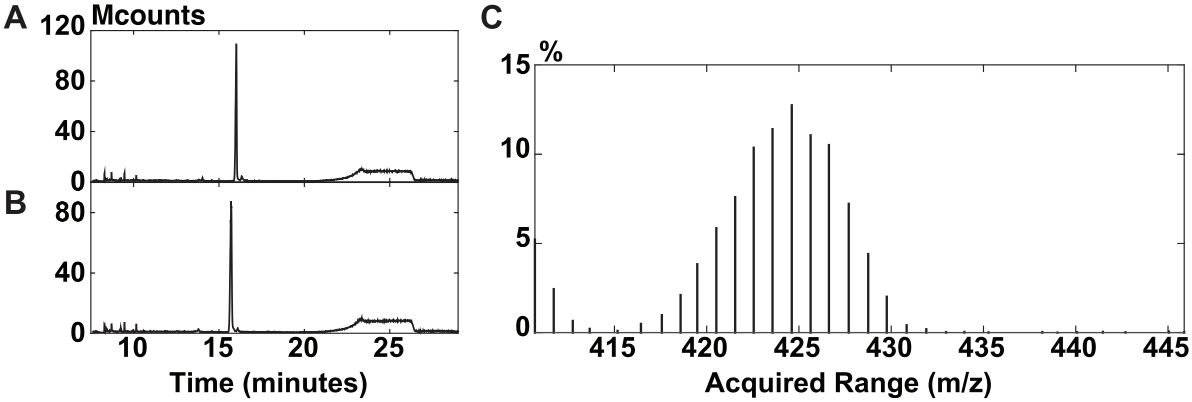

Figure 7.5: A) Commercial cholesterol and B) deuterated cholesterol purified from yeast were analyzed by GC-MS and the GC profiles are shown. The higher masses, representing unfragmented deuterated cholesterol (peak in B), are shown in C, with an average around 424.6, denoting an average replacement of 38 H by D

to stationary phase with shaking (3-4 days) at 30°C. The D-cholesterol was purified from harvested cells and analyzed by GC-MS as described[258]. The yield was approximately 10 *mg* purified D-cholesterol per liter of cell culture. Analysis of the GC-MS profile of the D-cholesterol showed a GC profile (figure. 7.5 B) identical to commercial cholesterol (figure7.5 A), except that the retention time of D-cholesterol was slightly faster than cholesterol. Examination of the high range of intact ions under the peak (figure 7.5 C) showed an average m/z of 424 denoting an average substitution of 38 hydrogen atoms by deuterium. Analysis of the D-cholesterol by NMR confirmed its purity and showed that all positions were substituted between 70 and 90%, consistent with the average of 82% substitution calculated from the MS profile. D7-cholesterol was obtained from Sigma-Aldrich and used without further purification.

Reagents

Cell culture reagents were obtained from Life Technologies or Lonza. Methyl-β-cyclodextrin, oleic acid, fatty acid free BSA and cholesterol were purchased from Sigma. D38-cholesterol or cholesterol / methyl-β-cyclodextrin stock complexes were prepared as described previously[260], using a methyl-β-cyclodextrin to cholesterol (D38-cholesterol) ratio of 6.2 to 1 and a final concentration of 45-50mM for D-38 cholesterol. Lipoprotein deprived serum (LPDS) was prepared from fetal bovine serum by potassium bromide density ultracentrifugation[261]. Oleic acid was complexed to fatty acid free BSA in a 8:1 ratio[34].

Cell culture and lipid administrations

Y1 cells were cultured in DMEM/F12 (1:1) with 15% horse serum and 2,5% FBS. Culture medium was supplemented with penicillin/streptomycin (100 U/ml each) and L-glutamine (2 mM). For lipid loadings Y1 cells were seeded in culture medium for 24 hours. Cells were washed three times with phosphate buffered saline (PBS) and incubated with DMEM/F12 medium containing 5% LPDS and 50 μM cholesterol/cyclodextrin, 45-50 μM D-38 cholesterol/cyclodextrin, 400 μM oleic acid/BSA (bovine serum albumin) or 400 μM oleic acid/BSA plus 50 μM D-38 cholesterol/cyclodextrin for 24 hours.

Lipid extraction and quantifications

Lipid extraction and quantifications were performed as described previously[262]. Lipids were extracted using chloroform:methanol in a 1:1 ratio. Solvents were evaporated under nitrogen and dried lipids were dissolved in chloroform:methanol (2:1 ratio). Lipid solutions were spotted on thin layer chromatography (TLC) plates and cholesteryl ester, triacylglycerols and free cholesterol were resolved by phase separation using hexane: diethylether: acetic acid 80:20:1. Cholesteryl ester, triacylglycerols and free cholesterol were quantified using ImageJ and normalized to protein content, measured by Bio-Rad protein determination.

	pump (nm)	Raman shift (cm^{-1})
CH range	820 - 803	2796.6 - 3054.8
CD range	880 - 855	19565.1 - 2297.4

Table 7.2: Pump wavelengths corresponding to the Raman shifts of interest for SRS hyperspectral interrogation at the C-H and C-D stretching ranges.

Sample preparation for SRS microscopy

Cells grown on coverslips were washed 2x with PBS and fixed with 4% paraformaldehyde for 15 minutes. Coverslips were rinsed several times with PBS, mounted in PBS and sealed with epoxy glue to prevent cells from drying.

Hyperspectral imaging with SRS microscopy

Stimulated Raman scattering (SRS) signals were obtained with the CRS microscope described in chapter 2. The pump wavelength for this experiment was tuned to two areas of interest noted in table 7.2, namely the deuterated stretching (CD) Raman window and the CH stretching Raman window. Hyperspectral scan were acquired from both windows, as well as individual images at the most prominent Raman shifts for each region, 2120 cm^{-1} and 2841 cm^{-1}, respectively. Images off resonance ($\sim$ 2500 cm^{-1}) were also acquired and subtracted from the resonant images to avoid background contributions in the analysis.

Additional spontaneous Raman spectra of pure cholesterol were acquired with a commercial Raman microscope (InVia Confocal; Renishaw, Wotton-under-Edge, Gloucestershire, UK).

Spectral analysis with vertex component analysis

Hyperspectral coherent Raman scattering imaging has been previously used to acquire simultaneous chemical and spatial information of biological samples[80,252,263]. In combination with multivariate analysis we can extract the spectral information form the hyperspectral stacks. In this case, we chose vertex component analysis to retrieve the most prominent spectral features in the hsSRS images[119,264], as described in chapter 3. The result can be nicely visualized in RGB color maps in which the colors denote the spectral class of each pixel.

7.2.3 Results

Characterization of D38-cholesterol

Deuterated lipids increase specificity for Raman, SRS and CARS imaging due to their specific C-D vibrational frequencies from 2000 to 2300 cm^{-1}, situated in a silent region of the Raman spectrum. The blue line in figure 7.6 shows the Raman spectrum of cholesterol. The strongest peaks in the spectrum are found at 2700 - 3100cm^{-1} (C-H stretching modes), with additional peaks at 1670 cm^{-1} (C=C stretching modes) and 1440 cm^{-1} (CH_2 scissoring mode). The Raman spectrum of commercially available D7-cholesterol, which has 7 hydrogen atoms replaced by deuterium, is shown in red in figure 7.6. The frequency of the C-D modes is shifted relative to the CH stretching band, giving rise to a Raman band in an otherwise silent region of the Raman spectrum from 2000 - 2300 cm^{-1}. However, because only 7 out of 46 possible positions are substituted with deuterium, the C-D spectral features of D7-cholesterol are relatively weak, while the C-H region remains the dominant contribution to the spectrum. The yellow line in figure 7.6 represents the Raman spectrum of D38-cholesterol.

By substituting 38 sites with deuterium (82.6% deuteration), the response in the 2000 - 2300 cm^{-1} is significantly improved, whereas the magnitude of the C-H stretching bands is considerably reduced. D38-cholesterol shows two main peaks in the CD band, centered at 2120 cm^{-1} and at 2211 cm^{-1}. The heavily deuterated cholesterol also exhibits a shift of the C=C stretching band to 1656 cm^{-1}, relative to natural cholesterol. A similar shift has previously

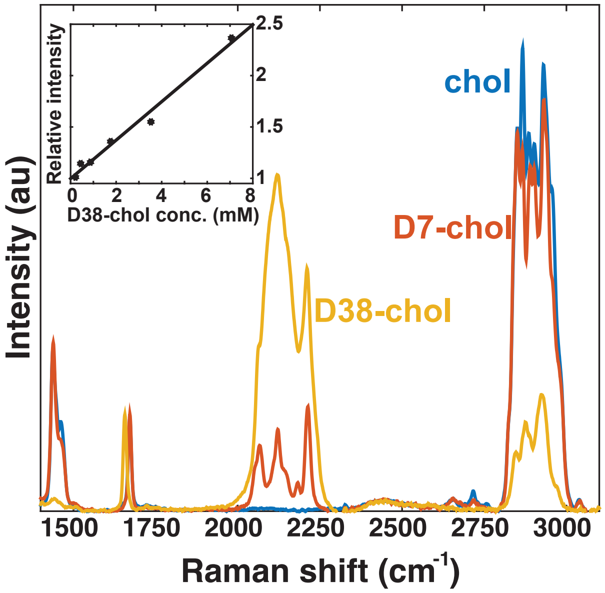

Figure 7.6: Raman spectra of cholesterol (blue), D38-cholesterol (yellow), and D7-cholesterol (red) are shown in the range from 1400 to 3100 cm^1. Inset: the SRS intensity of D38-cholesterol in cyclohexane relative to the noise floor increases linearly with the concentration of solute. The detection limit was found to be 220 μM.

been reported for the deuterated fatty acid D6-arachidonic acid[255]. Note that besides a significant reduction of the CH band, the spectral profile of the CH stretches of D38-cholesterol is markedly different from the spectral bandshape of natural cholesterol in this range. The contribution of the symmetric CH_2 stretching mode at 2845 cm^{-1} in D38-cholesterol is relatively weak, whereas the strongest contribution in this range is found at 2925 cm^{-1}. This characteristic bandshape provides an additional handle to identify D38-cholesterol, and, as shown below, can be utilized to discriminate lipid droplets with predominantly esterified cholesterol from lipid droplets with a high concentration of unesterified cholesterol.

The sensitivity of the SRS microscope to D38-cholesterol is depicted in the inset of figure 2. Here the SRS signal is measured relative to the noise floor of the experiment, as determined by the photothermal signal of glass. At 2120 cm^{-1}, we find a detection limit of 220 μM in cyclohexane at a pixel dwell time of 10 μs, when the SRS signal of D38-cholesterol approaches the noise floor. As expected, there is a linear dependence of the SRS signal on D38-cholesterol concentration[49].

D38-cholesterol: Uptake, metabolic processing and storage in lipid droplets

To examine the biocompatibility of D38-cholesterol in mammalian cells, we treated Y1 adrenal cells with 50 μM D38-cholesterol/cyclodextrin for 24 hours. Cyclodextrin forms a complex with cholesterol and transfers it to cells via the plasma membrane[265]. This treatment results in efficient cellular uptake of D38-cholesterol with a 2.9 fold increase in total cholesterol and 3.5 fold for cholesteryl esters (figure 7.7 A) compared to LPDS control. Using TLC, we determined that approximately 58% of the sequestered D38-cholesterol was esterified (figure 7.7 A), confirming enzymatic processing of D38-cholesterol and highlighting its superiority to fluorescent sterol analogs in regard to metabolic processing[33,254]. Importantly, we find that the levels of esterified D38-cholesterol are similar to the levels of esterified natural cholesterol under similar treatment conditions (figure 7.8) indicating that the deuterated probe does not affect acylCoA:Cholesterol acyltransferase (ACAT)-mediated esterification. Next, we performed SRS imaging of D38-cholesterol loaded cells. Figure 7.7 B-D show a cell treated with D38-cholesterol imaged at three different frequencies: 2325 cm^{-1} (off resonance), 2120 cm^{-1} (CD_2 stretches), and 2841 cm^{-1} (CH_2 symmetric stretches), respectively. The strongest signal at 2120 cm^{-1} derives from droplet-like structures, as does the more intense signal at 2841 cm^{-1}, indicative of intracellular lipid droplets. This observation provides evidence that D38-cholesterol has been processed by the cell and is stored in lipid droplets.

To compare the levels of esterification between natural cholesterol and D38-cholesterol, Y1 cells were loaded for 24 hours with sterol/cyclodextrin complex, and the content of free and esterified cholesterol was analyzed using TLC. The TLC results are shown in figure 7.8. We find that the levels of esterified D38-cholesterol are identical to the levels of esterified natural cholesterol under a similar treatment.

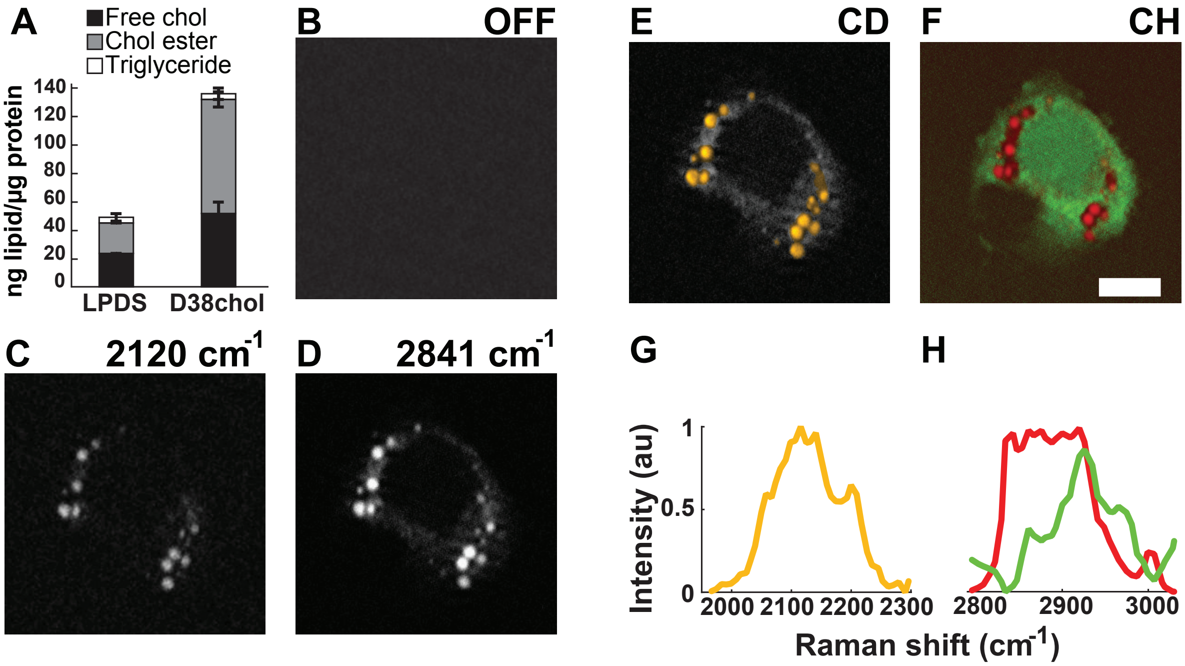

Figure 7.7: Y1 adrenal cells were treated with 50μM D38-cholesterol/cyclodextrin for 24 hours, and cells were used for lipid quantification (A) or fixed and subjected to SRS imaging (B) 2325 cm^1 , off resonance; (C) 2120 cm^1 , CD2 stretches; and (D) 2841 cm^1, CH2 symmetric stretches). The result of hyperspectral SRS imaging and multivariate analysis is depicted in yellow for D38- cholesterol in the CD region (E and G), overlaid on the maximum intensity projection of the CH spectral scan in gray scale, and in red for lipid and green for protein in the CH region (F and H). Normalized spectra. Scale bar = 10 μm.

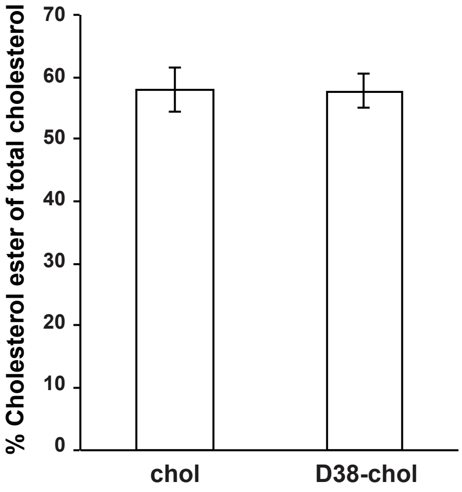

Figure 7.8: Esterification levels of D38-cholesterol match those of natural cholesterol.

To further prove the presence of D38 cholesterol in intracellular lipid droplets, we show the result of a hyperspectral SRS multivariate analysis (VCA) in both the CD and CH spectral regions. The CD range spanned from 1965 to 2297 cm^{-1}, with a step size of 8.5 cm^{-1}, whereas the CH region ranges from 2797 to 3055 cm^{-1}, with a step size of 6.6 cm^{-1}. The yellow areas in figure 7.7 E represent the spectrum depicted in figure 7.7 G. These locations indicate the presence of D38-cholesterol and spatially correlate with the lipid droplet areas, confirming that D38-cholesterol is stored in lipid droplets. A corresponding analysis in the CH range shows that the same droplets also contain non-deuterated lipids, whose spectral profile is depicted in red (figure 7.7 F and figure 7.7 H). These lipids largely represent, fatty acids esterified to D38-cholesterol, some pre-existing non-deuterated cholesterol, and a small fraction of triglycerides (5.1% of total neutral lipids), as confirmed by TLC. The green areas in figures 3F and 3H correspond to the protein-rich content of the cell, which is shown here for context. Hence, these combined results show that D38-cholesterol is processed by the cells, is esterified to a similar degree as natural cholesterol, and is stored in lipid droplets.

Hyperspectral SRS imaging of D38-cholesterol identifies subpopulations of esterified and unesterified cholesterol.

Besides identifying cholesterol in lipid droplets, the unique Raman spectrum of D38-cholesterol can be utilized to reveal additional information about the degree of cholesterol esterification. To access this information, we used hyperspectral-SRS imaging combined with VCA. Figure 4 shows a cell that contains two subsets of lipid droplets with different spectral profiles. The CD range reveals droplets that contain D38-cholesterol (figures 7.9 A and 7.7 C). A subset of these lipid droplets, depicted in blue, exhibit a CH spectrum that resembles the Raman spectrum of unesterified D38-cholesterol. In red, we show the subset of droplets that are represented by a spectrum indicative of both esterified D38-cholesterol and non-deuterated lipids (figures 7.9 B and 7.9 D). These droplets most likely consist of fatty acids esteri-

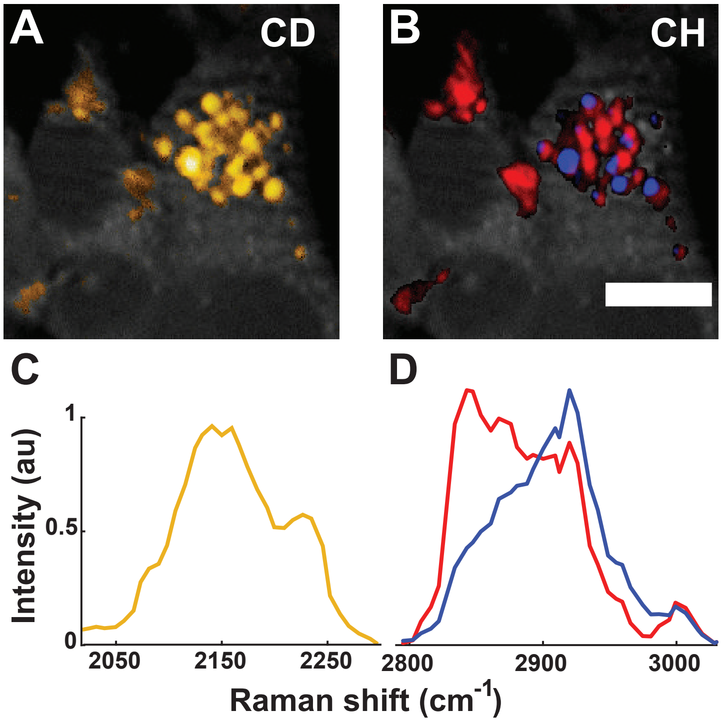

Figure 7.9: Y1 adrenal cells were treated with $50\mu M$ D38-cholesterol/cyclodextrin as in figure7.7. The result of hyperspectral SRS imaging and multivariate analysis is depicted here in yellow for D38-cholesterol in the CD region (A and C), and in red for esterified cholesterol and blue for free D38-cholesterol in the CH region (B and D). Normalized spectra. Scale bar $= 10\ \mu m$.

fied to cholesterol and a small amount of triglycerides and/or pre-existing non-deuterated cholesterol.

The CD range of the spectrum contains limited information about cholesterols state of esterification. However, the spectral information acquired in the CH range helps to discriminate between esterified and free cholesterol accumulations. By combining C-D imaging with hyperspectral analysis of the C-H region we thus demonstrate that lipid droplet heterogeneity may not only occur at the level of cholesterol ester and triglyceride partitioning, but also at the level of cholesterol esterification. Some lipid droplets show higher enrichment for free cholesterol than others.

Distinct cholesteryl ester and triacylglycerol containing lipid droplets visualized by D38-cholesterol and oleic acid administration

Studies based on fluorescent tracers have suggested that steroidogenic cells can store triglyceride and cholesterol esters in distinct lipid droplets resulting in lipid droplet heterogeneity[260]. However, this might result from altered properties of BODIPY labeled lipid analogs as compared to natural lipids[80]. Here we demonstrate lipid droplet heterogeneity without fluorescent lipid analogs by means of stimulated Raman scattering microscopy and D38-cholesterol.

Y1 cells were treated with 50 μM D38-cholesterol and 200 μM oleic acid for 24 hours. TLC analysis shows that this treatment results in a 5.8 fold increase in the accumulation of cholesteryl esters (131 $ng/\mu g$ protein) and a 38 fold increase in the level of triglycerides (107 $ng/\mu g$ protein) (figure 7.10 A). Cells subjected to this treatment are depicted in the SRS images shown in figure 7.10 (B-F). Lipid droplets containing D38-cholesterol are visualized at the 2120 cm^{-1} Raman shift in figure 7.10 C. The overall population of lipid droplets is visualized by tuning to the Raman shift of 2841 cm^{-1}, shown in figure 7.10 D, which marks lipid droplets irrespective of the presence of D38-cholesterol. Comparing the 2120 cm^{-1} and 2841 cm^{-1} images makes clear that the concentration of D38-cholesterol in the available droplets varies significantly. This is made clearer in the hyperspectral image of figure 7.10 E, which highlights the D38-cholesterol containing lipid droplets in yellow (see the corresponding spectra in figure 7.10 G). Some lipid droplets, irrespective of size, are seen to contain D38-cholesterol at appreciable levels, whereas others appear devoid of D38-cholesterol. The hyperspectral image obtained in the CH stretching range, shown in figure 7.10 F, reveals furthermore two subsets of droplets with different spectral profiles (figure 7.10 H). Most of the droplets depicted in red are those that also contain D38-cholesterol, while the droplets that appear in green in the CH range exhibit little to no CD signal. A third subset contains a mixture of both green and red spectra. These results show that intracellular lipid

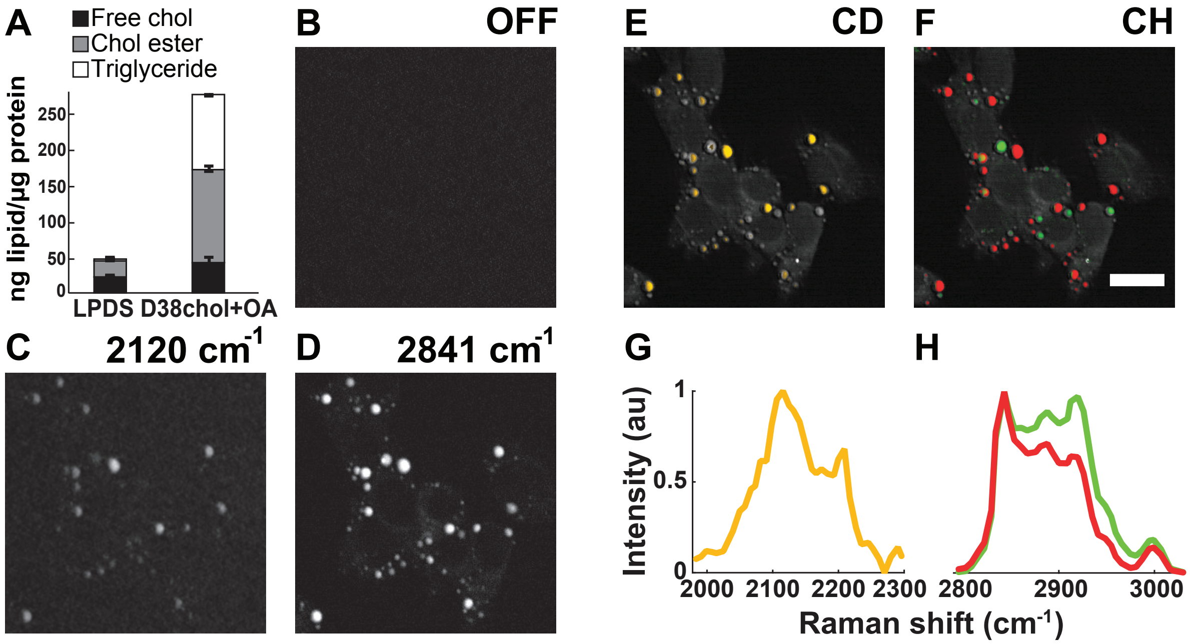

Figure 7.10: Y1 adrenal cells were treated with $50\mu M$ D38-cholesterol/cyclodextrin together with $200\mu M$ oleic acid for 24 hours. Cells were either used for lipid quantification (A) or subjected to SRS imaging [(B) 2325 cm^1, off resonance; (C) 2120 cm^1, CD_2 stretches; and (D) 2841 cm^1, CH_2 symmetric stretches]. (Note that LPDS control treatment is the same as in figure 7.7) The result of hyper- spectral SRS imaging and multivariate analysis is depicted in yellow for D38-cholesterol in the CD region (E and G), and in red and green for the lipids in the CH region (F and H). The results are overlaid on the maximum intensity projection of the CH spectral range, shown in gray scale, which outlines the cellular morphology. Normalized spectra. Scale bar = 20 μm.

droplets are heterogeneous in terms of chemical composition, and that cholesterol partitions inhomogenously among the available lipid reservoirs.

7.2.4 Discussion

The ability to identify cholesterol and follow its movement in cells is important for understanding changes in cellular cholesterol levels and distribution, and its implications in cholesterol related diseases. The availability of biocompatible probes that minimally interfere with the cells natural physiology is a critical component in studying cholesterol homeostasis. Given that fluorescent analogues to cholesterol have been shown to alter key aspects of cholesterol metabolism, most notably the level of ACAT-mediated esterification[266,267], the search for alternative probes has become a relevant research focus. In this regard, Raman labels are prime candidates for replacing fluorescent probes, as they are insensitive to photobleaching and can be engineered such as to improve biocompatibility while reducing cytotoxicity. Recent successes include the development of phenyldiyne cholesterol[254], which exhibits an exceptional Raman cross-section and was shown to be well tolerated by cells.

Compared to phenyl-diyne cholesterol, the Raman cross section of deuterated cholesterol is weaker. However, deuterated labels remain attractive because they generally exhibit excellent biocompatibility and very low cytotoxicity levels, as underlined by the widespread use of deuterated probes in clinical studies. It is known that deuterated cholesterol is non-toxic to humans[265,267], rendering D-cholesterol also a reliable Raman probe for in-depth studies at the cellular and small organism level. To improve the Raman cross-section of D-cholesterol, we produced D38-cholesterol using engineered yeast cells, which boosts the Raman signal intensity at 2100 cm^{-1} about 5 times relative to commercially available D-cholesterol. With this improvement, the SRS detection sensitivity of D38-cholesterol is $\sim$220 μM at a 10 μs pixel dwell time, which allows its detection at physiologically relevant concentrations in the cell. Our production procedure allows for cheap, batch produced D38-cholesterol in large quantities, which further accentuates the practical utility of this probe.

We have confirmed the biocompatibility of D38-cholesterol. We find that internalized D38-cholesterol is esterified by Y1 cells and stored in lipid droplets. Unlike BODIPY-cholesterol, D38-cholesterol does not appear to alter the ACAT-mediated esterification process. Concentration levels of cholesteryl esters stored in lipid droplets are well within SRS detection levels of D38-cholesterol under all conditions studied here. Therefore, using D38-cholesterol as an SRS probe offers an opportunity to study details of cellular cholesterol storage processes that have so far remained under-illuminated.

Besides using D38-cholesterols biocompatibility and its detectability in SRS imaging, we have extracted additional information about cholesterol storage through examining the spectral SRS content in both the vibrational range of the CD and CH stretching modes. In particular, spectral variations in the CH stretching range can be used to distinguish distributions of esterified D38-cholesterol from free D38-cholesterol. In this capacity, we have used hyperspectral SRS imaging of D38-cholesterol to highlight unanticipated heterogeneity in the chemical composition of stored neutral lipids between individual lipid droplets. First, hyperspectral SRS imaging of D38-cholesterol in Y1 adrenal cells revealed the presence of lipid droplets that contained a high concentration of unesterified cholesterol adjacent to lipid droplets containing predominantly esterified cholesterol. Moreover, in these cells cholesterol and triacylglycerols were deposited in distinct lipid droplets. Note that such heterogeneous distribution of neutral lipids was not detectable by hyperspectral SRS imaging in the absence of deuterated cholesterol[69].

Note also that it is not straightforward to discriminate subpopulations of lipid droplets based on the degree of cholesterol esterification by using Raman spectroscopy without the use of the D38-cholesterol probe. The characteristic C=O stretching mode of ester groups at 1740 cm^{-1}, which serves as a marker for cholesteryl esters[268], is not only weak but also overlaps spectrally with ester group vibrations of triacylglycerols. Given that triacylglycerols are ubiquitous in lipid droplets, the 1740 cm^{-1} marker band cannot be readily used as a unique probe for cholesteryl esters. Similarly, in the CH stretching range, the spectral signatures of free cholesterol are insufficiently different from esterified cholesterol to unambiguously discriminate subpopulations of lipid droplets with markedly different levels of esterification. The D38-cholesterol probe, on the other hand, exhibits a unique and characteristic bandshape in the CH stretching range, which enabled the identification of lipid droplet heterogeneity in terms of cholesterol esterification by using hyperspectral SRS imaging.

The non-uniform distribution of lipid droplet associated proteins between individual droplets is well appreciated[269]. Instead, the plausible heterogeneity in the distribution of the stored lipids has so far received little attention. This has largely been due to the lack of reliable imaging methods, with SRS imaging of D38-cholesterol now providing a novel approach. The accumulation of cholesteryl esters in lipid droplets is thought to act as a buffering mechanism to reduce the toxicity of excess free cholesterol in cellular membranes[270]. Here, we observed in addition to cholesteryl esters, free cholesterol deposition in a subset of lipid droplets. It is conceivable that this acts as an additional cholesterol detoxicifation mechanism, for instance, during atherogenesis when macrophages are challenged with large amounts of cholesterol.

We also report that cells specialized in steroid hormone production from cholesterol store triacylglycerols and cholesteryl esters in different lipid droplets. Whether such lipid sorting occurs in other cell types should be addressed in future studies. Overall, lipid droplet heterogeneity is a highly interesting phenomenon and has important implications for the mechanisms of lipid droplet formation and utilization as well as the biophysical properties of lipid droplets. For instance, we have recently observed that cholesteryl ester enrichment of lipid droplets increases their ordering[262]. Furthermore, lipid droplet heterogeneity necessitates the segregation of regulatory proteins, as shown for lipid droplet coat proteins[260]. This concept should also apply for the enzymes involved in neutral lipid metabolism.

7.2.5 Concluding remarks

In this work, we have generated D38-cholesterol and shown its utility for SRS imaging studies of cholesterol storage in cells. The main advancements of this work are as follows: 1) a procedure for the efficient and affordable production of D38-cholesterol; 2) demonstration of the cellular uptake and processing of D38-cholesterol with efficiencies that are similar to those of natural cholesterol; 3) the use of hyperspectral SRS to visualize D38-cholesterol while also providing insight into lipid metabolism through bandshape analysis in the CH-stretching range; and 4) the application of D38-cholesterol as a probe for heterogeneity in cholesterol storage among the pool of lipid droplets. We expect that the availability of D38-cholesterol will lead to new discoveries of cholesterol movement and distribution in cells, as exemplified here for the case of lipid droplet heterogeneity.

Deuterated low-density lipoprotein particles: next step

A sensible next step includes the examination of cholesterol distribution upon physiological administration. The present study forces cholesterol uptake by mediated methyl-β-cyclodextrin administration. A physiologically relevant rout in the the cellular uptake of cholesterol via LDL receptor-mediated endocytosis, as described in chapter 1. Cholesterol travels in the blood stream packed in low-density lipoproteins (LDL) that the cells uptake through the LDL receptor[15] . Imaging synthesized deuterated LDL, with D38-cholesterol on them, with hyperspectral SRS, or simply tuned to the 2120 cm^{-1} Raman mode, would provide visual information of the intracellular cholesterol trafficking and compartmentalization pathways.

Reconstruction of low-density lipoproteins has been successfully achieved for decades[271–273], usually to incorporate specific or labeled cholestryl esters in order to track their performance with biochemical assays. Theoretically, reconstruction with deuterated cholesterol should be analogous to those methods and would permit direct visualization of the cholesterol pathways.

A tentative protocol to label LDL with D38-cholesterol has been adapted from previous successful strategies to incorporate other labeled cholesteryl esters[271,274], and is depicted in figure 7.11. Free cholesterol however is present in very small concentration in the LDL particles, which contain high quantities of esterified cholesterol. Therefore, esterifying D38-cholesterol first, and then incorporating it into the LDL particles seems as a better strategy

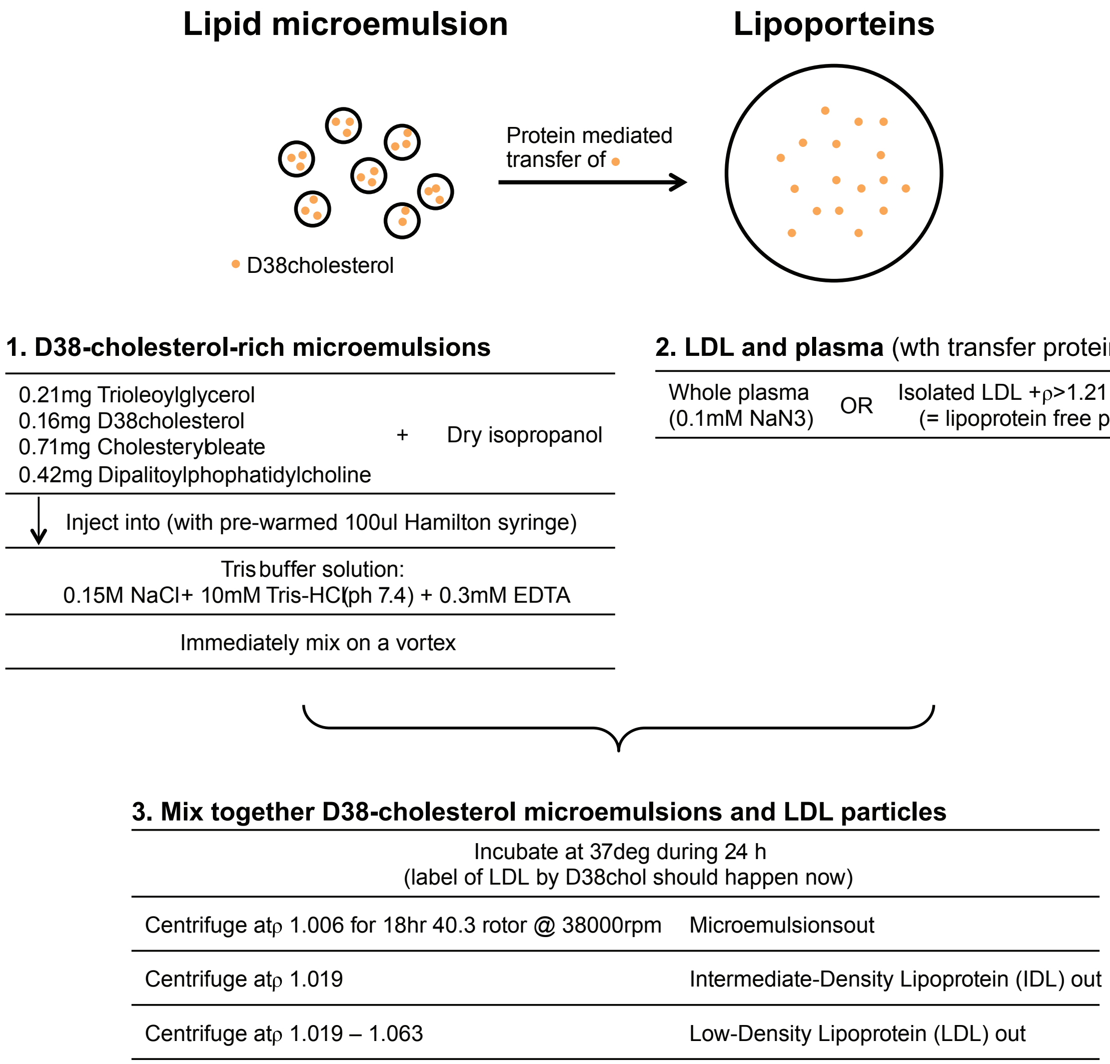

Figure 7.11: Schematic protocol to synthesize deuterated low-density lipoproteins (d-LDL) with D38-cholesterol. Adapted from[271,274].

if we aim for detectable SRS signals.

The first step consists on creating D38-cholesterol microemulsions. In parallel, the second step required the preparation of the LDL particles, which can be obtained from plasma. Whole plasma can be used as well, which might increase transfer efficiency, due to the presence of proteins that mediate the process. Otherwise, the LDL particles can be isolated and used in a lipoprotein free-plasma version. Finally, the microemulsions and the LDL particles are mixed together via incubation to let the transfer take place. A series of centrifugation steps would extract the labeled LDL particles with D38-cholesterol from the mixture debris.

Our first attempts failed to produce labeled LDL particles, as no dueterated cholesterol signal was found when the mixture was examined with Raman spectroscopy. Fine-tuning the parameters, and probably esterifying the D38-cholesterol, are required for a successful production of d-LDL, before imaging experiments take place.

Chapter 8

Conclusion

Visualizing the omnipresent lipids

Lipids are among the biomolecular components that enable life. They provide cellular structural support, energy, and hormonal signaling. Lipid metabolism is tightly regulated to ensure proper body function. Disruption of lipid homeostasis may result in life-threatening disease. Tools that enable in situ lipid visualization may provide valuable information about the altered elements of the physiological pathways.

Visualizing lipid metabolism is however a challenging task. Traditional biochemical assays provide quantitative information on lipid cellular composition at the expense of destroying the sample. Fluorescence microscopy enables the detection of general lipid classes and the tracking of certain lipid-related properties, such as membrane fluidity. But the lack of lipid-specific fluorophores and the disruption of the cellular integrity by some of the probes difficult a detailed analysis.

Label-free nonlinear optical microscopy techniques provide quantitative imaging with minimal sample perturbation. Among them, coherent Raman scattering (CRS) microspectroscopy enables lipid visualization in its natural environment, by probing the molecular vibrations of the sample. CRS microspectroscopy offers diffraction limited chemical maps with depth sectioning capabilities, and videorate detection. Such properties allow for in situ, three-dimensional, dynamic analysis that can be used alone or in combination with other nonlinear optical microscopy techniques, confocal fluorescence, or posterior biochemical assays.

Specific lipid Raman signatures

CRS chemical specificity derives from the Raman resonances of the molecules. Lipids are composed of carbon and hydrogen covalent bonds arranged in a finite number of motifs that generate strong vibrational signals, in particular when found at high concentrations, such as in lipid droplets. Different lipids exhibit different Raman spectra, offering a means of label-free identification. However, the cellular environment contains complex mixtures of several components that are probed together with a diffraction limited focal spot. Nonetheless, prominent lipids stand out and mixtures can be disentangled to a certain degree.

Some compilations of Raman spectra of specific components have been made available. Such compilations provide guidance to identify different components one encounters on the samples, but the lack of standard acquisition protocols prevent a reliable interpretation. In the case of lipids, Raman spectra in the literature are sparse and cumbersome to analyze in detail. To contribute to amend this situation, we started an online Raman spectra library of lipids, with a well-defined acquisition protocol, and with the capability of zooming in and out along the spectra to analyze its details. This is currently limited to a handful of lipids, but it allows expansion by other contributors. I believe this can be a good tool for newcomers to the Raman technique, as well as for specialist who need rapid references.

Hyperspectral CRS imaging, in particular hyperspectral stimulated Raman scattering imaging, reconstructs the Raman spectrum of samples by acquiring images at consecutive vibrational frequencies. The resulting big datasets contain spatial resolution that provide morphological cues of the sample, and chemical information that describes its composition. Multivariate analysis facilitates the extraction of meaningful information form these datasets, and new approaches implement machine learning methods that automate the analysis and retrieve statistical descriptions difficult to attain otherwise.

Coherent Raman scattering imaging was applied in this thesis to investigate the role of lipids in a variety of biological systems.

Meibum secretions characterized by multivariate analysis of hyperspectral SRS

Dry eye disease affects millions of elderly citizens and may result in vision loss. The causes of dry eye are related to the tear film lipid layer, that protects the cornea from evaporation, but the mechanisms that alter the teat film lipid layer remain unknown. As the major source of lipid on the tear film, Meibomian glands are at the center of interest. These glands in the upper and lower eyelids produce the lipids secreted to the eye upon blinking. Alterations in its lipid composition have previously been related to Meibomian gland dysfunction. In particular, it has been hypothesized that the protein content increases in the meibum secretions of unhealthy glands, and potentially contributes to the progression of dry eye disease. Stimulated Raman scattering microscopy imaging of meibum secretions from healthy subjects and dry eye diseases patients of varying severity were acquired to describe their biochemical composition. Due to the large dataset obtained in this experiment, imaging over a hundred samples, the analysis greatly benefited from a tailored multivariate analysis and machine learning based classification system. With the robust data analysis infrastructure designed specifically for this project, we expect to draw correlations with the clinical parameters that aid an objective diagnosis of dry eye disease, or even spurs treatment to alleviate it.

Lipid droplets as a target for exploring lipid metabolism

Lipid droplets are central in lipid metabolism. They act as reservoirs of cellular energy and building blocks to use upon demand. The liver in a major organ in lipid homeostasis, so much so, that it constitutes the starting and ending points of the body-lipid transport system. With the surge of extraterrestrial adventures, the effects of microgravity and spatial radiation on human health became a topic of interest. Bone density loss and muscle atrophy have already been characterized in spaceflight travels. Lipid metabolism however remains mysterious. A study performed on livers of mice aboard a spaceflight mission concluded that lipid metabolism may as well be altered. We analyzed the lipid droplet properties of the livers of spaceflight mice and those of control mice on Earth. Not only we found an increased lipid droplet size of the spaceflight mice, but also a loss of retinol that was related to the activation of hepatic stellate cells in the liver and to the upregulation of metabolic pathways that may lead to nonalcoholic fatty liver disease, which may have dramatic health consequences. This study included analysis from multiple biochemical assays in combination with CRS microscopy, Raman spectroscopy, and other imaging techniques, illustrating the power of synergistic multimodal analysis, and the potential for nonlinear optical microscopy for visualizing effects of anomalous expression of metabolic pathways.

CRS combined with FLIM for label-free metabolic markers

Macrophages are cells of the immune system present in inflammatory processes. Atherosclerosis is a prevalent chronic inflammatory process that results in the build-up of lipid-rich plaque within the arterial wall. Macrophages scavenge the lipid present in plaque to mitigate the lesion, but in some occasions they become foam cells that contribute to atheroprogression. Combining CARS microscopy and machine learning segmentation algorithms, we quantified the lipid storage capabilities of macrophages with opposing phenotypical traits. We found that, according to popular belief, proinflammatory macrophages rapidly become foam cells upon exposition to lipid-rich media, contrarily to prohealing macrophages. Despite this general trend, we encountered a fraction of prohealing macrophages that were not resistant to foam cell formation, which was a controversial observation also made by other groups.

Motivated by the lack of tools to assess the phenotype of macrophages at any give time, we implemented fluorescence lifetime imaging microscopy (FLIM) on these samples. Prohealing and proinflammatory macrophages differ in their glycolytic state, and this is reflected in the FLIM phasors, that identify different overall cellular lifetimes for each group, providing a label-free marker for probing cellular metabolic state in living cells. FLIM was also used to probe products of lipid oxidation without labels in adipose white tissue and stressed cells. A thorough characterization of these markers under different scenarios could lead to the standardization of their use for fundamental research and in vivo applications.

Label-free and minimally perturbing markers for cholesterol

Cholesterol is a particularly interesting lipid. Its altered homeostasis has a major impact in pathological disorders, including atherosclerosis. Methods to specifically detect cholesterol in living cells are scarce. We have observed a timid but robust Raman feature in lipid droplets of cells with upregulated cholesterol pathways, missing in the control counterparts. Its presence was found in the Raman spectra of lipid droplets from hepatitis C virus infected cells, and in some specific strains of retinal pigment epithelial cells with age-related macular degeneration diseased. Once again, biochemical assays were preformed in parallel and support the findings.

Despite cholesterol has a distinct Raman peak, it is too weak to efficiently target it with CRS microscopy. In need for stronger cholesterol markers, a highly deuterated cholesterol analog (D38-cholesterol) was synthesized by our collaborators, and we used it to track sterol compartmentalization in adrenal cells. Imaging in the deuterated stretching window of the Raman spectra, which is devoid of endogenous cellular signals, in combination with the CH stretching band, to detect triglycerides and other naturally occurring lipids, we demonstrated heterogeneous subpopulations of lipid droplet within the same cell. We expect that the availability of D38-cholesterol will lead to new discoveries of cholesterol movement and distribution in cells.

Biomedicine benefits from biophotonics developments

Overall this contribution illustrates the potential of label-free nonlinear optical microscopy techniques for unveiling complex physiological processes by direct visualization of the main elements in play, focused here on the omnipresent lipids. Advances on instrumentation and image processing strategies may permit a wide implementation of coherent Raman scattering microspectroscopy as one standard additional tool to investigate and quantify fundamental biology. Its combination with other linear and nonlinear microscopy techniques is poised to reveal complex dynamics of interactions among different classes of biomolecules. Nonlinear optical microscopy techniques are also translated to clinical settings. More successful implementations will rise from fundamental understanding of the underlying biological processes, the origin of the proposed label-free marker signals (and more to come), and new technical developments.

The advance of biophotonic sciences and engineering is an exciting pathway with direct repercussion in the advance of biomedicine. Optical microscopy is the gentlest way to observe biology as it unveils in front of our eyes, and I can't wait to see what we will accomplish next.

Bibliography

[1] Igor A Butovich. The Meibomian puzzle: combining pieces together. *Progress in Retinal and Eye Research*, 28(6):483–498, November 2009.

[2] E Fahy. A comprehensive classification system for lipids. *The Journal of Lipid Research*, 46(5):839–862, February 2005.

[3] Rossana C N Melo, Heloisa D'Ávila, Patricia T Bozza, and Peter F Weller. *Methods in Molecular Biology*, volume 689 of *Methods in Molecular Biology1064-37451940-6029*. Humana Press, Totowa, NJ, September 2010.

[4] A S Greenberg, J J Egan, S A Wek, N B Garty, E J Blanchette-Mackie, and C Londos. Perilipin, a major hormonally regulated adipocyte-specific phosphoprotein associated with the periphery of lipid storage droplets. *The Journal of biological chemistry*, 266 (17):11341–11346, June 1991.

[5] Kelly V Ruggles, Aaron Turkish, and Stephen L Sturley. Making, Baking, and Breaking: the Synthesis, Storage, and Hydrolysis of Neutral Lipids. *Annual Review of Nutrition*, 33(1):413–451, July 2013.

[6] Sally Martin and Robert G Parton. Lipid droplets: a unified view of a dynamic organelle. *Nature Reviews Molecular Cell Biology*, 7(5):373–378, March 2006.

[7] Michael A Welte. Proteins under new management: lipid droplets deliver. *Trends in Cell Biology*, 17(8):363–369, August 2007.

[8] Yusuke Miyanari, Kimie Atsuzawa, Nobuteru Usuda, Koichi Watashi, Takayuki Hishiki, Margarita Zayas, Ralf Bartenschlager, Takaji Wakita, Makoto Hijikata, and Kunitada Shimotohno. The lipid droplet is an important organelle for hepatitis C virus production. *Nature Cell Biology*, 9(9):1089–1097, August 2007.

[9] E Herker and M Ott. Unique ties between hepatitis C virus replication and intracellular lipids. *Trends in Endocrinology & Metabolism*, 2011.

[10] Yuki Ohsaki, Jinglei Cheng, Michitaka Suzuki, Akikazu Fujita, and Toyoshi Fujimoto. Lipid droplets are arrested in the ER membrane by tight binding of lipidated apolipoprotein B-100. *Journal of Cell Science*, 121(Pt 14):2415–2422, July 2008.

[11] A R Saltiel and C R Kahn. Insulin signalling and the regulation of glucose and lipid metabolism : Article : Nature. *Nature*, 2001.

[12] Christy A Olson, Nancy A Hamilton, and Virend K Somers. Percentage of REM sleep is associated with overnight change in leptin. *Journal of sleep research*, February 2016.

[13] R E Olson. Discovery of the lipoproteins, their role in fat transport and their significance as risk factors. *The Journal of nutrition*, 128(2 Suppl):439S–443S, February 1998.

[14] Chih-Hao Lee, Peter Olson, and Ronald M Evans. Minireview: Lipid Metabolism, Metabolic Diseases, and Peroxisome Proliferator-Activated Receptors. *Endocrinology*, 2003.

[15] Elina Ikonen. Cellular cholesterol trafficking and compartmentalization. *Nature Reviews Molecular Cell Biology*, 9(2):125–138, February 2008.

[16] K Simons. How Cells Handle Cholesterol. *Science*, 290(5497):1721–1726, December 2000.

[17] Jeffrey D Browning and Jay D Horton. Molecular mediators of hepatic steatosis and liver injury. *Journal of Clinical Investigation*, 114(2):147–152, July 2004.

[18] Christopher A Wassif, Cheryl Maslen, Stivelia Kachilele-Linjewile, Don Lin, Leesa M Linck, William E Connor, Robert D Steiner, and Forbes D Porter. Mutations in the human sterol delta7-reductase gene at 11q12-13 cause Smith-Lemli-Opitz syndrome. *American journal of human genetics*, 63(1):55, 1998.

[19] Allison B Reiss, Keith A Siller, Mohammad M Rahman, Edwin S L Chan, Jorge Ghiso, and Mony J de Leon. Cholesterol in neurologic disorders of the elderly: stroke and Alzheimer's disease. *Neurobiology of Aging*, 25(8):977–989, September 2004.

[20] Zhu Chen, Marina Ichetovkin, Marc Kurtz, Emanuel Zycband, Douglas Kawka, John Woods, Xuanmin He, Andrew S Plump, and Eric Hailman. Cholesterol in human atherosclerotic plaque is a marker for underlying disease state and plaque vulnerability. *Lipids in health and disease*, 9:61, 2010.

[21] Ala Alwan. Global status report on noncommunicable diseases 2010. 2011.

[22] Frederick R Maxfield and Ira Tabas. Role of cholesterol and lipid organization in disease. *Nature Cell Biology*, 438(7068):612–621, December 2005.

[23] Julia C Stokes Cecil E Kimbrough Kenneth L Burdon. Studies of the Common Aerobic Spore-forming Bacilli: I. Staining for Fat with Sudan Black B-safranin. *Journal of Bacteriology*, 43(6):717, June 1942.

[24] K D Kimura. daf-2, an Insulin Receptor-Like Gene That Regulates Longevity and Diapause in Caenorhabditis elegans. *Science*, 277(5328):942–946, August 1997.

[25] H Y Mak. Lipid droplets as fat storage organelles in Caenorhabditis elegans: Thematic Review Series: Lipid Droplet Synthesis and Metabolism: from Yeast to Man. *The Journal of Lipid Research*, 53(1):28–33, December 2011.

[26] René Koopman, Gert Schaart, and Matthijs K Hesselink. Optimisation of oil red O staining permits combination with immunofluorescence and automated quantification of lipids. *Histochemistry and Cell Biology*, 116(1):63–68, 2001.

[27] Suowen Xu, Yan Huang, Yu Xie, Tian Lan, Kang Le, Jianwen Chen, Shaorui Chen, Si Gao, Xiangzhen Xu, Xiaoyan Shen, Heqing Huang, and Peiqing Liu. Evaluation of foam cell formation in cultured macrophages: an improved method with Oil Red O staining and DiI-oxLDL uptake. *Cytotechnology*, 62(5):473–481, November 2010.

[28] P Greenspan, E P Mayer, and S D Fowler. Nile red: a selective fluorescent stain for intracellular lipid droplets. *The Journal of cell biology*, 100(3):965–973, March 1985.

[29] E J O'Rourke, A A Soukas, C E Carr, and G Ruvkun. C. elegans Major Fats Are Stored in Vesicles Distinct from Lysosome-Related Organelles. *Cell Metabolism*, 2009.

[30] Kelvin Yen, Thuc T Le, Ankita Bansal, Sri Devi Narasimhan, Ji-Xin Cheng, and Heidi A Tissenbaum. A comparative study of fat storage quantitation in nematode Caenorhabditis elegans using label and label-free methods. *PLoS ONE*, 5(9), 2010.

[31] Jean E Schaffer and Harvey F Lodish. Expression cloning and characterization of a novel adipocyte long chain fatty acid transport protein. *Cell*, 79(3):427–436, November 1994.

[32] Frederik W Lund, Michael A Lomholt, Lukasz M Solanko, Robert Bittman, and Daniel W stner. Two-photon time-lapse microscopy of BODIPY-cholesterol reveals anomalous sterol diffusion in chinese hamster ovary cells. *BMC Biophysics*, 5(1):1–1, October 2012.

[33] Maarit Hölttä Vuori, Riikka-Liisa Uronen, Jarmila Repakova, Emppu Salonen, Ilpo Vattulainen, Pertti Panula, Zaiguo Li, Robert Bittman, and Elina Ikonen. BODIPY-Cholesterol: A New Tool to Visualize Sterol Trafficking in Living Cells and Organisms. *Traffic*, 9(11):1839–1849, November 2008.

[34] Maarit Hölttä Vuori, Veijo T Salo, Yuki Ohsaki, Maximiliano L Suster, and Elina Ikonen. Alleviation of seipinopathy-related ER stress by triglyceride storage. 2013.

[35] Maarit Hölttä Vuori, Veijo T V Salo, Lena Nyberg, Christian Brackmann, Annika Enejder, Pertti Panula, and Elina Ikonen. Zebrafish: gaining popularity in lipid research. *Biochemical Journal*, 429(2):235–242, June 2010.

[36] Shaobing O Zhang, Rhonda Trimble, Fengli Guo, and Ho Yi Mak. Lipid droplets as ubiquitous fat storage organelles in C. elegans. *BMC cell biology*, 11:96, 2010.

[37] Vitali Matyash, Christian Geier, Annemarie Henske, Sushmita Mukherjee, David Hirsh, Christoph Thiele, Barth Grant, Frederick R Maxfield, and Teymuras V Kurzchalia. Distribution and Transport of Cholesterol inCaenorhabditis elegans. *Molecular biology of of the cell*, 2001.

[38] Friedhelm Schroeder, Judith K Woodford, Juraj Kavecansky, W Gibson Wood, and Clinton Joiner. Cholesterol domains in biological membranes. *Molecular Membrane Biology*, 12(1):113–119, July 2009.

[39] Frederick R Maxfield and Daniel Wüstner. Intracellular cholesterol transport. *Journal of Clinical Investigation*, 110(7):891–898, October 2002.

[40] Daniel Wüstner, Mousumi Mondal, Ira Tabas, and Frederick R Maxfield. Direct Observation of Rapid Internalization and Intracellular Transport of Sterol by Macrophage Foam Cells. *Traffic*, 6(5):396–412, March 2005.

[41] Frederick R Maxfield and Daniel Wüstner. *Analysis of Cholesterol Trafficking with Fluorescent Probes*, volume 108 of *Methods in Cell Biology.* Elsevier Inc., October 2001.

[42] K Gaus. Visualizing lipid structure and raft domains in living cells with two-photon microscopy. *Proceedings of the National Academy of Sciences of the United States of America*, 100(26):15554–15559, December 2003.

[43] Ottavia Golfetto, Elizabeth Hinde, and Enrico Gratton. Laurdan Fluorescence Lifetime Discriminates Cholesterol Content from Changes in Fluidity in Living Cell Membranes. *Biophysical Journal*, 104(6):1238–1247, March 2013.

[44] A M Grant, P K Hanson, L Malone, and J Wylie Nichols. NBD-Labeled Phosphatidylcholine and Phosphatidylethanolamine are Internalized by Transbilayer Transport across the Yeast Plasma Membrane - Grant - 2008 - Traffic - Wiley Online Library. *Traffic*, 2001.

[45] Keita Un, Kumiko Sakai-Kato, Yuki Oshima, Toru Kawanishi, and Haruhiro Okuda. Intracellular trafficking mechanism, from intracellular uptake to extracellular efflux, for phospholipid/cholesterol liposomes. *Biomaterials*, 33(32):8131–8141, November 2012.

[46] T Baumgart, A T Hammond, P Sengupta, S T Hess, D A Holowka, B A Baird, and W W Webb. Large-scale fluid/fluid phase separation of proteins and lipids in giant plasma membrane vesicles. *Proceedings of the National Academy of Sciences of the United States of America*, 104(9):3165–3170, February 2007.

[47] Prabar K Ghosh, Amit Vasanji, Gurunathan Murugesan, Steven J Eppell, Linda M Graham, and Paul L Fox. Membrane microviscosity regulates endothelial cell motility. *Nature Cell Biology*, 4(11):894–900, October 2002.

[48] Rémi Palmantier, Margaret D George, Steven K Akiyama, Frances M Wolber, Kenneth Olden, and John D Roberts. cis-Polyunsaturated Fatty Acids Stimulate $\beta 1$ Integrin-mediated Adhesion ofHuman Breast Carcinoma Cells to Type IV Collagen by Activating ProteinKinases C-ε and -μ. *Cancer Research*, 2001.

[49] Alba Alfonso Garcia, Richa Mittal, Eun Seong Lee, and Eric O Potma. Biological imaging with coherent Raman scattering microscopy: a tutorial. *Journal of Biomedical Optics*, 19(7):071407, July 2014.

[50] Satoshi Fukumoto and Toyoshi Fujimoto. Deformation of lipid droplets in fixed samples. *Histochemistry and Cell Biology*, 118(5):423–428, November 2002.

[51] Eric O Potma, Wim P de Boeij, Peter J M van Haastert, and Douwe A Wiersma. Real-time visualization of intracellular hydrodynamics in single living cells. *Proceedings of the National Academy of Science*, 2001.

[52] Eric O Potma and X Sunney Xie. Direct visualization of lipid phase segregation in single lipid bilayers with coherent anti-Stokes Raman scattering microscopy. *Chemphyschem : a European journal of chemical physics and physical chemistry*, 6(1): 77–79, January 2005.

[53] L Li, H Wang, and J X Cheng. Quantitative Coherent Anti-Stokes Raman Scattering Imaging of Lipid Distribution in Coexisting Domains. *Biophysical Journal*, 2005.

[54] Ondrej Burkacky, Andreas Zumbusch, Christian Brackmann, and Annika Enejder. Dual-pump coherent anti-Stokes-Raman scattering microscopy. *Optics letters*, 31(24): 3656–3658, 2006.

[55] Brian G Saar, L Rodrigo Contreras-Rojas, X Sunney Xie, and Richard H Guy. Imaging Drug Delivery to Skin with Stimulated Raman Scattering Microscopy. *Molecular pharmaceutics*, 2011.

[56] Lu Wei, Yong Yu, Yihui Shen, Meng C Wang, and Wei Min. Vibrational imaging of newly synthesized proteins in live cells by stimulated Raman scattering microscopy. *Proceedings of the National Academy of Sciences of the United States of America*, 110 (28):11226–11231, July 2013.

[57] Hiroyuki Yamakoshi, Kosuke Dodo, Masaya Okada, Jun Ando, Almar Palonpon, Katsumasa Fujita, Satoshi Kawata, and Mikiko Sodeoka. Imaging of EdU, an Alkyne-Tagged Cell Proliferation Probe, by Raman Microscopy. *Journal of the American Chemical Society*, 2011.

[58] Hiroyuki Yamakoshi, Kosuke Dodo, Almar Palonpon, Jun Ando, Katsumasa Fujita, Satoshi Kawata, and Mikiko Sodeoka. Alkyne-Tag Raman Imaging for Visualization of Mobile Small Molecules in Live Cells. *Journal of the American Chemical Society*, 2012.

[59] Lu Wei, Fanghao Hu, Yihui Shen, Zhixing Chen, Yong Yu, Chih-Chun Lin, Meng C Wang, and Wei Min. Live-cell imaging of alkyne-tagged small biomolecules by stimulated Raman scattering. *Nature methods*, 11(4):410–412, March 2014.

[60] Zhixing Chen, Daniel W Paley, Lu Wei, Andrew L Weisman, Richard A Friesner, Colin Nuckolls, and Wei Min. Multicolor Live-Cell Chemical Imaging by Isotopically Edited Alkyne Vibrational Palette. *Journal of the American Chemical Society*, 2014.

[61] J J Duindam, G J Puppels, C Otto, and J Greve. Imaging with Extrinsic Raman Labels. *Applied Spectroscopy*, 50(5):545–551, 1996.

[62] Aaron M Streets, Ang Li, Tao Chen, and Yanyi Huang. Imaging without Fluorescence: Nonlinear Optical Microscopy for Quantitative Cellular Imaging. *Analytical chemistry*, 86(17):8506–8513, September 2014.

[63] C V Raman and K S Krishnan. A new type of secondary radiation. *Nature*, 121: 501–502, March 1928.

[64] Jeffrey L Suhalim, John C Boik, Bruce J Tromberg, and Eric O Potma. The need for speed. *Journal of Biophotonics*, February 2012.

[65] M T Cicerone, K A Aamer, and Y J Lee. Maximum entropy and time-domain Kramers–Kronig phase retrieval approaches are functionally equivalent for CARS microspectroscopy - Cicerone - 2012 - Journal of Raman Spectroscopy - Wiley Online Library. *Journal of Raman . . .*, 2012.

[66] Wei Min, Christian W Freudiger, Sijia Lu, and X Sunney Xie. Coherent Nonlinear Optical Imaging: Beyond Fluorescence Microscopy. *Annual Review of Physical Chemistry*, 62(1):507–530, May 2011.

[67] Andreas Volkmer. Vibrational imaging and microspectroscopies based on coherent anti-Stokes Raman scattering microscopy. *Journal of Physics D: Applied Physics*, 38 (5):R59–R81, February 2005.

[68] Christian W Freudiger, Wei Min, Gary R Holtom, Bingwei Xu, Marcos Dantus, and X Sunney Xie. Highly specific label-free molecular imaging withspectrally tailored excitation-stimulated Ramanscattering (STE-SRS) microscopy. pages 1–7, January 2011.

[69] Dan Fu, Fa-Ke Lu, Xu Zhang, Christian Freudiger, Douglas R Pernik, Gary Holtom, and Xiaoliang Sunney Xie. Quantitative Chemical Imaging with Multiplex Stimulated Raman Scattering Microscopy. *Journal of the American Chemical Society*, 134:3623–3626, 2012.

[70] E R Andresen, P Berto, and H Rigneault. Stimulated Raman scattering microscopy by spectral focusing and fiber-generated soliton as Stokes pulse. *Optics letters*, 2011.

[71] H T Beier, G D Noojin, and B A Rockwell. Stimulated Raman scattering using a single femtosecond oscillator with flexibility for imaging and spectral applications. *Optics express*, 2011.

[72] Dan Fu, Gary Holtom, Christian Freudiger, Xu Zhang, and Xiaoliang Sunney Xie. Hyperspectral Imaging with Stimulated Raman Scattering by Chirped Femtosecond Lasers. *The Journal of Physical Chemistry B*, 117(16):4634–4640, April 2013.

[73] Thomas Hellerer, Annika M K Enejder, and Andreas Zumbusch. Spectral focusing: High spectral resolution spectroscopy with broad-bandwidth laser pulses. *Applied physics letters*, 85(1):25, 2004.

[74] Chao-Yu Chung and Eric O Potma. Biomolecular Imaging with Coherent Nonlinear Vibrational Microscopy. *Annual Review of Physical Chemistry*, 64(1):77–99, April 2013.

[75] Yong Yu, Prasanna V Ramachandran, and Meng C Wang. Biochimica et Biophysica Acta. *BBA - Molecular and Cell Biology of Lipids*, pages 1–10, March 2014.

[76] T T Le, S Yue, and J X Cheng. Shedding new light on lipid biology with coherent anti-Stokes Raman scattering microscopy. *The Journal of Lipid Research*, 51(11): 3091–3102, October 2010.

[77] Hilde A Rinia, Koert N J Burger, Mischa Bonn, and Michiel Müller. Quantitative Label-Free Imaging of Lipid Composition and Packing of Individual Cellular Lipid Droplets Using Multiplex CARS Microscopy . *Biophysical Journal*, 95(10):4908–4914, November 2008.

[78] C W Freudiger, W Min, B G Saar, S Lu, G R Holtom, C He, J C Tsai, J X Kang, and X S Xie. Label-Free Biomedical Imaging with High Sensitivity by Stimulated Raman Scattering Microscopy. *Science*, 322(5909):1857–1861, December 2008.

[79] Shuhua Yue, Juan Manuel Cárdenas-Mora, Lesley S Chaboub, Sophie A Lelièvre, and Ji-Xin Cheng. Label-Free Analysis of Breast Tissue Polarity by Raman Imaging of Lipid Phase. *Biophysical Journal*, 102(5):1215–1223, March 2012.

[80] Dan Fu, Yong Yu, Andrew Folick, Erin Currie, Robert V Farese, Jr., Tsung-Huang Tsai, Xiaoliang Sunney Xie, and Meng C Wang. In VivoMetabolic Fingerprinting of Neutral Lipids with Hyperspectral Stimulated Raman Scattering Microscopy. *Journal of the American Chemical Society*, page 140609160337008, June 2014.

[81] Joseph R Lakowicz. *Principles of Fluorescence Spectroscopy.* Springer Science & Business Media, December 2007.

[82] C A Sacchi, O Svelto, and G Prenna. Pulsed tunable lasers in cytofluorometry - Springer. *The Histochemical Journal*, 1974.

[83] S M Fernandez and R D Berlin. Cell surface distribution of lectin receptors determined by resonance energy transfer. *Nature*, 264(5585):411–415, December 1976.

[84] J Alsins, S Claesson, and H Elmgren. A simple instrumentation for measuring fluorescence lifetimes of probe molecules in small systems. *CHEMICA SCRIPTA*, 20(4): 183–187, 1982.

[85] Takaaki Minami, Masaki Kawahigashi, Yasuhide Sakai, Katsuyuki Shimamoto, and Satoshi Hirayama. Fluorescence lifetime measurements under a microscope by the time-correlated single-photon counting technique. *Journal of Luminescence*, 35(5): 247–253, August 1986.

[86] Akihiro Kusurni, Akihiko Tsuji, Masayuki Murata, Yasushi Sako, Akiyasu C Yoshizawa, Tsuyoshi Hayakawa, and Shun-ichi Ohnishi. Development Of A Time-Resolved Microfluorimeter With A Synchroscan Streak Camera And Its Application To Studies Of Cell Membranes. In Joseph R Lakowicz, editor, *1988 Los Angeles Symposium–O-E/LASE '88*, pages 350–351. SPIE, June 1988.

[87] T Oida, Y Sako, and A Kusumi. Fluorescence lifetime imaging microscopy (flimscopy). Methodology development and application to studies of endosome fusion in single cells. *Biophysical Journal*, 64(3):676–685, March 1993.

[88] Robert M Clegg, Brett A Feddersen, Enrico Gratton, and Thomas M Jovin. Time-resolved imaging fluorescence microscopy. In Joseph R Lakowicz, editor, *OE/LASE '92*, pages 448–460. SPIE, April 1992.

[89] Theodorus W J Gadella, Jr., Thomas M Jovin, and Robert M Clegg. Fluorescence lifetime imaging microscopy (FLIM): Spatial resolution of microstructures on the nanosecond time scale. *Biophysical Chemistry*, 48(2):221–239, December 1993.

[90] J R Lakowicz, H Szmacinski, K Nowaczyk, and M L Johnson. Fluorescence lifetime imaging of free and protein-bound NADH. *Proceedings of the National Academy of Sciences*, 89(4):1271–1275, February 1992.

[91] M Y Berezin and S Achilefu. Fluorescence lifetime measurements and biological imaging. *Chemical reviews*, 2010.

[92] Michelle A Digman, Valeria R Caiolfa, Moreno Zamai, and Enrico Gratton. The phasor approach to fluorescence lifetime imaging analysis. *Biophysical Journal*, 94(2):L14–6, January 2008.

[93] Ryan A Colyer, Claudia Lee, and Enrico Gratton. A novel fluorescence lifetime imaging system that optimizes photon efficiency. *Microscopy Research and Technique*, 71(3): 201–213, 2008.

[94] Zachary D Stephens, Skylar Y Lee, Faraz Faghri, Roy H Campbell, Chengxiang Zhai, Miles J Efron, Ravishankar Iyer, Michael C Schatz, Saurabh Sinha, and Gene E Robinson. Big Data: Astronomical or Genomical? *PLoS Biology*, 13(7):e1002195, July 2015.

[95] P J Keller, A D Schmidt, J Wittbrodt, and E H K Stelzer. Reconstruction of Zebrafish Early Embryonic Development by Scanned Light Sheet Microscopy. *Science*, 322(5904):1065–1069, November 2008.

[96] B C Chen, W R Legant, K Wang, L Shao, D E Milkie, M W Davidson, C Janetopoulos, X S Wu, J A Hammer, Z Liu, B P English, Y Mimori-Kiyosue, D P Romero, A T Ritter, J Lippincott-Schwartz, L Fritz-Laylin, R D Mullins, D M Mitchell, J N Bembenek, A C Reymann, R Bohme, S W Grill, J T Wang, G Seydoux, U S Tulu, D P Kiehart, and E Betzig. Lattice light-sheet microscopy: Imaging molecules to embryos at high spatiotemporal resolution. *Science*, 346(6208):1257998–1257998, October 2014.

[97] Suliana Manley, Jennifer M Gillette, George H Patterson, Hari Shroff, Harald F Hess, Eric Betzig, and Jennifer Lippincott-Schwartz. High-density mapping of single-molecule trajectories with photoactivated localization microscopy. *Nature methods*, 5 (2):155–157, January 2008.

[98] Jennifer Lippincott-Schwartz and Suliana Manley. Putting super-resolution fluorescence microscopy to work. *Nature methods*, 6(1):21–23, January 2009.

[99] Bo Huang, Mark Bates, and Xiaowei Zhuang. Super-Resolution Fluorescence Microscopy. *Annual Review of Biochemistry*, 78(1):993–1016, June 2009.

[100] Claire Lifan Chen, Ata Mahjoubfar, Li-Chia Tai, Ian K Blaby, Allen Huang, Kayvan Reza Niazi, and Bahram Jalali. Deep Learning in Label-free Cell Classification. *Scientific Reports*, 6:21471, 2016.

[101] Mihaela Balu, Amaan Mazhar, Carole K Hayakawa, Richa Mittal, Tatiana B Krasieva, Karsten König, Vasan Venugopalan, and Bruce J Tromberg. In vivo multiphoton NADH fluorescence reveals depth-dependent keratinocyte metabolism in human skin. *Biophysical Journal*, 104(1):258–267, January 2013.

[102] Josephine Y Fang, Shih-Jye Tan, Yi-Chen Wu, Zhi Yang, Ba X Hoang, and Bo Han. From competency to dormancy: a 3D model to study cancer cells and drug responsiveness. *Journal of translational medicine*, 14(1):38, 2016.

[103] M Pickl and C H Ries. Comparison of 3D and 2D tumor models reveals enhanced HER2 activation in 3D associated with an increased response to trastuzumab. *Oncogene*, 28 (3):461–468, November 2008.

[104] G Deka, W W Wu, and F J Kao. In vivo wound healing diagnosis with second harmonic and fluorescence lifetime imaging. *Journal of Biomedical Optics*, 18(6), 2013.

[105] James V Jester PhD, Brant R Ward PhD, Akira Takashima PhD, Joel Gatlin PhD, J Victor Garcia PhD, PhD H Dwight Caxanagh MD, and PhD W Matthew Petroll MD. Laboratory Science. *The Ocular Surface*, 2(1):10–20, December 2011.

[106] M Ji, D A Orringer, C W Freudiger, S Ramkissoon, X Liu, D Lau, A J Golby, I Norton, M Hayashi, N Y R Agar, G S Young, C Spino, S Santagata, S Camelo-Piragua, K L Ligon, O Sagher, and X S Xie. Rapid, Label-Free Detection of Brain Tumors with Stimulated Raman Scattering Microscopy. *Science Translational Medicine*, 5(201): 201ra119–201ra119, September 2013.

[107] R Mouras, P Bagnaninchi, and A Downes. Multimodal, label-free nonlinear optical imaging for applications in biology and biomedical science. *Journal of Raman Spectroscopy*, 44:1373–1378, 2013.

[108] Jonas Hagmar, Christian Brackmann, Tomas Gustavsson, and Annika Enejder. Image analysis in nonlinear microscopy. *Journal of the Optical Society of America. A, Optics, image science, and vision*, 25(9):2195–2206, September 2008.

[109] Christian Brackmann, Joakim Norbeck, Madeleine Åkeson, Daniel Bosch, Christer Larsson, Lena Gustafsson, and Annika Enejder. CARS microscopy of lipid stores in yeast: the impact of nutritional state and genetic background. *Journal of Raman Spectroscopy*, 40(7):748–756, July 2009.

[110] Nadine Vogler, Thomas Bocklitz, Melissa Mariani, Volker Deckert, Aneta Markova, Peter Schelkens, Petra Rösch, Denis Akimov, Benjamin Dietzek, and Jürgen Popp. Separation of CARS image contributions with a Gaussian mixture model. *Journal of the Optical Society of America A*, 27(6):1361–1371, 2010.

[111] Anna Medyukhina, Tobias Meyer, Michael Schmitt, Bernd F M Romeike, Benjamin Dietzek, and Jürgen Popp. Towards automated segmentation of cells and cell nuclei in nonlinear optical microscopy. *Journal of Biophotonics*, 5(11-12):878–888, July 2012.

[112] Wei-Wen Chen, Chen-Hao Chien, Chiung-Lin Wang, Huai-Hsien Wang, Yuh-Lin Wang, Shih-Torng Ding, Tzong-Shyuan Lee, and Ta-Chau Chang. Automated quantitative analysis of lipid accumulation and hydrolysis in living macrophages with label-free imaging. *Analytical and Bioanalytical Chemistry*, 405(26):8549–8559, August 2013.

[113] Xiaolin Nan, Eric O Potma, and X Sunney Xie. Nonperturbative Chemical Imaging of Organelle Transport in Living Cells with Coherent Anti-Stokes Raman Scattering Microscopy. *Biophysical Journal*, 91(2):728–735, July 2006.

[114] Marie Theres Hauser Antonio Heredia Notburga Gierlinger Batirtze Prats Mateu. Waterproofing in Arabidopsis: Following Phenolics and Lipids In situ by Confocal Raman Microscopy. *Frontiers in Chemistry*, 4, 2016.

[115] R S Lim, J L Suhalim, S Miyazaki-Anzai, M Miyazaki, M Levi, E O Potma, and B J Tromberg. Identification of cholesterol crystals in plaques of atherosclerotic mice using hyperspectral CARS imaging. *The Journal of Lipid Research*, 52(12):2177–2186, November 2011.

[116] Dan Fu and X Sunney Xie. Reliable Cell Segmentation Based on Spectral Phasor Analysis of Hyperspectral Stimulated Raman Scattering Imaging Data. *Analytical chemistry*, 86(9):4115–4119, May 2014.

[117] Sascha D Krauss, Dennis Petersen, Daniel Niedieker, Inka Fricke, Erik Freier, Samir F El-Mashtoly, Klaus Gerwert, and Axel Mosig. Colocalization of fluorescence and Raman microscopic images for the identification of subcellular compartments: a validation study. *The Analyst*, 140(7):2360–2368, April 2015.

[118] Samir F El-Mashtoly, Daniel Niedieker, Dennis Petersen, Sascha D Krauss, Erik Freier, Abdelouahid Maghnouj, Axel Mosig, Stephan Hahn, Carsten Kötting, and Klaus Gerwert. Automated identification of subcellular organelles by coherent anti-stokes Raman scattering. *Biophysical Journal*, 106(9):1910–1920, May 2014.

[119] J M P Nascimento and J M B Dias. Vertex component analysis: a fast algorithm to unmix hyperspectral data. *IEEE Transactions on Geoscience and Remote Sensing*, 43 (4):898–910.

[120] Milos Miljković, Tatyana Chernenko, Melissa J Romeo, Benjamin Bird, Christian Matthäus, and Max Diem. Label-free imaging of human cells: algorithms for image reconstruction of Raman hyperspectral datasets. *The Analyst*, 135(8):2002–2013, August 2010.

[121] L Breiman. Random forests. *Machine learning*, 2001.

[122] Kari B Green-Church, Igor Butovich, Mark Willcox, Douglas Borchman, Friedrich Paulsen, Stefano Barabino, and Ben J Glasgow. The International Workshop on Meibomian Gland Dysfunction: Report of the Subcommittee on Tear Film Lipids and Lipid–Protein Interactions in Health and Disease. *Investigative Opthalmology & Visual Science*, 52(4):1979, March 2011.

[123] Igor A Butovich. Experimental Eye Research. *Experimental Eye Research*, 117(c): 4–27, December 2013.

[124] Gary N Foulks. The Correlation Between the Tear Film Lipid Layer and Dry Eye Disease. *Survey of Ophthalmology*, 52(4):369–374, July 2007.

[125] N Nicolaides, J K Kaitaranta, T N Rawdah, J I Macy, F M Boswell, and R E Smith. Meibomian gland studies: comparison of steer and human lipids. *Investigative Opthalmology & Visual Science*, 20(4):522–536, April 1981.

[126] A McMahon, H Lu, and I A Butovich. The spectrophotometric sulfo-phospho-vanillin assessment of total lipids in human meibomian gland secretions. *Lipids*, 2013.

[127] I A Butovich. Cholesteryl esters as a depot for very long chain fatty acids in human meibum. *The Journal of Lipid Research*, 50(3):501–513, October 2008.

[128] Igor A Butovich. Fatty acid composition of cholesteryl esters of human meibomian gland secretions. *Steroids*, 75(10):726–733, October 2010.

[129] E Chabrol and R Charonnat. Une nouvelle reaction pour letude des lipides loleidemie. *Presse méd*, 45:1713, 1937.

[130] M A Lemp and G N Foulks. The definition and classification of dry eye disease. *The Ocular Surface*, 2007.

[131] Fabiana de Pinho Tavares, Raphael Stehling Fernandes, Taliana Freitas Bernardes, Adriana Alvim Bonfioli, and Eduardo Jorge Carneiro Soares. Dry Eye Disease. *Seminars in Ophthalmology*, 25(3):84–93, June 2010.

[132] Yusuke Oshima, Hidetoshi Sato, Ahmed Zaghloul, Gary N Foulks, Marta C Yappert, and Douglas Borchman. Characterization of Human Meibum Lipid using Raman Spectroscopy. *Current Eye Research*, 34(10):824–835, November 2009.

[133] Chia-Yu Lin, Jeffrey L Suhalim, Chyong Ly Nien, Miloš D Miljković, Max Diem, James V Jester, and Eric O Potma. Picosecond spectral coherent anti-Stokes Raman scattering imaging with principal component analysis of meibomian glands. *Journal of Biomedical Optics*, 16(2):021104, 2011.

[134] Jeffrey L Suhalim, Geraint J Parfitt, Yilu Xie, Cintia S De Pavia, Stephen C Pflugfelder, Tejas N Shah, Eric O Potma, Donald J Brown, and James V Jester. Effect of Desiccating Stress on Mouse Meibomian Gland Function. *The Ocular Surface*, 12 (1):59–68, January 2014.

[135] F P Baqai, D S Gridley, J M Slater, X Luo-Owen, L S Stodieck, V Ferguson, S K Chapes, and M J Pecaut. Effects of spaceflight on innate immune function and antioxidant gene expression. *Journal of Applied Physiology*, 106(6):1935–1942, May 2009.

[136] H W Lane, R J Gretebeck, and S M Smith. Nutrition, endocrinology, and body composition during space flight. *Nutrition Research*, 1998.

[137] J Li A J Spieker J Spatz R Ellman V L Ferguson T A Bateman G D Rosen M Bouxsein S B Rutkove M Sung. Spaceflight and hind limb unloading induce similar changes in electrical impedance characteristics of mouse gastrocnemius muscle. *Journal of musculoskeletal & neuronal interactions*, 13(4):405, December 2013.

[138] M V Narici and M D De Boer. Disuse of the musculo-skeletal system in space and on earth . *European journal of applied physiology*, 2011.

[139] T Lang, A LeBlanc, H Evans, and Y Lu. Cortical and Trabecular Bone Mineral Loss From the Spine and Hip in Long-Duration Spaceflight. *Journal of Bone and Mineral Research*, 2004.

[140] Matthew J Armstrong, Leon A Adams, Ali Canbay, and Wing Kin Syn. Extrahepatic complications of nonalcoholic fatty liver disease. *Hepatology*, 59(3):1174–1197, 2014.

[141] Gwo-Shing Sun Ph D, Janet C Tou Ph D, Kurt Liittschwager Ph D, Anna M Herrera B S, Esther L Hill Ph D, Beverly Girten Ph D, Debra Reiss-Bubenheim M S, and Marilyn Vasques M S. Evaluation of the nutrient-upgraded rodent food bar for rodent spaceflight experiments. *Nutrition*, 26(11-12):1163–1169, November 2010.

[142] Haruki Senoo. Structure and function of hepatic stellate cells. *Medical electron microscopy : official journal of the Clinical Electron Microscopy Society of Japan*, 37(1): 3–15, March 2004.

[143] Conor L Evans and X Sunney Xie. Coherent Anti-Stokes Raman Scattering Microscopy: Chemical Imaging for Biology and Medicine. *Annual Review of Analytical Chemistry*, 1(1):883–909, July 2008.

[144] Nelly Failloux, Isabelle Bonnet, Marie-Hélène Baron, and Eric Perrier. Quantitative analysis of vitamin A degradation by Raman spectroscopy. *Applied spectroscopy*, 57 (9):1117–1122, September 2003.

[145] Huawen Wu, Joanne V Volponi, Ann E Oliver, Atul N Parikh, Blake A Simmons, and Seema Singh. In vivo lipidomics using single-cell Raman spectroscopy. *Proceedings of the National Academy of Sciences of the United States of America*, 108(9):3809–3814, March 2011.

[146] Steven A Kliewer, Kazuhiko Umesono, Daniel J Noonan, Richard A Heyman, and Ronald M Evans. Convergence of 9-cis retinoic acid and peroxisome proliferator signalling pathways through heterodimer formation of their receptors. *Nature*, 358(6389): 771–774, August 1992.

[147] Maryam Rakhshandehroo, Bianca Knoch, Michael Müller, and Sander Kersten. Peroxisome Proliferator-Activated Receptor Alpha Target Genes. *PPAR Research*, 2010 (5):1–20, 2010.

[148] C K Glass and J L Witztum. Atherosclerosis: The Road Ahead Review. *Cell*, 2001.

[149] Norbert Leitinger. Oxidized phospholipids as modulators of inflammation in atherosclerosis. *Current opinion in lipidology*, 14(5):421–430, October 2003.

[150] Kristina Skålén, Maria Gustafsson, Ellen Knutsen Rydberg, Lillemor Mattsson Hultén, Olov Wiklund, Thomas L Innerarity, and Jan Borén. Subendothelial retention of atherogenic lipoproteins in early atherosclerosis. *Nature*, 417(6890):750–754, June 2002.

[151] C K Glass. The macrophage foam cell as a target for therapeutic intervention. *Nat Med*, 2002.

[152] Göran K Hansson. Inflammation, Atherosclerosis, and Coronary Artery Disease. *New England Journal of Medicine*, 352(16):1685–1695, April 2005.

[153] David M Mosser and Justin P Edwards. Exploring the full spectrum ofmacrophage activation. *Nature Publishing Group*, 8(12):958–969, December 2008.

[154] J W Pollard. Tumour-educated macrophages promote tumour progression and metastasis. *Nature Reviews Cancer*, 2004.

[155] Luke A J O'Neill Silvia Galván-Peña. Metabolic Reprograming in Macrophage Polarization. *Frontiers in Immunology*, 5, 2014.

[156] I M J Wolfs, M M P C Donners, and M P J de Winther. Differentiation factors and cytokines in the atherosclerotic plaque micro-environment as a trigger for macrophage polarisation. *Thrombosis and haemostasis*, 106(5):763–771, November 2011.

[157] James E McLaren, Daryn R Michael, Tim G Ashlin, and Dipak P Ramji. Cytokines, macrophage lipid metabolism and foam cells: Implications for cardiovascular disease therapy. *Progress in Lipid Research*, 50(4):331–347, October 2011.

[158] L L Stoll. Potential Role of Endotoxin as a Proinflammatory Mediator of Atherosclerosis. *Arteriosclerosis, Thrombosis, and Vascular Biology*, 24(12):2227–2236, December 2004.

[159] G Chinetti-Gbaguidi, M Baron, M A Bouhlel, J Vanhoutte, C Copin, Y Sebti, B Derudas, T Mayi, G Bories, A Tailleux, S Haulon, C Zawadzki, B Jude, and B Staels. Human Atherosclerotic Plaque Alternative Macrophages Display Low Cholesterol Handling but High Phagocytosis Because of Distinct Activities of the PPAR and LXR Pathways. *Circulation Research*, 108(8):985–995, April 2011.

[160] J Oh, A E Riek, S Weng, M Petty, D Kim, M Colonna, M Cella, and C Bernal-Mizrachi. Endoplasmic Reticulum Stress Controls M2 Macrophage Differentiation and Foam Cell Formation. *Journal of Biological Chemistry*, 287(15):11629–11641, April 2012.

[161] Anthony Rousselle, Fatimunnisa Qadri, Lisa Leukel, Rüstem Yilmaz, Jean-Fred Fontaine, Gabin Sihn, Michael Bader, Amrita Ahluwalia, and Johan Duchene. CXCL5 limits macrophage foam cell formation in atherosclerosis. *Journal of Clinical Investigation*, 123(3):1343–1347, February 2013.

[162] L J H van Tits, R Stienstra, P L van Lent, M G Netea, L A B Joosten, and A F H Stalenhoef. Oxidized LDL enhances pro-inflammatory responses of alternatively activated M2 macrophages: A crucial role for KrÃppel-like factor 2. 214(2):345–349, February 2011.

[163] J Lauran Stöger, Marion J J Gijbels, Saskia van der Velden, Marco Manca, Chris M van der Loos, Erik A L Biessen, Mat J A P Daemen, Esther Lutgens, and Menno P J de Winther. Distribution of macrophage polarization markers in human atherosclerosis. 225(2):461–468, December 2012.

[164] N Leitinger and I G Schulman. Phenotypic Polarization of Macrophages in Atherosclerosis. *Arteriosclerosis, Thrombosis, and Vascular Biology*, 33(6):1120–1126, May 2013.

[165] R Bartz, W H Li, B Venables, J K Zehmer, M R Roth, R Welti, R G W Anderson, P Liu, and K D Chapman. Lipidomics reveals that adiposomes store ether lipids and mediate phospholipid traffic,. *The Journal of Lipid Research*, 48(4):837–847, January 2007.

[166] W S Blaner, S M O'Byrne, N Wongsiriroj, and J Kluwe. Hepatic stellate cell lipid droplets: A specialized lipid droplet for retinoid storage. *Biochimica et Biophysica Acta*, pages 467–473, 2009.

[167] K Tauchi-Sato. The Surface of Lipid Droplets Is a Phospholipid Monolayer with a Unique Fatty Acid Composition. *Journal of Biological Chemistry*, 277(46):44507–44512, September 2002.

[168] Adrienne D Kinkel, Melinda E Fernyhough, Deri L Helterline, Janet L Vierck, Karen S Oberg, Tyler J Vance, Gary J Hausman, Rodney A Hill, and Michael V Dodson. Oil

red-O stains non-adipogenic cells: a precautionary note. *Cytotechnology*, 46(1):49–56, June 2005.

[169] X Nan. Vibrational imaging of lipid droplets in live fibroblast cells with coherent anti-Stokes Raman scattering microscopy. *The Journal of Lipid Research*, 44(11): 2202–2208, August 2003.

[170] Christian Matthäus, Sebastian Dochow, Gero Bergner, Annika Lattermann, Bernd F M Romeike, Eric T Marple, Christoph Krafft, Benjamin Dietzek, Bernhard R Brehm, and Juergen Popp. In vivo Characterization of Atherosclerotic Plaque Depositions by Raman-Probe Spectroscopy and in vitro CARS-Microscopic Imaging on a Rabbit Model. *Analytical chemistry*, August 2012.

[171] P Morgado, Y C Ong, J C Boothroyd, and M B Lodoen. Toxoplasma gondii Induces B7-2 Expression through Activation of JNK Signal Transduction. *Infection and Immunity*, 79(11):4401–4412, October 2011.

[172] Peter Libby, Paul M Ridker, and Göran K Hansson. Progress and challenges in translating the biology of atherosclerosis. *Nature*, 473(7347):317–325, May 2011.

[173] K Taylor E J Bartucci K Fischer-Dzoga J H Beeson S Glagov R W Wissler T Schaffner. Arterial foam cells with distinctive immunomorphologic and histochemical features of macrophages. *The American Journal of Pathology*, 100(1):57, July 1980.

[174] Jamila Khallou-Laschet, Aditi Varthaman, Giulia Fornasa, Caroline Compain, Anh-Thu Gaston, Marc Clement, Michaël Dussiot, Olivier Levillain, Stéphanie Graff-Dubois, Antonino Nicoletti, and Giuseppina Caligiuri. Macrophage plasticity in experimental atherosclerosis. *PLoS ONE*, 5(1):e8852, 2010.

[175] Jonathan E Feig, Sajesh Parathath, James X Rong, Stephanie L Mick, Yuliya Vengrenyuk, Lisa Grauer, Stephen G Young, and Edward A Fisher. Reversal of hyperlipidemia with a genetic switch favorably affects the content and inflammatory state of macrophages in atherosclerotic plaques. *Circulation*, 123(9):989–998, March 2011.

[176] F H Epstein and R Ross. Atherosclerosis—an inflammatory disease. *New England Journal of Medicine*, 1999.

[177] M Amine Bouhlel, Bruno Derudas, Elena Rigamonti, Rébecca Dièvart, John Brozek, Stéphan Haulon, Christophe Zawadzki, Brigitte Jude, Gérard Torpier, Nikolaus Marx, Bart Staels, and Giulia Chinetti-Gbaguidi. PPARγ Activation Primes Human Monocytes into Alternative M2 Macrophages with Anti-inflammatory Properties. *Cell Metabolism*, 6(2):137–143, August 2007.

[178] Aloke V Finn, Masataka Nakano, Rohini Polavarapu, Vinit Karmali, Omar Saeed, XiaoQing Zhao, Saami Yazdani, Fumiyuki Otsuka, Talina Davis, Anwer Habib, Jagat Narula, Frank D Kolodgie, and Renu Virmani. Hemoglobin Directs Macrophage Differentiation and Prevents Foam Cell Formation in Human Atherosclerotic Plaques. *Journal of the American College of Cardiology*, 59(2):166–177, January 2012.

[179] Alberto Mantovani, Paola Allavena, Antonio Sica, and Frances Balkwill. Cancer-related inflammation. *Nature*, 454(7203):436–444, July 2008.

[180] Bart Legein, Lieve Temmerman, Erik A L Biessen, and Esther Lutgens. Inflammation and immune system interactions in atherosclerosis. *Cellular and Molecular Life Sciences*, February 2013.

[181] Kathryn J Moore, Frederick J Sheedy, and Edward A Fisher. Macrophages in atherosclerosis:a dynamic balance. pages 1–13, August 2013.

[182] David M Mosser. The many faces of macrophage activation. *Journal of leukocyte biology*, 2003.

[183] S Fujisaka, I Usui, A Bukhari, M Ikutani, T Oya, Y Kanatani, K Tsuneyama, Y Nagai, K Takatsu, M Urakaze, M Kobayashi, and K Tobe. Regulatory Mechanisms for Adipose Tissue M1 and M2 Macrophages in Diet-Induced Obese Mice. *Diabetes*, 58(11):2574–2582, October 2009.

[184] Frances Y McWhorter, Tingting Wang, Phoebe Nguyen, Thanh Chung, and Wendy F Liu. Modulation of macrophage phenotype by cell shape. *Proceedings of the National Academy of Sciences of the United States of America*, 110(43):17253–17258, October 2013.

[185] U Muller, W Stenzel, G Kohler, C Werner, T Polte, G Hansen, N Schutze, R K Straubinger, M Blessing, A N J McKenzie, F Brombacher, and G Alber. IL-13 Induces Disease-Promoting Type 2 Cytokines, Alternatively Activated Macrophages and Allergic Inflammation during Pulmonary Infection of Mice with Cryptococcus neoformans. *The Journal of Immunology*, 179(8):5367–5377, October 2007.

[186] Ruben Orihuela, Christopher A McPherson, and Gaylia Jean Harry. Microglial M1/M2 polarization and metabolic states. *British Journal of Pharmacology*, May 2015.

[187] Subhra K Biswas and Alberto Mantovani. Orchestration of metabolism by macrophages. *Cell Metabolism*, 15(4):432–437, April 2012.

[188] K Eto. Role of NADH Shuttle System in Glucose-Induced Activation of Mitochondrial Metabolism and Insulin Secretion. *Science*, 283(5404):981–985, February 1999.

[189] Mary C McKenna, Helle S Waagepetersen, Arne Schousboe, and Ursula Sonnewald. Neuronal and astrocytic shuttle mechanisms for cytosolic-mitochondrial transfer of reducing equivalents: Current evidence and pharmacological tools. *Biochemical Pharmacology*, 71(4):399–407, February 2006.

[190] David L Halaney, Aydin Zahedivash, Jennifer E Phipps, Tianyi Wang, Jordan Dwelle, Claude Jourdan Le Saux, Reto Asmis, Thomas E Milner, and Marc D Feldman. Differences in forward angular light scattering distributions between M1 and M2 macrophages. *Journal of Biomedical Optics*, 20(11):115002, November 2015.

[191] Chiara Stringari, Amanda Cinquin, Olivier Cinquin, Michelle A Digman, Peter J Donovan, and Enrico Gratton. Phasor approach to fluorescence lifetime microscopy distinguishes different metabolic states of germ cells in a live tissue. *Proceedings of the National Academy of Sciences*, 108(33):13582–13587, 2011.

[192] Chiara Stringari, Jamison L Nourse, Lisa A Flanagan, and Enrico Gratton. Phasor fluorescence lifetime microscopy of free and protein-bound NADH reveals neural stem cell differentiation potential. *PLoS ONE*, 7(11):e48014, 2012.

[193] Kyle P Quinn, Gautham V Sridharan, Rebecca S Hayden, David L Kaplan, Kyongbum Lee, and Irene Georgakoudi. Quantitative metabolic imaging using endogenous fluorescence to detect stem cell differentiation. *Scientific Reports*, 3, December 2013.

[194] Melissa C Skala, Kristin M Riching, Annette Gendron-Fitzpatrick, Jens Eickhoff, Kevin W Eliceiri, John G White, and Nirmala Ramanujam. In vivo multiphoton microscopy of NADH and FAD redox states, fluorescence lifetimes, and cellular morphology in precancerous epithelia. *Proceedings of the National Academy of Sciences of the United States of America*, 104(49):19494–19499, December 2007.

[195] J Ma, T Chen, J Mandelin, A Ceponis, N E Miller, M Hukkanen, G F Ma, and Y T Konttinen. Regulation of macrophage activation. *Cellular and Molecular Life Sciences*, 60(11):2334–2346, November 2003.

[196] Chiara Stringari, Robert A Edwards, Kira T Pate, Marian L Waterman, Peter J Donovan, and Enrico Gratton. Metabolic trajectory of cellular differentiation in small intestine by Phasor Fluorescence Lifetime Microscopy of NADH. *Scientific Reports*, 2: 568, 2012.

[197] Rupsa Datta, Alba Alfonso Garcia, Rachel Cinco, and Enrico Gratton. Fluorescence lifetime imaging of endogenous biomarker of oxidative stress. *Scientific Reports*, 5: 9848, May 2015.

[198] Juan-Carlos Rodríguez-Prados, Paqui G Través, Jimena Cuenca, Daniel Rico, Julián Aragonés, Paloma Martín-Sanz, Marta Cascante, and Lisardo Boscá. Substrate Fate in Activated Macrophages: A Comparison between Innate, Classic, and Alternative Activation. 2010.

[199] D Vats, L Mukundan, J I Odegaard, L Zhang, and K L Smith. Oxidative metabolism and PGC-1β attenuate macrophage-mediated inflammation. *Cell Metabolism*, 2006.

[200] Belinda K Wright, Laura M Andrews, Mark R Jones, Chiara Stringari, Michelle A Digman, and Enrico Gratton. Phasor-flim analysis of NADH distribution and localization in the nucleus of live progenitor myoblast cells. *Microscopy Research and Technique*, 75(12):1717–1722, September 2012.

[201] Kathryn J Moore and Ira Tabas. Macrophages in the pathogenesis of atherosclerosis. *Cell*, 145(3):341–355, April 2011.

[202] Antonio Sica and Alberto Mantovani. Macrophage plasticity and polarization: in vivo veritas. *Journal of Clinical Investigation*, 122(3):787–795, 2012.

[203] Sophia Y Breusegem, Nabil Halaihel, Makoto Inoue, Hubert Zajicek, Eleanor Lederer, Nicholas P Barry, Victor Sorribas, and Moshe Levi. Acute and chronic changes in cholesterol modulate Na-Pi cotransport activity in OK cells. *American journal of physiology. Renal physiology*, 289(1):F154–65, July 2005.

[204] Y I Posudin, N P Massjuk, and G G Lilitskaya. Identification of Photoreceptor Pigments. *Photomovement of Dunaliella Teod.*, 2010.

[205] F T Wolf and M V Stevens. THE FLUORESCENCE OF CAROTENOIDS - Wolf - 1967 - Photochemistry and Photobiology - Wiley Online Library. *Photochemistry and Photobiology*, 1967.

[206] Jean-Michel I Maarek, Laura Marcu, Wendy J Snyder, and Warren S Grundfest. Timeresolved Fluorescence Spectra of Arterial Fluorescent Compounds: Reconstruction with the Laguerre Expansion Technique. *Photochemistry and Photobiology*, 71(2): 178–187, 2000.

[207] Laura Marcu, Jean-Michel I Maarek, and Warren S Grundfest. Time-resolved laser-induced fluorescence of lipids involved in development of atherosclerotic lesion lipid-rich core. In Robert R Alfano, editor, *BiOS '98 International Biomedical Optics Symposium*, pages 158–167. SPIE, April 1998.

[208] L I Laifer, K M O'Brien, M L Stetz, G R Gindi, T J Garrand, and L I Deckelbaum. Biochemical basis for the difference between normal and atherosclerotic arterial fluorescence. *Circulation*, 80(6):1893–1901, December 1989.

[209] Wulf Dröge. Free Radicals in the Physiological Control of Cell Function. *Physiological reviews*, 82(1):47–95, January 2002.

[210] B D'Autréaux and M B Toledano. ROS as signalling molecules: mechanisms that generate specificity in ROS homeostasis : Abstract : Nature Reviews Molecular Cell Biology. *Nature Reviews Molecular Cell Biology*, 2007.

[211] Toren Finkel. Signal transduction by reactive oxygen species. *The Journal of cell biology*, 194(1):7–15, July 2011.

[212] A C Maritim, R A Sanders, and J B Watkins. Diabetes, oxidative stress, and antioxidants: A review. *Journal of Biochemical and Molecular Toxicology*, 2003.

[213] H S Park, S R Kim, and Y C Lee. Impact of oxidative stress on lung diseases - PARK - 2008 - Respirology - Wiley Online Library. *Respirology*, 2009.

[214] Shigetada Furukawa, Takuya Fujita, Michio Shimabukuro, Masanori Iwaki, Yukio Yamada, Yoshimitsu Nakajima, Osamu Nakayama, Makoto Makishima, Morihiro Matsuda, and Iichiro Shimomura. Increased oxidative stress in obesity and its impact on metabolic syndrome. *Journal of Clinical Investigation*, 114(12):1752–1761, 2004.

[215] Naoto Matsuzawa-Nagata, Toshinari Takamura, Hitoshi Ando, Seiji Nakamura, Seiichiro Kurita, Hirofumi Misu, Tsuguhito Ota, Masayoshi Yokoyama, Masao Honda, Ken-ichi Miyamoto, and Shuichi Kaneko. Increased oxidative stress precedes the onset of high-fat diet–induced insulin resistance and obesity. *Metabolism*, 57(8):1071–1077, August 2008.

[216] Bayani Uttara, Ajay V Singh, Paolo Zamboni, and R T Mahajan. Oxidative Stress and Neurodegenerative Diseases: A Review of Upstream and Downstream Antioxidant Therapeutic Options. *Current Neuropharmacology*, 7(1):65–74, 2009.

[217] S Reuter, S C Gupta, and M M Chaturvedi. Oxidative stress, inflammation, and cancer: How are they linked? *Free Radical Biology and Medicine*, pages 1603–1616, 2010.

[218] V Crosignani, S Jahid, and A S Dvornikov. A deep tissue fluorescence imaging system with enhanced SHG detection capabilities. *Microscopy Research and Technique*, 2014.

[219] Mrittika Chattopadhyay, Vineet Kumar Khemka, Gargi Chatterjee, Anirban Ganguly, Satinath Mukhopadhyay, and Sasanka Chakrabarti. Enhanced ROS production and oxidative damage in subcutaneous white adipose tissue mitochondria in obese and type 2 diabetes subjects. *Molecular and cellular biochemistry*, 399(1-2):95–103, January 2015.

[220] Hiroyuki Shimasaki. [36] Assay of fluorescent lipid peroxidation products. pages 338–346. Elsevier, 1994.

[221] L Wojtczak and P Schönfeld. *Effect of fatty acids on energy coupling processes in mitochondria.* Biochimica et Biophysica Acta, 1993.

[222] Hendrik Gremmels, Lonneke M Bevers, Joost O Fledderus, Branko Braam, Anton Jan van Zonneveld, Marianne C Verhaar, and Jaap A Joles. Oleic acid increases mitochondrial reactive oxygen species production and decreases endothelial nitric oxide synthase activity in cultured endothelial cells. *European journal of pharmacology*, 751: 67–72, March 2015.

[223] D Débarre, W Supatto, A M Pena, and A Fabre. Imaging lipid bodies in cells and tissues using third-harmonic generation microscopy - Nature Methods. *Nature*, 2006.

[224] N Sitte, K Merker, T Grune, and T Von Zglinicki. Lipofuscin accumulation in proliferating fibroblasts in vitro: an indicator of oxidative stress. *Experimental gerontology*, 2001.

[225] Martin L Katz, Graig E Eldred, and W Gerald Robison, Jr. Lipofuscin autofluorescence: Evidence for vitamin A involvement in the retina. *Mechanisms of Ageing and Development*, 39(1):81–90, June 1987.

[226] Chiara Stringari. Label-free separation of human embryonic stem cells and their differentiating progenies by phasor fluorescence lifetime microscopy. *Journal of Biomedical Optics*, 17(4):046012, April 2012.

[227] Dietrich Schweitzer, Elizabeth R Gaillard, James Dillon, Robert F Mullins, Stephen Russell, Birgit Hoffmann, Sven Peters, Martin Hammer, and Christoph Biskup. Time-Resolved Autofluorescence Imaging of Human Donor Retina Tissue from Donors with Significant Extramacular Drusen. *Investigative Opthalmology & Visual Science*, 53(7): 3376, June 2012.

[228] Tivadar Orban, Grazyna Palczewska, and Krzysztof Palczewski. Retinyl Ester Storage Particles (Retinosomes) from the Retinal Pigmented Epithelium Resemble Lipid Droplets in Other Tissues. *Journal of Biological Chemistry*, 286(19):17248–17258, May 2011.

[229] Elina Ikonen. Mechanisms for cellular cholesterol transport: defects and human disease. *Physiological reviews*, 86(4):1237–1261, 2006.

[230] Kai Simons and Robert Ehehalt. Cholesterol, lipid rafts, and disease. *Journal of Clinical Investigation*, 110(5):597–603, September 2002.

[231] Khayriyyah Mohd Hanafiah, Justina Groeger, Abraham D Flaxman, and Steven T Wiersma. Global epidemiology of hepatitis C virus infection: New estimates of age-specific antibody to HCV seroprevalence. *Hepatology*, 57(4):1333–1342, 2013.

[232] M V Machado and A G Oliveira. Hepatic steatosis in hepatitis B virus infected patients: Meta-analysis of risk factors and comparison with hepatitis C infected patients. *Journal of Gastroenterology and Hepatology*, 2011.

[233] J Grebely and G J Dore. What is killing people with hepatitis C virus infection? *Seminars in Liver Diseases*, 2011.

[234] Laura Rubbia-Brandt, Rafael Quadri, Karim Abid, Emiliano Giostra, Pierre-Jean Malé, Gilles Mentha, Laurent Spahr, Jean-Pierre Zarski, Bettina Borisch, Antoine Hadengue, and Francesco Negro. Hepatocyte steatosis is a cytopathic effect of hepatitis C virus genotype 3. *Journal of Hepatology*, 33(1):106–115, July 2000.

[235] K Abid, V Pazienza, A de Gottardi, and L Rubbia-Brandt. An in vitro model of hepatitis C virus genotype 3a-associated triglycerides accumulation. *Journal of Hepatology*, 42:744–751, 2005.

[236] Laurence S Lim FRCSEd, Prof Paul Mitchell MD, Prof Johanna M Seddon MD, Prof Frank G Holz MD, and Prof Tien Y Wong MD. Age-related macular degeneration. *The Lancet*, 379(9827):1728–1738, May 2012.

[237] J M van der Walt, K K Nicodemus, and E R Martin. Mitochondrial Polymorphisms Significantly Reduce the Risk of Parkinson Disease. *The American Journal of Human Genetics*, 72:804–811, 2003.

[238] G Atzmon, M Rincon, P Rabizadeh, and N Barzilai. Biological evidence for inheritance of exceptional longevity. *Mechanisms of Ageing and Development*, 126:341–345, 2005.

[239] Daniele Ghezzi, Cecilia Marelli, Alessandro Achilli, Stefano Goldwurm, Gianni Pezzoli, Paolo Barone, Maria Teresa Pellecchia, Paolo Stanzione, Livia Brusa, Anna Rita Bentivoglio, Ubaldo Bonuccelli, Lucia Petrozzi, Giovanni Abbruzzese, Roberta Marchese, Pietro Cortelli, Daniela Grimaldi, Paolo Martinelli, Carlo Ferrarese, Barbara Garavaglia, Simonetta Sangiorgi, Valerio Carelli, Antonio Torroni, Alberto Albanese, and Massimo Zeviani. Mitochondrial DNA haplogroup K is associated with a lower risk of Parkinson's disease in Italians. *European Journal of Human Genetics*, 13(6):748–752, April 2005.

[240] M Houshmand, M H Sanati, F Babrzadeh, A Ardalan, M Teimori, M Vakilian, M Akuchekian, D Farhud, and J Lotfi. Population screening for association of mitochondrial haplogroups BM, J, K and M with multiple sclerosis: interrelation between haplogroup J and MS in Persian patients. *Multiple Sclerosis*, 11(6):728–730, December 2005.

[241] Hassan Hassani Kumleh, Massoud Houshmand, Mehdi Shafa Shariat Panahi, Gholam Hossein Riazi, Mohammad Hossein Sanati, Kurosh Gharagozli, and Mojdeh Ghabaee. Mitochondrial D-Loop Variation in Persian Multiple Sclerosis Patients: K and A Haplogroups as a Risk Factor!! *Cellular and Molecular Neurobiology*, 26(2): 119–125, May 2006.

[242] P F Chinnery, H R Elliott, A Syed, and P M Rothwell. Mitochondrial DNA haplogroups and risk of transient ischaemic attack and ischaemic stroke: a genetic association study. *The Lancet Neurology*, 2010.

[243] Aurora Gómez-Durán, David Pacheu-Grau, Ester López-Gallardo, Carmen Díez-Sánchez, Julio Montoya, Manuel J López-Pérez, and Eduardo Ruiz-Pesini. Unmasking the causes of multifactorial disorders: OXPHOS differences between mitochondrial haplogroups. *Human Molecular Genetics*, 19(17):3343–3353, 2010.

[244] Christian M Hagen, Frederik H Aidt, Paula L Hedley, Morten K Jensen, Ole Havndrup, Jørgen K Kanters, Johanna C Moolman-Smook, Severin O Larsen, Henning Bundgaard, and Michael Christiansen. Mitochondrial Haplogroups Modify the Risk of Developing Hypertrophic Cardiomyopathy in a Danish Population. *PLoS ONE*, 8(8): e71904, August 2013.

[245] Zanyar Movasaghi, Shazza Rehman, and Ihtesham U Rehman. Raman Spectroscopy of Biological Tissues. *Applied Spectroscopy Reviews*, 42(5):493–541, September 2007.

[246] Ursula Loizides-Mangold, Sophie Clément, Alba Alfonso Garcia, Emilie Branche, Stéphanie Conzelmann, Clotilde Parisot, Eric O Potma, Howard Riezman, and Francesco Negro. HCV 3a Core Protein Increases Lipid Droplet Cholesteryl Ester Content via a Mechanism Dependent on Sphingolipid Biosynthesis. *PLoS ONE*, 9(12): e115309, December 2014.

[247] S Mukherjee, X Zha, I Tabas, and F R Maxfield. Cholesterol distribution in living cells: fluorescence imaging using dehydroergosterol as a fluorescent cholesterol analog. 75(4):1915–1925, October 1998.

[248] Gary B Smejkal, George Hoppe, and Henry F Hoff. Filipin as a Fluorescent Probe of Lipoprotein-Derived Sterols on Thin-Layer Chromatograms. *Analytical Biochemistry*, 239(1):115–117, July 1996.

[249] Gerald Gimpl and Katja Gehrig-Burger. Cholesterol Reporter Molecules. *Bioscience Reports*, 27(6):335–358, August 2007.

[250] R Cicchi, C Matthäus, and T Meyer. Characterization of collagen and cholesterol deposition in atherosclerotic arterial tissue using non-linear microscopy. *Journal of Biophotonics*, 7(1-2):135–143, 2014.

[251] Se-Hwa Kim, Eun-Soo Lee, Jae Yong Lee, Eun Seong Lee, Bok-Soo Lee, Jeong Euy Park, and Dae Won Moon. Multiplex Coherent Anti-Stokes Raman Spectroscopy Images Intact Atheromatous Lesions and Concomitantly Identifies Distinct Chemical Profiles of Atherosclerotic Lipids. *Circulation*, 2010.

[252] Jeffrey L Suhalim, Chao-Yu Chung, Magnus B Lilledahl, Ryan S Lim, Moshe Levi, Bruce J Tromberg, and Eric O Potma. Characterization of Cholesterol Crystals in Atherosclerotic Plaques Using Stimulated Raman Scattering and Second-Harmonic Generation Microscopy. 102(8):1988–1995, April 2012.

[253] Ping Wang, Junjie Li, Pu Wang, Chun-Rui Hu, Delong Zhang, Michael Sturek, and Ji-Xin Cheng. Label-Free Quantitative Imaging of Cholesterol in Intact Tissues by Hyperspectral Stimulated Raman Scattering Microscopy. *Angewandte Chemie International Edition*, 52(49):13042–13046, October 2013.

[254] Hyeon Jeong Lee, Wandi Zhang, Delong Zhang, Yang Yang, Bin Liu, Eric L Barker, Kimberly K Buhman, Lyudmila V Slipchenko, Mingji Dai, and Ji-Xin Cheng. Assessing Cholesterol Storage in Live Cells and C. elegans by Stimulated Raman Scattering Imaging of Phenyl-Diyne Cholesterol. *Scientific Reports*, 5:7930, January 2015.

[255] Clara Stiebing, Christian Matthäus, Christoph Krafft, Andrea-Anneliese Keller, Karina Weber, Stefan Lorkowski, and Jürgen Popp. Complexity of fatty acid distribution inside human macrophages on single cell level using Raman micro-spectroscopy. *Analytical and Bioanalytical Chemistry*, 406(27):7037–7046, June 2014.

[256] Lu Wei, Yihui Shen, Fang Xu, Fanghao Hu, Jamie K Harrington, Kimara L Targoff, and Wei Min. Imaging Complex Protein Metabolism in Live Organisms by Stimulated Raman Scattering Microscopy with Isotope Labeling. *ACS Chemical Biology*, 10(3): 901–908, March 2015.

[257] D J Kushner, Alison Baker, and T G Dunstall. Pharmacological uses and perspectives of heavy water and deuterated compounds. *Canadian Journal of Physiology and Pharmacology*, 77(2):79–88, February 1999.

[258] Cleiton M Souza, Tatjana M E Schwabe, Harald Pichler, Birgit Ploier, Erich Leitner, Xue Li Guan, Markus R Wenk, Isabelle Riezman, and Howard Riezman. A stable yeast strain efficiently producing cholesterol instead of ergosterol is functional for tryptophan

uptake, but not weak organic acid resistance. *Metabolic Engineering*, 13(5):555–569, September 2011.

[259] R Shivapurkar, C M Souza, D Jeannerat, and H Riezman. An efficient method for the production of isotopically enriched cholesterol for NMR. *The Journal of Lipid Research*, 52(5):1062–1065, April 2011.

[260] K Hsieh, Y K Lee, C Londos, B M Raaka, K T Dalen, and A R Kimmel. Perilipin family members preferentially sequester to either triacylglycerol-specific or cholesteryl-ester-specific intracellular lipid storage droplets. *Journal of Cell Science*, 125(17):4067–4076, October 2012.

[261] Joseph L Goldstein, Sandip K Basu, and Michael S Brown. Receptor-mediated endocytosis of low-density lipoprotein in cultured cells. *Methods in enzymology*, 98:241–260, June 1983.

[262] Godofredo Bautista, Simon G Pfisterer, Mikko J Huttunen, Sanjeev Ranjan, Kristiina Kanerva, Elina Ikonen, and Martti Kauranen. Polarized THG Microscopy Identifies Compositionally Different Lipid Droplets in Mammalian Cells. 107(10):2230–2236, November 2014.

[263] Delong Zhang, Ping Wang, Mikhail N Slipchenko, Dor Ben-Amotz, Andrew M Weiner, and Ji-Xin Cheng. Quantitative Vibrational Imaging by Hyperspectral Stimulated Raman Scattering Microscopy and Multivariate Curve Resolution Analysis. *Analytical chemistry*, 85(1):98–106, January 2013.

[264] Joel T Tabarangao and Aaron D Slepkov. Mimicking Multimodal Contrast with Vertex Component Analysis of Hyperspectral CARS Images. *Journal of Spectroscopy*, 2015: 1–8, 2015.

[265] A E Christian, M P Haynes, M C Phillips, and G H Rothblat. Use of cyclodextrins for manipulating cellular cholesterol content. *The Journal of Lipid Research*, 38(11): 2264–2272, 1997.

[266] M J Amiot, D Knol, N Cardinault, M Nowicki, R Bott, C Antona, P Borel, J P Bernard, G Duchateau, and D Lairon. Phytosterol ester processing in the small intestine: impact on cholesterol availability for absorption and chylomicron cholesterol incorporation in healthy humans. *The Journal of Lipid Research*, 52(6):1256–1264, May 2011.

[267] D Lütjohann, C O Meese, J R Crouse, and K von Bergmann. Evaluation of deuterated cholesterol and deuterated sitostanol for measurement of cholesterol absorption in humans. *Journal of lipid research*, 34:1039–1046, 1993.

[268] K Czamara, K Majzner, M Z Pacia, K Kochan, A Kaczor, and M Baranska. Raman spectroscopy of lipids: a review. *Journal of Raman Spectroscopy*, 46(1):4–20, December 2014.

[269] N Kory, A R Thiam, R V Farese, and T C Walther. Protein Crowding Is a Determinant of Lipid Droplet Protein Composition. *Developmental Cell*, 2015.

[270] Bo Feng, Pin Mei Yao, Yankun Li, Cecilia M Devlin, Dajun Zhang, Heather P Harding, Michele Sweeney, James X Rong, George Kuriakose, Edward A Fisher, Andrew R Marks, David Ron, and Ira Tabas. The endoplasmic reticulum is the site of cholesterol-induced cytotoxicity in macrophages. *Nature Cell Biology*, 5(9):781–792, August 2003.

[271] I F Craig, D P Via, B C Sherrill, and L A Sklar. Incorporation of defined cholesteryl esters into lipoproteins using cholesteryl ester-rich microemulsions. *Journal of Biological Chemistry*, 257(1):330–335, January 1982.

[272] D P Via, I F Craig, G W Jacobs, and W B Van Winkle. Cholesteryl ester-rich microemulsions: stable protein-free analogs of low density lipoproteins. *Journal of lipid research*, 23:570–576, 1982.

[273] P Laggner, G M Kostner, and G Degovics. Structure of the cholesteryl ester core of human plasma low density lipoproteins: Selective deuteration and neutron small-angle scattering. In *Proceedings of the Natural Academy of Sciences*, volume 81, pages 4389–4393, 1984.

[274] John F Oram. Receptor-mediated transport of cholesterol between cultured cells and high-density lipoproteins. *Methods in enzymology*, 129:1–15, April 1986.